School of Science

Hyperspectral Remote Sensing Applied to Shallow Coastal Waters

Wojciech M. Klonowski

This thesis is presented for the Degree of

Doctor of Philosophy

of

Curtin University

April 2015

Declaration

To the best of my knowledge and belief this thesis contains no material previously published by any other person except where due acknowledgment has been made.

This thesis contains no material which has been accepted for the award of any other degree or diploma in any university.

Signature: .....

Date: .....

Abstract

Hyperspectral remote sensing, particularly from airborne or on orbit systems, is a valuable tool for the rapid and detailed appraisal of large areas of coastal water environments. The large number of spectral channels of such imaging systems helps capture important spectral features contained within the water leaving signal. By unravelling the different spectral signatures, important environmental indicators such as water quality, bathymetry and benthic habitat types can be extracted. However, the highly diverse and dynamic optical constituents that are present in many coastal water environments render the remote sensing signal complex and accordingly difficult to interpret.

In this work, a shallow water optical model was developed to interpret remotely sensed data in terms of the optically active marine constituents, water depth and benthic cover. Additionally, a look-up-table of empirical model coefficients was derived to account for the effects of sun position and sensor viewing geometry on the remote sensing signal. A numerical inversion scheme, based on analytical parameterisation, was implemented to simultaneously retrieve the concentrations of in-water constituents, water depth and benthic cover type, from hyperspectral remote sensing data.

The performance of the shallow water model was tested against simulated data that was computed with the well established and validated radiative transfer model Hydrolight. The simulations included the effects of sensor-specific noise, signal quantisation and spectral resolution, typical of common hyperspectral imaging systems. The results of these tests demonstrate that the model is well suited to retrieving in-water optical properties, water depth and benthic cover information over a wide range of realistic environmental conditions.

The numerical inversion scheme was applied to airborne hyperspectral imagery collected over two regions of the Western Australian coastline; Jurien Bay and the Ningaloo Marine Park. The temperate reef system within Jurien Bay and the large fringing coral reef within the Ningaloo Marine Park presented two diverse

and challenging environments for the shallow water model. The image-derived products were validated against ground truth data.

Model-retrieved in-water optical properties compared well with *in situ* measurements, despite the very low concentrations of constituents encountered. The mean difference for Phytoplankton and CDOM absorption was $\sim$ 30% or 0.01 m^{-1} and $\sim$ 50% or 0.02 m^{-1}, respectively. The bathymetry products were validated against acoustic survey data covering a range from 1 m to 18 m depth. The average RMS errors in depth retrieval were consistent for both coastal regions at $\sim$ 8%, equivalent to an absolute average error of $\pm$0.2 m. The validation of the benthic classification products was assessed by comparing inversion-derived benthic cover with a number of co-incident underwater video observations. The results demonstrated the models capability of discriminating between 3 key benthic cover classes with a good degree of confidence.

Acknowledgments

I would like to thank my supervisor, Professor Mervyn J. Lynch, for whom I have the greatest respect and for providing me with the opportunity to undertake this final degree. I would like to express my sincere gratitude to Merv, for the encouragement and invaluable advice he has provided me during this time. He has been and continues to be a valued mentor.

I would also like to thank Dr Peter Fearns, for his generosity in sharing his knowledge and understanding of remote sensing. His great sense of humor has been much appreciated over the years.

I have had the fortune of working along side my colleagues, Leon Majewski, Florian Goessman and Matthew Slivkoff who have all offered their specialist expertise and been a constant support. They have become close friends. I have been blessed to work with a friendly and cheerful group of fellow students at the Remote Sensing and Satellite Research Group.

I wish to thank my entire extended family for providing a loving environment and showing belief in my abilities. And lastly, my wife Emily for her continual moral support and encouragement.

I would like to acknowledge the following for their financial and logistic support;

- The Department of Imaging and Applied Physics, Curtin University
- The Remote Sensing and Satellite Research Group
- Curtin University Postgraduate Students Association
- The Stratiegic Research Fund for the Marine Environment
- CSIRO Marine & Atmospheric Research
- CSIRO Land and Water

Contents

List of Figures

List of Tables

List of Acronyms

ALUT	Adaptive Look-Up-Tree
AOP	Apparent Optics Properties
BIL	Band Interleaved by Line
BRDF	Bidirectional Reflectance Distribution Function
CDOM	Coloured Dissolved Organic Material
Chl-a	Chlorophyll-a
CLUT	Coarse Look-Up-Table
CZCS	Coastal Zone Colour Scanner
DALEC	Dynamic Above-water radiance (L) and irradiance (E) Collector
DN	Digital Number
DOM	Dissolved Organic Matter
FOV	Field-of-View
GPS	Global Positioning System
HPLC	High Precision Liquid Chromatography
IDL	Interactive Data Language
IFOV	Instantaneous Field-of-View
IOCCG	International Ocean Colour Coordinating Group
IOP	Inherent Optics Properties
LUT	Look-up-Table
MERIS	MEdium Resolution Imaging Spectroradiometer
MODIS	MODerate Resolution Imaging Spectroradiometer
NIR	Near Infra-red
NRL	Naval Research Laboratory
PPF	Particle Phase Function
RMS	Root Mean Squared
RMSE	Root Mean Squared Error
RTE	Radiative Transfer Equation
SeaWIFS	Sea-viewing Wide-Field-of-view Sensor
SNR	Signal-to-Noise Ratio
VIIRS	Visible Infrared Imaging Radiometer Suite
VSF	Volume Scattering Function
3-D	3 Dimensional

List of Symbols

Symbols	units	Description
a	m^{-1}	total absorption coefficient
a_{CDOM}	m^{-1}	absorption coefficient of Coloured Dissolved Organic Material
a_{phi}	m^{-1}	absorption coefficient of phytoplankton pigments
a_w	m^{-1}	absorption coefficient of water
b	m^{-1}	total scattering coefficient
b_b	m^{-1}	backscattering coefficient
b_f	m^{-1}	forward scattering coefficient
b_p	m^{-1}	scattering coefficient of suspended particles
b_w	m^{-1}	scattering coefficient of pure water
b_{bp}	m^{-1}	backscattering coefficient of suspended particles
b_{bw}	m^{-1}	backscattering coefficient of pure water
β	$\mathrm{m}^{-1}\mathrm{sr}^{-1}$	volume scattering function
$\hat{\beta}$	$\mathrm{m}^{-1}\mathrm{sr}^{-1}$	particle phase function
β_p	$\mathrm{m}^{-1}\mathrm{sr}^{-1}$	volume scattering function of suspended particles
β_w	$\mathrm{m}^{-1}\mathrm{sr}^{-1}$	volume scattering function of water
B_{sd}		bottom albedo of sediment
B_{sg}		bottom albedo of seagrass
B_{ba}		bottom albedo of brown algae
c	m^{-1}	beam attenuation coefficient
C	mgm^{-3}	concentration of phytoplankton
D_d		distribution function for downwelling light
D_u		distribution function for upwelling light
E	$\mathrm{Wm}^{-2}\mathrm{nm}^{-1}$	irradiance
E_d	$\mathrm{Wm}^{-2}\mathrm{nm}^{-1}$	downwelling irradiance
E_u	$\mathrm{Wm}^{-2}\mathrm{nm}^{-1}$	upwelling irradiance
E_0	$\mathrm{Wm}^{-2}\mathrm{nm}^{-1}$	scalar irradiance
E_{0d}	$\mathrm{Wm}^{-2}\mathrm{nm}^{-1}$	downwelling scalar irradiance
E_{0u}	$\mathrm{Wm}^{-2}\mathrm{nm}^{-1}$	upwelling scalar irradiance
H	m	water column depth
K	m^{-1}	diffuse attenuation coefficient
K_l	m^{-1}	diffuse attenuation coefficient for radiance

K_d	m^{-1}	diffuse attenuation coefficient for downwelling light
K_u	m^{-1}	diffuse attenuation coefficient for upwelling light
K_u^C	m^{-1}	upwelling diffuse attenuation from just the water
K_u^B	m^{-1}	upwelling diffuse attenuation from the seafloor
L	$\mathrm{Wm}^{-2}\mathrm{nm}^{-1}\mathrm{sr}^{-1}$	radiance
L_a	$\mathrm{Wm}^{-2}\mathrm{nm}^{-1}\mathrm{sr}^{-1}$	radiance from the atmosphere
L_b	$\mathrm{Wm}^{-2}\mathrm{nm}^{-1}\mathrm{sr}^{-1}$	radiance from the ocean bottom
L_s	$\mathrm{Wm}^{-2}\mathrm{nm}^{-1}\mathrm{sr}^{-1}$	water surface reflected radiance from sun and sky
L_{sky}	$\mathrm{Wm}^{-2}\mathrm{nm}^{-1}\mathrm{sr}^{-1}$	sky radiance
L_w	$\mathrm{Wm}^{-2}\mathrm{nm}^{-1}\mathrm{sr}^{-1}$	water leaving radiance
L_t	$\mathrm{Wm}^{-2}\mathrm{nm}^{-1}\mathrm{sr}^{-1}$	total above-water radiance
L_u	$\mathrm{Wm}^{-2}\mathrm{nm}^{-1}\mathrm{sr}^{-1}$	total upwelling radiance
Q	J	radiant energy
R		irradiance reflectance
r_{rs}	sr^{-1}	subsurface remote sensing reflectance
r_{rs}^W	sr^{-1}	r_{rs} emanating from the water column
r_{rs}^B	sr^{-1}	r_{rs} emanating from the sea bottom
r_{rs}^∞	sr^{-1}	r_{rs} for an infinitely deep water column
R_{rs}	sr^{-1}	above-water remote sensing reflectance
S	nm^{-1}	spectral slope parameter for CDOM absorption
t	s	time
Y		spectral slope parameter for particle backscattering
$\bar{\mu}_d$		average weighted cosine for downwelling light
$\bar{\mu}_u$		average weighted cosine for upwelling light
ρ		bottom irradiance reflectance
ρ_F		Fresnel internal reflectance
ρ_R		proportionality factor of surface reflected sky radiance
θ		zenith angle for defining polar coordinates
θ_s		solar zenith angle
θ_{sw}		subsurface solar zenith angle
θ_v		sensor viewing angle from nadir
θ_{wv}		subsurface sensor viewing angle

Φ	W	radiant flux
ϕ		azimuth angle for defining polar coordinates
ϕ_v		sensor viewing azimuth angle
λ	m	wavelength of light
ω_{max}		maximum ratio of bottom to total signal

Chapter 1

Introduction

Remote sensing of ocean colour plays an increasingly important role for understanding biological, chemical and physical processes in coastal and open oceans. Information about the optically active organic and inorganic marine constituents can be extracted from the upwelling light signals or "ocean color" that emanate from the water column. Earthward-pointing optical imaging systems, onboard airborne or satellite platforms, are capable of capturing data over vast expanses of marine waters, providing a synoptic view of the abundance of such constituents. Satellite platforms that support ocean colour remote sensing also provide global coverage with repetition cycles in the order of days, giving valuable insight into the spatial dynamics of marine constituents over time.

In the open ocean, phytoplankton and their degradation products are the predominantly occurring substances that can lead to variations in observed ocean colour. This is often referred to as "Case 1" waters (IOCCG, 2000). The optically active pigments found in phytoplankton are largely dominated by chlorophyll-a (Chl-a), a photosynthetic pigment that is green in appearance and is found in most plant life (Kirk, 1983). Varying concentrations of phytoplankton, and hence Chl-a, can change the apparent "greenness" of the ocean, where, this change can be detected by optical remote sensing. Empirical algorithms that relate the variations of observed ocean colour to the concentration of Chl-a, are able to be applied to satellite ocean colour data in order to estimate the abundance of

phytoplankton and primary productivity from space. Spectacular datasets, obtained from early ocean colour sensors, such as the Coastal Zone Color Scanner (CZCS) and the Sea-viewing Wide-Field-of-view Sensor (SeaWIFS), have led to some of the first quantitative observations of global phytoplankton distribution and their seasonal dynamics (Behrenfeld et al., 2001). Present day sensors, such as the MODerate resolution Imaging Spectroradiometer (MODIS), the MEdium Resolution Imaging Spectroradiometer (MERIS) and the newly launched Visible Infrared Imaging Radiometer Suite (VIIRS), continue to provide near-daily information of the oceans' phytoplankton abundance. This type of data is extremely valuable for climate change studies, since phytoplankton, through the process of photosynthesis, collectively act as a major uptake of atmospheric carbon dioxide (CO_2) (Behrenfeld et al., 2006). Additionally, since phytoplankton growth is sensitive to specific environmental conditions, such as ocean temperature and abundance of light and nutrients, they frequently become the first indicator of a change in their environment.

Perhaps equally as important to the plant life that occurs in the open ocean, is the organic and inorganic, plant and terrigenous material that is abundant within the coastal zone. Although, only encompassing a fraction of the total water mass on the planet, coastal waters often produce some of the highest concentrations of aquatic plant material on earth, greatly contributing to the regulation of atmospheric CO_2 and oxygen (Richardson and LeDrew, 2006). Added to that, the coastal zone encompasses a wide array of complex ecosystems, supporting an immense amount of biodiversity, including important fisheries, unique and sensitive habitats and natural resources. Sadly, the health of some of these important aquatic ecosystems is in decline. The reason for the deteriorating ecosystems are complex, however, the large and growing human population near the coast is a significant part of the problem. With about a half of the world's population residing within 100 km from the shoreline, coastal areas undergo intense anthropogenic activity. Factors such as; fertiliser and sediment runoff from agricultural

lands into nearby waterways; discharging of industrial and household pollutants into rivers and oceans; increases in maritime traffic; discharge and leaks from ships; port developments, including dredging; leaks from underwater pipelines; overfishing; environmental accidents; and recreational activity, continue to change the water quality that support these fragile aquatic ecosystems. These pressures can lead to loss of biodiversity, including loss of habitats (such as seagrass beds and algal cover), coral reef bleaching, toxic algal blooms and threat to human health through increased toxins found in fish and shellfish.

One of the major challenges for scientists, environmental managers and policy makers alike, is to minimise the steady decline of our coastal waters' natural resources due to increasing human needs. Understanding the current state of our natural resources and water quality, as well as studying any long term trends are vital for ecosystem preservation and sustainability. This challenge is met with the difficulty of extracting biological, chemical and physical information from optical remote sensing of coastal environments. The complex interactions and fluxes between land, ocean and atmosphere, all result in an equally complex optical environment, typically not seen in the open ocean case. Coastal waters are commonly classified as "Case 2" waters (IOCCG, 2000). This is where the presence of optically active constituents, notably suspended sediments and coloured dissolved organic matter (CDOM), in addition to phytoplankton, can uniquely influence the remotely detected signal. Additionally, in shallow waters, the presence of substrates and diverse benthic habitats can significantly modify the upwelling light signal. Given these confounding factors, remote sensing of Case 2 waters relies on advanced techniques for decoupling the various optical signals in order to retrieve key biological, chemical and physical parameters of interest. Despite these complexities, the science of remote sensing in coastal waters has matured significantly and is proving to be an invaluable tool for ecosystem studies.

Advances in sensor technology, new algorithm developments and powerful mathematical solutions have emerged in parallel to address the need for improved

interpretation of ocean colour data in Case 2 waters. The new generation of ocean colour sensors incorporate an increasing number of spectral channels, with improved detector sensitivity, which permit the observation of subtle changes in the spectrum of light leaving the water. For example, multi-spectral ocean colour sensors such as MODIS, MERIS and VIIRS incorporate between 15 to 36 spectral bands within the visible to infrared portions of the electromagnetic spectrum. Furthermore, the positions of these spectral bands have been chosen to be most sensitive to changes in concentrations of different marine constituents, permitting the separation and retrieval of Chl-a, CDOM and suspended sediment concentration. Under favorable conditions the accurate discrimination among different phytoplankton species may also be possible. Hyperspectral sensors, such as Hyperion, HyMap and Eagle possess hundreds of spectral bands providing improved spectral resolution. The increased spectral resolution together with better spatial resolution (typically between 1 m to 30 m), makes hyperspectral remote sensing an ideal tool for bottom feature mapping in shallow coastal waters. Processing techniques such as spectral un-mixing of hyperspectral imagery, can be used to identify and map various benthic habitat types, including seagrass beds, macro algal cover and coral reefs. Some techniques can also extract the water depth from changes in intensity and spectral shape of reflected light emanating from the water.

An improved understanding of how ocean colour is influenced by different water constituents has led to the development of new model-based approaches for remote sensing of Case 2 waters. The model-based methods incorporate mathematical equations that describe the underlying physics of how light interacts within natural media. This is explained by the well established theory of radiative transfer in natural seawater. Excellent treaties on radiative transfer theory in seawater are presented in Preisendorfer (1977), Kirk (1983) Mobley (1994), and Zaneveld et al. (2005). The equations of radiative transfer formulate the light field in and above the water as a function of absorption and scattering

properties of water and water constituents. Additional effects are accounted for, including multiple scattering from molecules and suspended particles, transpectral responses to inelastic scattering such as Raman scattering and fluorescence, as well as boundary conditions such as light reflection off the seafloor and propagation of light through the air-water interface. The set of equations that describe these interactions are considered "exact" however, there is no analytical solution for the radiative transfer equation (RTE). Instead, the solution of the RTE is presented as a "forward problem" and numerical methods such as Monte Carlo and Invariant Imbedding are adopted to simulate the emerging radiant flux leaving the water. Pioneering work of Plass and Kattawar (1972) and Kattawar and Plass (1972), used Monte Carlo to simulate a plane-parallel (infinite in horizontal extent) model of a flat ocean. In the process, a large number of computer-generated photons are simulated and tracked through the model ocean. The fate of photon propagation is governed by probabilistic functions which are related to the basic photon interaction principles within the medium, namely, absorption, scattering and reflection. Finally, the photons that emerge at the ocean surface are tallied up to represent the emerging radiant flux in order to simulate the real situation.

An alternative and vastly more efficient computation of the plane-parallel model of the ocean can be simulated using the Invariant Imbedding method, as described in Mobley (1994). Here, sophisticated mathematical operators are cleverly used to reduce the multidimensional nature of the RTE into a one dimensional problem. The commercially available computer code, Hydrolight (Sequioa, Inc.) is based on such a method. The program provides a tabulated output of the full radiance distribution of visible light for a given input of the optical properties of the water and physical properties at the boundaries, such as illumination conditions, wind blown ocean surface, water depth and seafloor reflectance. A novel numerical solution to the 3-D RTE, based on new computer science techniques, is presented in Hedley (2008). The approach uses radiosity concepts to simulate the reflections off complex 3-D benthic structures, such as coral reef communities

and seagrass canopies.

The goal of remote sensing is to determine the optical and physical properties of the water column from measurements of the water leaving radiance. This becomes the "inverse problem". The general approach to solving the inverse problem is to approximate the radiative transfer by using simplifying assumptions and/or investigations through numerical modelling. For a shallow water environment, where the seafloor may add to the upwelling light stream, and assuming a homogeneous water column without the effects of inelastic scattering, approximations to the RTE have been developed based on a two-flow approximation (Lyzenga, 1978); (Philpot, 1989); (Maritorena et al., 1994) and (Lee et al., 1998) (see Appendix 7.1). In general, the shallow water approximation takes the form (Lee et al., 1998),

$$S_u \approx S_u^{dp}[1 - \exp(-2KH)] + S_u^B \exp(-2KH), \tag{1.1}$$

where, S_u represents the total upwelling light signal (just below the water surface), S_u^{dp} is the upwelling light signal for an infinitely deep water column, S_u^B is the upwelling light signal from the bottom, K is an effective attenuation coefficient and H is the water column depth. K governs the rate at which diffuse light intensity diminishes through the water column and is related to the absorption and scattering properties of the water. The first term on the right hand side of Eq. 1.1 represents the contribution of light signal originating from only the water column between the surface and depth, H. The second term represents the bottom signal that has undergone attenuation through the water column. This situation reveals that attenuation, water depth and sea bottom reflectance are intimately connected with each other in shallow water environments. In order to analytically solve for a parameter in Eq. 1.1 from remote sensing measurements alone, the remaining parameters must be known or inferred. Past studies of bottom feature mapping and water depth estimation from high spatial resolution multi-spectral imaging, have explored various methods of solving the shallow

water approximation under different simplifying assumptions.

Lyzenga (1978), Philpot (1989), Bierwirth et al. (1993) and Stumpf and Holderied (2003), evaluated methods for accounting for the attenuation and deep-water signal terms by regressing spectral bands or ratios of spectral bands over areas with known depth. The terms were held fixed over the entire image scene in order to subsequently estimate the water depth for each pixel. Although this method provides rapid assessment of bathymetry, the assumption that the water column properties are invariant over the image scene does not always hold true and can cause erroneous depth retrievals for areas with variable or patchy concentrations of water constituents. In addition to this, the method is best suited for regions where the assumption of invariant substrate or albedo is valid or for areas where an independent map of bottom type is available. Similarly, LeDrew et al. (1995) and Mumby et al. (2001), detail techniques that separate the signals from the substrate in order to map benthic cover type from spectral classification. The approach requires that the water column attenuation for each spectral band is known as well as independent knowledge of depth for each pixel. However, for most practical situations, the high resolution bathymetry that is required is rare (Bierwirth et al., 1993). Hedley and Mumby (2003), developed a method for simultaneously extracting water column depth and subpixel composition of benthic cover from multi-spectral imagery. However, *a priori* knowledge for the water column attenuation terms was still required. Unfortunately, such simplifying assumptions for the aforementioned methods rarely apply on an operational basis (Holden, 2002).

Lee et al. (1998) and Lee et al. (1999) further expanded on Eq. 1.1 and developed a semi-analytical model for shallow water remote sensing. Analytical expressions that relate both the deep-water reflectance and water column diffuse attenuation as functions of water column properties were developed through numerical simulations of radiative transfer. Furthermore, parameterisation of the water column properties and substrate reflectance allowed for a non-linear optimi-

sation approach in order to simultaneously estimate various water column properties, water depth and bottom albedo. Lee et al. (1999), Lee et al. (2001) and Klonowski et al. (2003) demonstrated good retrieval of depth and water-column properties from field-measured hyperspectral data. However, the spectral shape of substrate reflectance was required and only areas with known sand and/or sea grass environments were explored. Recently, a number of authors extended the semi-analytical model developed by Lee et al. (1999) to account for variable benthic/substrate composition, typical of coastal water environments (Brando et al., 2009) (Giardino et al., 2007) (Goodman and Ustin, 2007) (Klonowski et al., 2007). In their approaches, substrate reflectance was paramaterised using a linear combination of two or more substrate reflectance endmembers which permitted the estimation of benthic cover composition, in addition to various water column properties and water depth, during the inversion process.

An alternative approach for the "inverse problem" is based on spectrally matching image data with a pre-computed spectral library of surface reflectances from numerical simulations of the RTE (Louchard et al., 2003) (Mobley et al., 2005). The spectral library covers a wide range of environmental conditions, including different combinations of water column properties, depths and bottom cover. The advantage here is that the image data is fitted to a spectral library or "Look-Up-Table" (LUT) of surface reflectances that are based on the actual RTE rather than an approximation to the RTE, as is the case for the semi-analytic approach. However, the forward modelling of such a large database takes considerable computing effort and may need to be generated on a case-by-case basis. Additionally, this approach requires appropriate discretisation of model parameters used in the numerical simulations of water column properties, depth and different combinations of benthic reflectances. The discrete step sizes in the parameters of RTE simulations need to be small enough to provide acceptable resolution for inversion, whilst also encompassing the required dynamic range that is anticipated for the region of interest. Hedley et al. (2009) describe the Adaptive

Look-Up-Tree (ALUT) method which efficiently sub-divides model parameters of arbitrary forward models in order to achieve a well represented database of reflectance spectra. In conjunction with a novel search algorithm, the method shows comparable accuracy with the popular non-linear optimisation methods, such as Levenberg-Marquardt, whilst also showcasing increased computation efficiency. However, only a semi-analytic forward model was investigated.

With either the semi-analytic or LUT based methods, an appropriate representation of the spectral inputs for water column optical properties and benthic reflectance endmembers are required for improved accuracy in the extraction of model parameters of interest. For remote sensing applications over complex coastal environments that exhibit a variety of benthic cover types with variable spatial distributions, the choice of benthic reflectance endmembers to be included in the model needs to be considered. Generally, the spectral inputs of benthic reflectance endmembers may be taken from either a spectral library of substrate reflectance generated from diver-based field measurements or from a generic set of substrate reflectances taken from literature. The choice of suitable endmembers, however, still requires some degree of knowledge of benthic cover that is expected for the region of interest. A number of methods that are described in an inter-comparison study of shallow water remote sensing algorithms (Dekker et al., 2011), attempt to address this issue by accounting for multiple combinations of substrate classes and seagrass species within the inversion process. Although the validation was somewhat limited, the results indicate that the models which account for multiple benthic classes perform the best in estimating water depth from hyperspectral imagery. The iterative methods in determining the combination of multiple benthic cover types that best fit the image data, also allows for benthic species classification maps to be generated. In the inter-comparison study, classification maps of different seagrass species compared favourably with ground truth data. However, only very shallow areas of up to 3 m depth were assessed. Although, these methods show very encouraging results for spectrally

discriminating benthic cover types to species level, from hyperspectral remote sensing, the applicability to other complex benthic environments, and understanding limitations in the ability of spectral discrimination is yet to be fully explained.

In this dissertation, a semi-analytical algorithm is developed for application to optical remote sensing in highly diverse and complex coastal environments. In developing the semi-analytical algorithm, particular attention is paid to improving the accuracy of the radiative transfer approximation for optically shallow waters that encompass variable benthic cover.

1.1 Research Aims

The key objective of this research are to:

1. Develop and implement a numerical retrieval scheme for extracting water quality, water depth and key benthic habitat types from Case 2 water hyperspectral data.

2. Test the shallow water numerical retrieval scheme against simulated data and investigate model performance in terms of model accuracy and highlight any limitations.

3. Apply the shallow water algorithm to airborne hyperspectral survey datasets and compare the retrieved products with available *in situ* data.

1.2 Outline

Chapter 2 introduces the shallow water remote sensing scenario, emphasising the physics of light propagation and interactions within shallow water. A review of the optically significant constituents in natural waters is given, and presents data that assists in noting the spectral variability in their absorption and scattering properties. Chapter 3 details the development of a semi-analytical model for Case

2 waters. In the process, analytical expressions relating to deep-water reflectance and diffuse attenuation of upwelling and downwelling light are investigated in detail. Improvements are made by tuning the analytical expressions to a large database of Hydrolight (Version 5.0) reflectances, that cover a wide range of environmental conditions. Particular attention is paid to the effects of solar and sensor geometries on both deep and shallow water reflectance. Chapter 3 concludes by presenting a numerical retrieval scheme for the simultaneous extraction of water column constituents, water depth and benthic cover types. A sensitivity analysis of the semi-analytic model is presented in Chapter 4. Model performance, in terms of retrieval accuracy, and key findings are discussed. Following this, Chapter 5 shows the results of application of the shallow water reflectance model to aerial hyperspectral data, captured over two test sites off the coast of Western Australia. Validation of various water column properties, bathymetry and benthic cover classification, with *in situ* data, is presented. Concluding remarks and recommendations for future work are presented in Chapter 6.

Chapter 2

Literature Review

Variations in the spectrum of visible radiation leaving the ocean surface is greatly influenced by the absorption and scattering of visible light within the water body. For coastal water regimes, light may be absorbed or scattered by pure water itself, as well as by the organic and inorganic, particulate and dissolved, material suspended within the water column. Additionally, in cases where the sea bottom is visible, the spectral reflectance of the sea bottom will also contribute to the optical properties of overlying seawater.

One of the aims of coastal water remote sensing is to understand how these substances independently influence the remotely detected signal. Understanding these influences assist in the development of algorithms that can separate and estimate the concentrations of substances suspended within the water column, and for shallow waters, provide information on the benthic composition as well as water depth.

This chapter outlines a number of physical processes that influence the variations in colour observed in coastal waters.

2.1 Remote Sensing over Shallow Water

Passive remote sensing of ocean colour makes use of the natural sunlight that penetrates thought the Earth's atmosphere, is reflected off a water body, and the

returned signal captured by an optical sensor onboard a remote platform such as a satellite, aircraft or marine vessel. Typically, the sensors are designed to collect the upwelling radiometric flux (or *radiance*) within a narrow instantaneous field-of-view (IFOV). This, combined with scanning ability and sequential data acquisition, enables a swath of data to be captured across a scene. With the forward motion of the sensor, swaths of data are built up line-by-line to provide an image over the water target. Furthermore, the sensors are designed to simultaneously capture a scene in many colour bands, termed *spectral* bands. For multi-spectral sensors, a number of light detectors (in the order of 10's) each with moderately narrow bandpass filters of different central wavelengths are used within the visible to near-infrared (NIR) portions of the electromagnetic spectrum. For hyperspectral sensors, diffraction gratings or prisms are employed to spectrally disperse light which is subsequently collected by an array of solid state semiconductive elements. This design allows for generally narrower spectral bands ($\sim$2 to $\sim$20 nm) with contiguous coverage over the visible to NIR spectral interval so that a complete spectrum is recorded at each spatial location in the image (pixel).

The mapping of water column constituents and/or benthic information from ocean colour remote sensing relies on the spectral information obtained from the water column and/or the seafloor. However, there are a number of pathways that a solar emitted photon can take before it is captured by an earthward-pointing optical sensor, which need to be considered.

An illustration of the shallow water remote sensing scenario is shown in Fig. 2.1. Photons emitted by the Sun enter the Earth's atmosphere and may be scattered off atmospheric constituents and directed towards the sensor. Those photons that have not been scattered may penetrate through the atmosphere and be reflected off the sea surface. Photons may also penetrate through the oceans surface and be scattered by the water body. Upwelling light that is scattered in the water would be attenuated on its journey from the sea surface to the sensor, due of the absorption and scattering by the intervening atmosphere. It is these

photons that are backscattered from the volume of water that carry any useful information on the water body's properties.

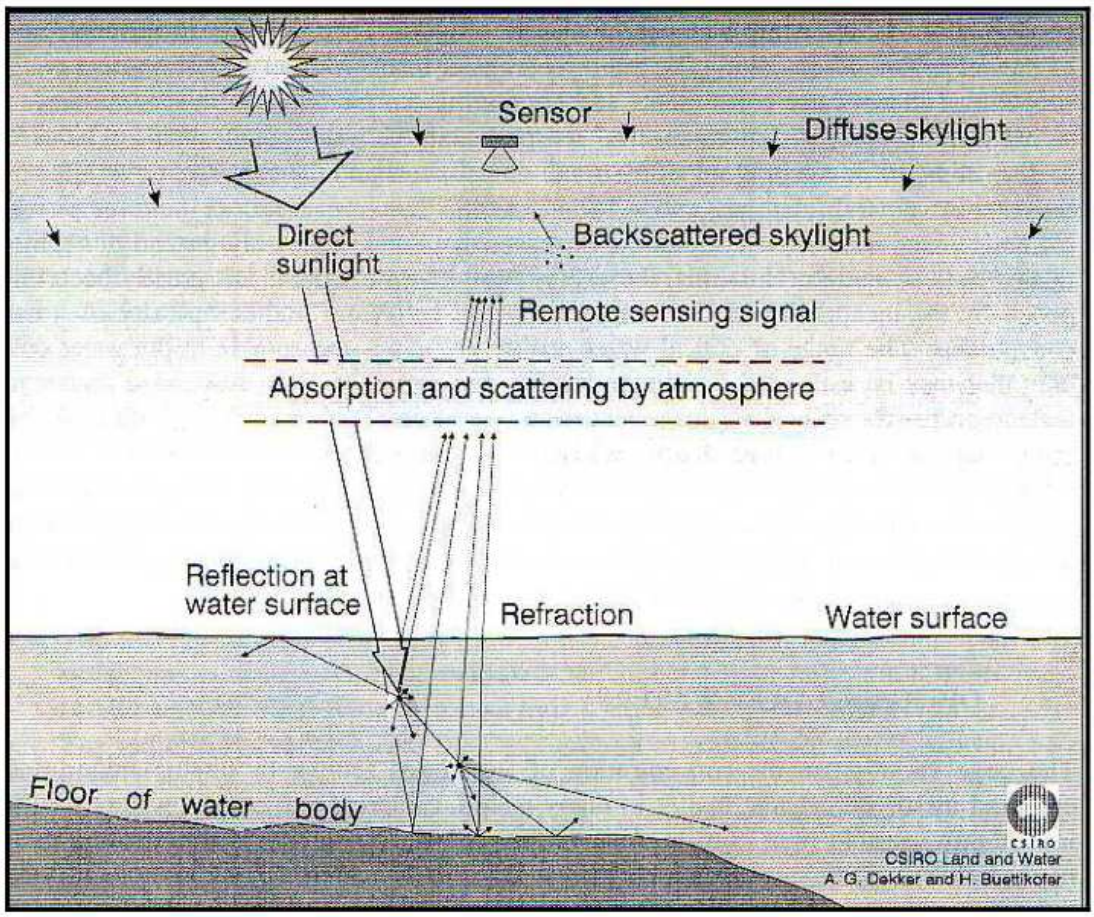

Figure 2.1: A schematic representation of the shallow water remote sensing scenario showing the various processes contributing to the signal measured by a remote sensor.

The total radiance captured by a remote sensor viewing the water target is therefore contaminated by the additional pathways that light may take. Ignoring self-emissive radiative flux originating in the atmosphere or in the water body, the components that add to the total upwelling radiance are:-

- L_a: the portion of the recorded radiance resulting from the downwelling solar and sky (direct and diffuse) radiation that never reaches the air-water interface. It therefore represents a return or backscatter from the atmosphere.

- L_s: the portion of the recorded radiance resulting from the downwelling

solar and sky radiation that reaches, but does not penetrate, the air-water interface. It therefore represents a reflection from the aquatic surface.

- L_{wv}: the portion of the recorded radiance resulting from the downwelling solar and sky radiation that penetrates through the air-water interface and re-emerges from the water column without encountering the bottom of the natural water body. It therefore represents a return from the volume of the water column.

- L_b: the portion of the recorded radiance resulting from the downwelling solar and sky radiation that penetrates the air-water interface, reaches the bottom of the natural water body, and re-emerges from the water column. It therefore represents a return from the seabed of the natural water body (the substrate).

The total radiance, L_t, reaching the remote sensor may be written as the sum of these components,

$$L_t = L_a + L_s + L_{wv} + L_b \tag{2.1}$$

In the context of ocean colour remote sensing the atmospheric contributions and reflection at the sea surface are regarded as noise and need to be eliminated. For a typical satellite sensor altitude, the atmospheric component accounts for more than 90% of the total light reaching the sensor over a water target (Bukata et al., 1995). Techniques for correcting the atmospheric components are termed "atmospheric correction" and form a very important aspect in the processing of ocean colour remote sensing data. Small errors in the estimation of the atmospheric contributions can lead to significant errors in the retrieval of the water leaving component.

Although atmospheric correction is an integral part in ocean colour remote sensing it is not the aim of this research to investigate the effects of the atmospheric impact on the estimation of the water leaving signal. Therefore, the reader is referred to such works as Gordon and Morel (1983) and Gordon and

Wang (1994).

2.2 The Underwater Light Field

There are a number of influences acting upon light within a water body of a shallow water environment, as depicted in Fig. 2.2. Direct sunlight and diffusely

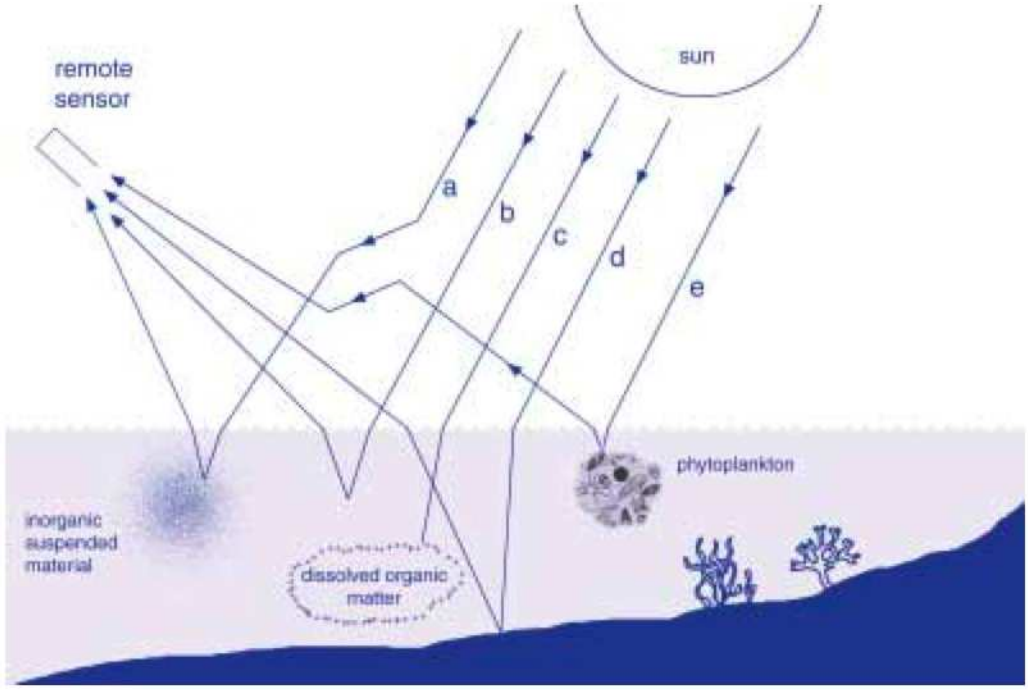

Figure 2.2: Schematic diagram of radiative transfer influenced by the main in-water constituents (phytoplankton, CDOM, suspended matter), and water molecules as well as different bottom types that contribute to the signal as measured by a remote sensor in shallow water (from IOCCG (2000)).

scattered skylight that penetrate through the air-water interface may be absorbed or scattered by water itself, and if present, by the dissolved and suspended matter that lies within the water column. In coastal water environments the constituents suspended within the water column are typically phytoplankton, CDOM, detrital material and inorganic suspended material. For clear and shallow water situations, light may penetrate through the water body and be reflected off the sea floor. This bottom reflected light may then penetrate upward through the water column adding to the light signal leaving the sea surface. Furthermore, the ab-

sorption and scattering properties of these substances are unique and vary with wavelength. Varying amounts of the constituents present within the water body as well as water column depth and the type of sea floor all influence the spectral shape of the upwelling light signal leaving the water body.

A formal description of how the underwater light field is influenced by the various absorption and scattering interactions within the water column is given by the theory of radiative transfer in natural seawater. First, the fundamental terms pertinent to the radiative transfer theory are introduced.

2.3 Fundamental Radiometric Quantities

The fundamental radiometric quantities that describe photon flux passing through or emitted from a particular area, are termed *radiance* and *irradiance*. Taking the radiant flux, Φ, to be the rate of flow of radiant energy through a plane surface, i.e. $\Phi = \frac{Q}{t}$, where Q is energy and t is time, irradiance is defined as the radiant flux per infinitesimal area, dS, passing through that point from all directions above the plane surface (see Fig. 2.3). This may be mathematically expressed as,

$$E \equiv \frac{d\Phi}{dS}. \tag{2.2}$$

Radiance, L, is defined as the flux of photons that is contained within an infinitesimal solid angle, impinging on a unit area perpendicular to the direction of photon flow (see Fig. 2.4),

$$L \equiv \frac{d^2\Phi}{dA d\Omega}, \tag{2.3}$$

where, dA represents the infinitesimal area perpendicular to the specified direction of photon propagation and $d\Omega$ is the infinitesimal solid angle containing the selected direction of photon propagation. For photons emanating from or impinging upon an infinitesimal surface area, dS, which is not normal to the surface

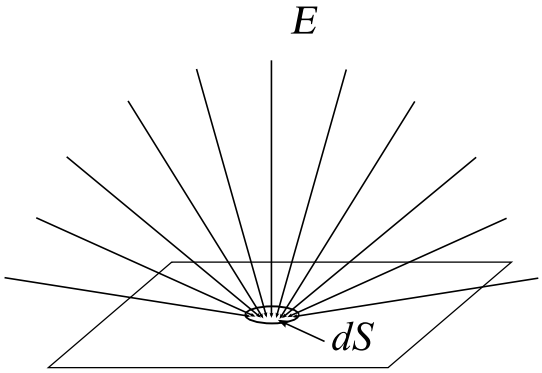

Figure 2.3: Conceptual illustration of irradiance.

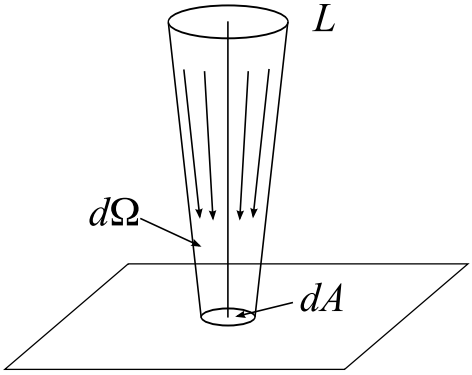

Figure 2.4: Conceptual illustration of radiance.

(see Fig. 2.5), the radiance in a specified direction (θ, ϕ) is equivalent to,

$$L(\theta, \phi) = \frac{d^2\Phi}{dS \cos\theta d\Omega}. \tag{2.4}$$

Combining Eqs. 2.2 and 2.4, and given that $d\Omega \equiv \sin\theta d\theta d\phi$, the inter-relationship between radiance and irradiance incident on a plane is expressed as,

$$E\left(\lambda\right) = \int_0^{2\pi} \int_0^{\frac{\pi}{2}} L\left(\lambda, \theta, \phi\right) \cos\theta \sin\theta \, d\theta d\phi. \tag{2.5}$$

The above definitions for radiance and irradiance include the flux of photons at all wavelengths. Specifying radiance and irradiance per unit wavelength interval is termed "*spectral radiance*" and "*spectral irradiance*", respectively. Spectral irradiance is defined as,

$$E(\lambda) \equiv \frac{d\Phi}{d\lambda}, \tag{2.6}$$

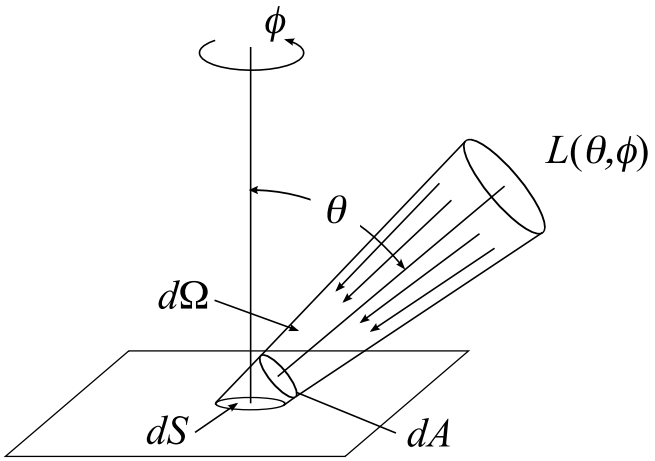

Figure 2.5: Conceptual illustration of directional radiance.

and spectral radiance as,

$$L(\lambda, \theta, \phi) \equiv \frac{dL(\theta, \phi)}{d\lambda}. \tag{2.7}$$

The *downward spectral irradiance*, $E_d(\lambda)$, incident on a plane surface from the above is,

$$E_d(\lambda) = \int_0^{2\pi} \int_0^{\frac{\pi}{2}} L(\lambda, \theta, \phi) \cos\theta \sin\theta \, d\theta d\phi. \tag{2.8}$$

Simiarly, the *upward spectral irradiance*, $E_u(\lambda)$, incident on a plane surface from below is,

$$E_u(\lambda) = -\int_0^{2\pi} \int_{\frac{\pi}{2}}^{\pi} L(\lambda, \theta, \phi) \cos\theta \sin\theta \, d\theta d\phi. \tag{2.9}$$

The negative sign in Eq. 2.9 is incorporated to ensure E_u is positive. Here, we see that the contribution of radiant flux falling on the plane surface at different angles is weighted by the cosine of the incident angle from normal. This is commonly referred to as the *cosine law of irradiance* and is purely a construct of the geometry. The radiant intensity at a point, which weights radiation from all directions equally, is termed *spectral scalar irradiance*, E_0, and is related to spectral radiance by,

$$E_0(\lambda) = \int_0^{2\pi} \int_0^{\pi} L(\lambda, \theta, \phi) \sin\theta \, d\theta d\phi. \tag{2.10}$$

The integral of the radiance distribution over the upper hemisphere gives the *downward spectral scalar irradiance*, E_{0d}, expressed as,

$$E_{0d}(\lambda) = \int_0^{2\pi} \int_0^{\frac{\pi}{2}} L(\lambda, \theta, \phi) \sin\theta \, d\theta d\phi. \tag{2.11}$$

Similarly, the integral of the radiance distribution over the lower hemisphere gives the *upward spectral scalar irradiance*, E_{0u}, expressed as,

$$E_{0u}(\lambda) = \int_0^{2\pi} \int_{\frac{\pi}{2}}^{\pi} L(\lambda, \theta, \phi) \sin\theta \, d\theta d\phi. \tag{2.12}$$

2.4 Apparent Optical Properties

In natural water bodies, the angular structure of the underwater light field is described by the full radiance distribution covering all zenith (θ) and azimuth (ϕ) directions. The underwater light field is highly variable, as it is modified by the directional structure of the ambient light field, as well as by the optical properties of the medium itself. By using certain ratios of radiometric quantities, termed *Apparent Optical Properties* (AOPs), the underwater light field can be described with reduced effects of the highly variable ambient light field, and thus become useful descriptors of the water body. Important AOPs used in the field of ocean optics are irradiance reflectance (R), remote sensing reflectance (R_{rs}), vertical diffuse attenuation (K), average cosine of light field ($\bar{\mu}$) and the distribution function (D).

2.4.1 Reflectances

The spectral irradiance reflectance, $R(z, \lambda)$, at depth, z, within a water body is defined as the ratio of the upwelling and downwelling irradiance,

$$R(z, \lambda) \equiv \frac{E_u(z, \lambda)}{E_d(z, \lambda)}, \tag{2.13}$$

where, R is a dimensionless quantity. *In situ* profiles of spectral irradiance reflectance are readily attainable from upward-pointing and downward-pointing underwater spectroradiometers, each equipped with optical diffusers that provide a near cosine response. $R(z, \lambda)$ is often evaluated just below the water surface, $(z = 0)$, denoted as $R(0^-, \lambda)$.

The spectral remote sensing reflectance within a water body, $r_{rs}(z, \theta, \phi, \lambda)$, at depth z, is defined as the upwelling radiance, $L_u(z, \theta', \phi, \lambda)$, normalised by the incident downwelling irradiance at the same depth,

$$r_{rs}(z, \theta', \phi, \lambda) \equiv \frac{L_u(z, \theta', \phi, \lambda)}{E_d(z, \lambda)}, \tag{2.14}$$

where θ' is the in-water zenith angle of upwelling radiance. r_{rs} is expressed in units of sr^{-1}. Utilising a downward pointing underwater radiance spectrometer, subtended with a narrow field of view, together with an upward pointing underwater irradiance spectrometer, *in situ* profiles of remote sensing reflectance can be made. The case where r_{rs} is evaluated just below the water surface is often termed "sub-surface remote sensing reflectance".

For the above water case, the spectral remote sensing reflectance, $R_{rs}(\lambda)$ of a water body is defined as the "water leaving" radiance, $L_w(\theta, \phi, \lambda)$, normalised by the incident downwelling irradiance, just above the water surface,

$$R_{rs}(\theta, \phi, \lambda) \equiv \frac{L_w(\theta, \phi, \lambda)}{E_d(0^+, \lambda)}, \tag{2.15}$$

where, L_w is the portion of upwelling radiance evaluated just below the water surface, $L_u(0^-, \theta, \phi, \lambda)$, that has emerged through the air-water interface after refraction and internal reflection loss,

$$L_w(\theta, \phi, \lambda) = L_u(0^-, \theta', \phi, \lambda) \frac{[1 - \rho_F(\theta'; \theta, \lambda)]}{n_w(\lambda)^2}, \tag{2.16}$$

where, $\rho_F(\theta'; \theta, \lambda)$ is the Fresnel internal reflectance for radiance from the sub-

surface zenith direction (θ') to the above-water zenith direction (θ) and n_w is the refractive index of the water body. θ' and θ are related through Snell's law, $\sin(\theta) = n_w \sin(\theta')$.

In practice, an optical radiance sensor viewing the water from above cannot measure L_w directly since there will always be a component of downwelling incident radiance from the sky (L_{sky}) that has been partially reflected off the water surface and directed into the path of the radiance sensor. This phenomenon is described through Fresnel reflectance, whereby, light incident on the ocean surface will be partially reflected and partially transmitted due to the change in refractive indexes of air and water and the angle of incidence of the incoming light. The upwelling radiance (L_u) measured by a downward pointing radiance sensor (just above the water surface), can therefore be described as,

$$L_u(0^+, \theta, \phi, \lambda) = L_w(\theta, \phi, \lambda) + \rho_R(\theta_i; \theta, \phi, \lambda) L_{sky}(\theta_i, \phi, \lambda), \tag{2.17}$$

where, ρ_R is a proportionality factor that relates the downwelling sky radiance to the reflected component of the sky radiance received by the detector at the complement viewing geometry. ρ_R is dependent on viewing direction, wavelength, sea-surface roughness (or wind speed), sensor Field-of-View (FOV) and the sky radiance distribution. For a flat ocean the proportionality factor is equivalent to the Fresnel reflectance.

Substituting Eq. 2.17 into Eqs. 2.15, the above-water remote sensing reflectance can be estimated using (Mobley, 2015),

$$R_{rs}(\theta, \phi, \lambda) = \frac{L_u(0^+, \theta, \phi, \lambda) - \rho_R(\theta_i; \theta, \phi, \lambda) L_{sky}(\theta_i, \phi, \lambda)}{E_d(0^+, \lambda)}, \tag{2.18}$$

where, ρ_R is known to vary with viewing direction, solar zenith angle and ocean surface roughness. For a calm ocean and a viewing direction away from the sun $\rho_R \approx 0.02$. For a wind blown ocean surface of 15 ms^{-1} and a viewing direction towards the sun, $\rho_R \approx 0.12$ (Mobley, 1999). Numerical simulations indicate that

the smallest change in ρ_R with sensor geometry occurs for viewing direction of 40° from nadir and 135° away from the sun. For this viewing geometry, $\rho_R \approx 0.028$ for wind speeds less than 5 ms^{-1} (Mobley, 1999).

2.4.2 Diffuse Attenuation

In natural water bodies, illuminated by the sun and sky, irradiance and radiance diminish in value with increasing water depth in an approximately inverse exponential manner. The rate of change of these properties with depth is conveniently described by the *vertical diffuse attenuation coefficient*. For downwelling irradiance, the downwelling vertical diffuse attenuation coefficient (K_d) is defined as,

$$K_d(z,\lambda) \equiv -\frac{d\ln E_d(z,\lambda)}{dz} = -\frac{1}{E_d(z,\lambda)}\frac{dE_d(z,\lambda)}{dz}. \tag{2.19}$$

Similarly, the vertical diffuse attenuation coefficient for upwelling irradiance (K_u) is,

$$K_u(z,\lambda) \equiv -\frac{d\ln E_u(z,\lambda)}{dz} = -\frac{1}{E_u(z,\lambda)}\frac{dE_u(z,\lambda)}{dz}, \tag{2.20}$$

and the diffuse attenuation coefficient for radiance (K) is,

$$K(z,\theta,\phi,\lambda) \equiv -\frac{d\ln L(z,\theta,\phi,\lambda)}{dz} = -\frac{1}{L(z,\theta,\phi,\lambda)}\frac{dL(z,\theta,\phi,\lambda)}{dz}, \tag{2.21}$$

Within optically deep and homogenous water bodies, K-functions vary weakly with depth making them useful descriptors of water bodies. K_d has been used to classify different water types (Jerlov, 1976) and is also an important coefficient which can be used to estimate the light availability at depth. For remote sensing of the ocean, the backscattered light signal comes from the upper layer of the water column with the geometrical depth approximately equal to $1/K_d$.

2.4.3 Average Cosines and Distribution Functions

A simple descriptor of the shape of the underwater radiance distribution is the weighted average cosine. For downwelling irradiance, it is the weighted average value of the cosine ($\bar{\mu}_d$) of the zenith angle of light for all directions that make up the downwelling radiance distribution. This is equivalent to,

$$\bar{\mu}_d(z,\lambda) \equiv \frac{E_d(z,\lambda)}{E_{0d}(z,\lambda)}. \tag{2.22}$$

Similarly, the average weighted cosine for an upwelling radiance distribution ($\bar{\mu}_u$) is,

$$\bar{\mu}_u(z,\lambda) \equiv \frac{E_u(z,\lambda)}{E_{0u}(z,\lambda)}. \tag{2.23}$$

For a collimated underwater light field, travelling downward in direction (θ', ϕ), $\bar{\mu}_d = \cos(\theta')$ and for a completely isotropic downwelling radiance distribution, $\bar{\mu}_d = 0.5$.

The distribution functions for downwelling (D_d) and upwelling (D_u) light fields are simply the reciprocals of the average cosines (Preisendorfer, 1977),

$$D_d(z,\lambda) \equiv \frac{1}{\bar{\mu}_d(z,\lambda)}, \tag{2.24}$$

and,

$$D_u(z,\lambda) \equiv \frac{1}{\bar{\mu}_u(z,\lambda)}. \tag{2.25}$$

2.5 Inherent Optical Properties

The class of optical properties that describe a medium, which are invariant to the ambient light field, are termed *Inherent Optical Properties* (IOPs), and therefore, are properties which are dependent only on the medium itself (Preisendorfer, 1977). In the study of ocean sciences, the fundamental IOPs are the spectral absorption coefficient, $a(\lambda)$, the spectral scattering coefficient, $b(\lambda)$, the spectral

volume scattering function, $\beta(\Psi, \lambda)$ and the spectral beam attenuation coefficient $c(\lambda)$.

The spectral absorption coefficient is defined as the loss of radiant flux , ΔA, due to absorption from incident radiance flux A, that passes through an infinitesimally small volume of medium of thickness, Δr,

$$a(\lambda) = \frac{\Delta A(\lambda)}{\Delta r}. \tag{2.26}$$

Similarly, for a loss of radiant flux, ΔB, due to scattering, the spectral scattering coefficient is expressed as,

$$b(\lambda) = \frac{\Delta B(\lambda)}{\Delta r}. \tag{2.27}$$

The loss of radiant flux due to the combined effects of absorption and scattering gives the spectral beam attenuation coefficient, defined as,

$$c(\lambda) \equiv a(\lambda) + b(\lambda). \tag{2.28}$$

Coefficients for absorption, scattering and beam attenuation are expressed in units of m^{-1}. Attenuation causes the radiant flux, $\Phi_r(\lambda)$, along the path of the beam, $\Phi_0(\lambda)$, travelling through a medium of thickness 0 to r, to decrease exponentially with distance (Kirk, 1983), and may be expressed as,

$$\Phi_r(\lambda) = \Phi_0(\lambda) e^{-c(\lambda)r}. \tag{2.29}$$

The radiant flux that has scattered away from the path of the incident beam is also an important consideration which affects the way light penetrates through a medium. The angular distribution of the scattered radiant flux has a characteristic shape for a given aquatic medium and is described by the *volume scattering function*, $\beta(\theta, \lambda)$, commonly abbreviated to VSF. If an infinitesimally small volume element of medium, dV, is illuminated by an incident parallel beam of monochromatic light of intensity $\Phi_0(\lambda)$, light will scatter in a direction (θ) away

from the beam, whereby the fraction of scattered radiant flux in this direction, per unit solid angle, $d\Omega$, is $d\Phi(\theta, \lambda)$. From this, $\beta(\theta, \lambda)$ is defined as the fraction of scattered radiant flux per unit of incident irradiance, per unit volume, and may be expressed as,

$$\beta(\theta, \lambda) \equiv \frac{d\Phi(\theta, \lambda)}{E(\lambda)dV}. \tag{2.30}$$

The integral of the VSF, over all angles from 0 to π, reveals the total scattering coefficient as in Eq. 2.27, where,

$$b(\lambda) = 2\pi \int_0^\pi \beta(\theta, \lambda) \sin\theta d\theta. \tag{2.31}$$

The VSF shape can be described by the particle phase function, $\tilde{\beta}(\theta, \lambda)$, defined as,

$$\tilde{\beta}(\theta, \lambda) \equiv \frac{\beta(\theta, \lambda)}{b(\lambda)}, \tag{2.32}$$

with the normalisation condition,

$$2\pi \int_0^\pi \tilde{\beta}(\theta, \lambda) \sin\theta d\theta = 1. \tag{2.33}$$

2.6 Radiative Transfer Equation

The theory of radiative transfer in the atmosphere and ocean deals with the laws that govern the transfer of radiant energy from one location to another. Based on this theory, the radiative transfer equation (RTE) mathematically describes the change in direction and intensity of light in response to absorption, scattering, fluorescence, inelastic scattering, air-sea interface effects and reflection off the seafloor. Radiative transfer theory forms a complicated and large body of work. The essential elements of the theory are reviewed in this section. However, various aspects of this subject are presented in more detail by Preisendorfer (1961), Preisendorfer (1977), Liou (1980) and Mobley (1994).

Solar radiation that enters an absorbing and scattering medium, in this case

seawater, has already been modified to some extent by the atmosphere and air-water interface. Absorption by various atmospheric gases and scattering by atmospheric aerosols change the intensity and directionality of the incident solar radiation arriving at the sea surface. In addition to the diminished direct solar radiation reaching the water, diffusely scattered sunlight forms a large contribution to the total downwelling solar irradiance, and depends on the nature and distribution of atmospheric constituents, and the apparent elevation of the sun in the above hemisphere (solar zenith angle). Reflection and refraction at the air-water interface further modifies the spectrum of light that enters the seawater. Wind that blows across the water creates an uneven surface, causing wave patterns, affecting the directionality of reflection and refraction, and hence, the distribution of light beneath the air-water interface.

For the light that has penetrated the seawater, a number of interactions occur and act to modify the underwater light field. As a beam of light traverses through seawater, different interactions with water and its constituents, cause a change in radiance due to:-

- loss of photons from the beam due to the process of annihilation, whereby, the transfer of radiant energy to non-radiant energy is conserved (absorption)

- loss of photons through scattering, in a direction away from the travelling beam, and without change in wavelength (elastic scattering)

- loss of photons through scattering with a change in wavelength (inelastic scattering)

- gain of photons by scattering from other directions into the travelling beam, without change in wavelength (elastic scattering)

- gain of photons by the beam from scattering with a change in wavelength (inelastic scattering)

- gain of photons by the beam due to the generation of photons from conservation of non-radiant energy to radiant energy (emission)

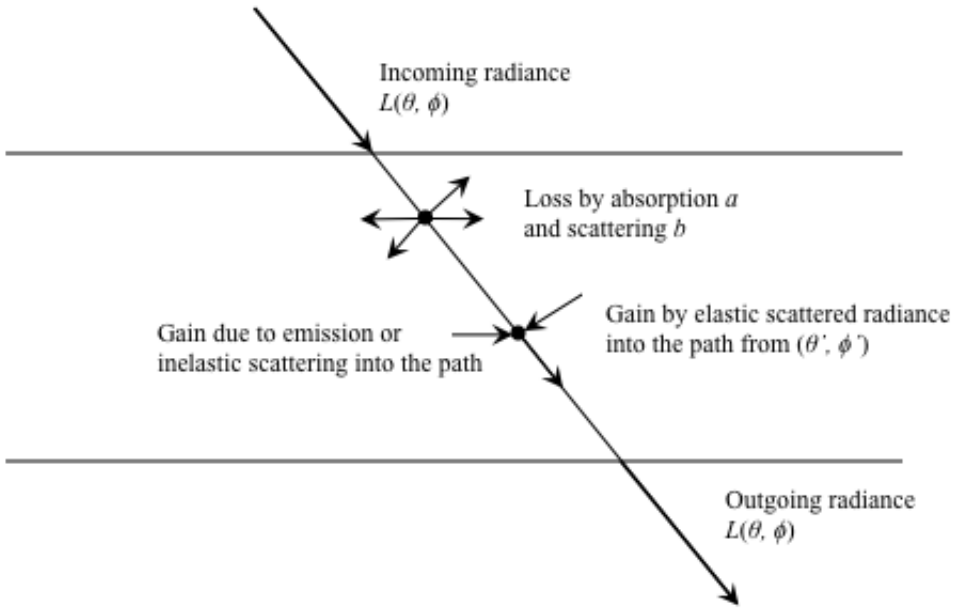

Figure 2.6: Illustration of radiance and the various interactions that affect it as it propagates through the medium.

The above interactions are mathematically quantified with the radiative transfer equation for radiance. A diagrammatic representation of how radiance is affected by the various interactions is presented in Fig. 2.6. Consider a beam of photons travelling in the direction (θ, ϕ) at an arbitrary location (x, y, z), denoted by the position vector $\overrightarrow{x}$, then the rate of change in radiance, dL, due to attenuation, along a path of infinitesimal distance, dr, is,

$$\frac{dL(\overrightarrow{x}, \lambda, \theta, \phi)}{dr} = -c(\overrightarrow{x}, \lambda)L(\overrightarrow{x}, \lambda, \theta, \phi), \tag{2.34}$$

where, the proportionality factor, c, is the attenuation coefficient and L is the incident radiance, as previously defined. This quantifies the relative loss of radiance due to attenuation. However, another consideration is that light from other directions, (θ', ϕ'), may be scattered into the traversing beam of photons, giving

rise to a gain in radiance. The change in radiance along the path of light propagation, due to scattering into the beam over all directions, 4π, can be expressed as,

$$\frac{dL(\overrightarrow{x},\lambda,\theta,\phi)}{dr} = \int_0^{4\pi} \beta(\overrightarrow{x},\lambda,\theta,\phi;\theta',\phi')L(\overrightarrow{x},\lambda,\theta',\phi')d\omega'. \tag{2.35}$$

Combining the losses due to attenuation and gains due to scattering, the general equation of radiative transfer for radiance, without considering internal sources, is obtained,

$$\frac{dL(\overrightarrow{x},\lambda,\theta,\phi)}{dr} = -c(\overrightarrow{x},\lambda)L(\overrightarrow{x},\lambda,\theta,\phi)+\int_0^{4\pi} \beta(\overrightarrow{x},\lambda,\theta,\phi;\theta',\phi')L(\overrightarrow{x},\lambda,\theta',\phi')d\omega'. \tag{2.36}$$

In this form, there is no analytical solution to Eq. 2.36. However, numerical methods such as Monte Carlo, can be adopted in order to compute the radiance distribution from inputs of IOP values (a and β). The time-dependant boundary conditions at the sea-surface and the sea-floor, as well as the inclusion of internal sources (inelastic scattering e.g. Raman scattering, and bioluminescence) can also be imposed on the forward computation. In principle, a large number of photons are directed toward the ocean, whereby, photon paths are traced until the moment they are absorbed or leave the ocean. The desired underwater or water leaving radiance distribution is then obtained by collecting photon density and direction.

With the plane-parallel assumption, whereby, horizontal gradients in radiance and IOPs are taken to be negligible compared to vertical gradients, the RTE is reduced to,

$$\cos\theta\frac{dL(z,\lambda,\theta,\phi)}{dz} = -c(z,\lambda)L(z,\lambda,\theta,\phi)+\int_0^{4\pi} \beta(z,\lambda,\theta,\phi;\theta',\phi')L(z,\lambda,\theta',\phi')d\omega', \tag{2.37}$$

with, $\cos\theta dr = dz$ and z representing geometric depth in meters. The invariant imbedding solution to this reduced form of the RTE is detailed in Mobley (1994) and is incorporated into the widely used and validated computer software,

Hydrolight (Sequoia, Inc), available commercially.

Hydrolight provides the numerical solution of the one dimensional, time-independent RTE, including a source term, $S(z, \lambda, \theta, \phi)$ which describes an internal light source such as bioluminescence, or inelastically scattered light from other wavelengths, to obtain the radiance distribution $L(z, \lambda, \theta, \phi)$. The inputs into the Hydrolight model consist of the absorption and scattering coefficients of pure water, phytoplankton, dissolved substances and inorganic material, as a function of depth and wavelength, the corresponding scattering phase functions, the sea-state, the incident sky radiance at the sea surface and the reflectance properties of the sea bottom.

From the full radiance distribution, other apparent optical properties, such as irradiances, reflectances and diffuse attenuation, may be determined using their definitions (see Sections 2.3 and 2.4). This link between various AOPs to IOPs makes Hydrolight a powerful tool for remote sensing algorithm development. For example, a large number of simulations can be carried out, that cover a wide range of different water bodies and illumination conditions, to study the range and variability of the underwater light field. From this, bio-geo-optical models can be formed to permit the extraction of IOPs from remote sensing measurements. Also, since the IOP inputs are known, the performance of the various models can be explored. This is the approach taken in this research.

2.7 Absorption

When a photon passes within the vicinity of a molecule there is a finite probability that it will be captured by the molecule. This process is termed *absorption*. If the photon is absorbed then the energy of the molecule must increase by an amount equal to the energy of that photon (Kirk, 1983). There are several means by which a molecule can internally store energy: (1) Electronic transitions from lower to higher energy levels of the molecule, (2) rotational transition from low to higher energy levels corresponding to the rotation of the molecule about its centre of mass

and (3) vibrational transitions from low to higher energy levels represented by the vibration of the molecule's constituent atoms (Serway et al., 1997). For photons of wavelengths in the far infrared/microwave region the energies are low and absorption can only cause rotational transitions within the molecule. For infrared wavelengths, absorption of photons will bring about vibrational transitions within the molecule. The absorption of photons with wavelengths in the visible part of the spectrum have energies that are sufficient enough to stimulate electronic transition from one energy level (usually the ground state) to an excited state of allowed energy levels within the molecule (Kirk, 1983).

In natural seawater, the optically active ingredients that bring about measurable absorption are pure seawater itself, phytoplankton, CDOM and detritus. The bulk absorption coefficients for a given volume of water is taken to be the sum of the absorption coefficients that correspond to the different components, expressed as,

$$a(\lambda) = a_w(\lambda) + a_{phi}(\lambda) + a_{CDOM}(\lambda) + a_{det}(\lambda) + ..., \tag{2.38}$$

where, the subscripts, w, phi, $CDOM$ and det, represent pure seawater, phytoplankton, CDOM and detritus, respectively.

The variations of the absorption coefficient with wavelength for pure water, phytoplankton ,CDOM and detritus are described in the following sections.

2.7.1 Absorption of Pure Water

The accurate knowledge of the spectral absorption of pure fresh and sea water, and its dependence on temperature and salinity, is vital for researchers making precise measurements of optical constituents in natural waters. The shape and magnitude of the absorption spectrum of pure water is largely due to the absorptive strength at unique fundamental frequencies of the various vibrational forms of the O-H molecular bond. Additionally, each fundamental vibration also exhibit

harmonic or overtone modes at higher frequencies that absorb light at different intensities (Pope and Fry, 1997). This leads to a very complex absorption spectrum of pure water which remains difficult to determine analytically. Generally, the absorption of pure liquid water is relatively high (> 1 m^{-1}) for most parts of the electromagnetic spectrum with only a small window of low absorption in the visible domain. The spectral absorption coefficient of pure water, $a_w(\lambda)$, for visible wavelengths has been experimentally determined by various researchers (Sullivan, 1963); (Irvine and Pollack, 1968); (Hale and Querry, 1973); (Kopelevich, 1976); (Morel and Prieur, 1977); (Tam and Patel, 1979); (Smith and Baker, 1981); (Stegelstein, 1981); (Shifrin, 1988); (Querry et al., 1991); (Pope, 1993); (Buiteveld et al., 1994): (Sogandares, 1991); (Pope and Fry, 1997) and generally show similar shape (see Fig. 2.7). The variability in numerical values may be

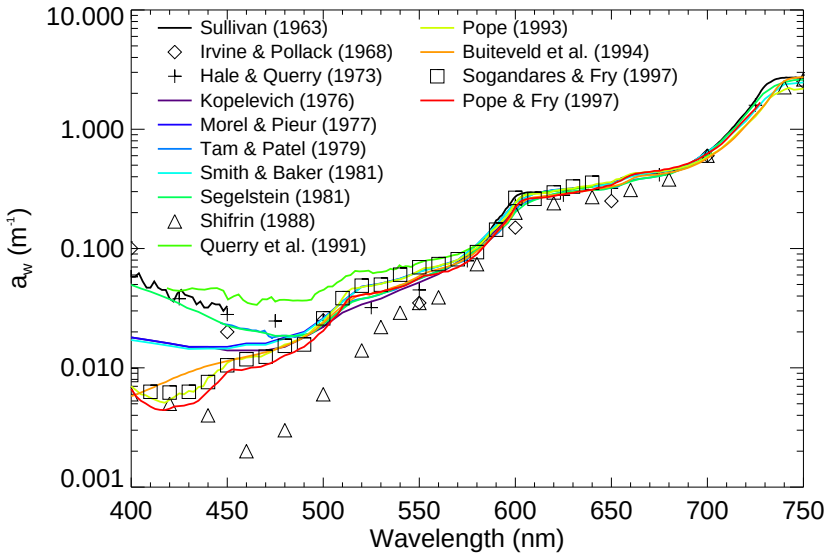

Figure 2.7: Experimentally determined pure water absorption by various researchers.

due to experimental difficulties, including the difficulty of obtaining pure water, instrumental design and sensitivity, and the assumptions made to determine their values (Buiteveld et al., 1994); (Mobley, 1994).

The shape and magnitude of absorption by pure water is further complicated by temperature and concentration of natural salts found in seawater, both of

which can affect the absorptive strength and frequency of different molecular vibrations. Temperature and salinity dependency of absorption by pure water have recently been investigated by Sullivan et al. (2006). The dependency of pure water absorption with salinity concentration was found to be negligible at visible to near-infrared wavelengths. The use of pure water absorption coefficients to represent pure seawater absorption coefficients is therefore adequate. Figure 2.8a shows a small temperature dependency on pure water absorption from 550 nm to 700 nm increasing rapidly at longer wavelengths and peaking at 740 nm. There is no significant effect for visible wavelengths shorther than $\approx$ 550 nm.

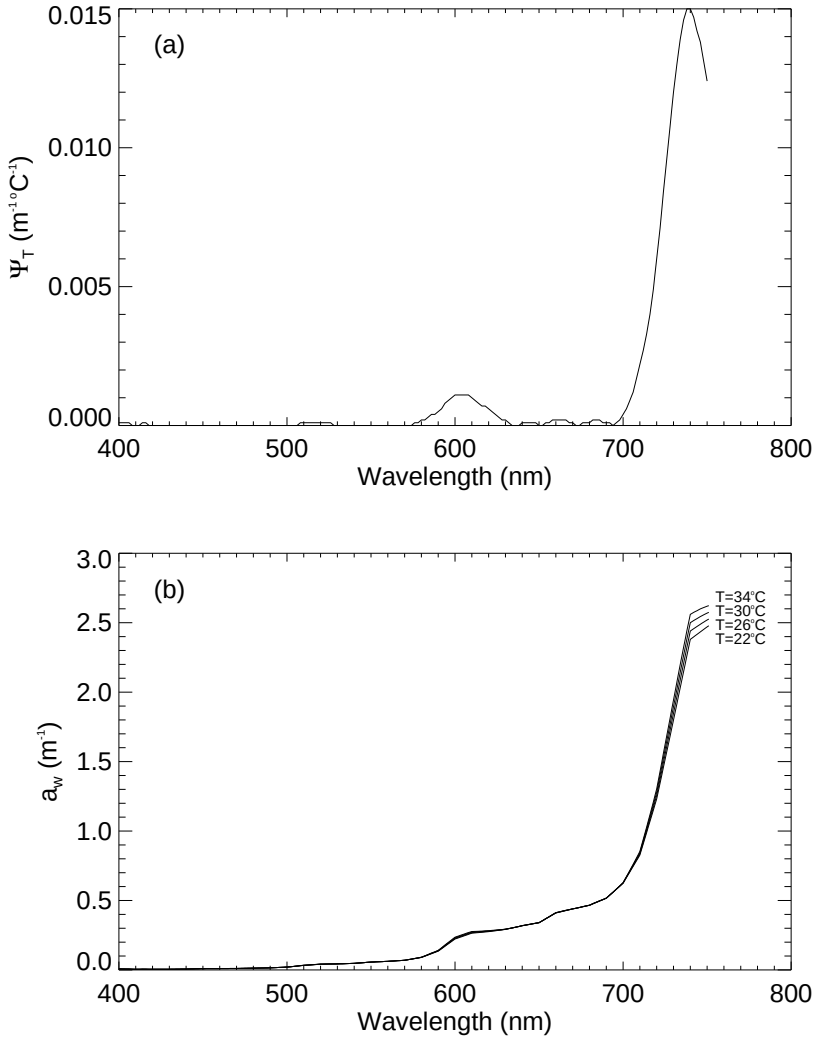

Figure 2.8: (a) Temperature dependency of absorption by pure water. Data taken from Table 2 in Sullivan et al. (2006) and (b) pure water absorption at temperatures shown calculated using Eq. 2.39.

At this time the consensus within the optical oceanographic community is that results from Pope and Fry (1997) represent the best measurements of pure water absorption (at $22°C$) to date (IOCCG, 2000) and are provided in Appendix 7.2. The coefficients for pure water absorption at temperatures, T, other than $22°C$ may be calculated using the temperature dependent absorption coefficients of pure water, $\Psi_T(\lambda)$, detemined by Sullivan et al. (2006),

$$a_w(\lambda, T) = a_w^{meas}(\lambda) + (T - T_{ref})\Psi_T(\lambda), \tag{2.39}$$

where, $a_w^{meas}(\lambda)$ are the Pope and Fry (1997) pure water absorption coefficients measured at a reference temperature, $T_{ref} = 22°C$.

Figure 2.8b shows the pure water absorption coefficients calculated using Eq. 2.39 at 4 different temperatures. A noticeable variation in pure water absorption is evident toward the NIR wavelengths, however there is no significant variation in pure water absorption with temperature at visible wavelengths (400 nm - 700 nm).

2.7.2 Phytoplankton Absorption

Phytoplankton is the collective term given to the photosynthetically active microscopic organisms that inhabit the upper layers of our oceans and bodies of fresh water. The collection of light energy by these aquatic organisms is carried out by the photosynthetic pigments present within the organism. These pigments consist of complex molecules whose structures are such that they efficiently absorb light in the visible domain of the electromagnetic spectrum.The two main classes of photosynthetic pigments present in all phytoplankton species are the chlorophylls and carotenoids. Some species, such as red algae, blue-green algae and cryptophytes also contain biliproteins as well (Kirk, 1983).

The spectral absorption characteristics of chlorophyll pigments, which include, chlorophyll-a, chlorophyll-b and chlorophyll-c, show pronounced absorption peaks

in the blue and red portions of the visible spectrum, and lower absorption in the green region. This results in the apparent green colour of these pigments. Carotenoid pigments absorb light at the short wavelength end of the visible range, resulting in characteristic colours of yellow, orange or red. Strong absorption peaks in biliprotein pigments are either in the blue or red regions of the spectrum, and hence appear either red or blue in colour. A typical phytoplankton absorption curve is shown in Fig. 2.9.

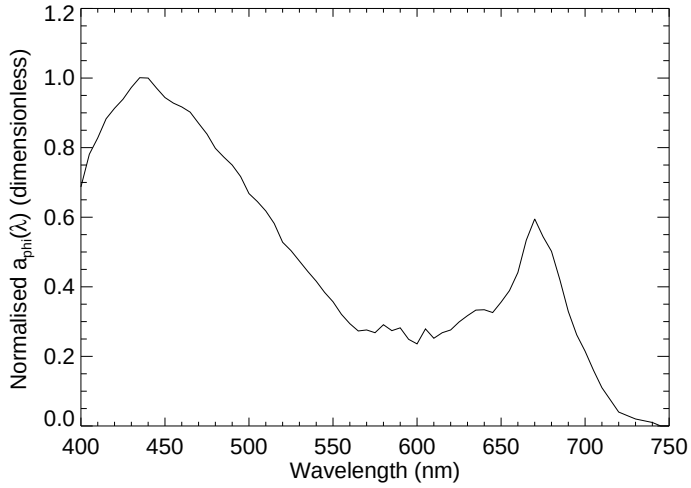

Figure 2.9: An average representative phytoplankton absorption spectrum normalised to 1 at 440 nm. Absorption coefficients are taken from Morel (1988), and are tabulated in Appendix 7.4.

Chlorophyll-a is the dominant photosynthetic pigment in all phytoplankton species. However, different phytoplankton species contain different distributions of the other photosynthetic pigments which alters their colour and therefore their spectral absorption characteristics. Additionally, the photosynthetic pigments are contained within cellular chloroplasts that are unevenly distributed throughout the phytoplankton cell. This localised distribution of pigments, termed "the package effect", tends to reduce the spectral absorption of those pigments compared to phytoplankton that contain evenly distributed pigments within the cell, or pigments that are uniformly dispersed in solution (Kirk, 1983).

The concentration of phytoplankton is generally described by the concentra-

tion of the dominant phytoplankton pigment, Chl-a or Chl-a plus its degradation products, pheo-pigments, expressed in mgm^{-3}. Measurements of phytoplankton absorption are commonly normalised by the phytoplankton concentration to yield a phytoplankton-specific absorption coefficient, $a^*_{phi}(\lambda)$, expressed in terms of $\mathrm{m}^2\mathrm{mg}^{-1}$. For low concentrations, the spectral absorption of phytoplankton, $a_{phi}(\lambda)$, may be expressed as the product of the phytoplankton concentration, C, and the specific absorption coefficient,

$$a_{phi}(\lambda) = C a^*_{phi}(\lambda). \tag{2.40}$$

Similarly, the phytoplankton specific absorption which is normalised to 1 at 440 nm, $a^N_{phi}(\lambda)$ (dimensionless), may be used to model phytoplankton absorption,

$$a_{phi}(\lambda) = a_{phi}(440) a^N_{phi}(\lambda), \tag{2.41}$$

where, $a_{phi}(440)$ is the phytoplankton absorption at 440 nm which is dependent on the phytoplankton concentration. For Case 1 water applications, Prieur and Sathyendranath (1981) relate $a_{phi}(440)$ to phytoplankton concentration as,

$$a_{phi}(440) = 0.06 C^{0.602}. \tag{2.42}$$

The magnitude and spectral form of specific phytoplankton absorption, representative of different natural phytoplankton assemblages, have been shown to be highly variable. Roesler and Perry (1995) show *in situ* measurements of specific phytoplankton absorption sampled in different marine environments, which include estuarine, fjord, coastal and oceanic (see Fig. 2.10). They report an 8 fold variability of specific phytoplankton absorption coefficients in the blue region of the spectrum among the representative environments. Similarly, Prieur and Sathyendranath (1981) show high $a^*_{phi}(\lambda)$ variability for over 80 *in situ* measurements representative of different marine regions. They point out that some of the

variability may be explained by changes in pigment composition, whereby spectrally distinct pigments other than Chl-a (namely, Chl-b, Chl-c , carotenoids, biliproteins, and pheopigments) can vary with species and physiological state of the cells. Another cause of variability may be due to the "package effect", whereby, absorption spectra of particles in suspension appear flatter compared with the same pigment content in solution. Duysens (1956), Kirk (1975a), Kirk (1975b), Kirk (1976) and Morel and Bricaud (1981) theoretically demonstrate that the flattening of phytoplankton absorption spectra varies according to size, shape, and optical density of phytoplankton.

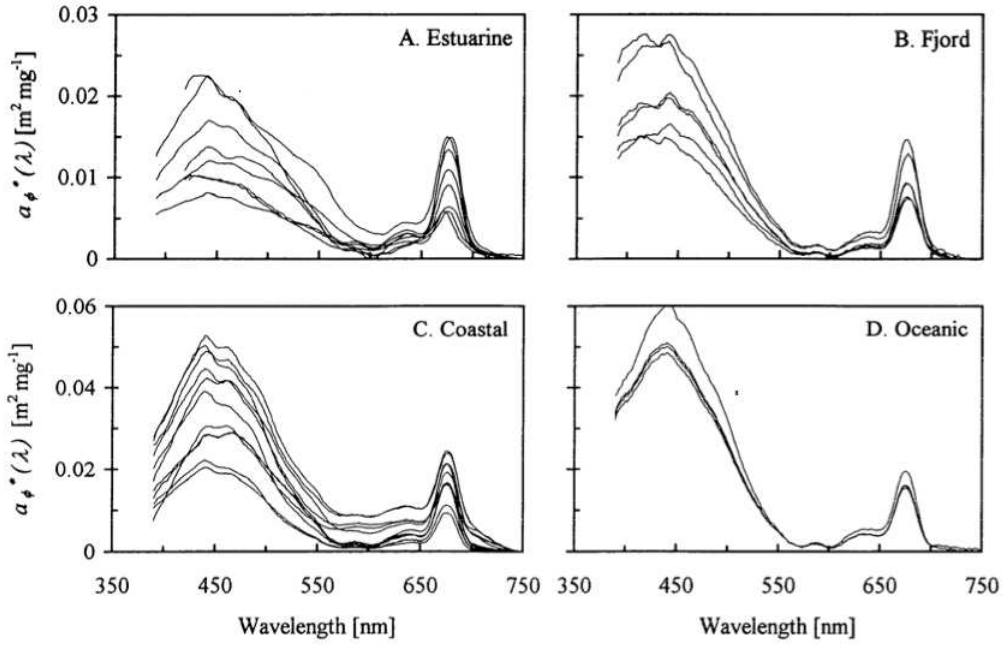

Figure 2.10: Chl-a specific phytoplankton absorption measurements (Roesler and Perry, 1995) representative of estuarine, fjord, coastal and oceanic water types, panel a), b), c) and d), respectively.

The effects of dominant cell size in natural phytoplankton assemblages, with respect to the spectral shape of phytoplankton absorption, were investigated by Ciotti et al. (2002). They studied 4 dominant cell size classes representing picoplankton ($< 2\ \mu m$), ultraplankton ($2 - 5\ \mu m$), nanoplankton ($5 - 20\ \mu m$) and mircoplankton ($> 20\ \mu m$). Their findings give a good example of intercellular shading (package effect) where large cell sizes are attributed to an increase in

intercellular shading and cause an apparent reduction of the specific phytoplankton absorption (see Fig. 2.11). Conversely, small cell sizes reduce intercellular shading and cause no noticeable reduction in specific phytoplankton absorption.

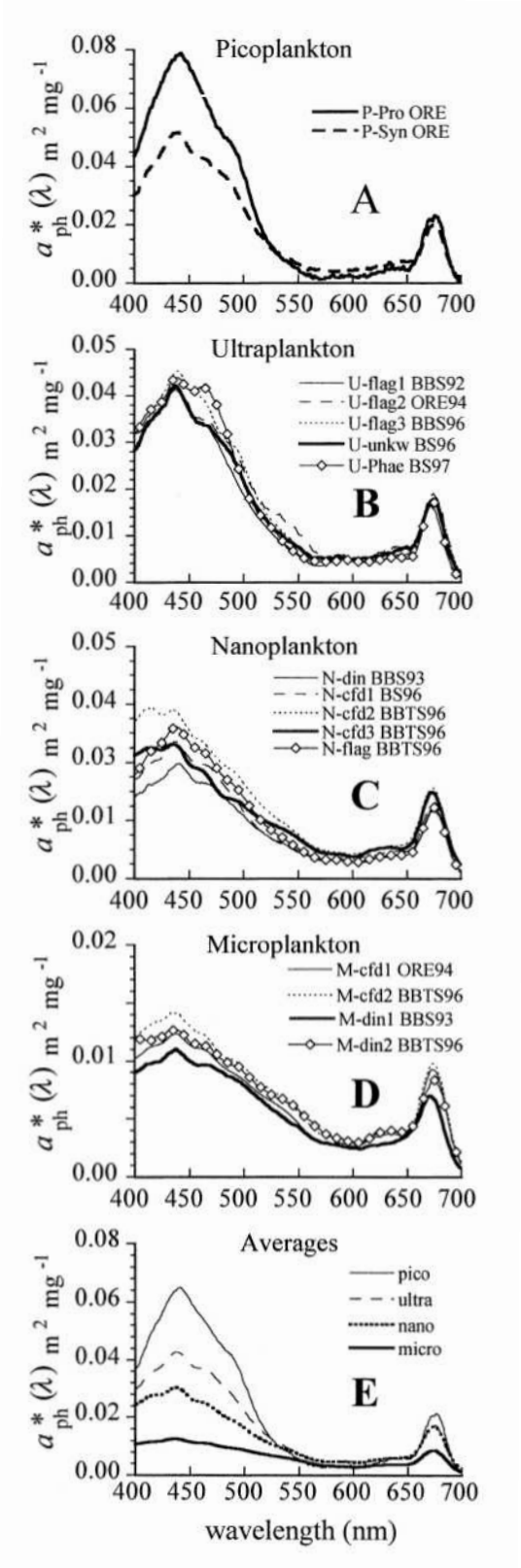

Figure 2.11: Chl-a specific phytoplankton absorption measurements of Ciotti et al. (2002) according to cell size range of dominant organism.

Lee et al. (1998) provide an empirical relationship between $a_{phi}(440)$ and phytoplankton absorption which accounts for the changes in spectral shape with the package effect and Chl-a concentration,

$$a_{phi}(\lambda) = \{a_0(\lambda) + a_1(\lambda)\ln[a_{phi}(440)]\}a_{phi}(440), \tag{2.43}$$

where the basis coefficients $a_0(\lambda)$ and $a_1(\lambda)$ have been empirically determined in Lee (1994). Figure 2.12 shows examples of modelled phytoplankton absorption spectra for 3 Chl-a concentrations using Eqs. 2.42 and 2.43.

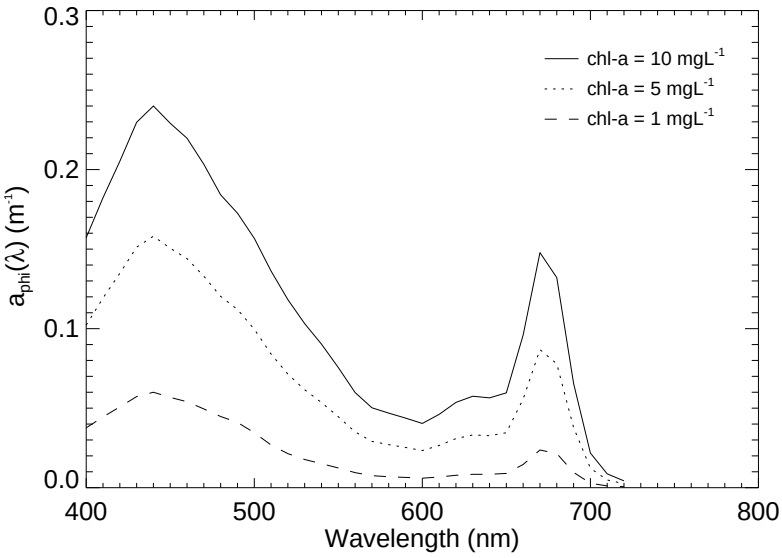

Figure 2.12: Example of phytoplankton absorption for different Chl-a conentrantions, calculated using Eq. 2.42 and 2.43.

2.7.3 CDOM Absorption

Coloured dissolved organic matter (CDOM), also known as yellow substance and gelbstoff, is the absorbing component of dissolved organic material (DOM) which is comprised of marine humic and fulvic acids. Theses acids are a by-product of decomposing biological matter. High concentrations of CDOM are most prevalent near land runoff (rivers) and coastal areas. CDOM absorption is dominated in the blue portion of the visible spectrum and closely follows an exponentially decaying

spectral shape as a function of increasing wavelength. In high concentrations, this imparts a yellow-brown colour to water.

From an optical aspect, CDOM refers to the collection of absorbing substances in water that have been passed through a 0.2 μm filter. Absorption of CDOM as a function of wavelength, $a_{CDOM}(\lambda)$, is commonly modelled with an exponentially decaying function of the form (Jerlov, 1976),

$$a_{CDOM}(\lambda) = a_{CDOM}(\lambda_{ref})e^{-S(\lambda-\lambda_{ref})}, \tag{2.44}$$

where, λ_{ref} is a reference wavelength, with 440 nm typically chosen. $a_{CDOM}(\lambda_{ref})$ is the magnitude of absorption at the reference wavelength and S is the spectral slope parameter describing the relative steepness of the absorption spectrum.

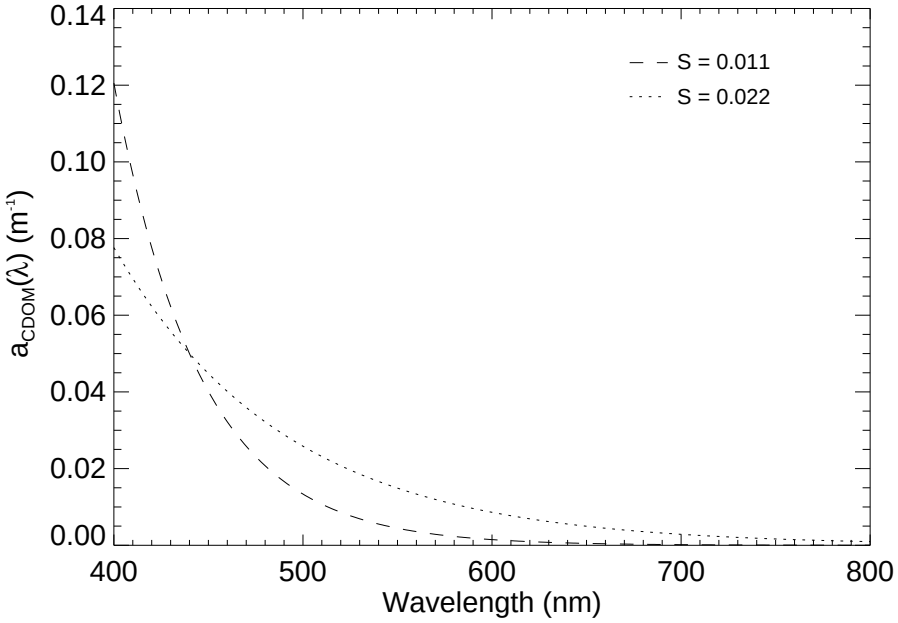

Figure 2.13: Example of spectral CDOM absorption for two different slopes at a fixed $a_{CDOM}(440)$ concentration of 0.05 m^{-1}, calculated using Eq. 2.44.

Published spectral slope values over an extensive range of water types are summarised in Twardowski et al. (2004). A number of investigators have reported mean spectral slopes of 0.014 nm^{-1} and 0.015 nm^{-1} with the latter being the recommended value suggested by Jerlov (1976) and Shifrin (1988). However, sev-

eral researchers report large differences from the recommended mean. Højerslev and Aas (2001) report an average spectral slope of 0.0243 ± 0.0036 nm^{-1}, with a range of 0.008 nm^{-1} to 0.042 nm^{-1}, whereas, Maske et al. (1998) report a spectral slope value of 0.007 nm^{-1}. More recently, Blondeau-Patissier et al. (2009) showed a large range of S values between 0.008 nm^{-1} and 0.032 nm^{-1}, with an average of 0.016 ± 0.006 nm^{-1} for inshore and reef waters in Queensland, Australia. Le et al. (2013) report average S values of 0.0174 ± 0.0011 nm^{-1} and 0.017 ± 0.00074 nm^{-1} for both wet and dry seasons, respectively, in Tambay Bay waters. Babin et al. (2003) and Tzortziou et al. (2006) reported average S values of 0.0176 nm^{-1} and 0.018 nm^{-1} for coastal water and estuarine water in Chesapeake Bay, respectively.

Twardowski et al. (2004) suggest that the observed discrepancies of spectral slopes in previous works can be largely explained by differences in the spectral range over which CDOM is modelled as well as the use of different fitting methods. In an attempt to reduce spectral slope variability Twardowski et al. (2004) propose a hyperbolic function to model CDOM absorption, given as,

$$a_{CDOM}(\lambda) = a_{CDOM}(\lambda_{ref}) \left(\frac{\lambda}{\lambda_{ref}} \right)^{S_h}, \tag{2.45}$$

where, S_h is the spectral slope parameter for the hyperbolic-type expression. Twardowski et al. (2004) analysed a large number of *in situ* spectrophotometric CDOM measurements from coastal waters surrounding the United States and determined a best fitting value for the hyperbolic spectral slope parameter, S_h, to be -6.92 ± 0.39 nm^{-1} for a reference wavelength of 412 nm. Absolute residuals between Eq. 2.45 and their measured spectra were generally less than 0.01 m^{-1}.

2.7.4 Detrital Absorption

The fraction of non-living organic particulate material produced from decomposing phytoplankton and zooplankton cells are termed “detritus”. Typically,

detritus includes the non-pigmented cell fragments of dead organisms as well as faecal pellets. As such, detritus is mainly of local biological origin, however, in Case 2 waters, bottom resuspension of organic material and proximity to land runoff areas, can also influence the suspension of detritus in the water column.

The spectral absorption characteristics of detritus is similar to that of CDOM, where relatively high absorption occurs at blue wavelengths and exponentially decreases to almost zero approaching red wavelengths. The separation of non-living detrital material to that of living phytoplankton from field measurements is considered difficult (Mobley, 1994) and as such, detrital absorption is usually determined by indirect means. However, Iturriaga and Siegel (1989) achieved direct examination of detrital absorption properties using microspectrophotometry. Detrital absorption is commonly measured using the filter pad technique (Yentsch, 1962); (Mitchell and Kiefer, 1984): (Mitchell and Kiefer, 1988) and (Kishino et al., 1985) whereby, particulate material from field samples is concentrated onto filters and subsequent spectrophotometric measurements are made before and after chemical extraction of phytoplankton pigments. The detrital absorption is then taken to be the residual absorption spectrum after phytoplankton pigment absorption is subtracted from the total particulate absorption of the filter pad measurement.

The spectral absorption of detritus can be satisfactorily modelled as (Babin et al., 2003),

$$a_{det}(\lambda) = a_{det}(\lambda_{ref})e^{-S_d(\lambda-\lambda_{ref})}, \tag{2.46}$$

where, λ_{ref} is a reference wavelength, with 440 nm typically chosen. $a_{det}(\lambda_{ref})$ is the magnitude of absorption at the reference wavelength and S_d is the spectral slope parameter describing the relative steepness of the detrital absorption spectrum.

Le et al. (2013) showed substantial variability in the spectral slope of detrital absorption in estuarine waters of Tampa Bay, ranging from 0.008 nm^{-1} to 0.0193 nm^{-1} with an average S_d of 0.0122 $\pm$ 0.002 nm^{-1}. For productive inland marine

waters, Roesler and Perry (1989) observed an average S_d of 0.011 ± 0.002 nm^{-1}. Babin et al. (2003) reports an average S_d of 0.0123 ± 0.0013 nm^{-1} for European waters and Blondeau-Patissier et al. (2009) gives an average S_d of 0.012 ± 0.001 nm^{-1} for inshore and reef waters in Queensland, Australia.

Given the spectral similarity to CDOM, the detrital component is usually integrated with CDOM parameterisation, denoted as $a_{CDM}(\lambda)$, for bio-optical models related to remote sensing (IOCCG, 2000).

2.8 Scattering

Another fundamental process which determines the propagation of light in seawater is scattering. When photons interact with some component of the aquatic medium, the scattering process causes changes in the direction of incident photon travel. In natural seawater, scattering can occur from the water molecules and salt ions that make up the liquid, as well as by the various particles that may be present in the seawater.

The scattering intensity as a function of scattering angle is described through the volume scattering function (Eq. 2.30). A measure of the sum of scattered photons over all angles is given by the total scattering coefficient, $b(\lambda)$. The total scattering coefficient can be partitioned through the forward scattering coefficient, $b_f(\lambda)$, and the backward scattering coefficient, $b_b(\lambda)$, where, $b(\lambda) = b_f(\lambda) + b_b(\lambda)$, with,

$$b_f(\lambda) = 2\pi \int_0^{\frac{\pi}{2}} \beta(\theta, \lambda) \sin\theta d\theta, \tag{2.47}$$

and,

$$b_b(\lambda) = 2\pi \int_{\frac{\pi}{2}}^{\pi} \beta(\theta, \lambda) \sin\theta d\theta. \tag{2.48}$$

Sunlight that is scattered in the backward direction significantly contributes to the water leaving radiance, making $b_b(\lambda)$ an important parameter for remote sensing.

The scattering properties of pure seawater, where the scattering centres are

very small compared to the wavelength of light, can be obtained from the theory of density fluctuation for liquids. Scattering values for seawater show little variability and are only slightly modified by changes in temperature and pressure. For the organic and inorganic particles present in seawater, where the sizes of particles are large compared to the wavelength of visible light, geometrical optics such as Mie theory can be used to predict the scattering properties of particles. Unlike pure seawater, particulate matter can greatly modify the scattering properties of natural seawater and quantification is made difficult due to the variability in particle composition, including concentration, particle size distribution, index of refraction and particle shape.

As with the total spectral absorption coefficient, Eq. 2.38, the scattering properties of seawater (subscript sw) may be added to the scattering properties of particle constituents (subscript p) to provide the bulk scattering properties of particle-laden seawater, with,

$$\beta(\theta, \lambda) = \beta_{sw}(\theta, \lambda) + \beta_p(\theta, \lambda), \tag{2.49}$$

and,

$$b(\lambda) = b_{sw}(\lambda) + b_p(\lambda). \tag{2.50}$$

2.8.1 Pure Water Scattering

Density fluctuation theory for optical scattering by pure water considers the continuous random motion of molecules which give rise to localised fluctuations of density. The fluctuation in the number of molecules within a small volume element, ΔV, alters the index of refraction, n, which ultimately determines the scattering properties of the medium. The interaction of electromagnetic radiation with these inhomogeneities is considered a treatment of statistical thermodynamics and has been solved by Smoluchowski (1908) and Einstein (1910).

The volume scattering function for either pure water or pure seawater has the

form (Mobley, 1994),

$$\beta_w(\theta, \lambda) = \beta_w(90°, \lambda) \left(\frac{\lambda_{ref}}{\lambda} \right)^{4.32} (1 + 0.835 \cos^2 \theta), \tag{2.51}$$

and the total scattering coefficient is,

$$b_w(\lambda) = 16.06 \left(\frac{\lambda_{ref}}{\lambda} \right)^{4.32} \beta_w(90°, \lambda), \tag{2.52}$$

which results in the phase function expressed as,

$$\tilde{\beta}_w(\lambda) = \frac{1}{16.06}(1 + 0.835 \cos^2 \theta). \tag{2.53}$$

As evidenced through Eq. 2.51, scattering by pure water is symmetrical for both forward and backward directions. The volume scattering function is shown in Fig. 2.51. This symmetry yields the backscattering coefficient of pure water or pure seawater to be $b_{bw}(\lambda) = 0.5 b_w(\lambda)$.

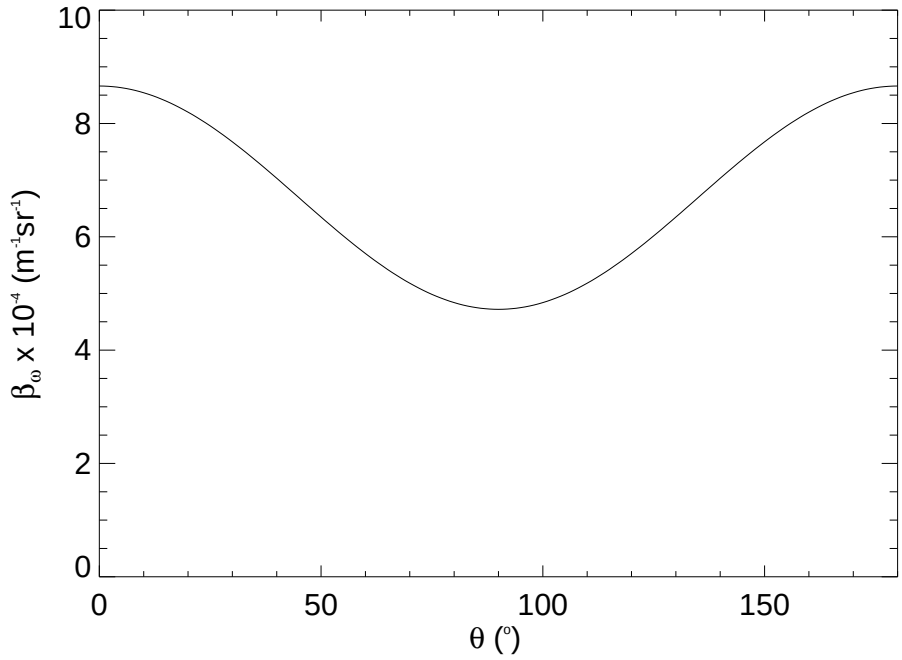

Figure 2.14: Volume scattering function of pure seawater at 400 nm. Calculated using Eq. 2.51 and tabulated values taken from Morel (1974).

The volume scattering function and total scattering coefficients for pure water and pure seawater have also been experimentally determined by a number of researchers. Morel (1974) observed scattering properties of filtered pure water and pure seawater using a laboratory-based scattering instrument, whereas Smith and Baker (1981) indirectly determined scattering properties for the clearest natural waters from diffuse attenuation measurements and radiative transfer theory. Coefficients of the volume scattering function (at 90°) and total scattering for both pure water (subscript fw) and pure seawater (subscript sw) determined by Morel (1974) are summarised in Table 2.1 and shown in Fig. 2.15.

Table 2.1: Volume scattering function coefficients at $\theta = 90°$ and total scattering as a function of wavelength for pure water (w) and pure seawater (sw) from Morel (1974). Values are multiplied by 10^4.

λ (nm)	$\beta_{fw}(90°)$ ($m^{-1}sr^{-1}$)	b_{fw} (m^{-1})	$\beta_{sw}(90°)$ ($m^{-1}sr^{-1}$)	b_{sw} (m^{-1})
350	6.47	103.5	8.41	134.5
375	4.80	76.8	6.24	99.8
400	3.63	58.1	4.72	75.5
425	2.80	44.7	3.63	58.1
450	2.18	34.9	2.84	45.4
475	1.73	27.6	2.25	35.9
500	1.38	22.2	1.80	28.8
525	1.12	17.9	1.46	23.3
550	0.93	14.9	1.21	19.3
575	0.78	12.5	1.01	16.2
600	0.68	10.9	0.88	14.1

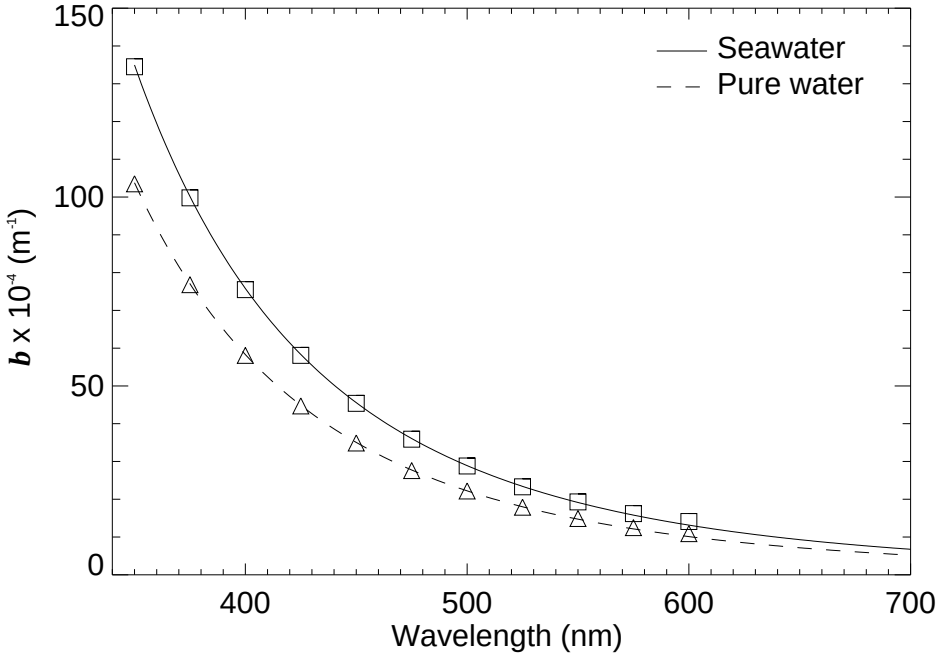

Figure 2.15: Total scattering coefficients of pure water as a function of wavelength. Symbols represent data in Table 2.1. The solid and dashed lines show total scattering coefficients for seawater and pure water, respectively, calculated using Eq. 2.51 and tabulated values taken from Morel (1974).

2.8.2 Particle Scattering

The suspension of particles, such as phytoplankton and inorganic material, within seawater, alters the VSF significantly. The VSF becomes highly peaked in the forward direction, whereby, up to 95% of scattering can be confined to within 5° (Petzold, 1977).

A theoretical basis for predicting the scattering properties of particles was developed by Mie (1908). The treatment provides the solution of Maxwell's equations for the interaction of electromagnetic waves with spherical particles that are considered a dielectric. A rigorous mathematical formulation is provided in Bohren and Huffman (2007). For spherical particles, the solution is exact and is valid for all sizes of particles (radius), indices of refraction, and wavelengths. For very small particles, the Mie solutions agrees with the Einstein-Smoluchowski theory for molecular scattering. For particles larger than a few wavelengths of light, the Mie solution predicts that the majority of scattering occurs in the forward direction. For a polydisperse suspension of spherical particles, scattering at small angles ($10° - 15°$) is dominated by diffraction, whereas, for larger angles, most of the scattering is dominated by reflection and refraction (Mobley, 1994).

Mie scattering calculations are able to predict the volume scattering function for a polydisperse suspension of natural particles that may be representative of natural seawater, provided the particle size distribution and the refractive indices as a function of wavelength are known. However, such measurements of natural seawater constituents are rarely made (Mobley, 1994).

Radiative transfer studies of the ocean typically incorporate VSFs that are taken from *in situ* measurements or their analytical approximations. A hand full of oceanic and coastal water VSF observations, from a limited number of field experiments, were made in the 1960s and 1970s and are reported in Tyler (1961), Kullenberg (1968) and Petzold (1977). Of these, the carefully made measurements reported by Petzold (1977) are widely used and are shown in Fig. 2.16. Kullenberg's (1968) measurements of a variety of different water bodies are shown

in Fig. 2.17.

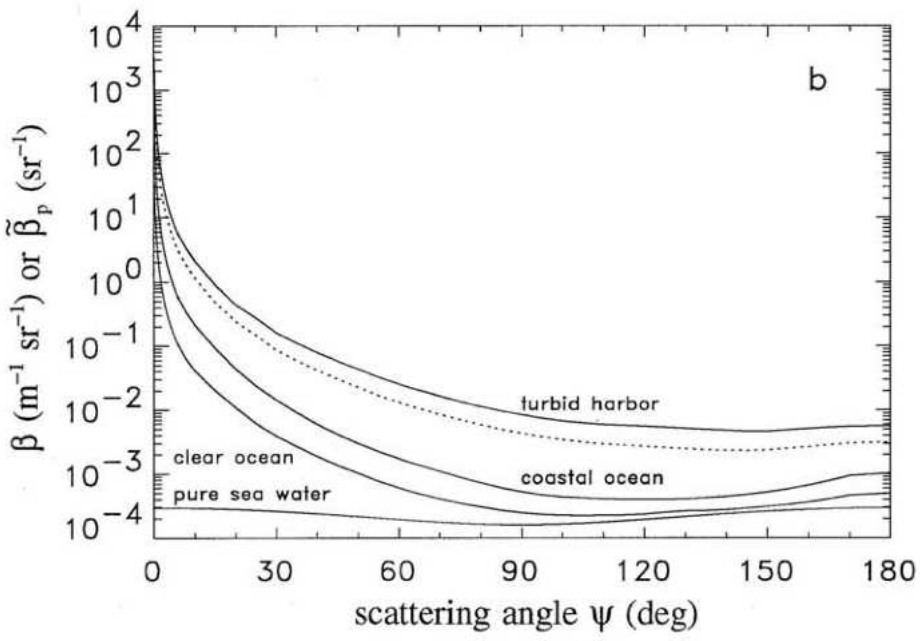

Figure 2.16: Particle scattering as a function of scattering angle (at $\lambda = 514nm$) after measurements of Petzold (1977) in oceanic water, coastal water and turbid water of San Diego harbour, California, with pure water scattering as a reference. Dashed line represents the "average particle" phase function. Figure from Mobley (1994)

The various VSF measurements show a marked increase in scattering magnitude in the forward direction (0° - 90°), as compared to pure seawater. An increase up to several orders of magnitude are evident, even for the clear open ocean. In the backward direction (90° - 180°), scattering coefficients as a function of angle rapidly decrease in magnitude with a minimum occurring between 110° - 120°. The ratio of backscattering to total scattering, b_b/b, is in the order of a few percent. For Petzold's scattering measurements, taken at 530 nm, b_b/b range from 0.044 in clear open ocean (dominated by biological particles) to 0.013 for coastal waters (dominated by inorganic particles). Differences in scattering coefficients between different water bodies are also evident, with VSFs for turbid water up to a factor of a 50 times greater than clear ocean VSFs. Although the differences in VSF magnitude can be quite large, the general VSF shapes are strikingly similar over the variety of water types sampled. Given the similarity of

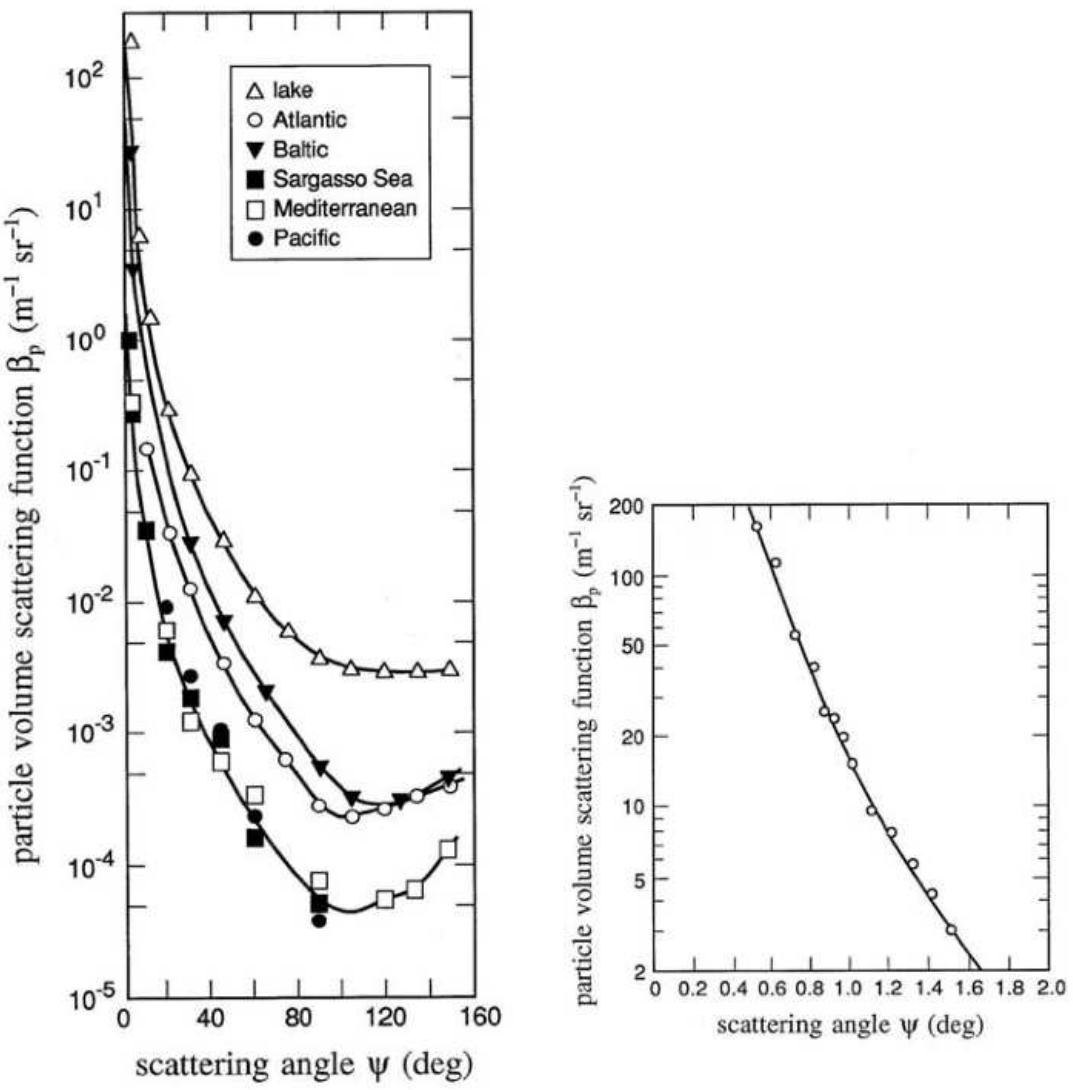

Figure 2.17: *in situ* measurements of particle volume scattering function taken in various waters, from Kullenberg (1968). Figure taken from Mobley (1994).

Petzold's measured VSF shapes, Mobley et al. (1993) determined a phase function which is a reasonable representative of an average ensemble of particles, the "average particle" phase function. This is incorporated into Hydrolight and has been selected for the radiative transfer modelling presented here.

More recently, Chami et al. (2005) reported on the first spectral VSF measurements (443 nm, 490 nm and 555 nm) over a wide range of scattering angles (0.6 - 177.3 degrees) using a new device deployed near the coast of Crimea, in the Black Sea. Although the spectral VSF data was not presented, they report on the analysis of the spectral backscattering ratio. In their study, the backscattering ratio ranged from 0.012 - 0.032 with an average value of 0.019, which is consistent with Petzold's measurements. The average backscattering ratio was found to vary spectrally within 4%. However, high variability up to 30% of the spectral slope of the backscattering ratio was observed. This spectral variability of the backscattering ratio has implications for radiative transfer calculations which assume a constant spectrally invariant particulate phase function, like those based on Hydrolight.

2.8.3 Particle Backscattering

Particle backscattering coefficients as a function of wavelength, $b_{bp}(\lambda)$ is an important consideration for remote sensing, since reflectance of a water body is directly proportional to the ratio of total backscattering ($b_w(\lambda)+b_{bp}(\lambda)$), to total absorption, a(λ), $R(\lambda) \propto b_b(\lambda)/a(\lambda)$ or $R_{rs}(\lambda) \propto b_b(\lambda)/(a(\lambda) + b_b(\lambda))$ (Gordon et al., 1983).

$b_{bp}(\lambda)$ is commonly expressed as (Morel and Prieur, 1977), (Bricaud et al., 1981), (Smith and Baker, 1981), (Bricaud and Morel, 1986), (Gordon et al., 1988), (Sathyendranath et al., 1989), and (Lee et al., 1998),

$$b_{bp}(\lambda) = b_{bp}(\lambda_{ref}) \left(\frac{\lambda_{ref}}{\lambda} \right)^{y}, \tag{2.54}$$

where, the reference wavelength, λ_{ref} is usually taken as 550 nm (Snyder et al., 2008) (Lee et al., 1998). The spectral slope parameter, y, can range from -1 for highly turbid waters to a value of 3 for clear waters (Aurin et al., 2010) (Blondeau-Patissier et al., 2009) (Snyder et al., 2008) (Lee, 1994). The magnitude of $b_{bp}(550)$ can be highly variable and in coastal waters can range from 0.1 - 0.5 m^{-1} and higher (Aurin et al., 2010) (Blondeau-Patissier et al., 2009) (Snyder et al., 2008).

2.9 Bottom reflectance

In coastal waters, where the water column is sufficiently shallow and the water sufficiently clear, light reflected off the seafloor can influence the colour of the water, as seen by a remote sensor. The influence of the bottom signal to the total upwelling light is dependent on the depth of the water, the optical clarity of the water and the type of cover present on the seafloor. The seafloor cover may comprise of a variety of sandy, shelly or rocky sediments, of which may be covered by benthic biological organisms, such as algae, seagrasses, molluscs and corals. Furthermore, due to differences in pigment composition, structure and illumination conditions, light that is reflected off the various benthic cover types varies in magnitude and wavelength. The spectral nature of reflected light by different bottom cover types is therefore an important consideration for remote sensing in shallow coastal waters.

The reflective properties of the seafloor can be described by the bidirectional reflectance distribution function ($BRDF$). The $BRDF$ is defined as (Nicodemus et al., 1977),

$$BRDF(\lambda, \theta_i, \phi_i, \theta_r, \phi_r) \equiv \frac{dL_r(\lambda, \theta_r, \phi_r)}{L_i(\lambda, \theta_i, \phi_i) \cos\theta_i d\Omega_i}, \tag{2.55}$$

where, L_i and L_r are incident and reflected radiance, respectively, with incident zenith and azimuth angles denoted as θ_i, ϕ_i and reflected zenith and azimuth angles denoted as θ_r and ϕ_r. Figure 2.18 illustrates the $BRDF$ geometry.

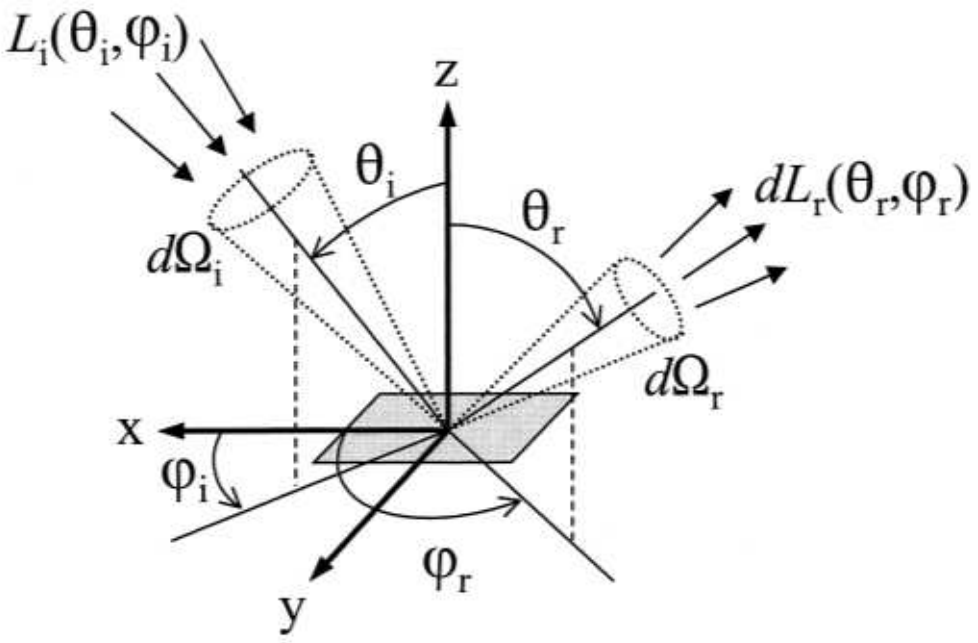

Figure 2.18: Geometry of incident and reflected radiance used in defining the $BRDF$ of a level surface.

Due to the difficulties in performing in-water measurements of $BRDF$, only a handful of such measurements have been made to date (Voss et al., 2000); (Zhang et al., 2003). The reflectance properties of different bottom types are commonly described by the irradiance reflectance (R), defined as (Mobley et al., 2003),

$$R(\lambda) = \frac{E_u(\lambda)}{E_d(\lambda)} = \frac{\int_{2\pi_r} L_r(\lambda, \theta_r, \phi_r)|\cos\theta_r| d\Omega_r}{\int_{2\pi_i} L_i(\lambda, \theta_i, \phi_i)|\cos\theta_i| d\Omega_i}, \tag{2.56}$$

where the upwelling irradiance (E_u) and downwelling irradiance (E_d) are evaluated at the surface. For practical reasons, in-water $R(\lambda)$ of the seafloor are usually determined from spectral upwelling and downwelling irradiance measurements made as close to the bottom target as possible.

Partly owing to the lack of in-water $BRDF$ measurements, the reflectance properties of benthic cover is often assumed to be Lambertian (Gordon and Brown, 1974); (Maritorena et al., 1994); (Lee et al., 1999), whereby, the surface reflects radiance equally in all directions. With the Lambertian assumption

the $BRDF$ reduces to,

$$BRDF(\lambda, \theta_i, \phi_i, \theta_r, \phi_r) = \frac{\rho(\lambda)}{\pi}, \tag{2.57}$$

where, $\rho(\lambda)$ is termed the spectral reflectivity of the surface. By definition, for a Lambertian-type surface, the magnitude of reflected radiance can change with incident irradiance, but because the idealised surface reflects light equally in all directions, the reflected radiance remains directionally isotropic. This provides a practical convenience in modelling the underwater light field of shallow waters. However, it is thought that all materials, to some extent, exhibit non-isotropic reflective properties making them non-Lambertian in nature (Mobley et al., 2003). This departure from an ideal Lambertian reflectance will ultimately induce errors when modelling a "real world" underwater light field using a Lambertian-type bottom.

An investigation into the effects of using both measured and idealised $BRDF$s on upwelling radiances was performed by Mobley et al. (2003). They showed that simulations of water-leaving radiance that were computed with non-Lambertian $BRDF$s can be substituted with Lambertian $BRDF$s of the same irradiance reflectance, with relatively small errors, typically less than 10%. Furthermore, they demonstrated that these errors are somewhat less than the errors caused by a 10% difference in the measurement of the overall magnitude of the non-Lambertian $BRDF$. These results suggest that modelling the bottom with the Lambertian assumption may be adequate for most remote sensing applications, with accurate measurements of benthic irradiance reflectance being the critical factor.

Irradiance reflectance measurements of different bottoms types are shown in Fig. 2.19. The data was sourced from bottom reflectance data files that were distributed with Hydrolight 5.0.

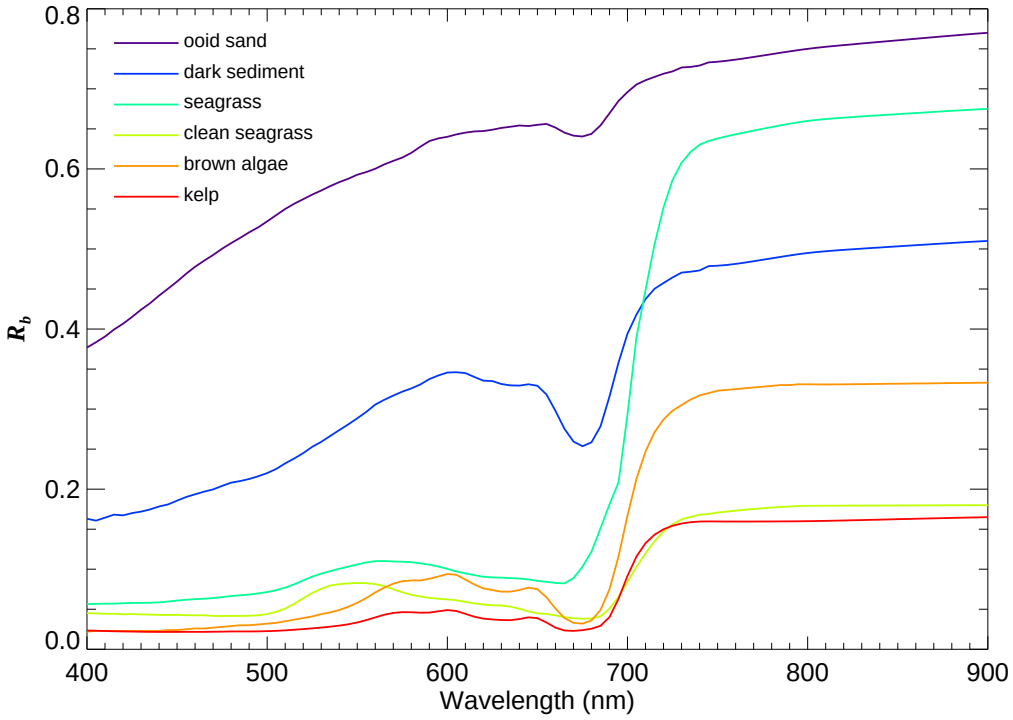

Figure 2.19: Measured irradiance reflectance of various bottom types.

Chapter 3

Semi-analytic Shallow Water Model

In optically shallow coastal waters, where reflectance from the sea bottom may add to the total water leaving radiance, a useful approximation for modelling r_{rs} is formed by expressing separate terms for the reflectance where light interacts just with the water column (r_{rs}^{W}) and where light interacts with the sea bottom and propagates back to the surface (r_{rs}^{B}), i.e.

$$r_{rs} \approx r_{rs}^{W} + r_{rs}^{B}. \tag{3.1}$$

From single scattering theory and numerical modelling of radiative transfer (Gordon et al., 1975), (Maritorena et al., 1994), (Lee et al., 1998), (Lee et al., 1999), approximation 3.1 may be expanded such that,

$$r_{rs}(\lambda) = r_{rs}^{\infty}(\lambda)\left\{1 - e^{-2K(\lambda)H}\right\} + \frac{\rho(\lambda)}{\pi}e^{-2K(\lambda)H}, \tag{3.2}$$

where, $r_{rs}^{\infty}(\lambda)$ represents the subsurface remote sensing reflectance for an infinitely deep water column, $K(\lambda)$ is the effective diffuse attenuation coefficient, $\rho(\lambda)$ is the irradiance reflectance of the sea bottom and H is the water column depth.

In early studies of water depth mapping from multispectral and/or hyperspec-

tral imagery (Lyzenga, 1978), (Philpot, 1989), the deep water reflectance term in Eq. 3.2 was typically replaced with adjacent deep-water signals within the image and the effective diffuse attenuation coefficients were taken from field measurements or empirically determined, whereby, reflectances over areas of known depths were regressed with Eq. 3.2 in order to calculate K. This approach allows for rapid image processing, however, is limited to regions where the conditions the empirical determination of the deep-water signals and diffuse attenuation coefficients exist. Furthermore, the approach assumes that the water column properties are invariant across the imaged scene which is often not the case. In coastal waters, the concentrations of water column constituents can be patchy and may lead to variability in optical properties within an image.

More recent studies of shallow water remote sensing use a combination of analytical and empirical expressions to account for the deep-water reflectance and diffuse attenuation in order to permit the simultaneous retrieval of water column properties as well as water depth and bottom albedo (Lee et al., 1999)(Klonowski et al., 2007)(Goodman et al., 2008)(Fearns et al., 2011)(Garcia et al., 2014a)(Jay and Guillaume, 2014)(Zoffoli et al., 2014)(McKinna et al., 2015)(Pacheco et al., 2015)(Eugenio et al., 2015). In their work, the semi-analytical model developed by Lee et al. (1999) was adopted, whereby, $r_{rs}^{\infty}(\lambda)$ and $K(\lambda)$ are expressed as a function of absorption (a) and backscattering (b_b) coefficients. The semi-analytic model of Lee et al. (1999) is presented below.

Numerical simulations and theoretical analysis of the radiative transfer equation (Gordon et al., 1975), (Morel and Gentili, 1991) and (Lee et al., 1999) suggest that the subsurface remote sensing reflectance for optically deep waters may be expressed as a function of the ratio $b_b/(a+b_b)$, with

$$r_{rs} = gu, \tag{3.3}$$

where,

$$u \equiv \frac{b_b}{a + b_b}. \tag{3.4}$$

The above approximation (Eq. 3.3) is commonly expressed as a polynomial expansion (Gordon et al., 1975), (Lee et al., 1998) and (Lee et al., 1999) giving,

$$g = g_0 + g_1 u, \tag{3.5}$$

where g_0 and g_1 are coefficients to be determined. Given that the underwater radiance distribution is generally non-isotropic (Loisel and Morel, 1998), the angular dependency in Eq. 3.3 is included in the g parameter. Early Monte Carlo computations of radiative transfer in the ocean, over a range of Case 1 water conditions, were conducted by Gordon et al. (1988), who reported $g_0 = 0.0949$ and $g_1 = 0.0794$. In a similar manner, Lee et al. (1999) later revisited the same approach using Hydrolight simulations over a wider range IOPs and illumination conditions and they reported $g_0 = 0.084$ and $g_1 = 0.170$ for nadir viewing applications.

Diffuse attenuation is an apparent optical property that is dependent on the nature of the light field as well as the spectral absorption and backscattering coefficients of the water. Because the directional nature of upwelling and downwelling light are generally different from each other, and because the diffuse attenuation of upwelling light originating from the sea bottom may be different from that of light originating from the water column itself, the effective diffuse attenuation is separated into the diffuse attenuation of downwelling light (K_d), the diffuse attenuation of upwelling light originating from the water column (K_u^C) and the diffuse attenuation of upwelling light that has been reflected off the sea bottom (K_u^B). Substituting these terms into Eq. 3.2 gives,

$$r_{rs} = r_{rs}^{\infty}\{1 - e^{-\left(K_d + K_u^C\right)H}\} + \frac{\rho}{\pi} e^{-\left(K_d + K_u^B\right)H}. \tag{3.6}$$

Generally, diffuse attenuation is empirically expressed as a function of the bulk

water absorption and backscattering coefficients with,

$$K = D\kappa, \tag{3.7}$$

where D represents a distribution function which accounts for the directional structure of the underwater light field and

$$\kappa \equiv a + b_b. \tag{3.8}$$

Specifically,

$$K_d = D_d\kappa, \quad K_u^C = D_u^C\kappa \quad \text{and} \quad K_u^B = D_u^B\kappa. \tag{3.9}$$

For downwelling irradiance just below the water surface, the distribution function can be approximated by,

$$D_d = \frac{1}{\cos(\theta_{sw})}, \tag{3.10}$$

where, θ_{sw} represents the subsurface solar angle. For downwelling irradiance at depths other than just below the water surface, a more accurate representation of K_d is given by Lee et al. (2005),

$$\overline{K}_d(0 \to z) = m_0(z, \theta_s)a + m_1(z, \theta_s)\left(1 - m_2(z, \theta_s)e^{-m_3(z,\theta_s)a}\right) b_b, \tag{3.11}$$

where, $\overline{K}_d(0 \to z)$ is the average K_d between depths 0 and z. The model coefficients m_i are dependent on solar zenith angle and water depth, and have been determined by Lee et al. (2005) for selected solar zenith angles and water depths.

For shallow water remote sensing applications, only the sum of K_d and K_u^C and the sum of K_d and K_u^B are important. By using Eq. 3.10, any directional dependency in K_d is transferred to D_u^C and D_u^B.

The distribution functions for upwelling radiance can be approximated with a Kirk K-type formula (Kirk, 1991),

$$D_u = D_0\sqrt{1.0 + D_1 u}, \tag{3.12}$$

where, D_0 and D_1 are model coefficients to be determined. In particular,

$$D_u^C = D_0^C \sqrt{1 + D_1^C u}, \tag{3.13}$$

and

$$D_u^B = D_0^B \sqrt{1 + D_1^B u}. \tag{3.14}$$

In a similar manner to deriving the model coefficients for deep-water remote sensing reflectance, Lee et al. (1999) determined the distribution coefficients for nadir viewing applications as,

$$D_0^C \approx 1.03,\ D_1^C \approx 2.4, \text{ and}$$

$$D_0^B \approx 1.04,\ D_1^b \approx 5.4.$$

The full form of the semi-analytic shallow water reflectance model may be re-written as,

$$\begin{aligned} r_{rs} &\approx (0.084 + 0.170u)\, u \left\{ 1 - \exp\left[-\left(\tfrac{1}{\cos\theta_{sw}} + 1.03\sqrt{1 + 2.4u} \right) \kappa H \right] \right\} \\ &+ \tfrac{\rho}{\pi} \exp\left[-\left(\tfrac{1}{\cos\theta_{sw}} + 1.04\sqrt{1 + 5.4u} \right) \kappa H \right]. \end{aligned} \tag{3.15}$$

The semi-analytic shallow water reflectance model presented in Eq. 3.15 is only relevant for nadir-view applications since the model coefficients were determined for such a case. However, low altitude remote sensing imaging systems are typically designed to extend the view geometry generally from 30° to 40° off nadir, increasing the swath width and thereby increasing their effectiveness for rapid surveying of large areas. To extend the applicability of the shallow water reflectance model for larger viewing angles, a $\frac{1}{\cos\theta_{wv}}$ term is included to account for the increase in path length of upwelling photons. This gives,

$$\begin{aligned} r_{rs} &\approx (0.084 + 0.170u)\, u \left\{ 1 - \exp\left[-\left(\tfrac{1}{\cos\theta_{sw}} + \tfrac{1.03\sqrt{1+2.4u}}{\cos\theta_{wv}} \right) \kappa H \right] \right\} \\ &+ \tfrac{\rho}{\pi} \exp\left[-\left(\tfrac{1}{\cos\theta_{sw}} + \tfrac{1.04\sqrt{1+5.4u}}{\cos\theta_{wv}} \right) \kappa H \right], \end{aligned} \tag{3.16}$$

where, θ_{wv} is the subsurface viewing angle. Additionally, an empirical parameter ϵ is used to scale the effective scattering for changing sensor-solar geometry such that b_b in Eq. 3.4 and Eq. 3.8 are replaced by b'_b, where,

$$b'_b = b_{bw}(\lambda) + \epsilon(\lambda) b_{bp}(\lambda). \tag{3.17}$$

For r_{rs} at 90° azimuth from the solar plane, ϵ can be approximated as (Lee et al., 1999),

$$\epsilon(\lambda) \approx 1.0 + \left[0.1 + \frac{0.8 b_{bp}(\lambda)}{b_b(\lambda)}\right] \sin\theta_{wv} \sin\theta_{sw}. \tag{3.18}$$

Since airborne and satellite sensors measure reflected light above the water surface, quantities of above-water remote sensing reflectance (R_{rs}) are typically derived as opposed to sub-surface remote sensing reflectance. For remote sensing applications, it is therefore required that the sub-surface remote sensing reflectance, as approximated in Eq. 3.16, be scaled to the above-water remote sensing reflectance quantity. This is achieved with the exact equation,

$$R_{rs} = \frac{\zeta r_{rs}}{1 - \Gamma r_{rs}}, \tag{3.19}$$

where, ζ accounts for the water-to-air radiance divergence (Lee et al., 1998) and the term, $1 - \Gamma r_{rs}$ accounts for internal reflection. The model parameters ζ and Γ are dependent on solar-sensor geometry and water column properties including sea surface roughness and the refractive index of the bulk water column. For remote sensing observation angles, Lee et al. (1999) determined the model coefficients by comparing Eq. 3.19 with Hydrolight-generated R_{rs} and r_{rs} to give $\zeta \approx 0.5$ and $\Gamma \approx 1.5$.

The semi-analytical model for shallow waters, presented in Eqs. 3.16 through to 3.19, allows approximations of the above-water remote sensing reflectance spectrum for a given input of absorption, backscattering, irradiance reflectance values of the sea bottom, water column depth, solar zenith and sensor viewing angle. Lee et al. (1998) compared a large number of Hydrolight simulated r_{rs} spectra

which covered a wide range of water column IOPs, water depths and bottom albedos (of a spectrally constant bottom reflectance) with r_{rs} calculated using Eqs. 3.16 through to 3.18, and report a mean error of approximately 3% for nadir view geometry. This excellent agreement with simulated data indicates that the semi-analytical model is well suited for use in shallow water mapping applications over a wide range of environmental conditions, at least for the nadir view case. Because it is desirable to incorporate the semi-analytical model for applications that view the water at angles beyond nadir, and given that the model coefficients were largely derived for nadir view only, the accuracy of the semi-analytical model is assessed, in what follows, for a range of common sensor viewing angles. The accuracy test is performed using a new database of Hydrolight $R_{rs}(\lambda)$ simulations described in Section 3.1. The simulations cover a large range of water column IOPs from clear to turbid cases, a large range of water column depths from 0.1 m to 20 m and realistic bottom reflectance spectra typical of sand, seagrass and brown algae. For each Hydrolight-$R_{rs}(\lambda)$ spectrum in the database, the modelled-$R_{rs}(\lambda)$ spectrum was calculated with the equations given in 3.16 through to 3.19 using the exact same inputs of $a(\lambda)$, $b_{bw}(\lambda)$, $b_{bp}(\lambda)$, $\rho(\lambda)$, H, θ_{sw} and θ_{wv} as used for each corresponding Hydrolight input. Figures 3.1a to 3.1e show a series of scatter plots comparing analytically modelled-R_{rs} with Hydrolight-R_{rs} for a range of sensor viewing angles in the plane 90° from the solar azimuth. As expected, the comparison shows close agreement between modelled R_{rs} and Hydrolight R_{rs} for nadir sensor viewing with a mean error of $\sim 3.6\%$. However, for increasing sensor viewing angles the mean error steadily increases to more than double that of the nadir mean error at 40° ($\sim 8.0\%$). Figure 3.1f also shows the comparison for a 40° sensor viewing angle at 135° from the solar plane (a commonly used geometry for ship-based above-water remote sensing reflectance measurement (Mobley, 1999)(Mueller and Fargion, 2002) with a calculated mean error of $\sim 8.2\%$. It is likely that the error dependency with larger viewing angles is a consequence of using model coefficients that were derived for nadir viewing applications and/or the

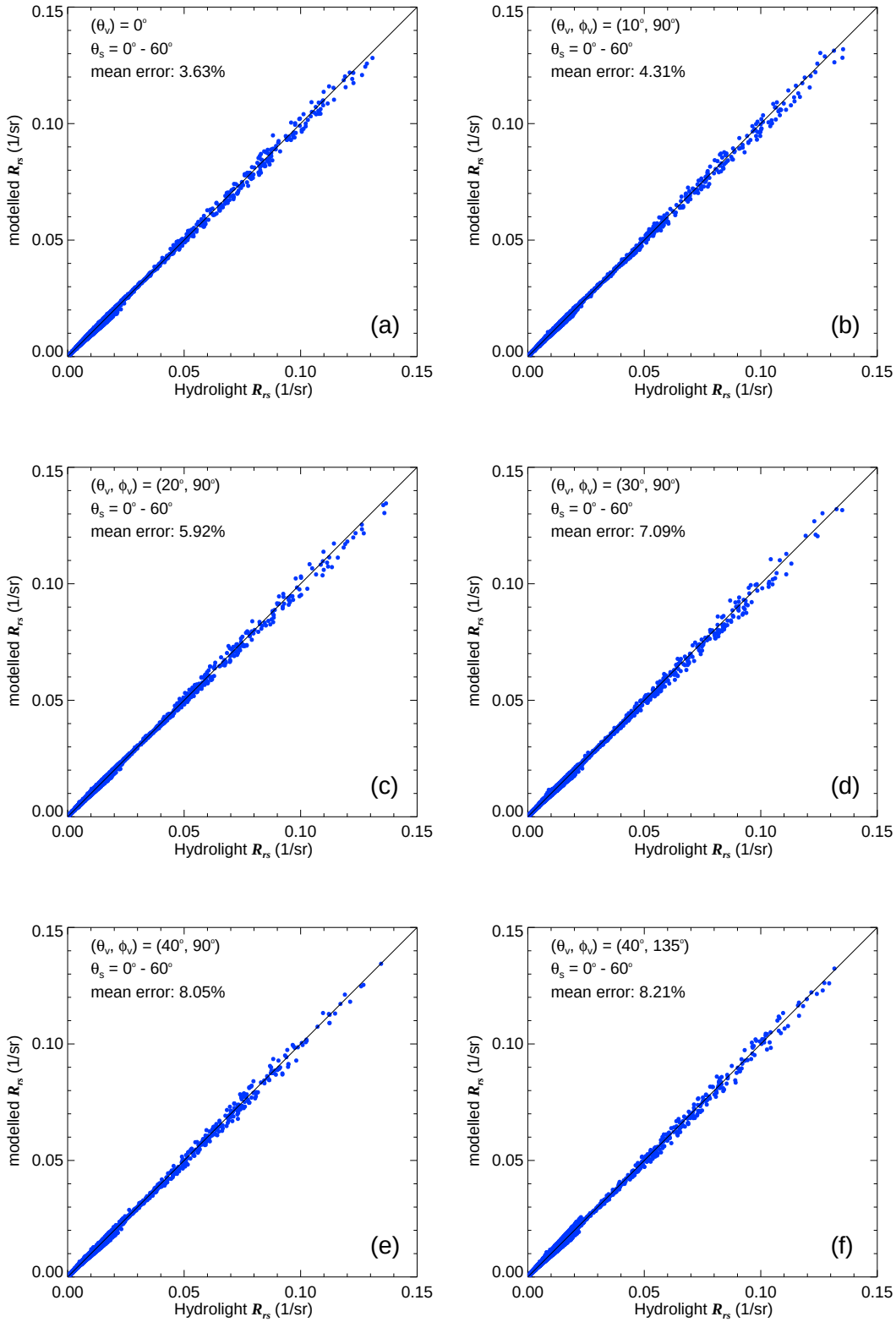

Figure 3.1: Modelled R_{rs} versus Hydrolight R_{rs}.

$1/\cos\theta_{wv}$ in Eq. 3.16 does not fully account for the path elongation of upwelling radiance at larger viewing angles.

Since the shallow water model is intended for the retrieval of water column properties, water depth and benthic cover from hyperspectral imagery, an increase in mean error with increasing sensor viewing angles may in turn lead to retrieval errors that are dependent on viewing geometry. For hyperspectral survey applications, angle-dependent retrieval errors may lead to artefacts in image-derived products (e.g. bathymetry), especially when merging a series of overlapping flightlines collected with different solar, water surface and sensor geometries.

In an attempt to improve the shallow water model performance over a wide range of illumination and sensor viewing geometries, a Look-Up-Table (LUT) of model coefficients has been derived for a range of different θ_s, θ_v and ϕ_v values. The approach taken effectively tuned the empirical model coefficients in the analytical expressions for the deep-water remote sensing reflectance, the distribution functions and the air-water interface for different solar-sensor geometries. As will be subsequently shown, this approach leads to an improved comparison between modelled and Hydrolight R_{rs}. Derivations of the new LUT of model coefficients and model performance are presented in the following sections.

3.1 Numerical Simulations of R_{rs} and r_{rs}

The derivation of the shallow water model coefficients presented above rely on R_{rs} and r_{rs} data with associated spectral absorption and backscattering coefficients, particle phase function, water depth, benthic reflectance and geometrical information. With this data, the model coefficients may be computed through curve fitting techniques. It would have been ideal to determine the model coefficients using "real" measurements, however, actual observations of $R_{rs}(\theta, \phi, \lambda)$ and $r_{rs}(\theta, \phi, \lambda)$ that include the necessary co-incident measurements of in-water IOPs, water depths and bottom reflectances, which also cover the necessary range of environmental conditions, do not exist. Instead, radiative transfer computations

were adopted. These enabled a large number of $R_{rs}(\theta, \phi, \lambda)$ and $r_{rs}(\theta, \phi, \lambda)$ spectra to be generated that covered a wide range of IOP inputs, bottom reflectances and water depths. With numerical computation of radiative transfer, each simulated radiance distribution output contains the associated environmental information used to generate them. With this controlled environment, derivation of model coefficients for specific conditions is made possible. Additionally, the simulated data is well suited to test model inversion performance, whereby, model inversion retrieval of parameters of interest can be compared to known simulation inputs.

Numerical simulations were performed with the commercially-available computer program Hydrolight 5.0. Hydrolight is a well established and validated numerical radiative transfer model used by many researchers for a wide range of applications. The program computes the exact solution of the radiative transfer forward model using "invariant imbedding theory" providing simulations of the full radiance distribution for any desired environmental condition. Details of the radiative transfer model and a software user's guide are presented in Mobley et al. (1993) and Mobley (1994), respectively.

Several large databases of Hydrolight-simulated R_{rs} and r_{rs} were generated covering a wide range of different environmental conditions, each intended to investigate different aspects of the shallow water model. Specific details of the different databases are presented in the subsections below. For all Hydrolight simulations, a 4 component Case-2 model with a homogeneous water column was used. The Gregg and Carder (1990) irradiance model was used to simulate the direct and diffuse downwelling irradiance for a cloudless sky at five different solar zenith angles (0°, 15°, 30°, 45° and 60°). The sky radiance distribution was computed with the Harrison and Coombes (1988) model and the surface roughness at the air-water interface was modelled using the Cox and Munk (1954) wave slope statistics for a wind speed of 5 kts. Pure water absorption coefficients were taken from Pope and Fry (1997). Phytoplankton absorption was modelled with Eqs. 2.41 and 2.42 and CDOM absorption modelled using Eq. 2.44 with

$S = 0.014$ and $\lambda_{ref} = 440$ nm. Scattering coefficients for pure seawater were taken from Smith and Baker (1981) with a Rayleigh phase function whereas particle scattering was modelled as (Gordon and Morel, 1983),

$$b_p(\lambda) = B[Chl - a]^{0.62}(550/\lambda), \tag{3.20}$$

with B representing an empirical value used to scale the overall magnitude of particle scattering. For particle scattering, a Petzold's "Average particle" phase function was used. For simplicity, inelastic scattering, detrital absorption, mineral particle absorption and scattering were excluded from these simulations.

Each Hydrolight simulation provides a discretised output of the full radiance distribution, $L(z, \theta, \phi, \lambda)$, that is gridded in spherical co-ordinates for both above and below the air-water interface. The standard Hydrolight quad layout was used, where ϕ is partitioned into 24 quads from 0° to 360°, giving an azimuthal resolution $\Delta\phi = 15°$. θ is partitioned into 20 quads from $-90°$ to 90°, giving a resolution $\Delta\theta = 10°$. Above-water reflectance representing each quad was calculated as,

$$R_{rs}(\Omega, \lambda) = \frac{L_u(0^+, \Omega, \lambda)}{E_d(0^+, \lambda)}, \tag{3.21}$$

and sub-surface remote sensing reflectance (just below the air-water interface) as,

$$r_{rs}(\Omega', \lambda) = \frac{L_u(0^-, \Omega', \lambda)}{E_d(0^-, \lambda)}, \tag{3.22}$$

with (θ, ϕ) and (θ', ϕ') denoted as Ω and Ω', respectively.

3.1.1 Database 1: Deep-water reflectance

The database was composed of 7100 deep-water $r_{rs}(\Omega')$ spectra, computed with an infinitely deep and homogeneous water column. To provide a wide range of realistic conditions, total absorption and scattering was modelled with randomised values of $Chl - a$, $a_{CDOM}(440)$ and B over a range that covered very clear to

highly turbid water types. Computations were made over a spectral range from 400 nm to 700 nm with 5 nm resolution. The range of Hydrolight inputs are summarised in Table 3.1.

Table 3.1: Parameters used in Hydrolight simulations to generate Database 1.

Variable	Inputs
Solar zenith angle	0°, 15°, 30°, 45°, 60°
$Chl-a$ [μgm^{-3}]	0.1 - 5 (n=1000)
$a_{CDOM}(440)$ [m^{-1}]	0.01 - 0.2 (n=1000)
B	0.1 - 3.0 (n=1000)
Particle phase function	Petzold's "Average Particle"
λ	$400-700$, every 5 nm

3.1.2 Database 2: Shallow-water reflectance (3 bottom types)

The database was composed of 7100 shallow-water $R_{rs}(\Omega)$ and $r_{rs}(\Omega')$ spectra, computed for a range of randomised water depths and 3 different bottom reflectance spectra. Bottom irradiance reflectance spectra, representing "Ooid sand", "Average seagrass" and "Brown algae" , were taken from bottom reflectance data that is provided with Hydrolight 5.0. Bottom reflectance was assumed to be Lambertian. The range of Hydrolight inputs are summarised in Table 3.2.

Table 3.2: Parameters used in Hydrolight simulations to generate Database 2.

Variable	Inputs
Solar zenith angle	0°, 15°, 30°, 45°, 60°
$Chl-a$ [μgm^{-3}]	0.1 - 5 (n=1000)
$a_{CDOM}(440)$ [m^{-1}]	0.01 - 0.2 (n=1000)
B	0.1 - 3.0 (n=1000)
Particle phase function	Petzold's "Average Particle"
Depth [m]	0.1 - 25 (n=1000)
Bottom Type	Ooid sand, Average seagrass, Brown algae
λ	$400-700$, every 5 nm

3.1.3 Database 3: Shallow-water reflectance (mixtures of 3 bottom types)

The database was composed of 7100 R_{rs} spectra, simulated over a range of randomised water depths and randomised mixtures of "Ooid sand", "Average seagrass" and "Brown algae" irradiance reflectances. Mixtures of bottom irradiance reflectance were modelled as,

$$\rho(\lambda) = f_{os}\rho_{os}(\lambda) + f_{as}\rho_{as}(\lambda) + f_{ba}\rho_{ba}(\lambda), \tag{3.23}$$

where the subscripts "os", "as" and "ba" represent "Ooid sand", "Average seagrass" and "Brown algae", respectively. $\rho_i(\lambda)$ represents the irradiance reflectance of each bottom type and f_i is the fractional mixture of each bottom type with the criterion $f_{os} + f_{as} + f_{ba} = 1$. The range of Hydrolight inputs are summarised in Table 3.3.

Table 3.3: Parameters used in Hydrolight simulations to generate Database 3.

Variable	Inputs
Solar zenith angle	0°, 15°, 30°, 45°, 60°
$Chl-a$ [μgm^{-3}]	0.1 - 5 (n=1000)
$a_{CDOM}(440)$ [m^{-1}]	0.01 - 0.2 (n=1000)
B	0.1 - 3.0 (n=1000)
Particle phase function	Petzold's "Average Particle"
Depth [m]	0.1 - 25 (n=1000)
Bottom Type	Ooid sand, Average seagrass, Brown algae
f_i	randomised between 0 and 1 (n=1000)
λ	$400-700$, every 5 nm

3.2 Algorithm Development

3.2.1 Deep-water r_{rs}

The derived coefficients in Eq. 3.5 were computed for nadir viewing sensor geometry, and therefore, may limit their applicability for remote sensing studies

whereby sensor viewing angles up to 40° from nadir are commonplace. For sensor viewing angles away from nadir, it is suggested that the g_i coefficients in Eq. 3.5 be separately determined (Lee et al., 1999).

In a similar manner to Lee et al. (1998) and Lee et al. (1999), numerical simulations of r_{rs} for a wide variety of environmental conditions were performed in the current research to investigate the angular dependence of the g parameter in Eq. 3.3. The simulations used here are described in Section 3.1.1. Only deep-water subsurface remote sensing simulated with an infinitely deep water column were used.

The relationship between r_{rs} and $b_b/(a + b_b)$ for selected solar and sensor geometries, and for a Petzolds "average particle" phase function with $b_{bp}/b_p = 0.0183$, is shown in Figs. 3.2 and 3.3. Both figures also show the relationship using the coefficients as in Lee et al. (1999) for reference. Figure 3.2 shows the non-linear dependence of r_{rs} on $b_b/(a + b_b)$ for different sensor viewing angles (from nadir) at an azimuth angle of 90° from the solar plane. For nadir viewing geometry, approximation 3.3 calculated with the coefficients determined by Lee et al. (1999) (black triangle symbols) follows the simulated r_{rs} (black dotted line) data closely. At increasing sensor viewing angles however, the simulated r_{rs} tends to deviate away from the Lee et al. (1999) approximation with larger deviation apparent at increasing solar zenith angles (see Fig. 3.2). This apparent deviation at increasing solar zenith angles is due to approximation 3.3 not accounting for the variations of the underwater radiance distributions due to solar-sensor geometries and the volume scattering function. Figure 3.3 shows r_{rs} as a function of $b_b/(a+b_b)$ for different solar zenith angles at selected sensor geometry. For nadir viewing, the solar zenith angle shows negligible difference in r_{rs} as a function of $b_b/(a+b_b)$. At increasing sensor viewing angles, however, the difference becomes more apparent (Figs. 3.2a and b). This indicates that the approximation between r_{rs} and $b_b/(a + b_b)$ vary with different solar and sensor geometry, and since the curves appear to be well behaved, derivation of separate g_i coefficients corresponding to

separate solar-sensor geometry is likely.

An added complexity in attempting to determine the g relationship for a variety of solar and sensor geometries is that the redistribution of scattered photons for molecular scattering (by water molecules) can be significantly different from that of particle scattering. The measure of upwelling radiance in a specific direction will therefore be dependent on the relative proportions of molecular and particle scattering. To account for the changes in angular distribution of bulk water that result from particle introduced angular variation, Lee et al. (2004)Lee et al. (2011), rewrote Eq. 3.3 by partitioning the molecular and particle scattering contributions with,

$$r_{rs} = g_w \frac{b_{bw}}{a + b_b} + g_p \frac{b_{bp}}{a + b_b}. \tag{3.24}$$

Rearranging Eq. 3.24 in a form analogous to Eq. 3.3 gives,

$$g = g_w \frac{b_{bw}}{b_b} + g_p \frac{b_{bp}}{b_b}, \tag{3.25}$$

with g_p empirically determined to take the form,

$$g_p = G_0 \left[1 - G_1 \exp\left(-G_2 \frac{b_{bp}}{a + b_b} \right) \right]. \tag{3.26}$$

Here, the total bulk water backscattering, b_b, is taken as the sum of pure water backscattering, b_{bw}, and particle backscattering, b_{bp}. The model parameters, g_w, G_0, G_1 and G_2 are constants (for a specified light geometry) to be determined.

Using the Hydrolight-simulated $r_{rs}(\Omega')$ (interpolated to sub-surface viewing angles), a set of $g_w(\Omega')$, $G_0(\Omega')$, $G_1(\Omega')$ and $G_2(\Omega')$ coefficients were determined with Levenberg-Marquardt non-linear optimisation (see Section 3.4). For each set of radiance-solar geometry, the best fit model parameters were determined by minimising the difference between modelled-$r_{rs}(\Omega')$ and Hydrolight-$r_{rs}(\Omega')$.

From Eq. 3.24, the residual g_p coefficients may be calculated using the Hydrolight r_{rs} simulations together with the derived $g_w(\Omega')$. Figure 3.4 shows calculated g_p as a function of $b_{bp}/(a + b_b)$ (blue points) and g_p modelled with Eq. 3.26 (solid

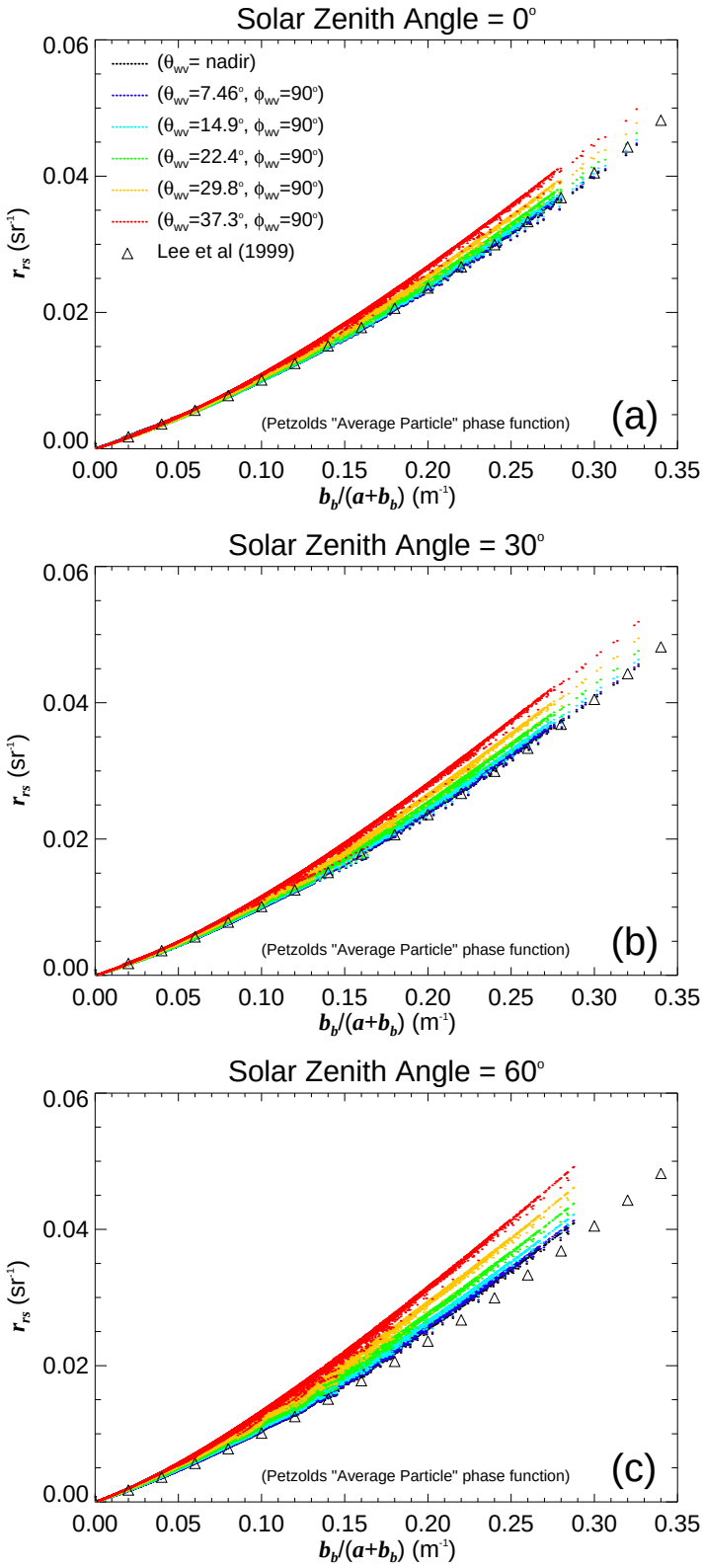

Figure 3.2: Hydrolight-generated r_{rs} versus $b_b/(a + b_b)$ for different subsurface sensor viewing angles (θ_{wv}, ϕ_{wv}) with a solar zenith angle of 0°, 30° and 60° (a, b and c, respectively).

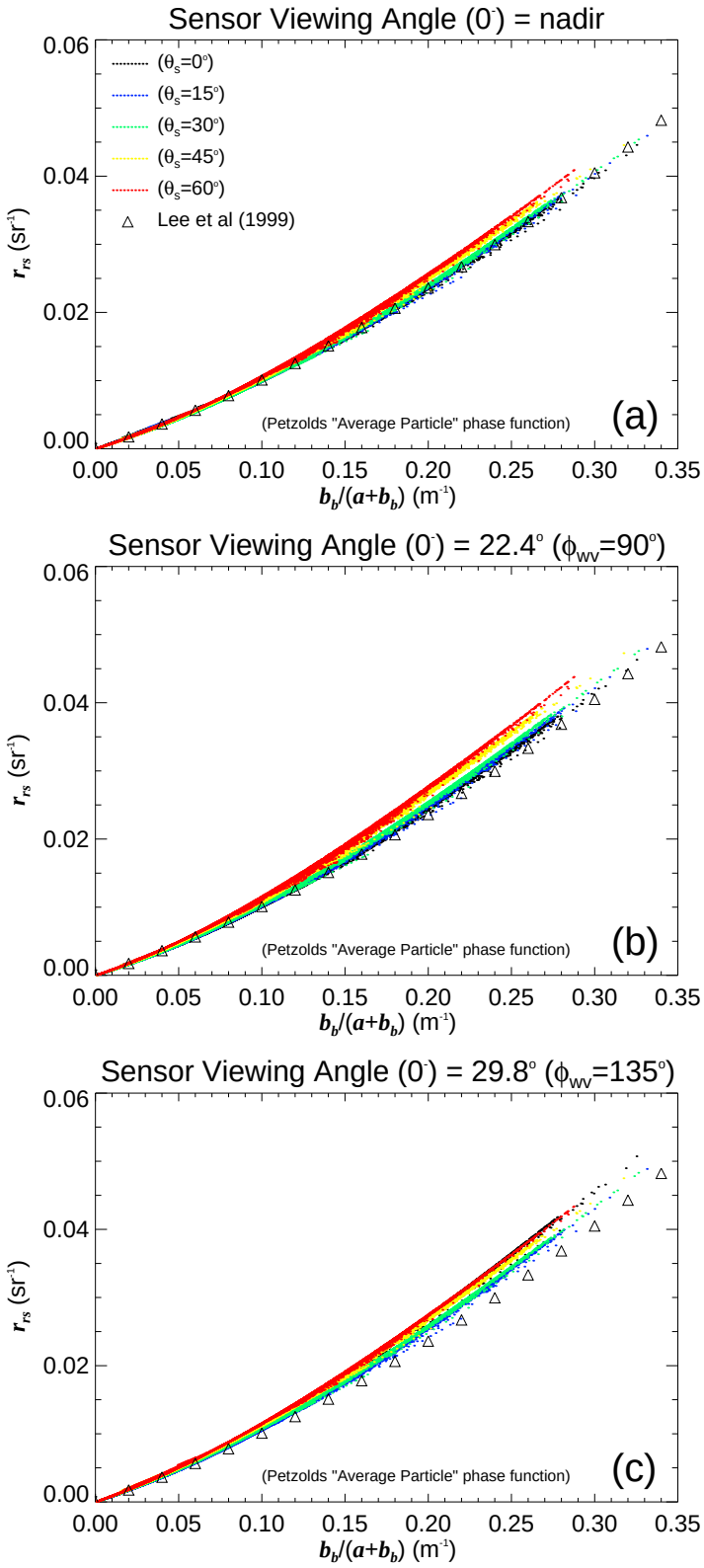

Figure 3.3: Hydrolight-generated r_{rs} versus $b_b/(a + b_b)$ for different solar zenith angles (θ_s) with a subsurface sensor viewing angle of 0°, 22.4° and 29.8° (a, b and c, respectively).

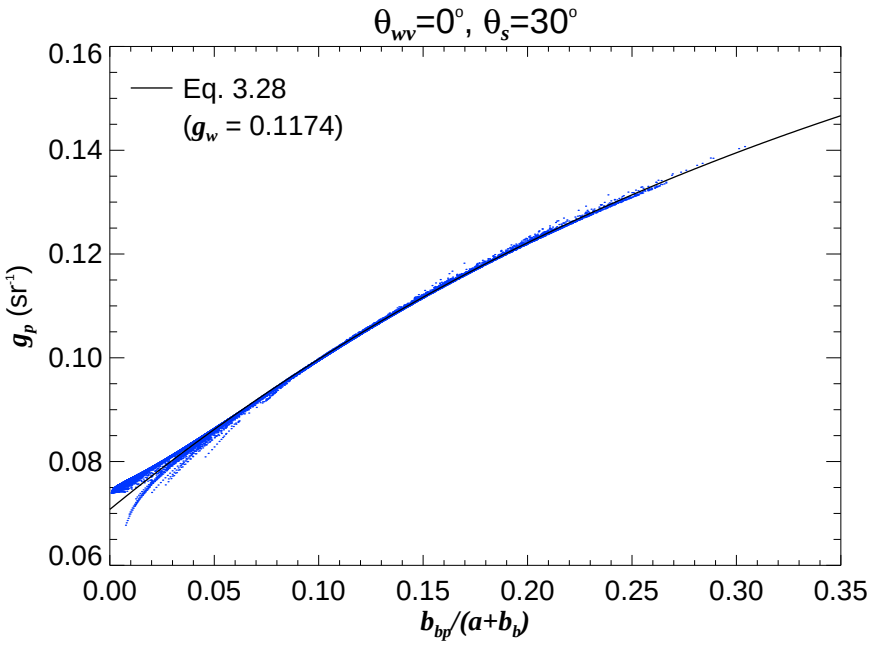

Figure 3.4: Calculated g_p versus $b_{bp}/(a+b_b)$ (blue points) and model fit g_p using Eq. 3.26 (solid line) for nadir view and 30° solar zenith angle. The derived value for g_w is shown.

line) for nadir viewing geometry and a 30° solar zenith angle, using the best fit model coefficients $\{g_w, G_0, G_1, G_2\} \approx \{0.1174, 0.1989, 0.6441, 2.5627\}$. Generally, the calculated g_p points appear to form a well behaved curve and are adequately modelled with Eq. 3.26 for $b_{bp}/(a+b_b) \gtrapprox 0.08$. For $b_{bp}/(a+b_b) \lessapprox 0.08$, g_p points appear to show some spread. This is likely due to molecular-particle interscattering as discussed in Lee et al. (2004). To account for the interscattering contribution, an additional term in approximation 3.24 is introduced to give,

$$r_{rs} = g_w \frac{b_{bw}}{a+b_b} + g_p \frac{b_{bp}}{a+b_b} + g_{wp} \frac{b_{bw} b_{bp}}{(a+b_b)^2}, \tag{3.27}$$

where, g_{gp} is a new model coefficient representing the molecule-particle interscattering contribution and g_p modified with the inclusion an additional G_3 model coefficient, reformulated as,

$$g_p = G_0 \left[1 - G_1 \exp\left\{ -G_2 \left(\frac{b_{bp}}{a+b_b} \right)^{G_3} \right\} \right]. \tag{3.28}$$

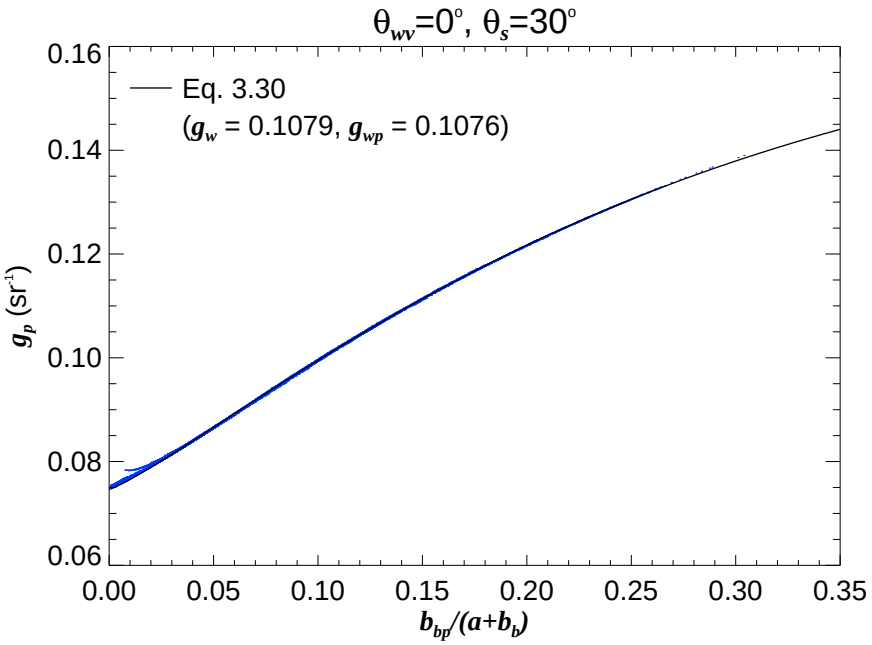

Figure 3.5: Calculated g_p versus $b_{bp}/(a + b_b)$ (blue points) and model fit g_p with Eq. 3.28 (solid line) for nadir view and 30° solar zenith angle. The derived values for g_w and g_{wp} are provided.

Again, Levenberg-Marquardt non-linear optimisation was employed to derive the best fit model parameters presented in Eq. 3.27 and Eq. 3.28. The computations were performed over the range of Hydrolight sub-surface sensor viewing geometry (θ'_{wv}, ϕ'_{wv}) and the 5 simulated solar zenith angles (θ_s) resulting in a final LUT of $g_w(\Omega')$, $G_0(\Omega')$, $G_1(\Omega')$, $G_2(\Omega')$, $G_3(\Omega')$ and $g_{wp}(\Omega')$ values.

The effect of incorporating the extra interscattering term in Eq. 3.27 and the G_3 model coefficient in Eq. 3.28 is illustrated in the example shown in Fig. 3.5. Here, Eq. 3.27 was rearranged in order to calculate g_p from Hydrolight data together with the newly derived g_w and g_{wp} values. The calculated g_p as a function of $b_{bp}/(a + b_b)$ (blue points) and Eq. 3.28 (solid line) for nadir viewing geometry and a 30° solar zenith angle is shown. The best fit model coefficients used for plotting Eq. 3.28 are $\{g_w, G_0, G_1, G_2, G_3, g_{wp}\} = \{0.1079, 0.1684, 0.5567, 4.6437, 1.1776, 0.1076\}$. The data presented here show a very well behaved and predictable pattern of g_p with a much improved model fit (Eq. 3.28) to the g_p values as compared to those in Fig. 3.4.

Values of derived model coefficients ($g_w(\Omega')$, $G_0(\Omega')$, $G_1(\Omega')$, $G_2(\Omega')$, $G_3(\Omega')$ and $g_{wp}(\Omega')$) for a selection of common remote sensing observation angles are listed in Appendix 7.6 and graphically presented in Figs. 3.6 to 3.8. Figure 3.6 shows variations of the derived model coefficients as a function of solar zenith angle for 6 different sensor view angles. The model coefficients exhibit smooth but seemingly unpredictable non-linear curves with changing solar zenith angle and for different sensor viewing angles. Similarly, Figs. 3.7 and 3.8 show the derived model coefficients as a function of sensor viewing nadir angle and sensor view azimuth angle for 5 different solar zenith angles. Again, all model parameters show variation with changing sensor geometry. These variations highlight the potential usefulness of incorporating a Look-Up-Table of model coefficients, where values for specific geometry can be used, in order to better model the deep-water sub-surface remote sensing reflectance as a function of absorption and backscattering. An assessment of the LUT potential was evaluated by comparing modelled-r_{rs} (using Eq. 3.27 and the LUT model coefficients) with Hydrolight-r_{rs} over a wide range of geometries which include sensor viewing angles from nadir to 40° and solar zenith angles from 0° to 60°. The scatter plot in Fig. 3.9 shows that the modelled-r_{rs} compares extremely closely to Hydrolight-r_{rs} for the wide range of IOPs and geometry, with a calculated RMS error of only 0.18%. The results are very encouraging, however, it must be noted that the comparison of the deep-water r_{rs} approximation was made with the very same data that was used in deriving its model coefficients, effectively tuning the approximation to the environmental conditions that were simulated. Additionally, the simulated Hydrolight-r_{rs} data were generated in a controlled environment using a single particle phase function to describe the directional scattering. Of course, a series of different model coefficient LUTs can be generated for spanning a range of different particle phase functions (PPFs). However, assigning the most appropriate PPF-dependent LUT of model coefficients is challenging, especially since accurate determination of PPFs from remotely sensed data alone is not yet possible. The

task here was to describe the development of a deep-water r_{rs} approximation with the intention of extending the model to cover a wide range solar-sensor geometries, and therefore, potentially improving the shallow water reflectance model. To show this, the commonly used Petzold's "Average Particle" phase function was employed. Also, because the focus of this dissertation is the shallow-water model, where reflectance from the bottom adds to the complexity of upwelling signals, the deep-water r_{rs} approximation is likely to be less important, especially for situations where the contribution from bottom reflectance dominates the total upwelling signal. An investigation of the effect of different PPFs for the shallow water model as a whole is presented in the following section.

3.2.2 Diffuse attenuation coefficients

The general approximation for subsurface remote sensing reflectance of shallow waters presented in Eq. 3.6 incorporate three effective diffuse attenuation terms; (1) the diffuse attenuation of downwelling irradiance, K_d, (2) the diffuse attenuation of upwelling radiance from the water column, K_u^C and (3) the diffuse attenuation of upwelling radiance reflected from the seafloor, K_u^B. The diffuse attenuation terms are important parameters which describe the rate at which light intensity diminishes as it propagates through the water column. Incorporating the diffuse attenuation terms into the shallow water reflectance model permits the accurate estimation of light intensity that reaches the seafloor and the light intensity that reflects off the seafloor and propagates up to the air-water interface. Since the diffuse attenuation terms are apparent optical properties which are dependent on the nature of their respective light fields, the model coefficients that are used to approximate the respective attenuation terms are also functions of solar illumination and sensor viewing geometry as well as particle phase function. Using the Kirk (Kirk, 1991) K-type expressions for approximating the

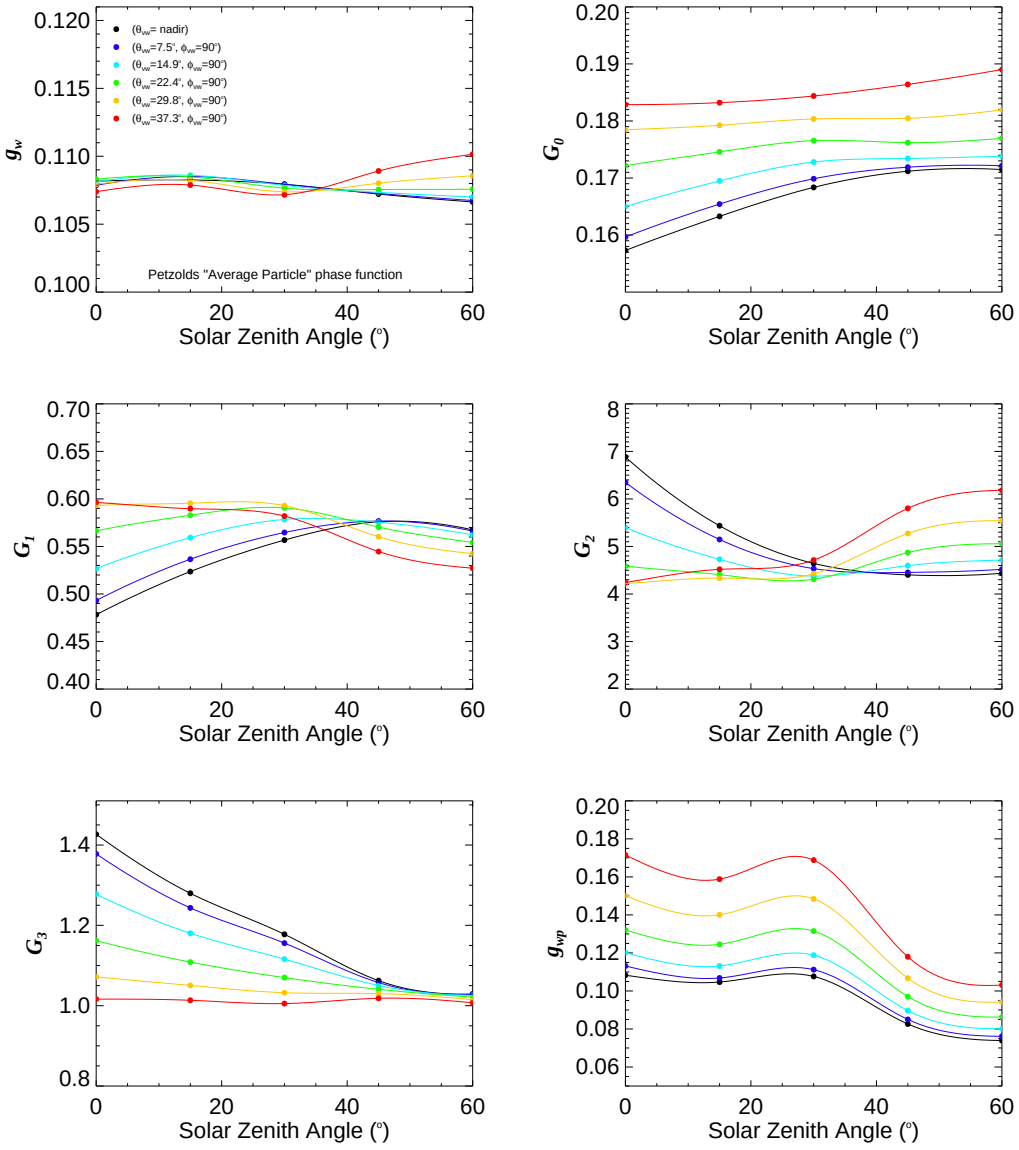

Figure 3.6: Derived coefficients, g_w, G_0, G_1, G_2, G_3 and g_{wp} versus solar zenith angle for selected sensor viewing angles.

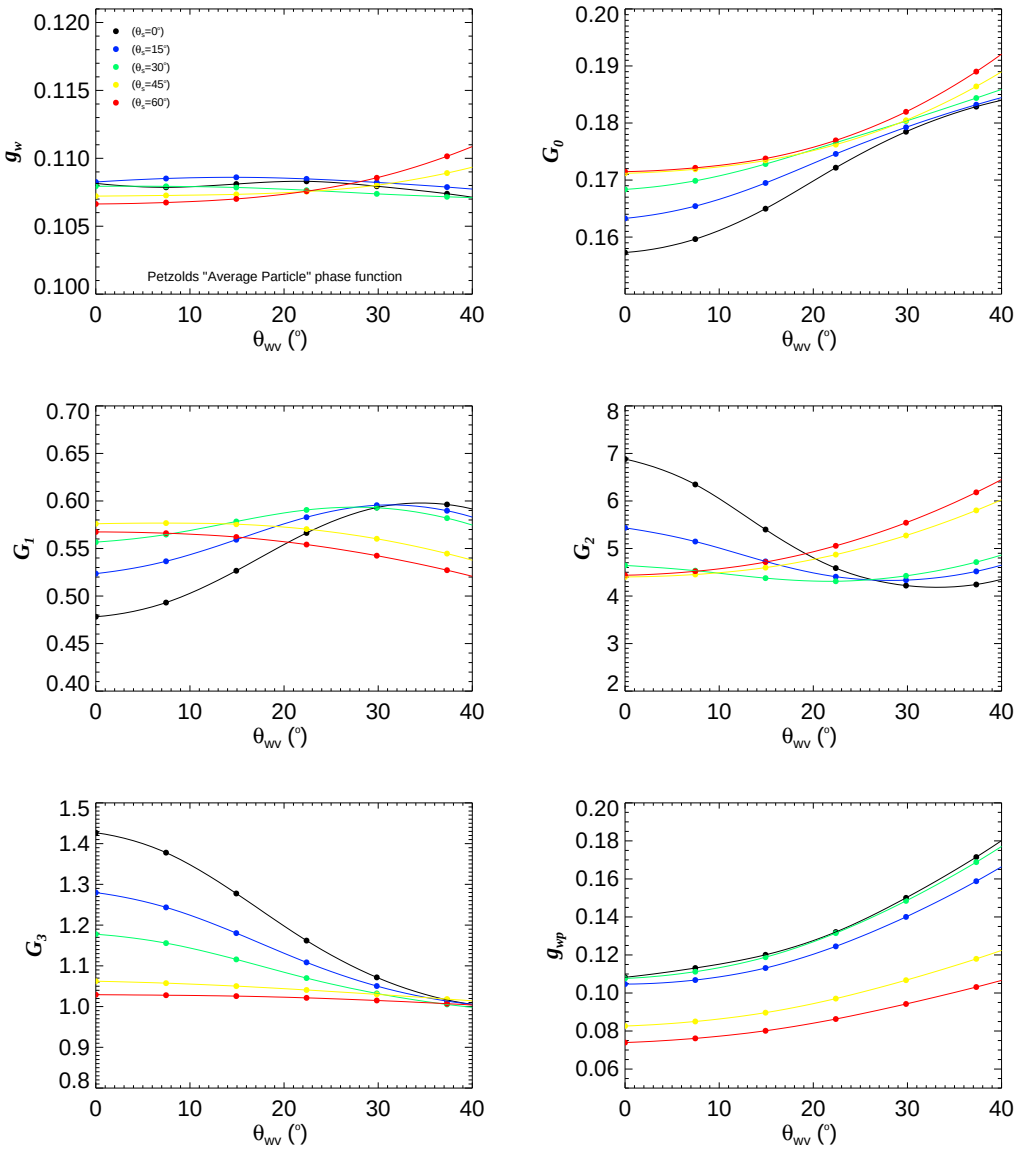

Figure 3.7: Derived coefficients, g_w, G_0, G_1, G_2, G_3 and g_{wp} versus sensor viewing angle (in the plane 90° from the solar azimuth) for selected solar zenith angles.

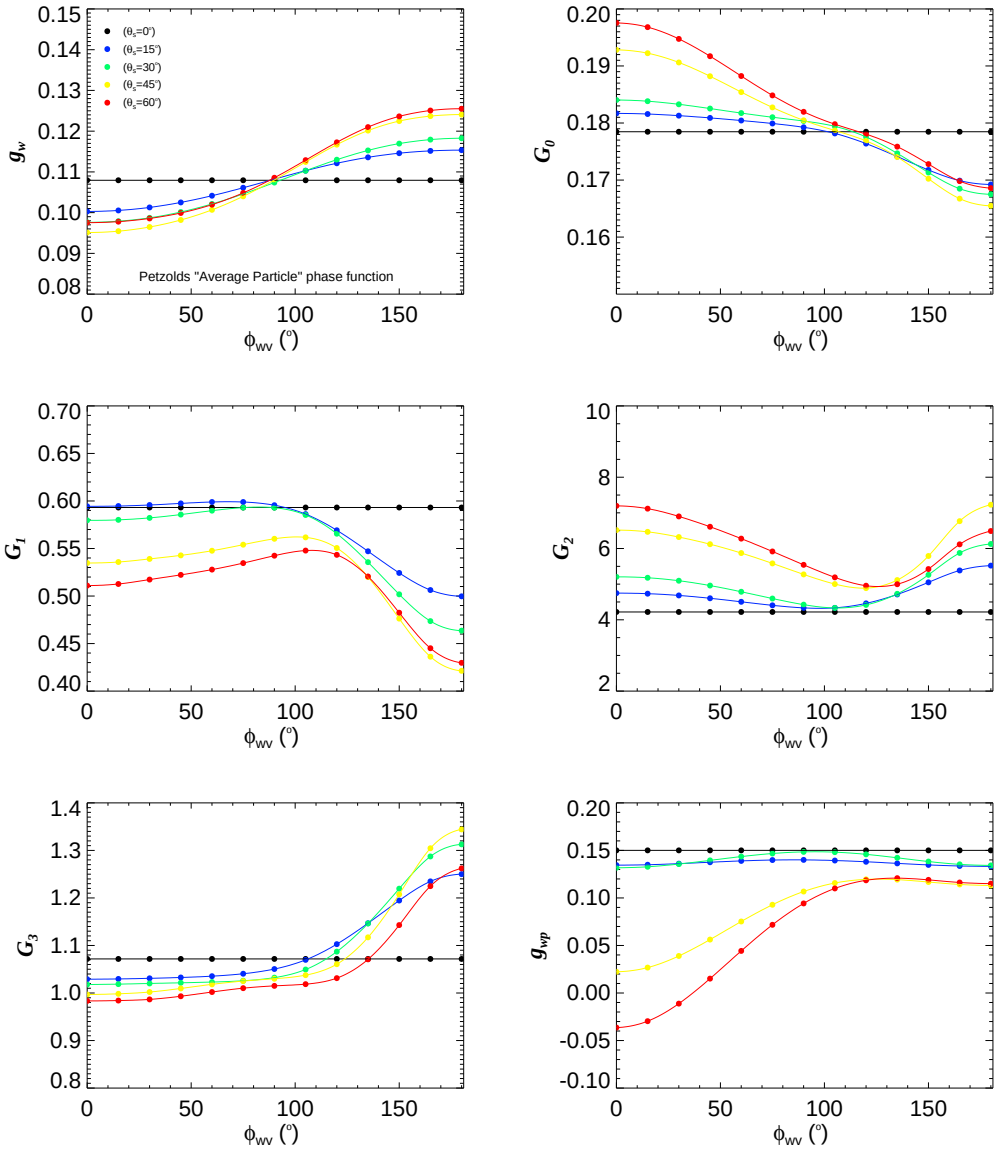

Figure 3.8: Derived coefficients, g_w, G_0, G_1, G_2, G_3 and g_{wp} versus sensor viewing azimuth (sensor view angle 30° from nadir) for selected solar zenith angles.

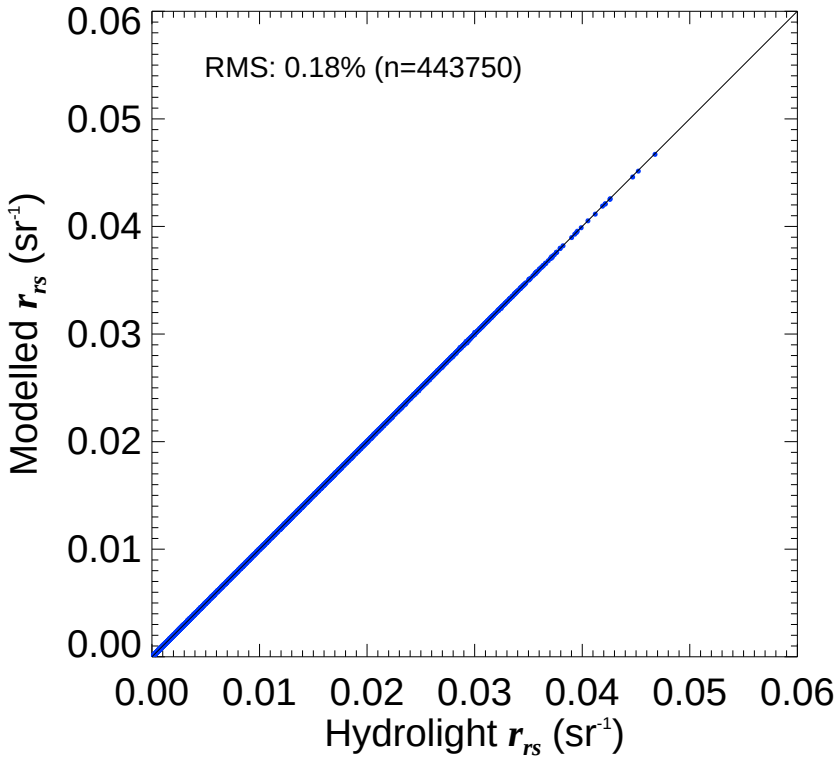

Figure 3.9: Comparison between Hydrolight-r_{rs} and r_{rs} modelled with Eq. 3.27 and the derived LUT of model coefficients over a wide range of IOPs and solar-sensor geometries.

distribution functions for upwelling radiance we have,

$$K_u^C(\Omega') = D_0^C(\Omega')\sqrt{1.0 + D_1^C(\Omega')u}(a + b_b), \tag{3.29}$$

and

$$K_u^B(\Omega') = D_0^B(\Omega')\sqrt{1.0 + D_1^B(\Omega')u}(a + b_b), \tag{3.30}$$

where the geometry-dependent model coefficients, $D_0^C(\Omega')$, $D_1^C(\Omega')$, $D_0^B(\Omega')$ and $D_1^B(\Omega')$ are to be determined.

Strictly speaking, the above model coefficients are also functions of water column depth, and bottom boundary BRDF. Even for a homogeneous water column, the underwater light field changes with depth, and therefore, derived model coefficients for different water column depths are likely to be different. The same is true for different bottom types exhibiting different BRDFs since this also affects the underwater light field. A LUT of model coefficients for different Ω'-geometry, water column depth and bottom type BRDF would most likely provide very good approximations of shallow water remote sensing reflectance. However, the appropriate selection of distribution function model coefficients from the LUT would require *a priori* knowledge of water column depth and BRDF. Since the goal here is to retrieve water depth and benthic cover information from remote sensing, such an LUT is not desirable. Instead, only a Ω'-dependent LUT of newly derived model coefficients is proposed. This way, the model coefficients are represented with average values that have been derived over a range of water column depths and bottom types.

Values for $D_0^C(\Omega')$, $D_1^C(\Omega')$, $D_0^B(\Omega')$ and $D_1^B(\Omega')$ were derived using the simulated Hydrolight-r_{rs} data of Database 2 that cover a wide range of random IOPs, random water column depths ranging from 0.1 m to 20 m and different bottom types, typical of sand, seagrass and brown algae. Because the radiance distributions that are output in Hydrolight 5.0 do not distinguish between the upwelling radiance emanating from the water column and the upwelling radiance reflected

off the seafloor, investigation of the distribution functions separately was not possible. Therefore, the model coefficients were determined by fitting Eq. 3.6 to Hydrolight-r_{rs} with Levenberg-Marquardt non-linear optimisation. The previously determined LUT of $g_w(\Omega')$, $G_0(\Omega')$, $G_1(\Omega')$, $G_2(\Omega')$, $G_3(\Omega')$ and $g_{wp}(\Omega'$, were used to model the deep-water reflectance term in Eq. 3.6 along with the Hydrolight inputs of absorption, backscattering, depth and bottom reflectance. The derived model coefficients ($D_0^C(\Omega')$, $D_1^C(\Omega')$, $D_0^B(\Omega')$ and $D_1^B(\Omega')$ for a selection of common remote sensing observation angles are listed in Appendix 7.7.

Figures 3.10 to 3.12 show examples of the derived D_u^C and D_u^B model coefficients for selected solar-sensor viewing geometries. The data illustrates that the derived model coefficients vary with solar zenith angle and sensor viewing geometries. For example, Fig. 3.10 shows that for a sensor viewing azimuth at 90° from the solar plane, D_0^C values are shown to range between 0.65 to 1.0 for different solar-sensor angles, with the nadir view exhibiting the largest variability with solar zenith angle. D_1^C shows the largest variability out of the 4 model coefficients with a range from 2.0 to 9.0. Again, with nadir view exhibiting the largest variability with solar zenith angle. D_0^B values range between 1.1 and 1.4, and D_1^B values range between 4 and 6.5. The reported values of the same model coefficients determined by Lee et al. (1999) lie within the ranges of the values derived here, except for D_0^C whose range of values are lower than Lee et al. (1999).

The shallow water model for sub-surface remote sensing reflectance, expressed in terms of the angle-dependent model coefficients for deep-water r_{rs} and diffuse attenuation distribution functions derived here, is given as,

$$\begin{aligned} r_{rs}(\Omega') &\approx r_{rs}^{\infty}(\Omega')\left\{1-\exp\left[-\left(\tfrac{1}{\cos\theta_{sw}}+D_0^C(\Omega')\sqrt{1+D_1^C(\Omega')u}\right)\kappa H\right]\right\} \\ &+ \tfrac{\rho}{\pi}\exp\left[-\left(\tfrac{1}{\cos\theta_{sw}}+D_0^B(\Omega')\sqrt{1+D_1^B(\Omega')u}\right)\kappa H\right]. \end{aligned} \tag{3.31}$$

The performance of incorporating the angle-dependent model coefficients in Eq.3.31 to model-r_{rs} over an extended range of solar-sensor geometry was evaluated by comparing modelled-r_{rs} (Eq. 3.31) and Hydrolight-r_{rs}. The comparison was con-

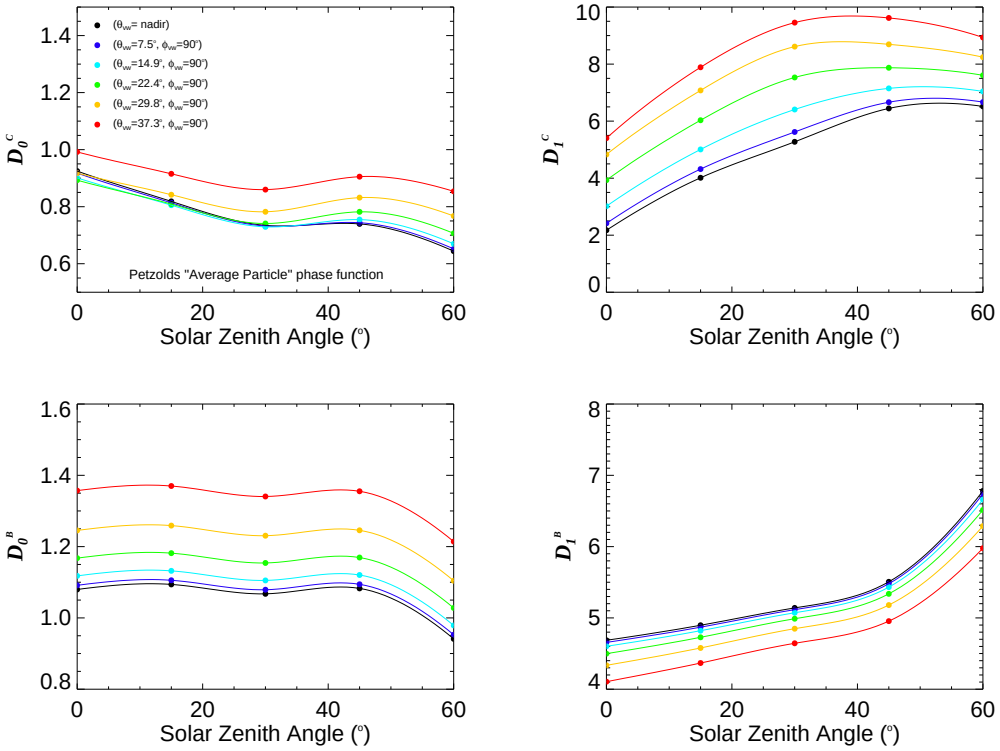

Figure 3.10: Derived coefficients, D_0^C, D_1^C, D_0^B and D_1^B versus solar zenith angle for selected sensor viewing angles.

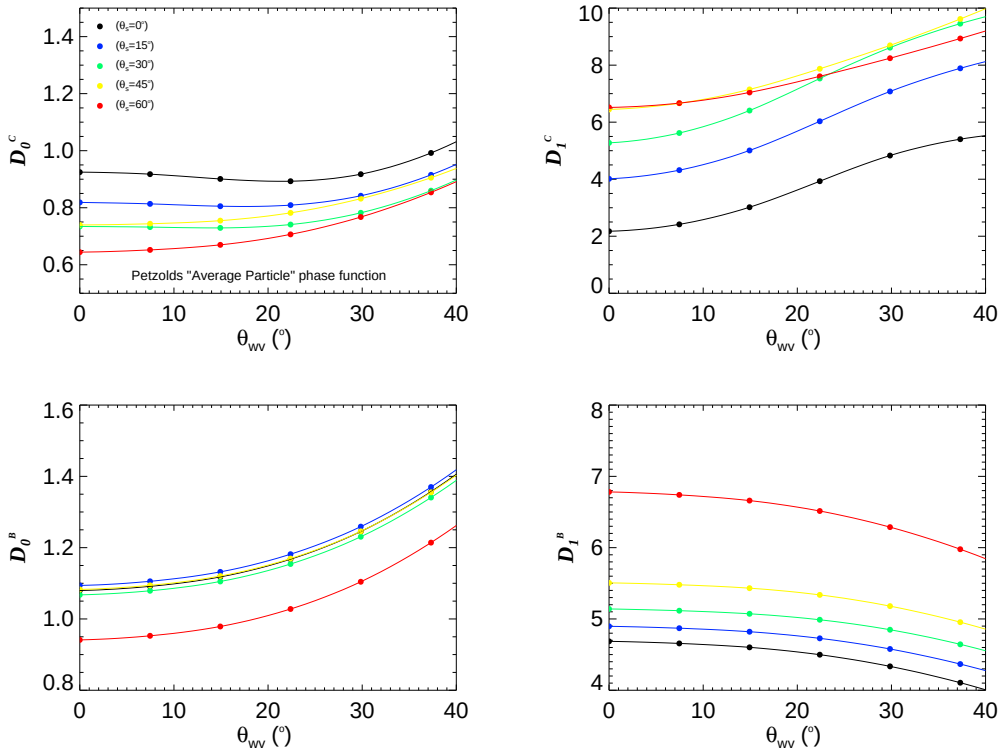

Figure 3.11: Derived coefficients, D_0^C, D_1^C, D_0^B and D_1^B versus sensor viewing angle (in the plane 90° from the solar azimuth) for selected solar zenith angles.

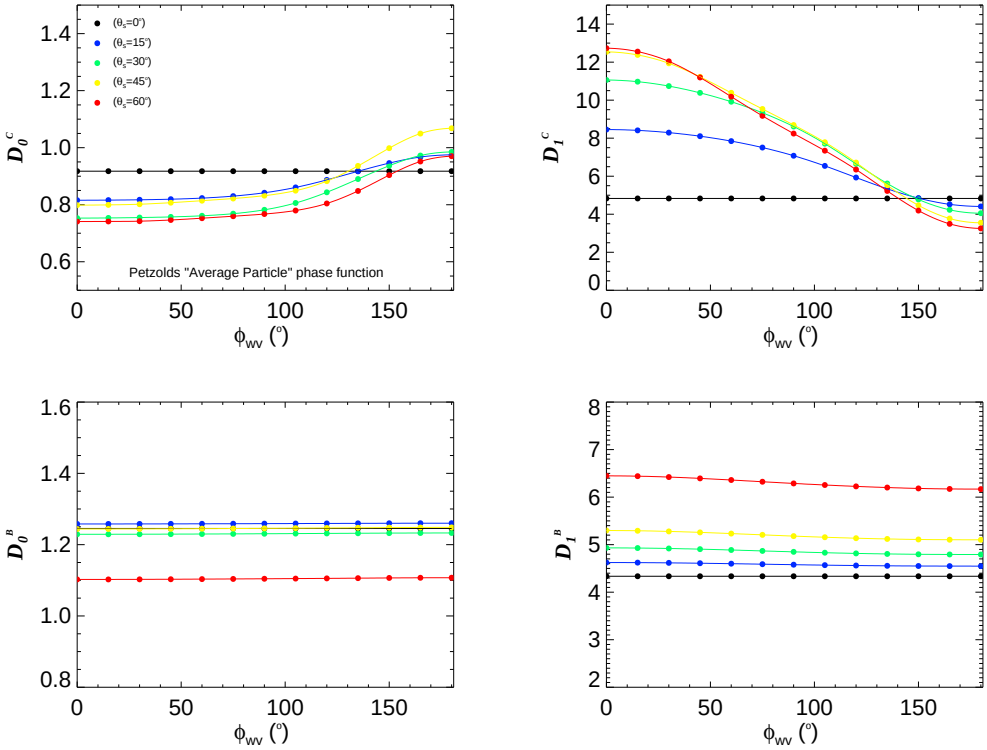

Figure 3.12: Derived coefficients, D_0^C, D_1^C, D_0^B and D_1^B versus sensor-viewing azimuth angle (sensor view angle 30° from nadir) for selected solar zenith angles.

ducted using simulated Hydrolight-r_{rs} data taken from Database 2 for a selection of common remote sensing geometries, which include sensor viewing angles from nadir to 40° and solar zenith angles from 0° to 60°. The comparison scatter plot in Fig. 3.13 shows that modelled-r_{rs} compares well with Hydrolight-r_{rs} with a calculated RMS error of $\sim$ 1% (n = 1331250). The maximum RMS error of $\sim$ 20% was calculated for this comparison data set and corresponds to a very clear, and very shallow (0.1 m) water depth. This deviation is likely due to multiple reflections between the seafloor and air-water interface adding to the total sub-surface reflectance signal which is not accounted for in the shallow water reflectance model. Figure 3.14 shows calculated RMS error as a function of sensor viewing angle (in the plane 90° from the sun's azimuth). There is no noticeable trend with changing sensor viewing geometry indicating that the incorporation of the LUT's of model coefficients are well suited in approximating r_{rs} over a wide range of solar-sensor geometries appropriate to remote sensing observations.

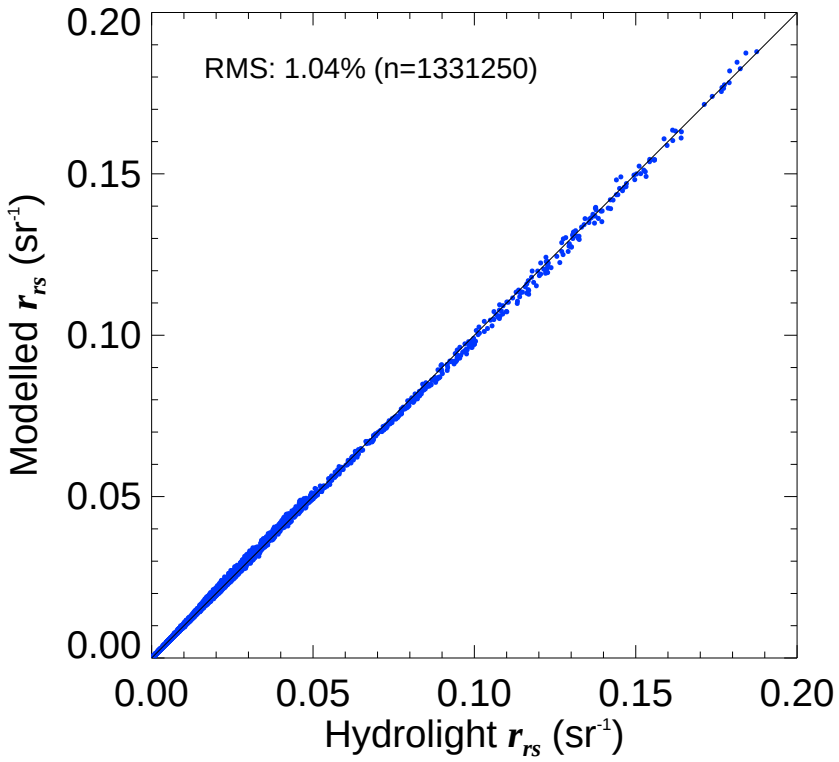

Figure 3.13: Comparison between Hydrolight-r_{rs} and modelled-r_{rs} calculated using Eq. 3.31 for a wide range of IOPs and solar-sensor geometries.

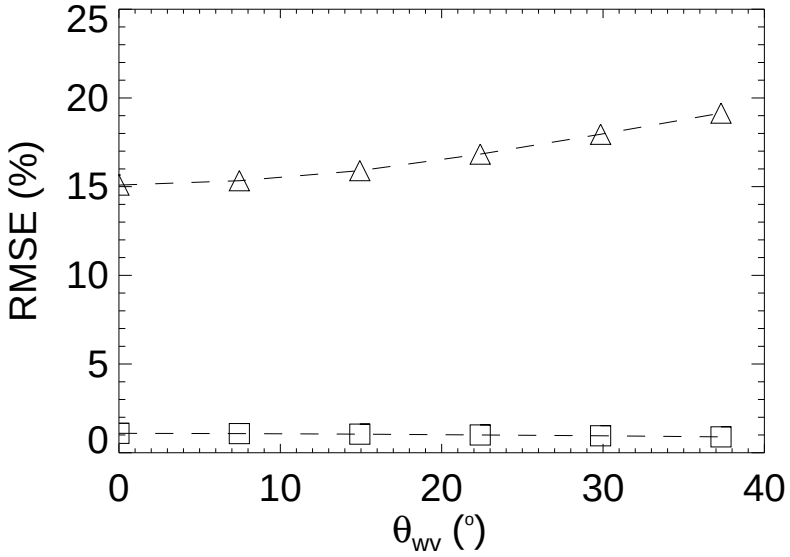

Figure 3.14: RMS error of Hydrolight and modelled r_{rs} as a function of sensor viewing angle (in the plane 90° from the sun). The square and triangle symbols represent the mean RMS error and maximum RMS error, respectively.

3.2.3 Air-water Interface

For remote sensing applications, whereby, for a variety of reasons, water targets are commonly viewed at a range of sensor viewing angles, the above-water remote sensing reflectance for different solar-sensor geometry, $R_{rs}(\Omega)$, can be related to subsurface remote sensing reflectance, $r_{rs}(\Omega')$, as in Eq. 3.19, where,

$$R_{rs}(\Omega) = \frac{\zeta(\Omega')r_{rs}(\Omega')}{1 - \Gamma(\Omega')r_{rs},(\Omega')}, \tag{3.32}$$

where, $\zeta(\Omega')$ and $\Gamma(\Omega')$ are geometry-dependent model coefficients to be determined.

In an analogous approach to that used in Sections 3.2.1 and 3.2.2, a LUT of air-water interface model coefficients were determined from simulated Hydrolight data. $R_{rs}(\Omega)$ and $r_{rs}(\Omega')$ were taken from Database 2 so that a wide range of environmental conditions, including different bottom types and a range of water column depths, were incorporated in retrieving the model coefficients in Eq. 3.32. Again, Levenberg-Marquardt non-linear optimisation was used, whereby Hydrolight-$r_{rs}(\Omega')$ was substituted into Eq. 3.32 and fitted to Hydrolight-$R_{rs}(\Omega)$ over the Hydrolight output grid.

Computed model coefficients, ζ and Γ, for a selection of solar-sensor geometries are shown in Figs. 3.15 to 3.17 and tabulated in Appendix 7.8. Derived ζ values show minimal variation with changing solar-sensor geometry with a range from 0.48 to 0.53. On the other hand, Γ values show a more pronounced variation with solar-sensor geometry, with derived values ranging from 1.3 to 1.5.

Finally, combining the previously determined LUT coefficients for deep-water r_{rs} and diffuse attenuation, with the LUT of air-water interface coefficients, and together with Eqs. 3.31 and 3.32, achieves the forward model of above-water remote sensing reflectance for any desired solar-sensor geometry. Using the same water column IOP inputs as for Hydrolight database 2, the comparison between forward modelled-$R_{rs}(\lambda)$ and Hydrolight-$R_{rs}(\lambda)$ is shown in Fig. 3.18. The panel

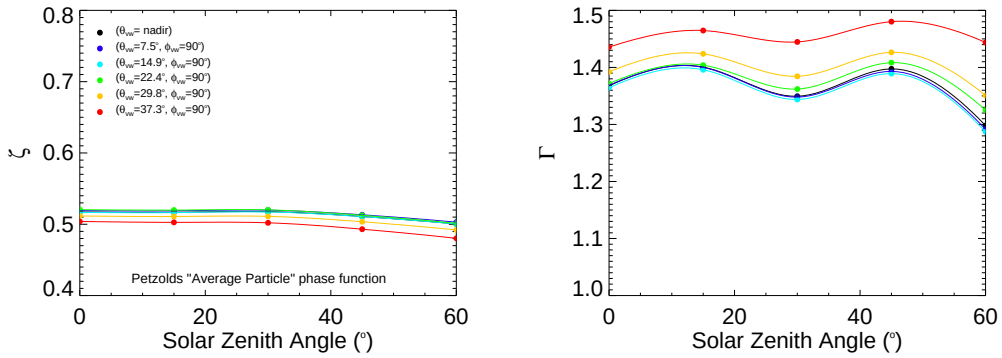

Figure 3.15: Derived coefficients, ζ and Γ versus solar zenith angle for selected sensor viewing angles.

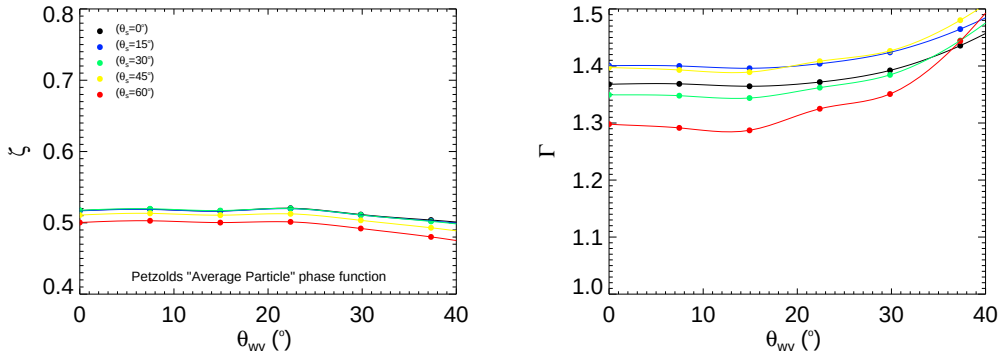

Figure 3.16: Derived coefficients, ζ and Γ versus sensor viewing angle (in the plane 90° from the solar azimuth) for selected solar zenith angles.

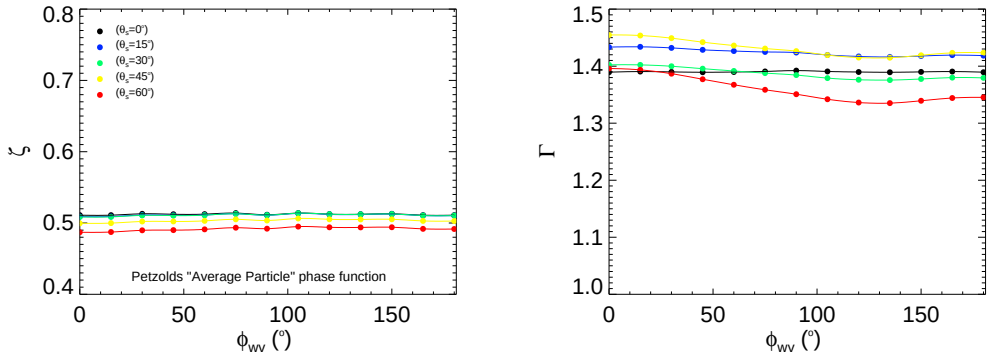

Figure 3.17: Derived coefficients, ζ and Γ versus sensor viewing azimuth (sensor view angle 30° from nadir) for selected solar zenith angles.

of comparison scatter plots shows excellent correspondence between modelled and Hydrolight $R_{rs}(\lambda)$ for the selected solar-sensor geometries presented. The

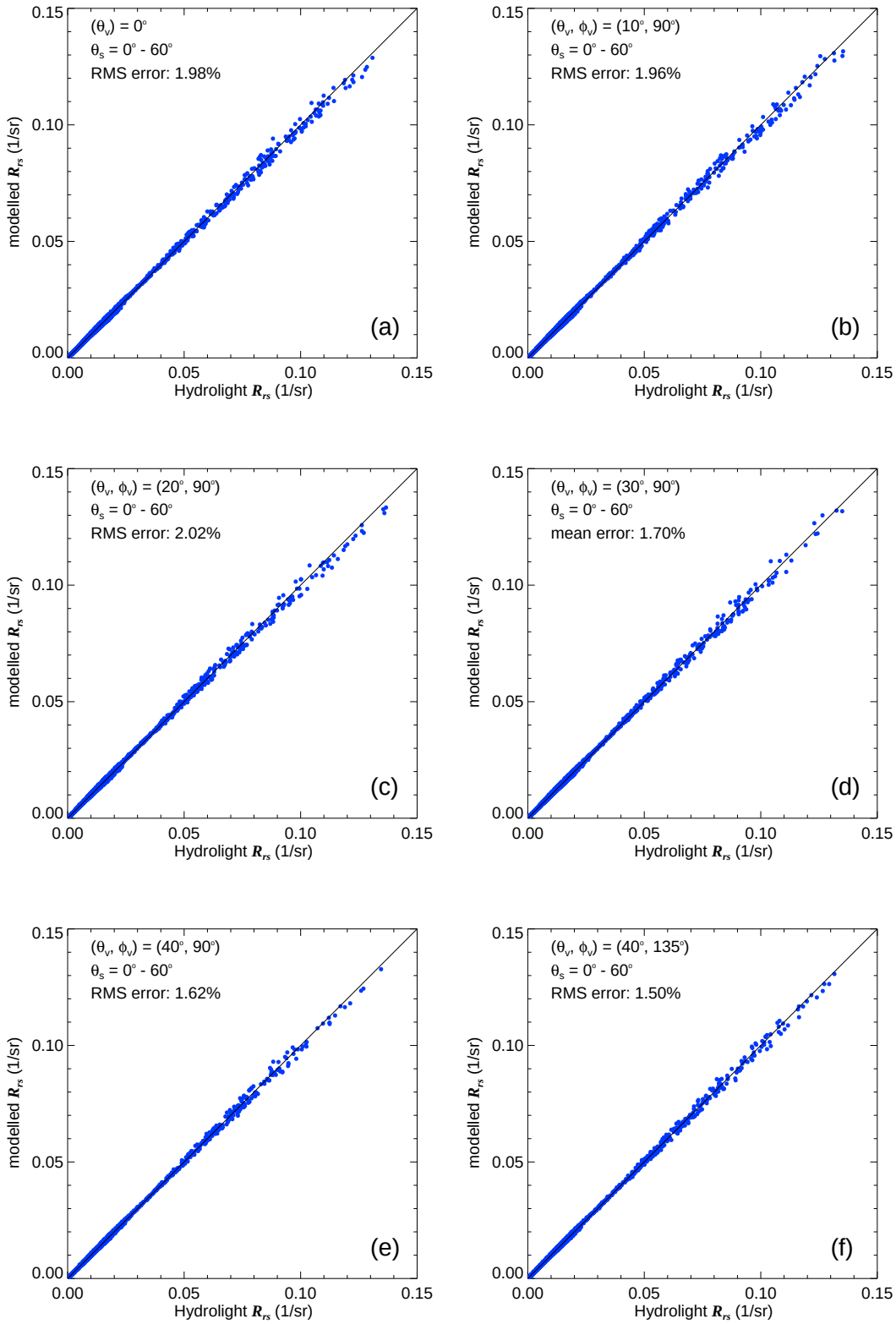

Figure 3.18: Modelled R_{rs} from LUT coefficients versus Hydrolight R_{rs} for selected solar-sensor viewing geometries.

calculated RMS errors between modelled and Hydrolight $R_{rs}(\lambda)$ (displayed in the top left corner within each panel) indicate stable model performance over the different solar-sensor geometries, with RMS errors between 1.5% to 2%. This improved accuracy and added stability in modelling $R_{rs}(\lambda)$ over a broad range of solar-sensor geometries, highlights one of the benefits of incorporating angle-dependent model coefficients as opposed to the fixed coefficients such as those presented in Eq. 3.16.

3.3 Parameterisation

The algorithm development presented above yields a forward model that requires at least 3 spectral inputs [$a(\lambda)$, $b_b(\lambda)$ and $\rho(\lambda)$] and 1 scalar input [H] to generate a R_{rs} spectrum. All other remaining coefficients required by the model may be extracted from the LUTs. However, since the long standing goal of remote sensing is to remotely derive water constituents, benthic cover and depth, the situation is reversed, whereby, $a(\lambda)$, $b_b(\lambda)$, $\rho(\lambda)$ and H, become the unknown quantities with $R_{rs}(\lambda)$ taken as the measurement. This is the "inverse problem". To invert an R_{rs} spectrum with n spectral channels, the number of unknowns to be deduced would be $3n+1$. By reducing the number of unknowns through parameterisation of $a(\lambda)$, $b_b(\lambda)$ and $\rho(\lambda)$, a solution is made possible.

For most coastal water environments, $a(\lambda)$ may be adequately expressed as the sum of the contributions from absorption of pure water, $a_w(\lambda)$, phytoplankton, $a_\phi(\lambda)$, CDOM, $a_{CDOM}(\lambda)$, and detritus, $a_{det}(\lambda)$,

$$a(\lambda) = a_w(\lambda) + a_{phi}(\lambda) + a_{CDOM}(\lambda) + a_{det}(\lambda). \tag{3.33}$$

$a_w(\lambda)$ coefficients can be taken from tabulated data in Pope and Fry (1997) (see Appendix 7.2). The magnitude and shape of the absorption of phytoplankton

pigments can be simulated with the single parameter model as in Eq. 2.41,

$$a_{phi}(\lambda) = a_{phi}(440)a^*_{phi}(\lambda), \tag{3.34}$$

where, $a_{phi}(440)$ is the phytoplankton absorption coefficient at 440 nm and $a^*_{phi}(\lambda)$ is an average representation of phytoplankton absorption normalised to 1 at 440 nm. $a^*_{phi}(\lambda)$ can be taken from field measurements or from published results. Unless otherwise specified, tabulated data of $a^*_{phi}(\lambda)$ from Morel (1988) are used in subsequent inversions (see Appendix 7.4).

The absorption coefficients of CDOM can be expressed as in Eq. 2.44,

$$a_{CDOM}(\lambda) = a_{CDOM}(440)e^{-S(\lambda-440)}, \tag{3.35}$$

where, $a_{CDOM}(440)$ is the absorption coefficient of CDOM at 440 nm and S is the spectral slope of the exponential curve. Since, the absorption by detritus is ignored in the Hydrolight simulations, $a_{det}(\lambda)$ is not included in the parameterisation at this point.

The total backscattering coefficients can be expressed as the sum of pure water backscattering, $b_{bw}(\lambda)$, and particle scattering, $b_{bp}(\lambda)$,

$$b_b(\lambda) = b_{bw}(\lambda) + b_{bp}(\lambda), \tag{3.36}$$

with values of $b_{bw}(\lambda)$ taken from Morel (1974) (see Appendix 7.3) and particle backscattering modelled as in Eq. 2.54 (Lee et al., 1998),

$$b_{bp}(\lambda) = b_{bp}(550)\left(\frac{550}{\lambda}\right)^Y, \tag{3.37}$$

where, $b_{bp}(550)$ is the particle backscattering at 550 nm and Y is the spectral slope parameter.

The spectral reflectance of the seafloor is a necessary boundary condition in the shallow water reflectance equation. For applications of the shallow water

reflectance model, where the bottom type is known, the bottom reflectance term, $\rho(\lambda)$, in Eq. 3.31 may be expressed as (Lee et al., 1999),

$$\rho(\lambda) = B_m \rho^*_{type}(\lambda), \tag{3.38}$$

where, $\rho^*_{type}(\lambda)$ is a measured bottom irradiance reflectance spectrum normalised to 1 at 550 nm. B_m represents the modelled albedo at 550 nm, which effectively scales the magnitude of bottom reflectance term.

For situations where the bottom environment is variable i.e. regions with patches of sand, seagrass and/or brown algae that are mixed at the pixel scale, the use of a single bottom reflectance spectrum may be inappropriate and in turn may lead to retrieval errors in depth, bottom albedo and water column parameters. In an attempt to improve the above single-substrate parameterisation for applications over variable bottom types, additional bottom reflectance spectra are linearly combined to simulate the appropriate bottom reflectance term. For a combination of 3 bottom substrates the parameterisation may be expressed as (Klonowski et al., 2007) (Fearns et al., 2011) (Garcia et al., 2014b),

$$\rho(\lambda) = B_{sd}\rho^*_{sd}(\lambda) + B_{gs}\rho^*_{gs}(\lambda) + B_{ba}\rho^*_{ba}(\lambda), \tag{3.39}$$

where, $\rho^*_{sd}(\lambda)$, $\rho^*_{gs}(\lambda)$, and $\rho^*_{ba}(\lambda)$ represent the 550 nm-normalised spectral irradiance reflectance of sediment, green seagrass and brown algae, respectively (see Appendix 7.5). B_{sd}, B_{gs} and B_{ba} are the effective area equivalent weighting coefficients for each corresponding bottom reflectance. Each weighting coefficient effectively combines values of bottom albedo at 550 nm as well as the fractional component of each bottom reflectance that may be collected within a sensor's Instantaneous Field-of-View (IFOV).

With the above considerations, the shallow water remote sensing reflectance model is described by up to 9 adjustable parameters [$a_{phi}(440)$, $a_{CDOM}(440)$, S, $b_{bp}(550)$, Y, B_{sd}, B_{sg}, B_{ba} and H] that uniquely influence the shape of the

modelled R_{rs} spectrum. This permits the solution of the 9 unknown model parameters to be obtained from measured R_{rs} spectra by incorporating non-linear curve fitting methods, termed *nonlinear optimisation*, or alternatively, *nonlinear least squares minimisation*.

3.4 Levenberg-Mardquardt Inversion

The Levenberg-Marquardt method is a widely used technique for solving non-linear least squares problems. The method is effectively a predictor-corrector scheme, whereby, iterative adjustments to model parameter values are made in order to reduce the sum of the squares of errors (χ^2) between the function and the measured data. χ^2 is calculated as,

$$\chi^2 = \sum_{i=1}^{n_\lambda} \left[\frac{y_i - \hat{y}_i}{w_i} \right]^2, \tag{3.40}$$

where, y_i are the measured data, $\hat{y}_i$ are the curve-fit function data and w_i is a measure of the error in measurement y_i.

The appropriate step size and direction of the parameter adjustments in response to the χ^2 error are determined by the Levenberg-Marquardt algorithm (Levenberg, 1944); (Marquardt, 1963). The Levenberg-Marquardt algorithm combines two general minimisation curve-fitting methods; the steepest descent method and Gauss-Newton method. At large distances from the function minimum, the algorithm adaptively varies the parameter updates using the steepest descent method in response to the gradient of the objective function. As the solution approaches the optimal value, the algorithm acts as the Gauss-Newton method, whereby, the sum of the squared error is reduced by assuming the local function is quadratic, and calculating the minimum of the quadratic.

Due to its robustness and ease of use, the Levenberg-Marquardt curve-fitting method was chosen in this research. The approach has been implemented in the Interactive Data Language (Exelis, 2015) routine MPFIT.pro (Markwardt,

2012). The MPFIT routine provides capability of holding specific parameter values fixed during the inversion, as well as imposing boundary constraints to parameter values. The inversion process terminates when in successive iterations a) the relative change in χ^2 error falls below a specified threshold (default value is $1e^{-10}$), b) the χ^2 error falls below a threshold and c) the number of iterations reaches the specified value (1000 iterations).

3.4.1 Levenberg-Mardquardt Implementation

A number of studies into multispectral and hyperspectral inversion over shallow coastal waters have implemented various forms of the Lee et al. (1999) semi-analytic model using the Levenberg-Marquardt optimisation approach (Lee et al., 1999) (Klonowski et al., 2007) (Goodman et al., 2008) (Fearns et al., 2011) (Garcia et al., 2014a) (Garcia et al., 2014b) (Giardino et al., 2014) (Eugenio et al., 2015).

The inversions are performed on a pixel-by-pixel basis, whereby, the scalar model parameters (e.g. P, G, X, B, H as in Lee et al. (1999)), are adjusted by the Levenberg-Marquardt routine until the difference, χ^2, between measured and modelled reflectance spectra converge to a minimum, as in Eq. 3.40, with the calculations typically performed over the available wavelengths between 400 nm and 800 nm. Once convergence occurs for each pixel, the values of model parameters are returned as the best fit model solution.

The Levenberg-Marquardt algorithm requires an initial best guess of the model parameters to initiate the minimisation process. The selection of the initial guess values are an important consideration with Levenberg-Marquardt algorithm. Different initial guess values can lead to convergence at different local minima (Garcia et al., 2014a) (Garcia et al., 2014b). Previous implementations of the Lee et al. (1999) semi-analytic model have used both scene-wide fixed initial guesses (Lee et al., 2001) (Klonowski et al., 2007) (Fearns et al., 2011) and pixel-wise variable initial guesses based on empirical relationships with R_{rs} (Eugenio et al., 2015) (Dekker et al., 2011) (Lee et al., 1999). Recently, Garcia et al.

(2014a) and Garcia et al. (2014b) implemented a two-stage procedure to assist the Levenberg-Marquardt in locating the best local minimum on a per pixel basis. Garcia et al. (2014a) use the update-repeat method, whereby, the initial guess parameters are randomly perturbed by 10% of their value until their threshold criteria is met. Garcia et al. (2014b) use the Latin Hypercube Sampling routine that dynamically searches the solution space for a set of optimal initial guess parameters.

Chapter 4

Inversion Performance

A semi-analytic model for shallow water remote sensing reflectance, which incorporates newly derived model coefficients for different solar-sensor geometry, was described in Chapter 3. In addition to the angle-dependant LUT of model coefficients, the remote sensing reflectance is modelled by a set of parameters which account for the absorption and backscattering of various water column constituents, bottom reflectances and water depth. Using an inversion technique, such as Levenberg-Marquardt optimisation, the set of model parameters can be retrieved from a remote sensing reflectance spectrum. The model parameters which are retrieved by inversion are phytoplankton absorption at 440 nm ($a_{phi}(440)$), CDOM absorption at 440 nm ($a_{CDOM}(440)$), CDOM absorption spectral slope (S), particle backscattering at 550 nm ($b_{bp}(550)$), particle backscattering spectral slope (Y), water depth (H), the bottom reflectance at 550 nm of the different bottom types used ($B_i(550)$), and a spectrally constant offset (Δ).

Since the model is an approximation of the radiative transfer equation, differences in modelled and "true" remote sensing reflectance results in an inherent error in model parameter retrieval. Selection of the appropriate parameterisation approach in modelling the spectral shapes of absorption, backscattering and bottom reflectance, as well as the sensitivity of different model parameters with respect to changes in remote sensing reflectance also has an impact on the accuracy of the inversion.

This chapter investigates inversion performance under the influence of model error itself, different parameterisation approaches in modelling phytoplankton absorption or bottom reflectance, initial conditions used during the inversion process and different sensor characteristics, such as sensor noise and spectral resolution. The analysis was performed using Hydrolight as outlined in Chapter 3, whereby, the model inversion was applied to R_{rs} simulations and the retrieved model parameters were compared to the Hydrolight input parameters, over a number of different scenarios.

4.1 Model error

An assessment of the performance of the inversion process for the situation where the spectral shape of bottom reflectance is assumed known *a priori* is presented here. The model inversions were applied to the above-water $R_{rs}(\lambda, \theta, \phi)$ Hydrolight Database 2 (Section 3.1.2). This database covers a wide range of water column IOPs and water depths with 3 different bottom types specified in the simulations. The single bottom type was assumed homogenous within the sensor FOV, either "Ooid sand", "average seagrass" or "average brown algae". During the inversion process, total water column absorption and backscattering were modelled using the parameterisations outlined in Eqs. 3.33 to 3.37. The spectral slope parameters for CDOM (S in Eq. 3.35) and backscattering (Y in Eq. 3.37) were held fixed at 0.014 and 1.0, respectively. The bottom reflectance was parameterised with a single bottom type as,

$$\rho(\lambda) = B_i \rho_i^*(\lambda), \tag{4.1}$$

where, the bottom reflectance used in each simulation was normalised to 1 at 550 nm, represented by $\rho_i^*(\lambda)$ with B_i representing the bottom albedo. The subscript i denotes either sand, seagrass or brown algae.

To avoid initial guess issues in the Levenberg-Marquardt optimisation scheme,

the initial values used to invert each simulated $R_{rs}(\lambda, \theta, \phi)$ spectrum were taken from the same values as the Hydrolight inputs. An assessment of initial guess problems are given in Section 4.2.

Figure 4.1 shows the comparison between retrieved model parameters and the reference Hydrolight inputs. Inversion results from simulations using bottom types "Ooid sand", "average seagrass" and "brown algae" are represented by blue, green and red data points, respectively. The formulation includes solar zenith angles ranging from 0° to 60°, and above-water sensor viewing angles from 0° to 40° (90° from the solar plane). For the parameters relating to water column absorption, the retrievals (see Figs. 4.1(a) and 4.1(b), respectively) agree with the Hydrolight inputs very closely, with a calculated RMS error of 3.7% for $a_{phi}(440)$ and 3.4% for $a_{CDOM}(440)$. For particle backscattering, see Fig. 4.1(c), the majority of retrieved $b_{bp}(550)$ agrees very closely with Hydrolight $b_{bp}(550)$. However, a number of outliers are present and give rise to an elevated RMS error of 10.1%. Retrieved depths, see Fig. 4.1(d), agree with Hydrolight input depths very closely up to ~ 7 m. For depths deeper than ~ 7 m, the retrievals are poor and are typically underestimated with differences up to 18 m at deeper depths. The overall RMS error in depth retrieval is 33%. The retrieved bottom albedo at 550 nm, see Fig. 4.1(e), shows a low correlation with Hydrolight input albedos. A large spread in albedo between 0 and 1 is apparent for all 3 bottom types and gives and RMS error of 88.2%. The comparison between the best-fit R_{rs} and the input Hydrolight R_{rs}, see Fig. 4.1(f), show very close agreement with an RMS error of 0.9%. No apparent outliers are evident, indicating that the inversion scheme was sufficiently robust and able to converge over all Hydrolight R_{rs} input spectra. This suggests that the poor performance in depth and albedo retrieval is not due to the model not fitting correctly to the Hydrolight R_{rs} data, but rather due to a decrease in model sensitivity for an increase in water depth and/or attenuation.

For a reliable retrieval in both depth and bottom albedo, there should be

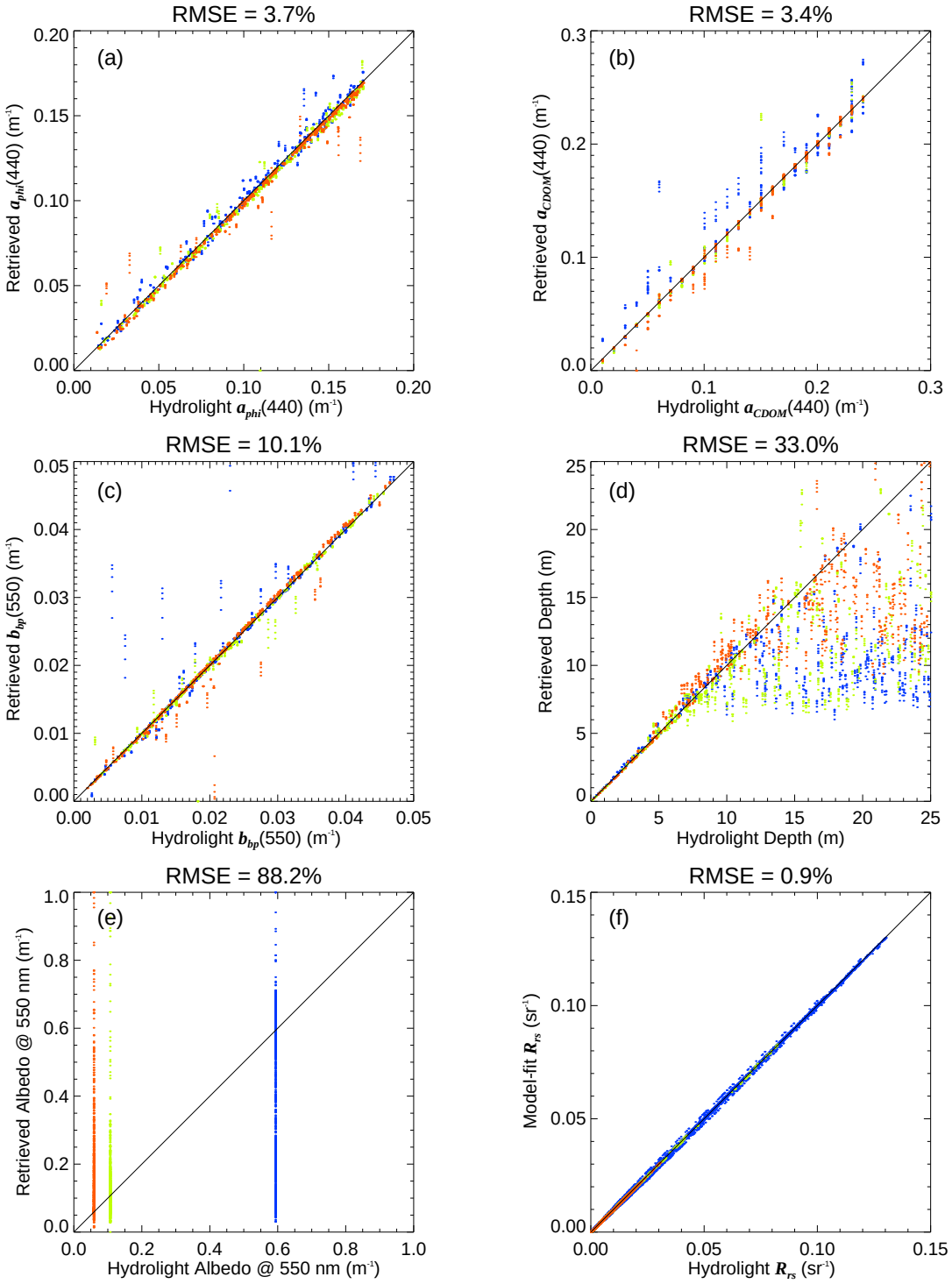

Figure 4.1: a) to e) Inversion retrieved model parameters versus Hydrolight inputs for bottom types, sand (blue dots), average seagrass (green dots) and brown algae (red dots). Results shown are for solar zenith angles from 0 to 60° and sensor viewing angles from nadir to 40°, at 90° from the sun's azimuth. Bottom reflectance was modelled with one bottom type and its spectral shape was assumed known. Initial guess values for inversion were taken as the Hydrolight input. f) model-fit R_{rs} versus Hydrolight R_{rs}.

an adequate amount of signal from the bottom that reaches the remote sensor. With increasing water depth and water column attenuation, or decreasing bottom albedo, the bottom component signal at the remote sensor decreases, which will have an impact on inversion performance for retrieving depth and bottom albedo. Conversely, at shallower depths and/or increasing bottom brightness, the total remote sensing reflectance signal is dominated by the bottom component, thereby, reducing the relative strength of the signal from the water column itself. This may also have impact on the inversion performance for the retrieval of water column properties.

This suggests that a level of guidance of the LM optimisation is required to discern between optically shallow and optically deep reflectance spectra in order to mask out unreliable retrievals. Brando et al. (2009) and Giardino et al. (2014) introduced the noise-equivalent remote sensing reflectance difference, $NE\Delta_{rsE}$, to establish whether the inversions are performed in optically deep and/or in optically shallow water. This takes into account the sensor spectral resolution, noise, the depth and composition of the water column and the spectral characteristics of the bottom reflectance in the measure of bottom signal detectability. Threshold values of $NE\Delta_{rsE}$, based on modelled data are then incorporated to remove unreliable data within the image scene. Similarly, Botha et al. (2013) introduced a normalised spectral similarity measure, $nSSM$, as a means of discriminating between optically shallow and optically deep reflectance spectra. Based on modelled data, optically deep and optically shallow waters with $nSSM < 0.15$ were considered indistinguishable from each other. Garcia et al. (2014a) used propagation of noise on modelled r_{rs} spectra at 550 nm and the computed pseudo signal-to-noise ratio SNR to examine the relative uncertainty of depth retrieval. They observed that for SNR's above 20, the relative uncertainty of the retrieved depth is less than 10% whereas for SNR's below 20 the relative uncertainty in the retrieved depth drastically increases up to greater than 100%. Garcia et al. (2014b) computed the uncertainties of the derived model parameters from the

optimisation process. The uncertainties of the derived model parameters were estimated by the noise propagation technique developed by Hedley et al. (2010) that takes into consideration both sensor and environmental noise. For each r_{rs} spectrum, spectral noise was added to generate a set of m noise-perturbed spectra that were inverted to obtain a set of m optimised model parameters. The standard error and average from this set were taken as the uncertainty and retrieved value, respectively. Using this novel approach the ability mask out unreliable retrievals can be determined by setting appropriate thresholds of the computed uncertainty.

A simple approach in discriminating between optically deep and optically shallow reflectances can be evaluated from the ratio of the modelled bottom contribution to the total signal as in Lee et al. (1999). The maximum ratio of bottom contribution to the total signal can be calculated with inversion-derived data as,

$$w_{max} = \texttt{max}\left[\frac{r_{rs}^{B}(\lambda)}{r_{rs}(\lambda)}\right]. \tag{4.2}$$

The difference between model-retrieved parameters and Hydrolight inputs versus w_{max} is presented in Fig. 4.2. For $a_{phi}(440)$, see Fig. 4.2(a), the differences are generally low up to w_{max} values approaching 0.9. Beyond 0.9, the differences become relatively large. Similarly, for $a_{CDOM}(440)$ and $b_{bp}(550)$ (see Figs. 4.2(b) and 4.2(c), respectively), the differences are low up to w_{max} of 0.8 and become large beyond 0.8. Very large differences, for both depth and bottom albedo are apparent at low w_{max}, and the differences fall sharply at $w_{max} \sim 0.1$, as shown in Figs. 4.2(d) and 4.2(e), respectively. The residual model error χ^2 (Eq. 3.40) steadily rises at increasing w_{max}, as shown in Fig. 4.2(f). This is due to the increase in the overall R_{rs} magnitude that coincides with an increase in w_{max}, whereby, any small relative errors in the model fit, sum up to a large value for increasing R_{rs}.

For low w_{max}, reliable depth and bottom albedo retrievals are not expected due to the relatively low signal contribution from the bottom. To exclude the

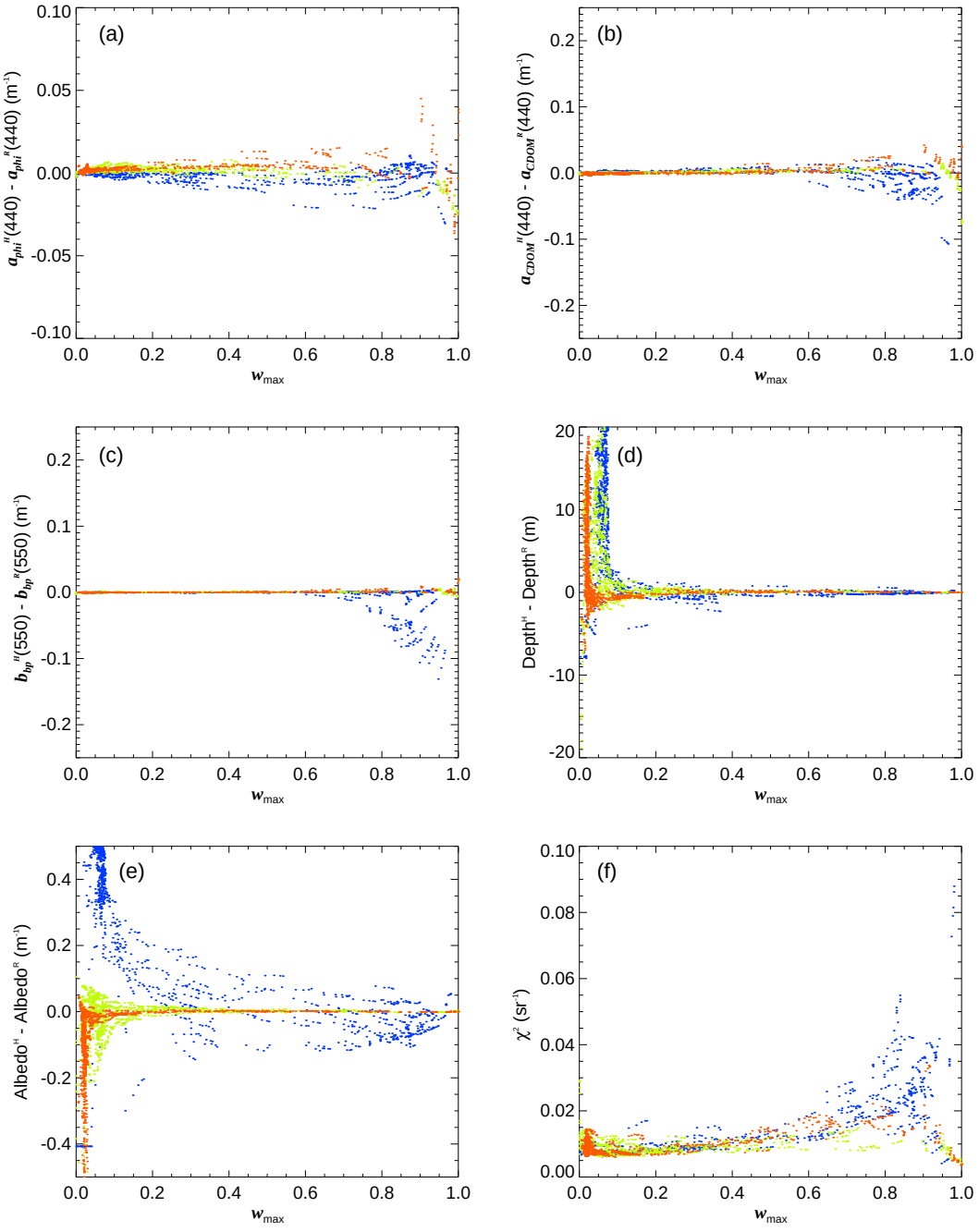

Figure 4.2: The difference between model retrieved parameters and Hydrolight inputs versus the ratio of the bottom signal to the total remote sensing reflectance, w_{max}, calculated using Eq. 4.2 and inversion-derived data. The superscripts H and R in the y-axis variables denote Hydrolight and model-retrieved variables, respectively.

majority of unreliable depth and bottom albedo retrievals, data with w_{max} values less than a threshold value of 0.15 are omitted. This is the same approach used in Lee et al. (1999). Conversely, for high w_{max}, reliable $a_{phi}(440)$, $a_{CDOM}(440)$ and $b_{bp}(550)$ retrievals are also not expected. This is due to the relatively low water column signal compared to the total signal. Most of this unreliable data can be filtered out by discarding retrieved water column parameters with corresponding w_{max} values greater than 0.85. Since w_{max} is calculated from the inversion-derived values alone, the above criteria can be an effective operational constraint.

Figure 4.3 shows the inversion results after filtering out data using the above criteria. As expected, the RMS errors for each of the model parameters are reduced, as compared with the RMS errors in Figs. 4.2(a) to 4.2(e). For the water column parameters, a total of 253 data points from a possible 3750 were discarded using $w_{max} > 0.85$. The RMS errors for $a_{phi}(440)$, $a_{CDOM}(440)$ and $b_{bp}(550)$ were reduced to 2.7%, 2.5% and 3.6%, respectively. For depth and bottom albedo, the criterion of $w_{max} < 0.15$ reduced n to 1154 data points giving a significant reduction in calculated error, with an RMS error of 3.3% for depth retrieval and an RMS error of 5.8% for bottom albedo retrieval. Further analysis of the filtered data revealed that the maximum depth retrieval of $\sim$ 19 m occurred over sand. The maximum retrieved depth over seagrass was $\sim$ 15.5 m and $\sim$ 14 m over brown algae. After filtering out unreliable data, the retrieved bottom albedo compares well to the Hydrolight inputs (see Fig. 4.3(e)), especially for seagrass and brown algae. Over sand, the bottom albedo retrievals show good agreement with the Hydrolight input value of 0.593 m^{-1}, with some spread between 0.4 and 0.8 m^{-1} apparent.

4.2 Initial Conditions

Generic curve-fitting algorithms for solving nonlinear least squares problems require initial guess values for the function parameters to start the minimisation process. For well-behaved functions, the Levenberg-Marquardt algorithm often

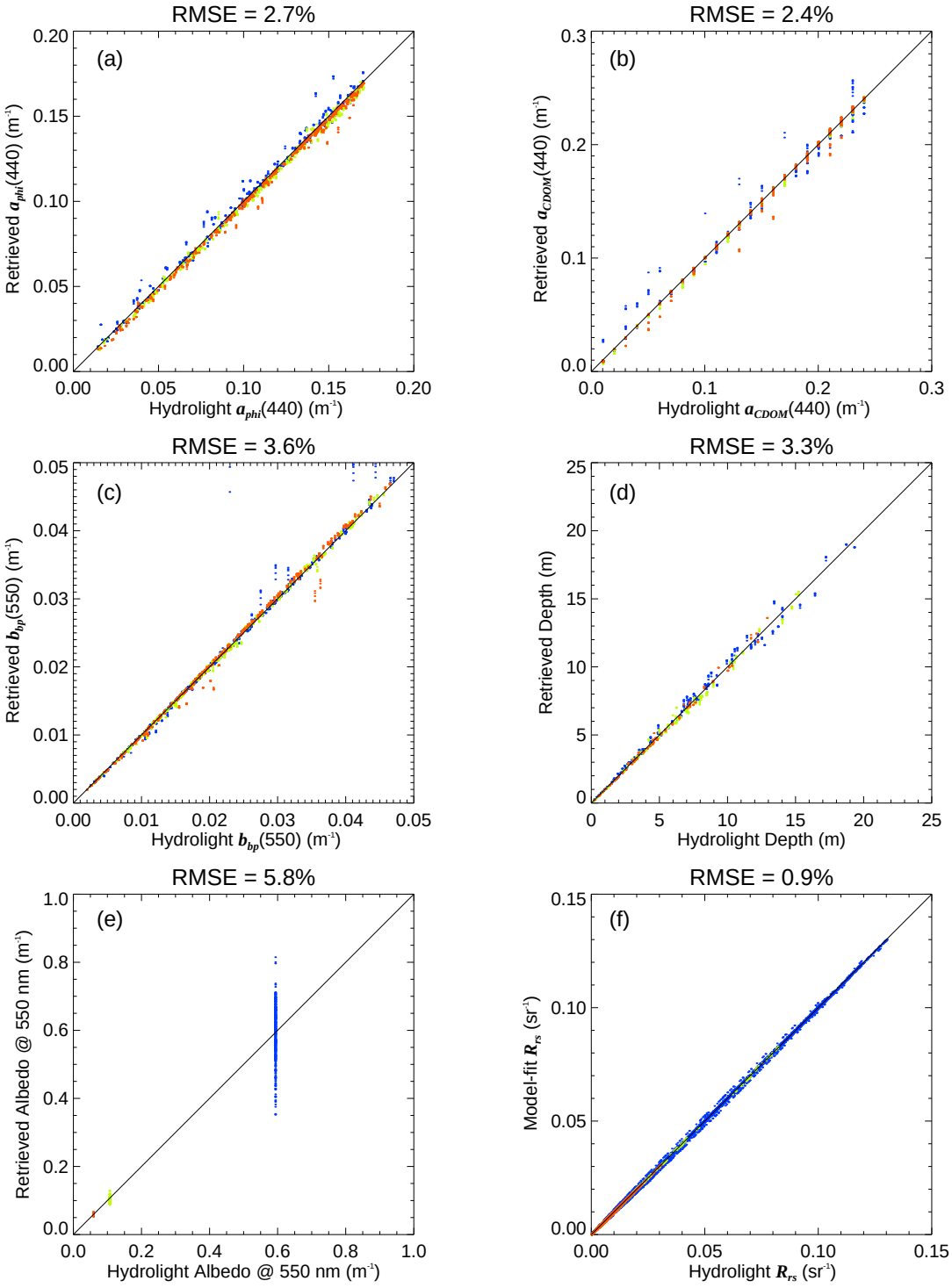

Figure 4.3: a) to e) Inversion retrieved model parameters versus Hydrolight inputs after filtering out unreliable retrievals. Data corresponding to $w_{max} > 0.85$ were omitted for $a_{phi}(440)$, $a_{CDOM}(440)$ and $b_{bp}(550)$ and data corresponding $w_{max} < 0.15$ were omitted for depth and bottom albedo retrievals. f) model-fit R_{rs} versus Hydrolight R_{rs} remains unchanged since all spectra are included.

finds a solution even if the initial guess values are far from the final minimum. For more complex nonlinear problems, such as the semi-analytical model, the solution space can contain multiple local minima. Depending upon initial guess values, measurement noise and parameterisation, the Levenberg-Marquardt algorithm can converge to different local minima. In some instances, if the initial guess values are sufficiently far from the correct solution, the curve fitting may not converge at all.

For some focused remote sensing studies, the best available estimates of the desired parameters as the initial guess generally will be appropriate. For more large-scale studies, the often large dynamic range in water column IOPs, and highly variable bottom topography, can become a problem in choosing the best available initial guess estimates to cover this range.

The inversion performance in response to initial conditions was tested by applying the shallow water model to Hydrolight computed reflectance data for different initial guesses of the model parameters. The water column constituents and bottom reflectance shape were parameterised as in Section 4.1. Three separate numerical tests were performed ("LOW", "MID" and "HIGH"), representative of relatively low, mid and high initial guess values. The initial guess values used in each numerical test are summarised in Table 4.1. Since the Hydrolight simulations cover a wide range of water column IOPs and water depths, using fixed initial guess values over the entire database will result in a large number of scenarios where the initial guess values are far removed from the optimum choices. In an attempt to provide reasonable initial guess values that cover the range of simulated Hydrolight data inputs, a method for dynamically adjusting the initial values in response to the input $R_{rs}(\lambda)$ spectrum is proposed. First, a coarse Look-Up-Table of forward-modelled $R_{rs}(\lambda)$ ("CLUT") is generated by coarsely gridding the parameter space of the shallow water remote sensing reflectance model. A simple binary search algorithm is then used to determine the set of parameter values with the lowest Euclidean distance between the CLUT-$R_{rs}(\lambda)$

and the input $R_{rs}(\lambda)$, and used as the initial guess values.

Table 4.1: Initial conditions used in inversion tests

	LOW	MID	HIGH
$a_{phi}(440)$	0.02	0.1	0.15
$a_{CDOM}(440)$	0.01	0.15	0.2
$b_{bp}(550)$	0.001	0.025	0.04
H	1.0	10.0	18.0
B_i	0.2	0.5	0.8

A fourth numerical test was conducted by inverting the shallow water model using initial guess values that were derived from "CLUT". The CLUT of forward-modelled $R_{rs}(\lambda)$ was generated using discretised parameter values outlined in Table 4.2, resulting in 10x10x20x50 = 100,000 $R_{rs}(\lambda)$ spectra. S, Y and Δ were fixed at 0.014, 1.0 and 0.0, respectively. The bottom reflectance shape and albedo were taken from Hydrolight inputs. The CLUT derived initial guess

Table 4.2: Coarsely gridded parameter space used to generate CLUT-$R_{rs}(\lambda)$.

	Range	n increments	step size
$a_{phi}(440)$	0.01-0.2	10	0.021
$a_{CDOM}(440)$	0.01-0.25	10	0.027
$b_{bp}(550)$	0.001-0.05	20	0.0026
H	0.1-20.0	50	0.41

values versus Hydrolight input values are presented in Fig. 4.4. For absorption and backscattering related parameters, Figs. 4.4(a), 4.4(b) and 4.4(c), the initial guess values match the Hydrolight input values reasonably well over the simulated range. On average, the CLUT-derived initial guess values were within 30% of the Hydrolight inputs. The initial guess estimates for depth, Fig. 4.4(d), show close agreement with Hydrolight depths up to $\sim$ 7 m but display a large spread for deeper depths. On average, initial depth estimates were within 38% of Hydrolight input depths.

The inversion results of the above 4 numerical tests, applied with different initial conditions, are summarised in Table 4.3. For reference, the inversion results

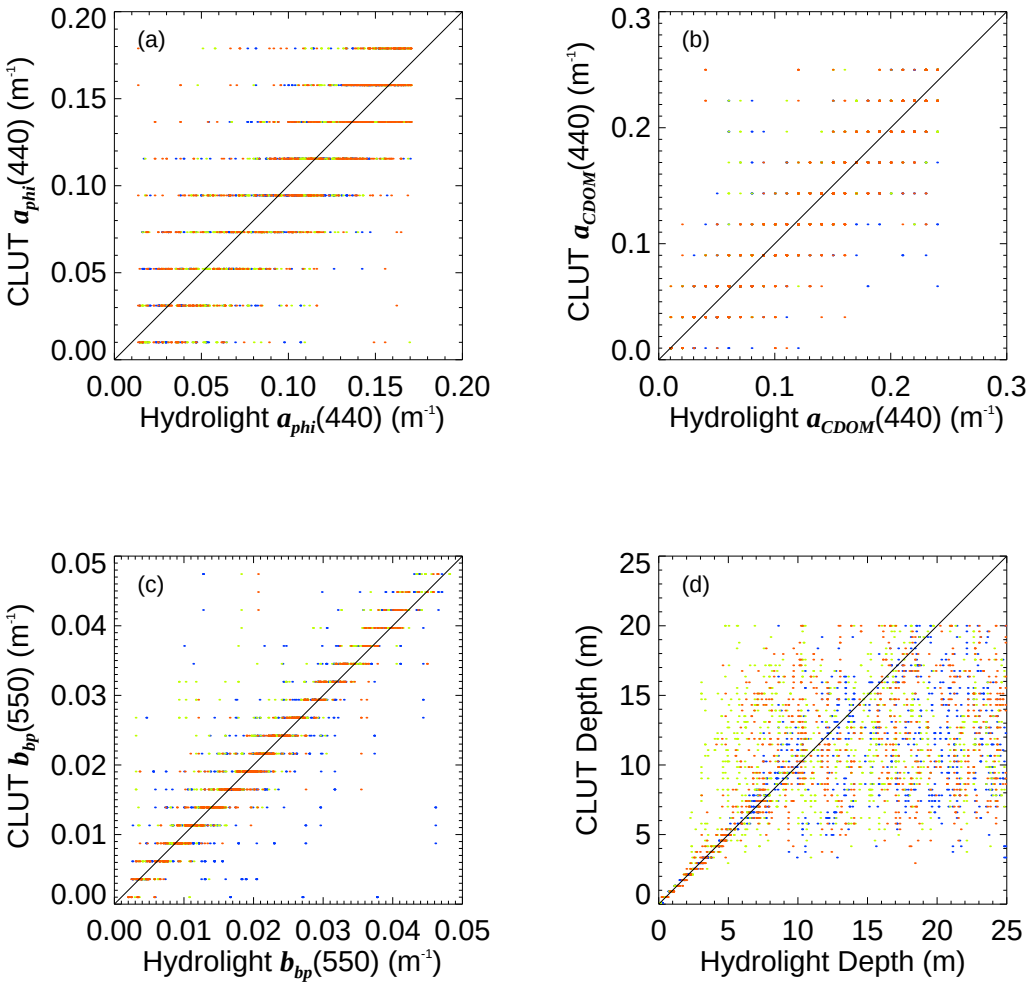

Figure 4.4: Initial conditions determined from the CLUT method versus Hydrolight inputs.

obtained using Hydrolight inputs as the initial conditions (Section 4.1) are also given in Table 4.3.

The inversion results are presented as the RMS error between model retrieved parameters and Hydrolight inputs. The data encompasses solar angles that range from 0° to 60°, and above-water sensor viewing angles from 0° to 40° (90° from the solar plane). As in Section 4.1, data with w_{max} above the threshold of 0.85 were omitted from the RMS error calculations for $a_{phi}(440)$, $a_{CDOM}(440)$ and $b_{bp}(440)$. Likewise, retrieved depth, H, and bottom albedo, B_i, with corresponding w_{max} values below the threshold of 0.15, were also excluded from the results.

Table 4.3: RMS errors for the inversion tests under different initial conditions.

	RMS error (%)				
	Hydrolight	LOW	MID	HIGH	CLUT
$a_{phi}(440)$	2.7	3.4	114.6	158.7	2.7
$a_{CDOM}(440)$	2.4	5.9	228.7	215.2	2.4
$b_{bp}(550)$	3.6	16.3	164.1	176.2	3.6
H	3.3	3.4	6.3	5.3	3.3
$\rho(550)$	5.8	5.7	7.0	7.7	5.8
R_{rs}	0.9	1.6	1.8	2.3	0.9

The results presented in Table 4.3 indicate that initial conditions do have a significant effect on the shallow water model retrievals. The situation where relatively low initial guess values were used appear to give reasonable retrievals with small RMS errors close to what was achieved with known Hydrolight inputs as the initial conditions. For the MID and HIGH inversion tests, the inversion performance in retrieving water column absorption and scattering parameters is very poor, with RMS errors between 100% and 200%. For the depth and bottom albedo parameters, the retrievals perform well but still give elevated RMS errors between 5% and 8% which are slightly higher than the Hydrolight case. Compared to the Hydrolight case, the RMS errors between modelled-$R_{rs}(\lambda)$ and Hydrolight-$R_{rs}(\lambda)$ for LOW, MID and HIGH test cases are approximately double (between 1.6% and 2.3%). This is due to a number of inversions that failed to converge during optimisation but still output the last computed set of model parameters

evaluated at the preset number of maximum iterations (presently set at 1,000).

Out of the 4 numerical tests, the inversion retrievals using initial guess estimates, derived from the CLUT-$R_{rs}(\lambda)$, performed the best, giving the same RMS errors as the Hydrolight case. Even though the initial guess values were, on average, out by 30% to 40% of the Hydrolight input values, the Levenberg-Marquardt optimisation was able to converge for all input $R_{rs}(\lambda)$. This suggests that deriving initial guess estimates purely from the input R_{rs} spectrum is adequate for shallow water model inversions. All subsequent numerical inversion tests in the following sections incorporate the CLUT method to estimate the initial guess values.

4.3 Bottom Reflectance Parameterisation (3 Bottom Types)

For the various inversion tests performed in the previous sections, the bottom reflectance term in the model was parameterised with a single normalised bottom reflectance shape (known *a priori*) multiplied by the bottom albedo at 550 nm in order to effectively scale for magnitude. For the situation where the bottom cover is not known, a linear combination of different bottom types or spectral endmembers may be used to model the bottom reflectance. For the inversion tests performed here, a linear combination of sand, seagrass and brown algae bottom reflectance endmembers were used. The 3 bottom component parameterisation is expressed as,

$$\rho(\lambda) = f_{sd} S_{sd} \rho_{sd}(\lambda) + f_{sg} S_{sg} \rho_{sg}(\lambda) + f_{ba} S_{ba} \rho_{ba}(\lambda), \tag{4.3}$$

with the criterion,

$$f_{sd} + f_{sg} + f_{ba} = 1. \tag{4.4}$$

The new model parameters f_{sd}, f_{sg} and f_{ba} represent the fractional components of each in the FOV, specifically sand (subscript sd), seagrass (subscript sg) and brown algae (subscript ba), respectively. ρ_{sd}, ρ_{sg} and ρ_{ba} are the measured irradiance reflectance spectra for each bottom type (non-normalised). Scaling parameters, S_{sd}, S_{sg} and S_{ba} are included to scale the magnitude of each endmember in order to account for possible uncertainty in irradiance reflectance measurements and any changes in reflectance magnitude caused by the structure of the benthic cover (i.e sloping topography, shadows or leaf orientation). For scenarios where the magnitudes of the irradiance reflectance endmembers differ from the actual, increased errors in the depth retrieval and/or fractional cover are likely without the inclusion of the scaling parameters. For example, consider the case where an R_{rs} measurements is made over a shallow, sandy bottom environment with a bottom albedo of 0.15 at 550 nm. Then, if the bottom albedo at 550 nm of the input irradiance reflectance for sand was taken as a lower value, say 0.13, the model would only be able to achieve a maximum bottom albedo of 0.13 at 550 nm, which would be lower than needed. To account for this difference, the model would compensate by setting a shallower water depth than actual in order to increase the apparent signal contribution from the bottom. With the inclusion of the scaling terms, the model would be able to achieve the correct bottom albedo for the sand component without the need of setting a shallower water depth. However, the inclusion of the scaling terms gives additional degrees of freedom to the model which may impact on the retrieval of the other model parameters. For subsequent inversion tests, the model parameters S_{sd}, S_{sg} and S_{ba} were included and constrained by a lower bound of 0.75 and an upper bound of 1.25, allowing each endmember spectrum to be scaled by $\pm 25\%$.

For inversions applied to Hydrolight data that are simulated with a sandy bottom type, the desired retrieval of the fractional components would be 1 for f_{sd} and 0 for both f_{sg} and f_{ba} since neither seagrass or brown algae would be present in the simulations. Similarly, for inversions over seagrass, the desired retrievals

would be 0 for f_{sd}, 1 for f_{sg} and 0 for f_{ba}. And lastly, for inversions over brown algae, the desired retrievals would be 0 for f_{sd} and f_{sg}, and 1 for f_{ba}.

4.3.1 Inversions over different but homogeneous bottom cover

The inversion performance of the shallow water model, which incorporates the linear combination of the 3 bottom components (Eq. 4.4), was tested against Hydrolight Database 2. The initial guess values were derived from the previously generated CLUT of $R_{rs}(\lambda)$. Since the bottom type was not assumed to be known in this case, the initial guess values were determined by comparing each Hydrolight $R_{rs}(\lambda)$ against a total of 300,000 CLUT-$R_{rs}(\lambda)$ that includes forward model (shallow water reflectance model) computations to cover albedo inputs for the 3 separate bottom types.

The comparison between inversion retrieved model parameters and the Hydrolight inputs is shown in Fig. 4.5. The results show that the retrieved model parameters match the Hydrolight inputs very well, with small RMS errors achieved for all model parameters, similar to the case where the bottom type was known (Section 4.1). The retrievals of $a_{phi}(440)$ and $a_{CDOM}(440)$ give RMS errors of 2.8% and 2.1%, respectively. The retrieval of $b_{bp}(550)$ generally shows a high level of accuracy when compared with Hydrolight giving an overall RMS error of a low 1.8%. However, a number of outliers are evident. The outliers mainly occur over sandy bottom simulations, with high bottom-to-total reflectance ratios (w_{max}) between 0.8 and 0.85. Improved removal of unreliable data may be achieved by adjusting the w_{max} threshold from the current value of 0.85 to 0.8. The comparison of retrieved depth is excellent, giving an RMS error of 3.2%. This is equivalent to an error of $\pm$0.18 m over the simulated range of 0.1 m - 25 m. The total bottom reflectance at 550 nm, $\rho(550)$ (Eq. 4.4), shows high accuracy as compared to Hydrolight data that are simulated with seagrass and brown algae bottom types. Over sand simulations, the total bottom albedo shows a variation

of ± 0.02 from the true value, resulting in an overall RMS error of 6.3%. Accurate model-fits are achieved with an RMS error of 0.9%.

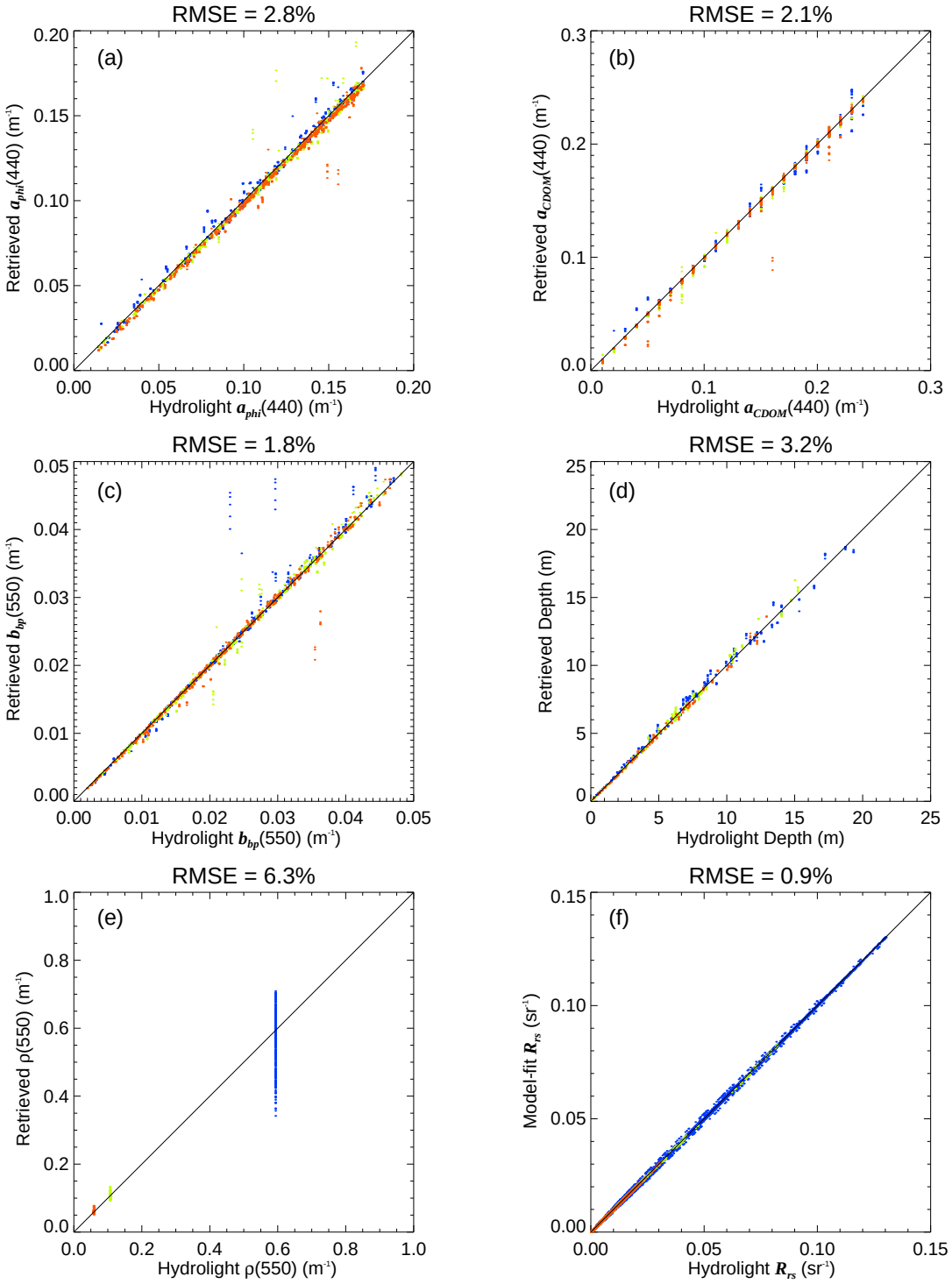

Figure 4.5: a) to d) Model retrieved parameters versus Hydrolight inputs for the shallow water model using a linear combination of 3 bottom types. As before, data corresponding to $w > 0.85$ were omitted for $a_{phi}(440)$, $a_{CDOM}(440)$ and $b_{bp}(550)$ and data corresponding $w < 0.15$ were omitted for depth and total bottom albedo retrievals. e) compares the total retrieved bottom albedo, $\rho(550)$ as returned from the 3 bottom component model against the Hydrolight total bottom albedo. f) model-fit R_{rs} versus Hydrolight R_{rs}.

The good inversion performance suggests that the incorporation of the additional parameters in the 3 bottom component model do not have a negative impact on the retrieval of the main model parameters. The additional bottom reflectance parameters also contain information on the proportion of bottom reflectance endmembers used in the model fit, giving insight into the type of benthic cover that may be present.

The effective albedo at 550 nm for each bottom component combines the model retrieved fractional component and scaling factor with the endmember reflectance at 550 nm, denoted as, B_{sd} , B_{sg} and B_{ba}, where,

$$B_{sd} = f_{sd} S_{sd} \rho_{sd}(550), \tag{4.5}$$

$$B_{sg} = f_{sg} S_{sg} \rho_{sg}(550), \tag{4.6}$$

and,

$$B_{ba} = f_{ba} S_{ba} \rho_{ba}(550), \tag{4.7}$$

The modelled bottom albedos at 550 nm, B_{sd}, B_{sg} and B_{ba} are displayed in Fig. 4.6. Each panel shows histograms of the 3 retrieved bottom albedos for each Hydrolight simulated bottom type. The dashed line in each panel represents the Hydrolight input albedo at 550 nm for the respective bottom types simulated. The dotted lines either side of the dashed lines are $\pm 25\%$ of the Hydrolight input albedo. For Hydrolight data that were simulated with the bottom type ooid sand, the majority of B_{sd} retrievals (top panel) show a distribution within $\pm 25\%$ of the input albedo. The model effectively retrieved a target value near 0.0 for both B_{sg} and B_{ba}. A small proportion of B_{sg} and B_{ba} values were retrieved between 0.0 and 0.1, however, compared to the bright albedo of sand the residual values are relatively small. This suggests that the bottom reflectance parameterisation using 3 bottom types appropriately models the sand reflectance shape for simulations over sandy bottom environments. For Hydrolight data simulated with a seagrass bottom reflectance (middle panel), the model-retrieved albedo for seagrass, B_{sg},

are slightly lower than the target Hydrolight input of 0.106, with the majority of retrieved values within ±25% of the seagrass input albedo. Again, the albedos for sand and brown algae, both of which were not used in the simulation, were largely retrieved with values of 0.0. However, the slight underestimation in B_{sg} is compensated with relatively small contributions of B_{sd} and B_{ba}. The bottom panel of Fig. 4.6 shows a narrow distribution of retrieved B_{ba} with a high frequency of values near the target albedo of 0.058. In general, for sediment substrates, high values of B_{sd} and low values of B_{sg} and B_{ba} albedos are retrieved. For seagrass substrates, high B_{sg} and low B_{sd} and B_{ba} albedos are retrieved and for brown algae substrates, high B_{ba} and low B_{sd} and B_{sg} albedos are retrieved. These results demonstrate the potential of the shallow water model to discriminate 3 key classes of substrate (sand, seagrass and brown algae) by appropriate retrievals of the 3 bottom components.

Figure 4.7 shows the total bottom reflectance spectrum, $\rho(\lambda)$, as derived from inversion results and Eq. 4.4. The modelled $\rho(\lambda)$ show close agreement with the spectral features of the Hydrolight input bottom reflectance spectra, with magnitudes mostly within the ±25% range. For modelled $\rho(\lambda)$ over a sand substrate (top panel), a proportion of results fall below the -25% range and appear to include spectral features at 600 nm and 650 nm that are consistent with a brown algae spectrum. These deviations from the sand substrate spectral form occur at low w_{max} values. As w_{max} approaches 0.15, the spectral window of the ratio between the bottom signal to the total signal, $w(\lambda)$, reduces to a range between $\approx$ 450 nm and $\approx$ 600 nm, with the maximum peak typically occurring at $\approx$ 570 nm (see Fig. 4.8). With this reduced spectral window, the inversions are largely insensitive to the discriminating spectral features of the brown algae spectrum beyond 600 nm. This allows a contribution of either brown algae or seagrass spectra in modelling the bottom reflectance over sand during inversion, without greatly impacting on the total modelled $R_{rs}(\lambda)$ at $\lambda >$600 nm. With this consideration, the filtering criterion using w_{max} that is less than some threshold, should ensure

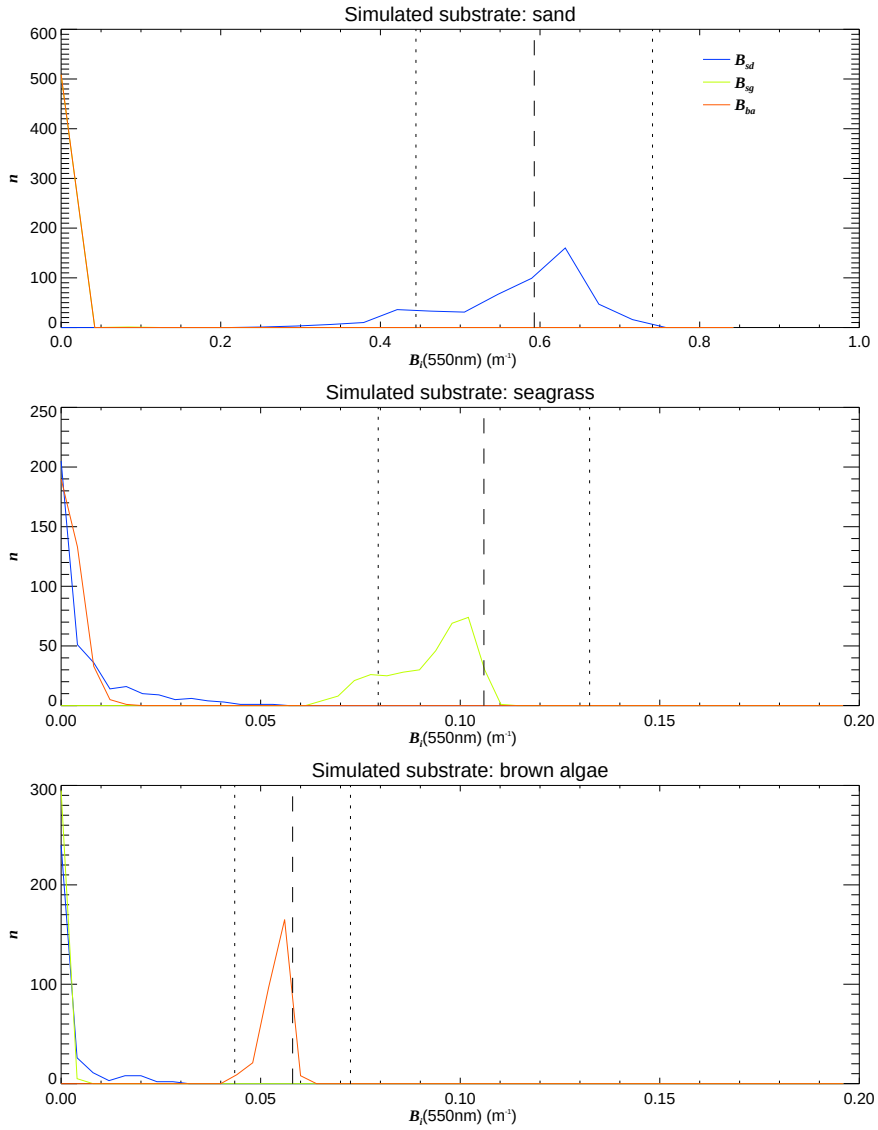

Figure 4.6: Distribution of bottom albedos at 550 nm, B_{sd} (blue lines), B_{sg} (green lines) and B_{ba} (red lines) from inversions applied to Hydrolight data simulated with a sand bottom reflectance (top), a seagrass bottom reflectance (middle) and brown algae bottom reflectance (bottom). The dashed line in each panel represents the Hydrolight input albedo at 550 nm for the respective bottom types simulated with dotted lines of either side denoting the $\pm 25\%$ value.

that data with an appropriate $w(\lambda)$ signal from at least 600 nm is only included in the results. Figure 4.9 shows the inversion derived bottom reflectance spectra after filtering out data using the criterion of $w(600) < 0.1$. The modelled $\rho(\lambda)$ spectra shows excellent correspondence to the target Hydrolight input bottom reflectance spectra. Although, this filtering criteria tends to decrease the number modelled ρ, the strict quality control results in greater confidence of appropriately

distinguishing dense bottom type cover from remote sensing.

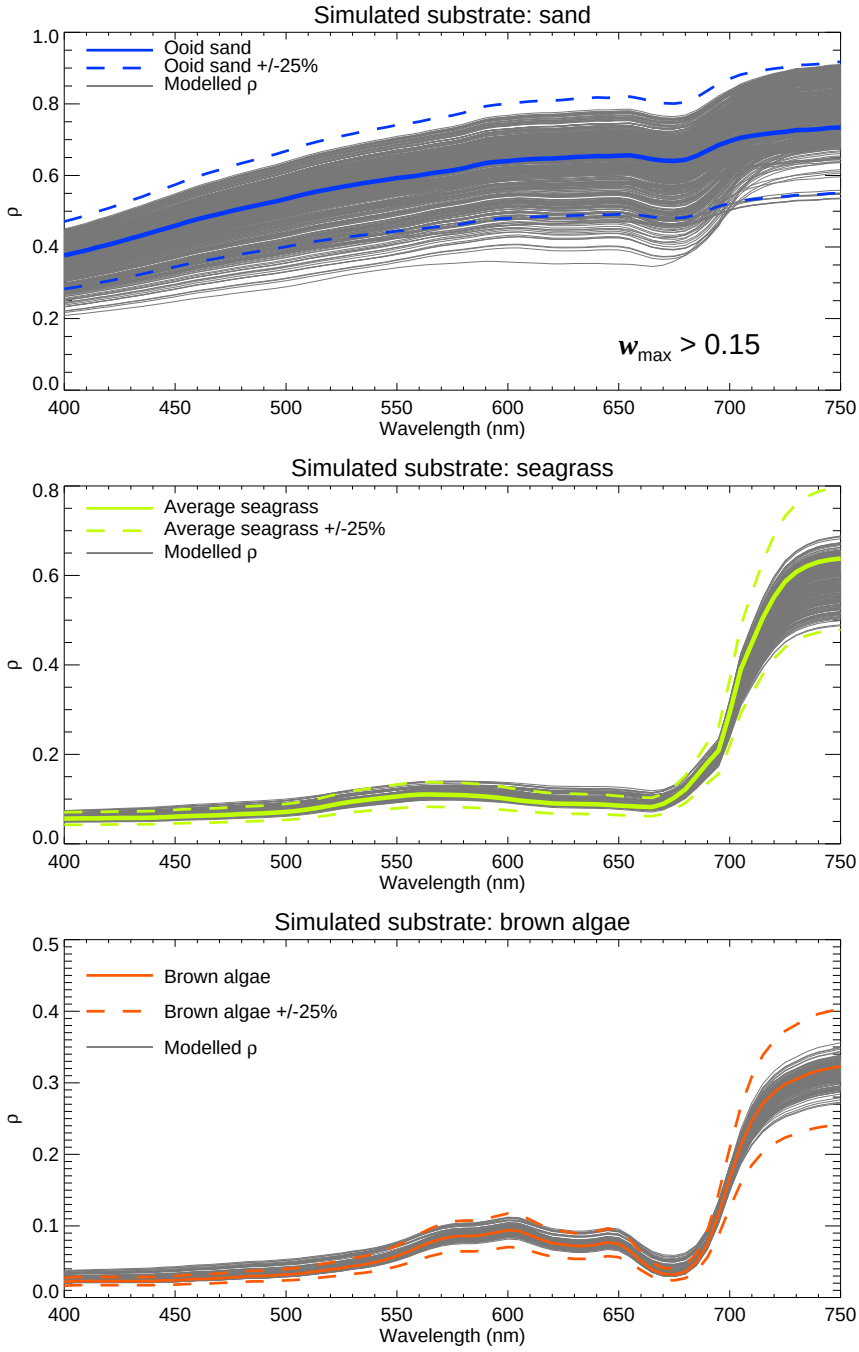

Figure 4.7: Derived total bottom reflectance spectra, $\rho(\lambda)$, from simulated R_{rs} over sand (top panel), seagrass (middle panel) and brown algae (bottom panel). The coloured solid lines represent the Hydrolight simulated spectrum in each panel and the coloured dashed lines represent the input bottom reflectance scaled by $\pm 25\%$. Data with w_{max} <0.15 has been omitted.

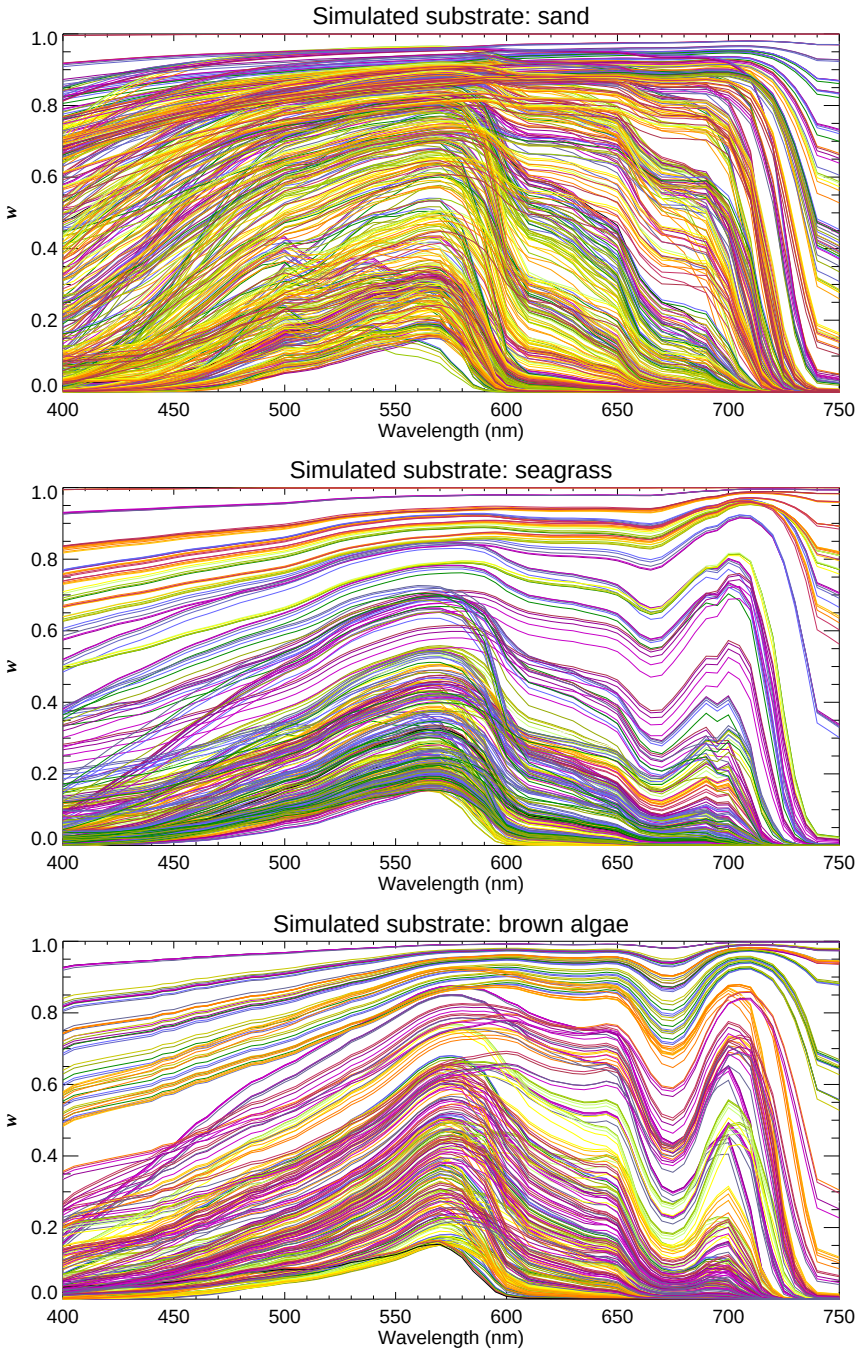

Figure 4.8: Spectra of the ratio of the bottom signal to the total signal, $w(\lambda)$, after filtering out data where w_{max} <0.15.

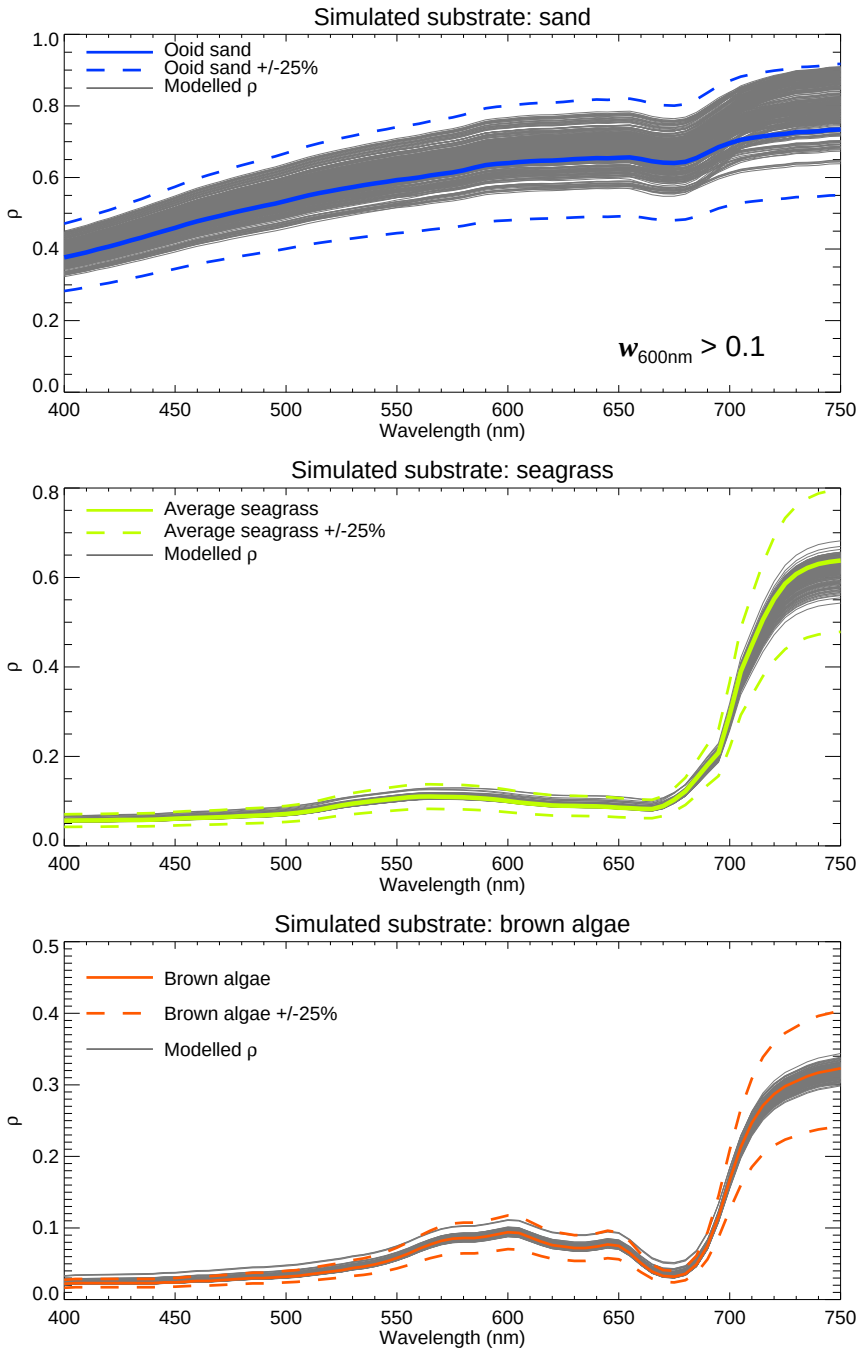

Figure 4.9: Derived total bottom reflectance spectra, $\rho(\lambda)$, from simulated R_{rs} over sand (top panel), seagrass (middle panel) and brown algae (bottom panel). The coloured solid lines represent the Hydrolight simulated spectrum in each panel and the coloured dashed lines represent the input bottom reflectance scaled by $\pm 25\%$. Data where $w(600)$ <0.1 has been omitted.

4.3.2 Inversions over bottom cover mixtures

The above inversion tests were performed over Hydrolight data that were generated with bottom types that were considered homogenous within the simulated sensor's FOV. However, with spatial resolutions typically between 1 m - 30 m for common hyperspectral imaging sensors, it is possible that the benthic cover imaged within a pixel may contain mixtures of different substrate types. To test the applicability of the 3 bottom component shallow water model, inversion tests were performed against Hydrolight Database 3. The $R_{rs}(\lambda)$ simulations in Database 3 also cover a wide range water column IOPs and water depths, as in Database 2, however, a range of bottom reflectances were modelled using random mixtures of ooid sand, average seagrass and brown algae to simulate the case where mixtures of different substrate types are present within a sensor's FOV. To account for initial guess estimates with different combinations of bottom mixtures, a new CLUT of $R_{rs}(\lambda)$ was generated using the same coarsely gridded parameters for water column IOPs and depths as in Table 4.2, except with additional coarsely gridded fractional bottom components, f_{sd}, f_{sg} and f_{ba}, to model a variety of bottom reflectance mixtures.

The inversion results over variable bottom type mixtures are shown in Fig. 4.10. Overall, the comparison between retrieved model parameters and Hydrolight inputs correlate well with each other, with RMS errors similar to the results obtained for homogenous bottom cover. For the water column parameters, $a_{phi}(440)$, $a_{CDOM}(440)$ and $b_{bp}(550)$, the calculated RMS errors are 2.7%, 1.9% and 1.8%, respectively. The depth comparison shows good correlation up to $\sim$20 m with an RMS error of 4.0%. The modelled total albedo at 550 nm ($B_{sd} + B_{sg} + B_{ba}$), corresponds well to the simulated benthic cover mixtures, especially at low bottom albedos. For increasing total bottom albedo inputs, the error in retrieved total bottom albedo at 550 nm tends to increase to approximately $\pm$0.15 and results in an overall RMS error of 6.8%. Again, good model-fits are achieved with an RMS error of 1.0%.

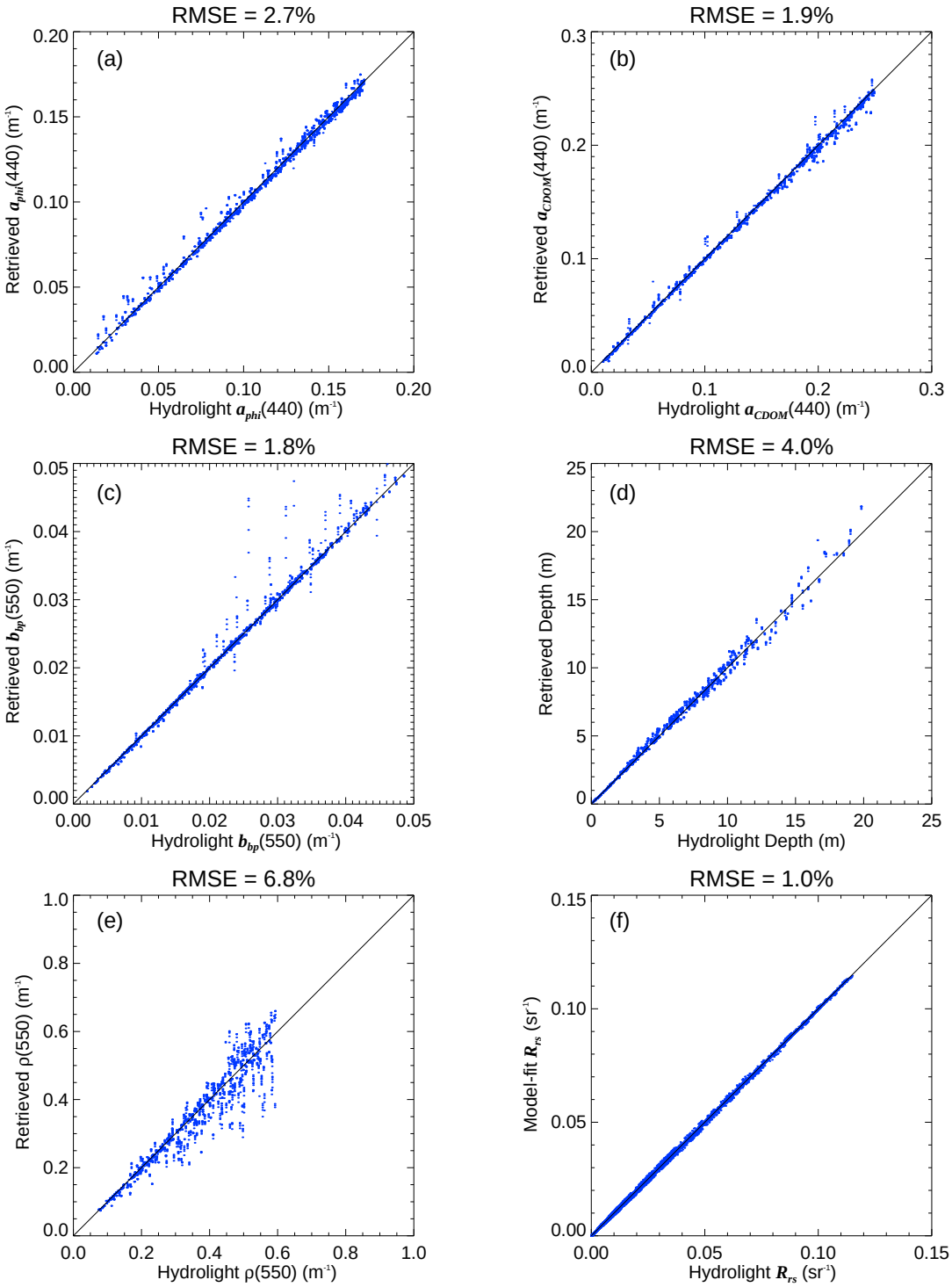

Figure 4.10: a) to e) Inversion retrieved model parameters versus Hydrolight inputs over variable mixtures of bottom cover. As before, data corresponding to $w_{max} > 0.85$ were omitted for $a_{phi}(440)$, $a_{CDOM}(440)$ and $b_{bp}(550)$ and data corresponding $w_{max} < 0.15$ were omitted for depth and bottom albedo retrievals. The bottom albedo scatter plot in e) compares the total retrieved bottom albedo, calculated as the sum of the 3 separate bottom albedos (i.e. $B_{sd} + B_{sg} + B_{ba}$). f) model-fit R_{rs} versus Hydrolight R_{rs}.

An estimate of the relative proportions of benthic cover type are given by the fractional components of sand, seagrass and brown algae, f_{sd}, f_{sg} and f_{sd}. The comparisons between model retrieved fractional components and the relative proportions of bottom reflectance mixtures that were used in the Hydrolight simulations are shown in Fig. 4.11. The relative proportion of sand (top) is modelled very well with an average difference of 3.3% between assumed and retrieved values. Retrieved f_{sd} compares very closely to Hydrolight f_{sd} at low values. At increasing Hydrolight f_{sd}, the spread in data steadily increases up to approximately 28%. In contrast, the relative proportions of seagrass (middle) and brown algae (bottom), show a larger spread in data at low values (max difference ∼38%) and tend to show a stronger correlation toward higher fractional cover. Overall the average difference between modelled fractional cover and Hydrolight simulated fractional cover is 7.5% for seagrass and 7.0% for brown algae. These results suggest that the model can provide a good estimate of the relative proportions of key benthic cover types (sand, seagrass and brown algae) from remote sensing.

For data with $w(600) > 0.1$, the classification accuracy of the dominant benthic cover fraction is 93.4%, for the next dominant fraction 67.1% and the least dominant at 73.7%.

4.4 Instrument Noise and Resolution

The inversion performance assessments, detailed in the previous sections, were all carried out on noise and error free data. However, remote sensing measurements collected with an optical sensor inherently contain effects of electronic noise, digitisation error and spectral resolution, which degrade the quality of the water leaving signal and therefore may have an impact on the overall inversion performance. Lee and Carder (2002) investigated the influence of spectral resolution and channel placement on the retrieval accuracy of water column and bottom properties from ocean colour data. Their results suggest that retrievals for sensors characterised with 10 nm-contiguous spectral bands provide almost

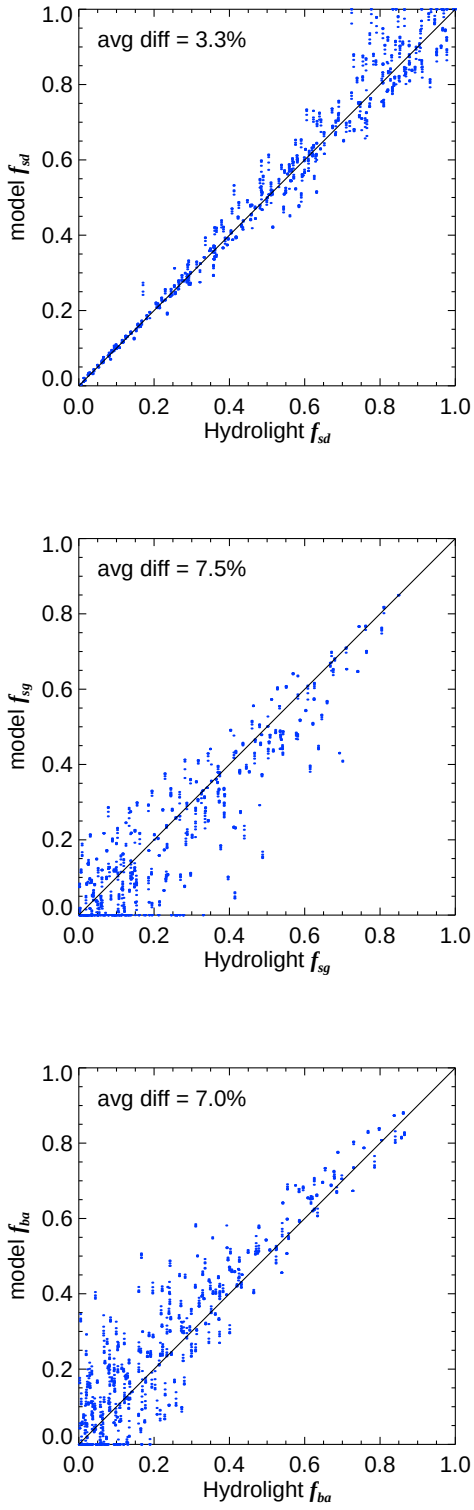

Figure 4.11: Inversion retrieved fractional components of sand (top), seagrass (middle) and brown algae (bottom) compared with Hydrolight simulated fractional components. Data with $w(600) > 0.1$ have been discarded from the comparison.

identical results as for bands every 5 nm, whereas bands every 20 nm introduce additional retrieval errors. However, the effects of instrument noise and digitisation were not considered in their evaluation and only data over sandy bottom environments were studied. Moses et al. (2012) assessed the impact of sensor noise on the space-borne HICO hyperspectral sensor; specifically on the estimation of water constituents in Case 2 waters. Their results demonstrated that sensor noise alone can result in relative errors of 50% or more in the retrieved constituent concentrations.

Botha et al. (2013) compared the substratum detectability of an airborne hyperspectral imager (CASI with 30 spectral bands), and two multispectral satellite sensors (WorldView-2 with 8 bands, and QuickBird with 4 bands). Using modelled reflectances of two contrasting water types (reef-oceanic and coastal), with $NE\Delta_{rsE}$ typical of each sensor, it was demonstrated that as the spectral resolution increases from 4 to 8 to 30 bands, the substratum end-members can be resolved to greater depths, in their case, from 2 to 6 m. Garcia et al. (2015) investigated the number and type of distinguishable benthic classes for three sensors, HICO (87 bands), HyMap (126 bands, 21 in the visible spectrum) and Worldview-2 (8 bands). The investigation was performed on modelled r_{rs} spectra using 22 benthic reflectance end-members over a wide range of water column properties with the addition of noise properties typical of each sensor. Hierarchical clustering using linear Discriminant Coordinates was used to asses the separability of benthic classes above noise and water column attenuation. Analysis of the clustering for the three sensors showed that a reduction in spectral resolution reduced the spectral separability between classes and hence reduced the number of distinct classes. For instance, on average, HICO bands can detect seagrass *A. antartica* to depths 2.7 times greater than Worldview-2 bands and 1.2 times greater than HyMap bands across the clustering accuracies and water types. Garcia et al. (2014a) demonstrated the impact that SNR has on the accuracy of water column depth retrieval from HICO data. Thier modelling showed that the accuracy of

depth retrievals diminish with decreasing SNR with errors greater than 100% for SNR's of less than 20. For the above studies on benthic separability (Botha et al., 2013)(Garcia et al., 2015) and depth retrievals (Garcia et al., 2014a), the modelling of noise for each sensor combined the effect of sensor noise and environmental noise arising from atmospheric, sun-glint and water-to-air interface corrections.

To evaluate the accuracy of remote sensing retrievals under the influence of sensor characteristics alone, that are typical of common hyperspectral imaging systems, a number of inversion tests were conducted using Hydrolight data that were modelled to include the additional effects of sensor noise, digitisation and spectral resolution. The noise modelling exercise considered sensor characteristics that emulate three popular hyperspectral sensors; Eagle (Specim Inc,), Ocean PHILLS (NRL) and HyMap (HyVista Corp.). The Eagle and Ocean PHILLS are push-broom imagers that incorporate CCDs and diffracting prism assemblies, whereas, the HyMap system is a whisk-broom imager which incorporates a VIS spectrometer and opto-electronic scanning technology. The Eagle sensor possesses 965 spectral channels between 400 nm and 900 nm with 1.25 nm nominal spacing and is realised with a 12 bit analog-to-digital converter (ADC). With on-chip spectral binning the spectral band spacings become 2.5 nm and the digitisation effectively becomes a 13 bit system. The Ocean PHILLS is a 14 bit ADC system, with a spectral range between 400 nm and 900 nm into 4 - 5 nm bandwidths. The HyMap has relatively coarse spectral resolution of approximately 15 nm bandwidths from 450 nm to 2500 nm, but has superior quantisation of 16 bits.

The noise modelling was applied to the previously generated Hydrolight simulations of Database 3. Rather than applying a level of noise to the remote sensing reflectance spectra, the noise was added to each water leaving radiance spectrum, after radiometric conversion, to simulate radiometric measurements in terms of instrument digital numbers (DN). This provides a representation of "raw instrument data" that is proportional to photoelectric counts, and allows

for appropriate modelling of photon noise (shot noise), electronic readout noise, dark noise and digitisation errors.

The electronic readout noise and dark noise of a particular sensor configuration may be obtained from a "dark" image, usually acquired by closing a shutter within the imaging system. For HyMap, Ocean PHILLS and Eagle noise simulations, the combined dark and readout noise was modelled with normal-distributed random numbers with a standard deviation of ±2 counts, ±1.5 counts and ±1 count, respectively, representative of actual dark measurements obtained during their respective airborne surveys.

The photon noise or shot noise is primarily caused by fluctuations in detected photons per unit time and follows a Poisson distribution of standard deviation equal to the square root of the total number of detected photons (Moses et al., 2012). Thus the modelling of noise is dependent on the magnitude and spectral shape of the radiance received at the sensor. The conversion of digital counts to the number of photons, $n_{photons}$, reaching the imaging detector was calculated using (Rock et al., 2013),

$$n_{photons} = Counts \times \frac{FWC}{2^{ADC\_bit\_depth} \times QE}, \tag{4.8}$$

where, FWC is the imaging detector's full well capacity, QE is the detector's quantum efficiency. A conservative approach was taken in modelling shot noise, whereby, the electron well depth of a silicon diode array was assumed to be 45,000 e^- with a QE of 0.7. By substituting each sensor's ADC bit depth into Eq. 4.8, the number of photons per count was calculated as ~ 1, ~ 4 and ~ 8 for HyMap, Ocean PHILLS and Eagle, respectively. Thus, the photon noise was modelled with normally distributed random numbers whose standard deviation was $\sigma_{photon}^{HyMap} = \sqrt{counts}$, $\sigma_{photon}^{PHILLS} = \sqrt{(counts/4)}$, and $\sigma_{photon}^{Eagle} = \sqrt{(counts/8)}$.

The spectral resolutions of the 3 sensors were also incorporated into the noise modelling by interpolating Hydrolight-$L_w(\lambda)$ to the sensors central wavelengths (shown in Table 4.4). The interpolated water leaving radiance spectra were rep-

resented as "raw" instrument data by dividing L_w with a radiance calibration curve typical of a hyperspectral sensor (see Fig. 4.12). The instrument counts were scaled so that the maximum DN of the brightest spectrum within the Hydrolight database achieves a value close to the instrument specific digitisation (i.e, 8192, 16384 or 65536 counts). This resembles the situation where a sensor is required to capture data within its dynamic range but not saturate the signal when imaging a sandy beach or other bright objects typical of a coastal scene. After introducing the signal-dependent photon noise, electronic readout noise and dark noise to the instrument specific measurement simulations, the same radiometric calibration coefficients were used to yield noise-induced water leaving radiances, and finally to give noisy remote sensing reflectance spectra by division of the associated Hydrolight $E_d(\lambda)$.

The signal-to-noise ratio (SNR) of a sensor is often specified from laboratory based measurements of a spectrally uniform reflectance plaque, and represented by a single number obtained from the maximum calculated value. However, for sensors that operate over water, the reflectance is often low and results in a much lower SNR than the prescribed SNR, and is very much dependent on the magnitude and spectral shape of the radiance collected by the sensor. For the wide range of environment conditions simulated in Hydrolight Database 3, the peak SNR ranges from about 20:1 for deep, high CDOM loaded water up to a SNR of near 250:1 which occurs for highly reflective turbid water. Figure 4.13 shows the maximum and minimum peak SNR curves.

An example of noise-affected R_{rs} spectra for low, moderate and high reflectances are shown in Fig. 4.14. For high reflectance, the apparent noise is relatively small compared "ideal" Hydrolight R_{rs}. For moderate R_{rs} the noise is more noticeable, whereas for low R_{rs} the effect of noise is pronounced.

Figure 4.15 show the comparisons between retrieved model parameters and Hydrolight inputs from inversions performed over the noise-induced $R_{rs}(\lambda)$ as modelled for the Eagle, PHILLS and HyMap sensors. Data corresponding to

Table 4.4: Centre wavelengths for HyMap, Ocean PHILLS and Eagle imaging sensors.

Sensor	Centre wavelengths (nm)
HyMap	454.8, 468.9, 483.8, 498.6, 512.9, 528.1, 543.3, 557.9, 572.7, 587.6, 602.4, 616.9, 631.2, 645.8, 660.4, 674.9, 689.3, 704.0, 718.5, 732.6, 746.8
PHILLS	402.4, 407.3, 412.2, 417.1, 422.0, 426.9, 431.8, 436.7, 441.6, 446.5, 451.4, 456.3, 461.1, 466.0, 470.9, 475.8, 480.7, 485.6, 490.5, 495.3, 500.2, 505.1, 510.0, 514.9, 519.7, 524.6, 529.5, 534.3, 539.2, 544.1, 549.0, 553.8, 558.7, 563.5, 568.4, 573.3, 578.1, 583.0, 587.8, 592.7, 597.5, 602.4, 607.3, 612.1, 617.0, 621.8, 626.7, 631.5, 636.3, 641.2, 646.0, 650.9, 655.7, 660.6, 665.4, 670.2, 675.1, 679.9, 684.7, 689.6, 694.4, 699.2, 704.1, 708.9, 713.7, 718.5, 723.4, 728.2, 733.0, 737.8, 742.6, 747.5
Eagle	400.7, 403.0, 405.2, 407.4, 409.7, 411.9, 414.1, 416.4, 418.6, 420.8, 423.1, 425.3, 427.5, 429.8, 432.0, 434.2, 436.5, 438.8, 441.1, 443.4, 445.7, 448.0, 450.3, 452.6, 454.9, 457.2, 459.5, 461.8, 464.1, 466.4, 468.7, 471.0, 473.3, 475.6, 477.9, 480.2, 482.5, 484.9, 487.1, 489.5, 491.8, 494.0, 496.4, 498.7, 501.0, 503.3, 505.6, 507.9, 510.2, 512.5, 514.8, 517.1, 519.4, 521.7, 524.0, 526.3, 528.6, 530.9, 533.2, 535.5, 537.8, 540.1, 542.4, 544.7, 547.0, 549.4, 551.8, 554.2, 556.6, 559.0, 561.3, 563.7, 566.1, 568.5, 570.9, 573.3, 575.7, 578.1, 580.4, 582.8, 585.2, 587.6, 590.0, 592.4, 594.8, 597.2, 599.5, 601.9, 604.3, 606.7, 609.1, 611.5, 613.9, 616.2, 618.6, 621.0, 623.4, 625.8, 628.2, 630.6, 633.0, 635.3, 637.7, 640.1, 642.5, 644.9, 647.3, 649.7, 652.0, 654.4, 656.8, 659.2, 661.6, 664.0, 666.3, 668.7, 671.1, 673.5, 675.9, 678.3, 680.7, 683.0, 685.4, 687.8, 690.2, 692.6, 695.0, 697.3, 699.7, 702.1, 704.5, 706.9, 709.3, 711.7, 714.0, 716.4, 718.8, 721.2, 723.6, 726.0, 728.3, 730.7, 733.1, 735.5, 737.9, 740.3, 742.7, 745.0, 747.4

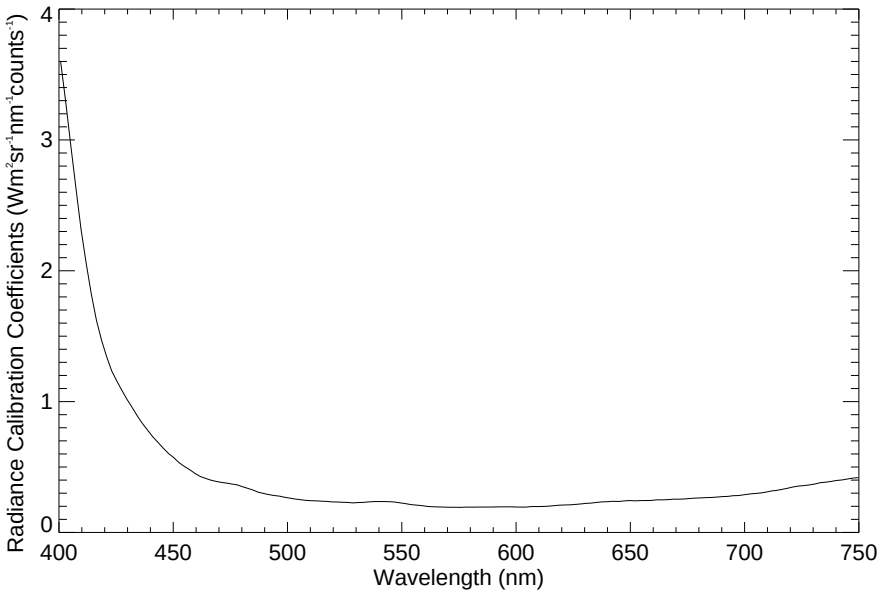

Figure 4.12: Radiance calibration coefficients of the Eagle sensor. This data is used to convert spectrometer digital numbers to radiance.

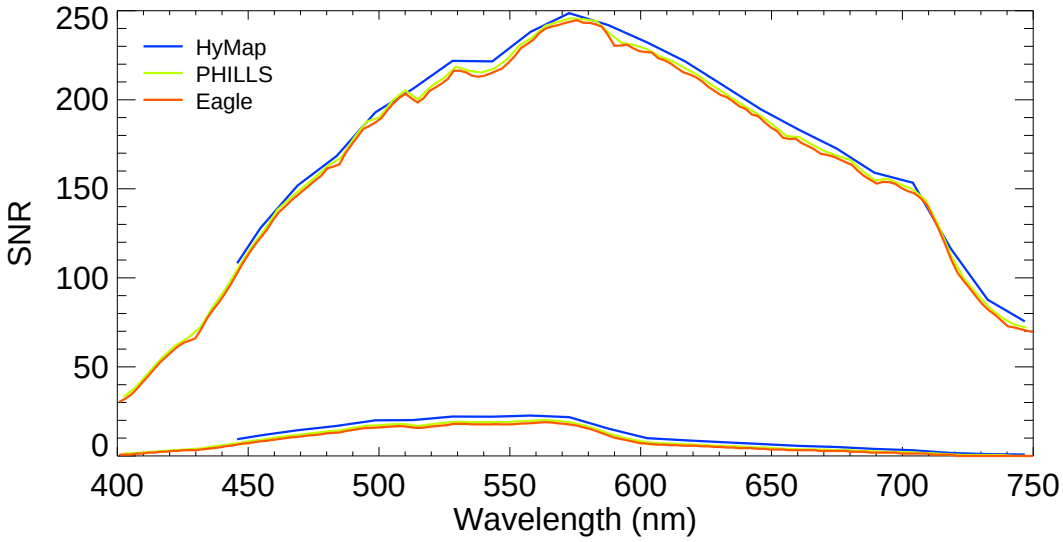

Figure 4.13: Signal-to-noise ratios representative of a bright (top curve) and mild (lower curve) water leaving radiance from Hydrolight Database 3, with the addition of modelled noise.

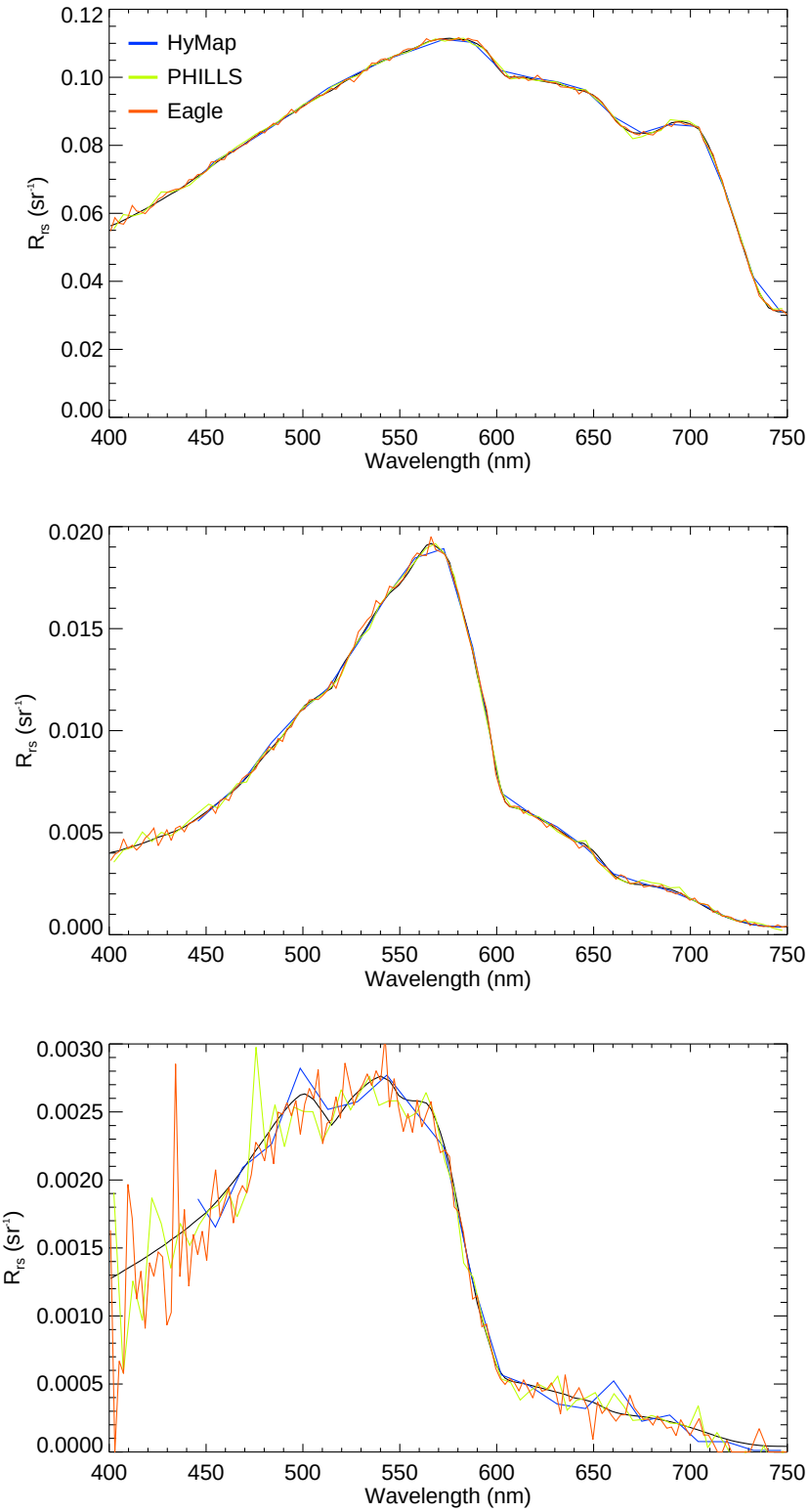

Figure 4.14: Examples of R_{rs} spectra, modelled with noise, for high reflectance (top), moderate reflectance (middle) and low reflectance (bottom). The smooth black line in each panel represents the "ideal" Hydrolight R_{rs} spectra.

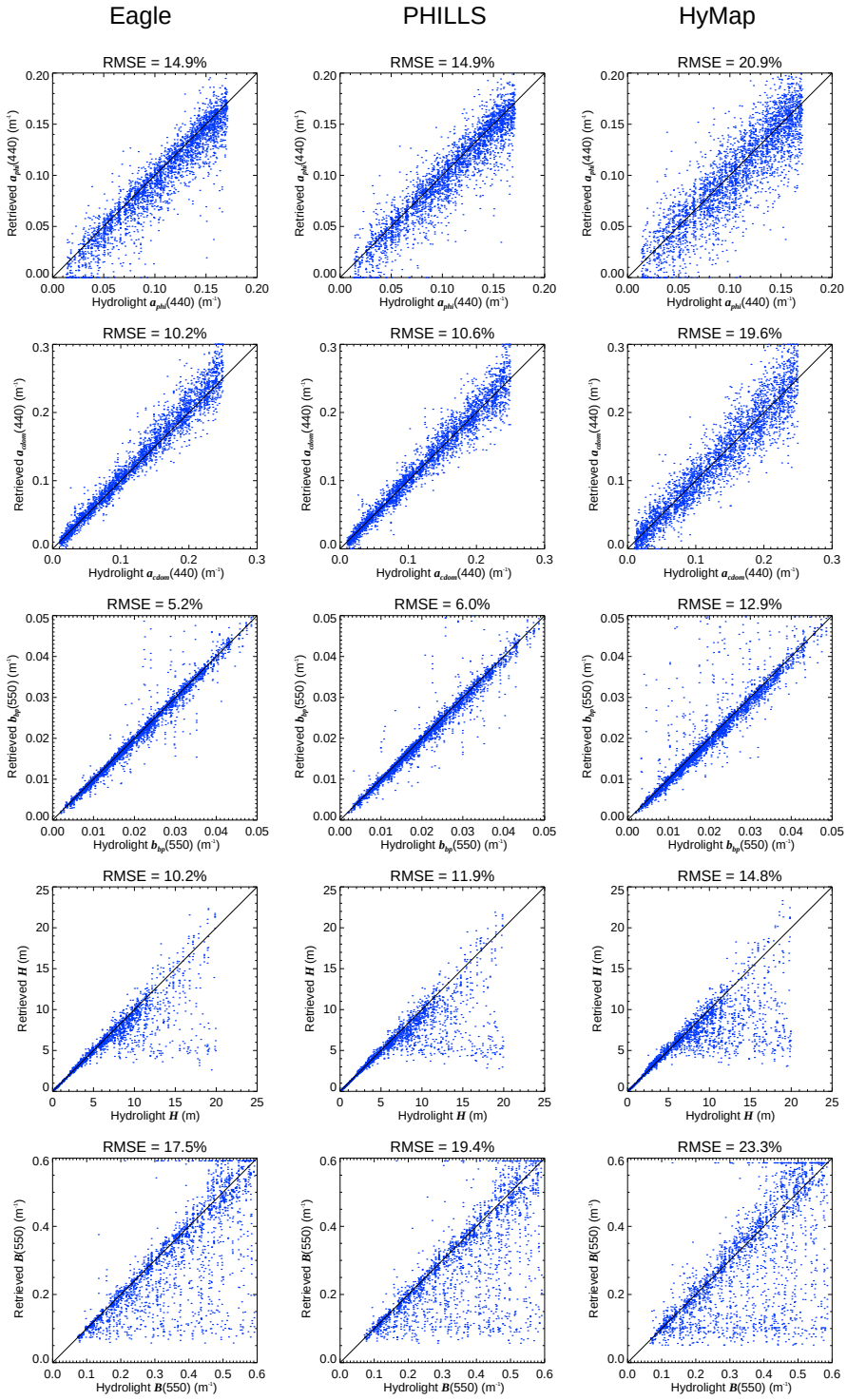

Figure 4.15: Scatter plots comparing inversion retrieved model parameters with Hydrolight inputs over sensor-specific R_{rs} spectra representative of the Eagle (first column), Ocean PHILLS (middle column) and HyMap (Last column). Data corresponding to $w_{max} > 0.85$ were omitted for $a_{phi}(440)$, $a_{CDOM}(440)$ and $b_{bp}(550)$ retrievals and data corresponding $w_{max} < 0.15$ were omitted for depth and bottom albedo retrievals

$w_{max} > 0.85$ were omitted for $a_{phi}(440)$, $a_{CDOM}(440)$ and $b_{bp}(550)$ retrievals and data corresponding $w_{max} < 0.15$ were omitted for depth and bottom albedo retrievals. The results indicate that there is a pronounced effect on the retrieval accuracy due to the combination of sensor-specific noise, digitisation and spectral resolution. For the water column model parameters, the retrieved values correlate reasonably well to the Hydrolight inputs, although the spread in data points about the 1:1 reference line is more pronounced as compared to the results obtained from "ideal" $R_{rs}(\lambda)$ (Fig. 4.10). For $a_{phi}(440)$ retrievals, the overall RMS errors range from 14.9% to 20.9%. For $a_{cdom}(440)$, the relative errors range between 10.2% and 19.6%, and for $b_{bp}(550)$, between 5.2% to 12.9%.

For water depth and bottom albedo retrievals, the comparison scatter plots show a high relative proportion of values that agree well with hydrolight inputs, however, the remainder of data values show significant underestimation, up to 22 m for depth and 0.6 m^{-1} for total bottom albedo. The overall RMS errors for depth retrievals range from 10.2% to 14.8%, and for total bottom albedo, between 17.5% and 23.3%.

Overall the inversion performance over data modelled with the eagle sensor achieves the highest accuracy, with the Ocean PHILLS sensor RMS errors only marginally greater. Given the relatively high spectral resolutions for both of the latter sensors, the increase in retrieval errors are mainly due to the effects of sensor noise. For the HyMap sensor, the decrease in spectral resolution and the number of spectral bands appear to further increase the RMS errors in model retrievals even though the overall SNR, due to the higher 16 bit digitisation, is greater.

The underestimation in both water depth and bottom albedo occurs for data simulated with moderate to high absorption and backscattering values. With this increase in water column attenuation, the depth and bottom albedo model parameters become less sensitive to changes in overall reflectance. For increasing Hydrolight depths beyond approximately 5 m, the model appears to compensate

for the underestimated depths by retrieving low albedos, without affecting the overall magnitude and spectral shape of the modelled R_{rs}. This effect was also seen for inversions performed with "ideal" Hydrolight R_{rs} (Fig. 4.1), however, the unreliable data were appropriately discarded using the criterion $w_{max} < 0.15$, as seen in Fig. 4.3. For noise-induced R_{rs}, the increase in uncertainty of water column IOP retrieval, results in an increase in modelled w_{max} uncertainty, and therefore, reduces the effectiveness of masking out the unreliable data with the criterion $w_{max} < 0.15$.

The difference between model retrieved depth and hydrolight depth as a function of modelled w_{max} for HyMap simulated data is shown in Fig. 4.16. The data shows an increased amount of error in depths at values greater than the threshold of 0.15 (dashed line) but contained within $w_{max} = 0.4$. This suggests a more stringent threshold needs to be applied to retrievals using noisy R_{rs} for adequate filtering of unreliable data. Fig. 4.17 shows the comparisons for depth and bottom albedo retrievals after filtering out data associated with w_{max} values less than 0.45. The results show good confidence in the estimation of depth, up to approximately 20 m, with an RMS error reduced to 6.2%. Similarly, the estimation of total albedo from HyMap simulated data also show good agreement with Hydrolight input albedo with an RMS error of 9.1%.

The addition of sensor-specific noise and spectral resolution attributes also has a marked effect on the inversion performance in estimating the relative proportions of benthic cover type. The relative proportions of sand, seagrass and brown algae show an average difference of 8.5%, 15.5% and 13.6%, respectively, as compared with Hydrolight assumed proportions. However, after incorporating a more stringent filtering criterion where $w(600) < 0.2$, the comparisons achieve average differences of 6.2% for sand, 12.3% for seagrass and and 10.8% for brown algae. Under this criterion, the classification accuracy of the dominant benthic cover fraction is 89.8%, with a much lower accuracy of 56.8% for the next dominant fraction and 64.3% for the least dominant of the three.

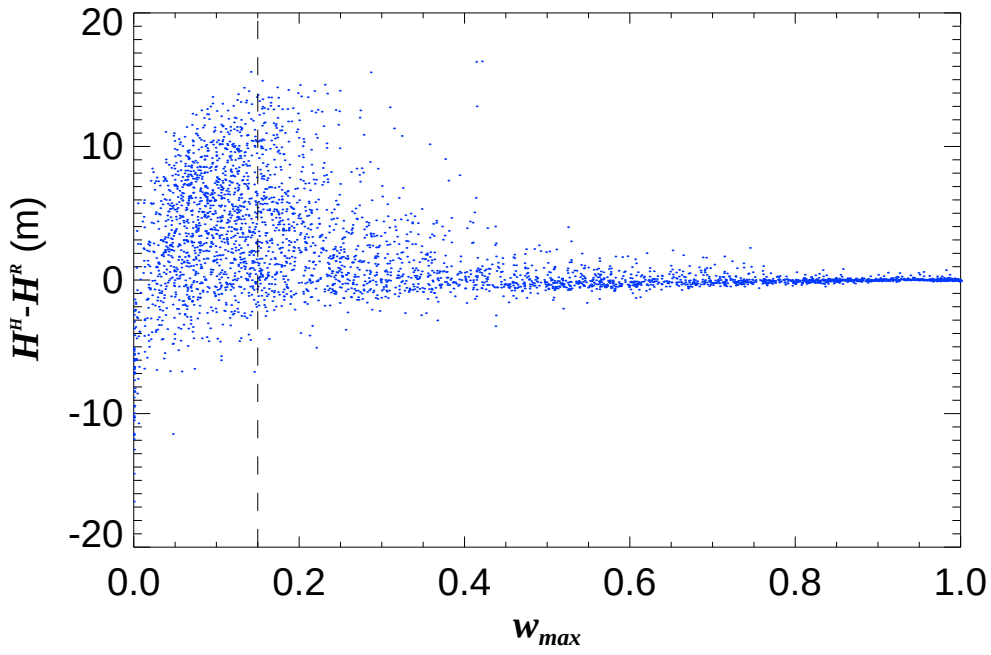

Figure 4.16: Depth retrieval error as a function of modelled w_{max} from inversions over HyMap simulated R_{rs}.

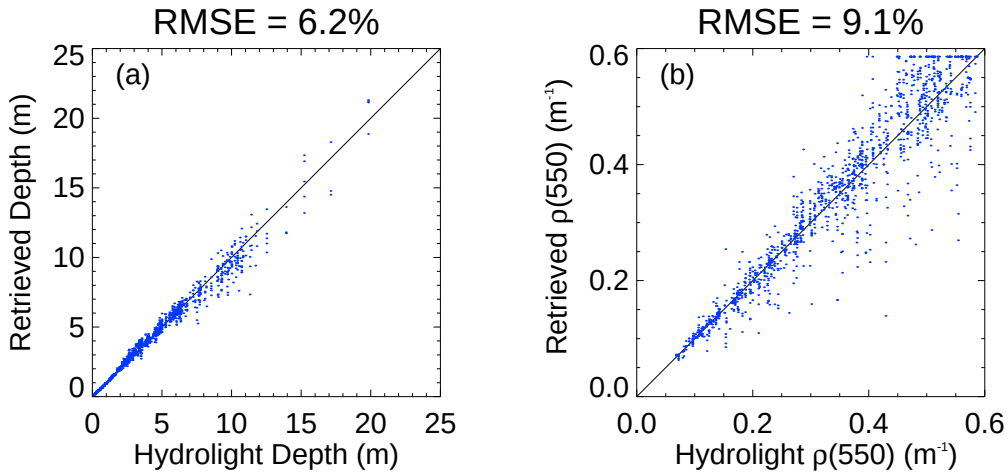

Figure 4.17: Comparison of model retrieved depth and bottom albedo with Hydrolight inputs after more stringent filtering of unreliable data using $w_{max} < 0.45$.

4.5 Summary

This chapter has presented a number of examples of model inversion performance based on computer simulated Hydrolight data. This allowed for testing over a controlled model environment which covered a wide range of optical conditions that simulate those encountered in typical coastal waters.

For the simplest scenario, where the bottom reflectance shape is assumed known and the initial guess values taken from Hydrolight inputs, the retrievals of water column parameters compare very well with Hydrolight, with errors of 3-4% for absorption and $\sim 10\%$ for backscattering. The retrieval of water column depth is excellent up to approximately 7 m. However, large errors are apparent in both retrieved depth and bottom albedo at depths beyond 7 m. This highlights the limitations of the model itself, whereby, at moderate-to-high water attenuation and low bottom albedo, the model output gives ambiguous results due to the low signal returned from the bottom. Based on comparisons between the ratio of the bottom signal to the total signal (w_{max}) and model error, the majority of significant depth and albedo errors occurred for $w_{max} < 0.15$. The masking out of unreliable data based on thresholds of w_{max} was shown to work well, and because w_{max} is calculated from the model itself, it provides a useful operational constraint.

After filtering out erroneous data, the retrieval errors were reduced to 2-4% for water column properties and depth, and 6% for bottom albedo. This demonstrates that the shallow water model and retrieval scheme would work well for a wide range of coastal water conditions, and since the comparisons included data for sensor viewing angles up to 40° and solar zenith angles up to 60°, the model is well suited for most hyperspectral imaging platforms.

Further inversion performance tests demonstrated that initial guess values, used to start the minimisation process, are an important consideration for accurate model retrieval using the Levenberg-Marquardt optimisation approach. Retrieval errors over 200% were shown for situations where assumed initial con-

ditions are far from the optimal solution. Using a coarse look-up-table of modelled R_{rs} to dynamically adjust initial values, in response to input R_{rs}, provided excellent inversion performance, and gave the same calculated RMS errors in parameter retrieval as for the case where known Hydrolight inputs were used as the initial guess values.

To account for variable benthic cover types, the bottom reflectance was parameterised using a linear combination of 3 spectrally distinct bottom reflectance endmembers representative of sand, seagrass and brown algae. The inversion performance was firstly tested against Hydrolight data that were simulated with different but homogenous bottom cover. The results showed good model parameter retrievals equivalent to the results where the bottom reflectance term was assumed known. Additionally, it was demonstrated that the model was able to adequately discriminate between the various bottom types to retrieve the appropriate bottom reflectance spectra. The modelled bottom reflectances matched the spectral form of the Hydrolight input bottom spectra with magnitudes within $\pm 25\%$ measurement error.

The inversion performance of the model was also assessed using Hydrolight data that were simulated with random mixtures of bottom reflectance endmembers. The results showed strong correlation between all model retrieved parameters and hydrolight inputs. The extra degrees of freedom that is introduced by the bottom reflectance parameterisation appears to appropriately account for the varying mixtures of bottom reflectance, and in turn, is able to provide good estimates of water column properties (RMS errors between 1.8% and 2.7%) and water column depth (RMS error of 4% between 0.1 m and 20 m). The relative proportions of benthic cover types, obtained from the bottom reflectance parameterisation, agreed favourably with the random proportions assumed in the Hydrolight simulations. For the sand component, which is characterised by a spectrally uniform shape and high albedo, the average difference between model estimated fractional cover and Hydrolight inputs was 3.3%. For seagrass and brown algae

components, which are both characterised by spectrally distinct spectral forms but with a much lower albedo than sand, the average difference obtained was 7.5% for seagrass and 7.0% for brown algae. The somewhat larger average differences obtained for seagrass and brown algae are due to the higher errors that occur at small fractional cover. This situation occurs when the bottom mixture is dominated by the relatively bright sand component, leaving only a small fraction of either seagrass or brown algae. Since the albedos of the two are relatively low, the model seems to be less sensitive to their respective weighting terms and thus model selection can interchange between the two endmembers without much effect on the overall remote sensing reflectance.

The introduction of sensor-specific noise, digitisation and spectral resolution to the remote sensing reflectance showed a pronounced negative effect on the model inversion performance. The retrieval error of $a_{phi}(440)$ increased to 20.9%. For $a_{cdom}(440)$, the retrieval error was 19.6% and for $b_{bp}(550)$ the RMS error was 12.9%. The increase in retrieval errors for water column absorption and backscattering components reduced the accuracy of modelling the ratio of bottom signal to the total signal (w_{max}). The comparison between modelled w_{max} and retrieval errors in depth and bottom albedo showed a much higher proportion of erroneous retrievals beyond the masking threshold of 0.1, with large retrieval errors still apparent at w_{max} up to a value of 0.4. This means that for noisy R_{rs}, a more stringent masking threshold is required to omit erroneous retrievals in depth and albedo. Increasing the w_{max} threshold to 0.45 resulted in effective masking out of bad retrievals. For depth retrievals, the RMS error was 6.2% and even after the stringent masking still showed good depth retrievals up to 20 m. Similarly, after incorporating a more stringent filtering criterion for bottom albedo for noisy R_{rs} data, good estimates of the relative proportions of sand, seagrass and brown algae were obtained.

The modelling results presented here demonstrate the potential use of the shallow water model over the relatively low signal-to-noise ratios that are typically

encountered over coastal water targets. However, it must be noted that the effects of systematic errors caused by fixed pattern noise, absolute radiometric uncertainty, image distortions, stray light and improper removal of atmospheric contributions have not been considered. Additionally, the retrieval errors due to improper model parameterisation (i.e use of different endmember spectral shapes) and tests over a range of particle phase functions were also not investigated. Therefore, the retrieval accuracies reported here represent a lower bound of what would be obtained operationally. The application of the shallow water model to data collected by an airborne hyperspectral imager is presented in the next chapter.

Chapter 5

Inversion of Hyperspectral Imagery

The shallow water model was applied to airborne hyperspectral survey data collected over two regions of the Western Australian coastline; Jurien Bay and the Ningaloo Marine Park (see Figs. 5.1 and 5.7). The model allowed for the simultaneous retrieval of image based products relating to water quality, bathymetry and benthic cover. The temperate reef system within Jurien Bay and the large fringing coral reef within the Ningaloo Marine Park presented two diverse and challenging environments for testing the shallow water model. The image-derived products were validated against ground truth data. Jurien Bay was an opportunistic, proof of concept study over a temperate reef system dominated by sand, brown algae and seagrasses. The Ningaloo Marine Park study attempted to extend the model applicability over a more challenging environment, encompassing a highly diverse and large coral reef ecosystem. A large scale field campaign was conducted to coincide with the aerial survey to enable collection of a full suite of validation data including above water radiometric observations, echo sounder bathymetry, underwater video recordings and water sampling.

5.1 Jurien Bay Marine Park Study

The Jurien Bay aerial survey was planned to coincide with a focused ground truthing field campaign to validate the image-derived products. Unfortunately, the sensor was flown a week after the *in situ* data collection. Therefore, the validation presented here, focuses only on bathymetry and benthic cover products, using historical hydro-acoustic depth data and underwater video footage collected after the flight.

5.1.1 Jurien Bay Region Description

The study area selected for evaluation encompasses a small portion (1.5 km by 1.5 km) of the Jurien Bay Marine Park, located approximately 300 km north of Perth, Western Australia (see Fig. 5.1). The benthic cover within this study region is highly variable, composed largely of sediment, seagrass and pavement/reef. The sediment that is most common to this region is white carbonate sand. The dominant seagrass species that is abundant in this region is *Posidonia Australis*. Small pockets of the seagrasses *Amphibolus Grifithii* and *Halophila Ovalis* also occur. The brown algae's, *Sargassum.sp* and *Ecklonia.sp* are also abundant in this region and reside mainly on the reef and pavement areas with varying density. Occurring in much sparser growth is the fleshy and coralline red epiphytes that attach themselves onto seagrass shoots. The topography of the area is also highly variable and includes extensive shallow water areas with depths ranging overall from 0 m -15 m.

5.1.2 *In situ* Hyperspectral Field Data

Spectral measurements of a variety of bottom types, common to Jurien Bay coastal waters, were acquired to build up a spectral library of benthic reflectance endmembers and provide region-specific parameterisation of three key benthic cover types. The spectral measurements were carried out as part of the Strategic

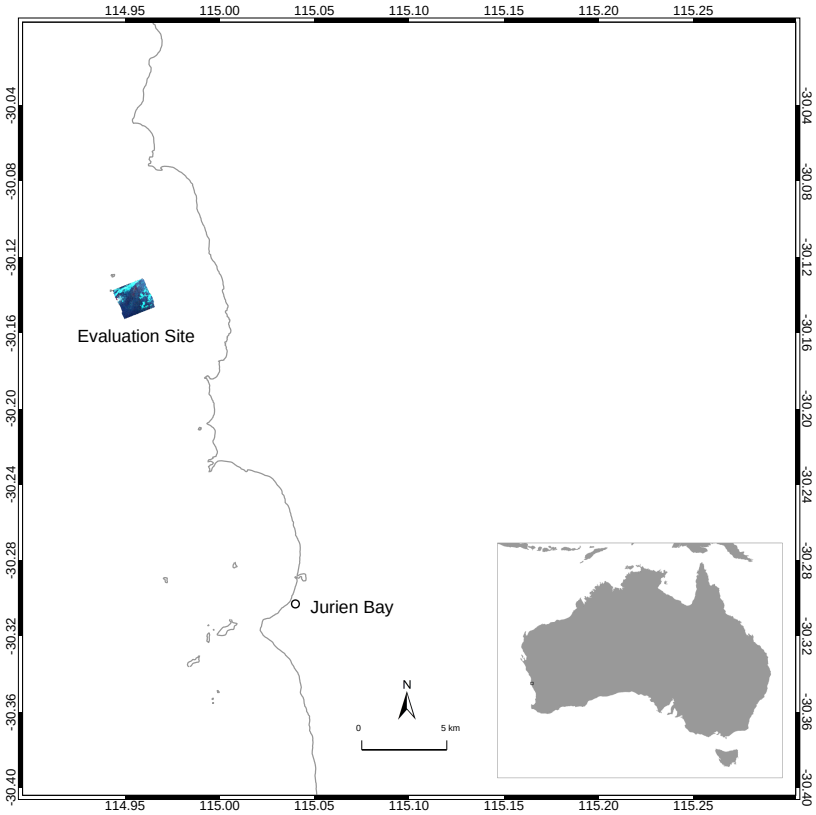

Figure 5.1: Map of the Jurien Bay coastline showing the portion of HyMap coverage evaluated in this study (blue square)

Research Fund for the Marine Environment, SRFME field campaign (Klonowski, 2006). Benthic reflectance measurements were acquired with a custom built dual-channel, hand-held spectroradiometer referred to hereafter as the Zeiss. The Zeiss incorporates two Carl Zeiss MMS UV/VIS enh. spectrometers which record light into 256 spectral channels from 350 nm to 1100 nm with a 3.3 nm nominal bandwidth. The two optical heads permit simultaneous capture of downwelling irradiance and upwelling radiance when appropriately aligned over the desired target. Bottom samples were collected and spread out on a large low reflectance black plastic surface ensuring only the sample was imaged within the 30° FOV radiance channel. Triplicates of 100 continuous spectral recordings were acquired for each sample. Dark current counts were recorded between each subsequent measurement and their average subtracted from the raw digital counts of each sample. By use of predetermined calibration responsivity coefficients, the dark current-corrected digital counts of the corresponding upwelling and downwelling signals were converted to radiance, L, and irradiance, E, respectively. Spectral irradiance reflectance, ρ, of each sample was calculated using the expression,

$$\rho = \frac{\pi L_u}{E_d}. \tag{5.1}$$

The reflectance spectra of the various bottom cover types sampled are shown in Fig. 5.2.

5.1.3 Airborne Hyperspectral Image Acquisition

A spectral image of the study area (Fig. 5.3) was captured with the airborne HyMap imaging system (HiVista Corporation.) on the 23^{th} of April 2004. The conditions on the day were calm (wind approx. 5 kts) and the sky condition was visually assessed as cloud free. The HyMap sensors record light into 126 spectral channels covering the 450 nm to 2500 nm spectral range with a typical bandwidth of 15 -16 nm. The imaging system was mounted on a gyro-stabilised platform

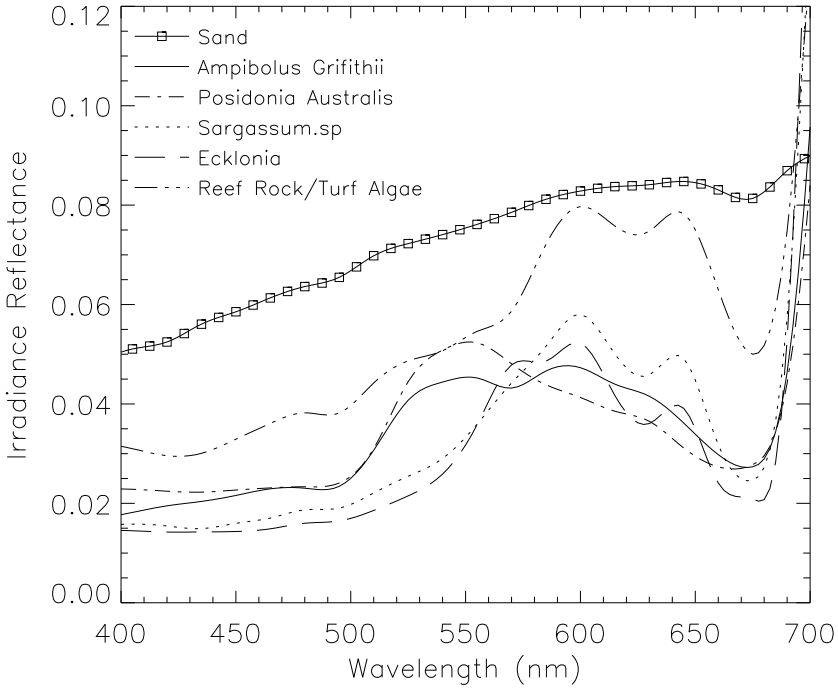

Figure 5.2: Spectral irradiance reflectance of a variety of substrates measured with the dual-channel Zeiss. Note: sand and limestone spectra are scaled by 30%.

(Boeing C-MIGITS II) that utilises a 3-axis accelerometer system which monitors the distortion effects induced by aircraft pitch, roll and yaw. The recorded image was taken at an altitude of approximately 1500 m which translates to a ground spatial resolution of 3.5 m. The HyMap image data was pre-processed and provided by HiVista Corp. and included at-sensor radiance, surface reflectance and geocorrection data files (HyVista Corporation, 2004). The radiance imagery was processed with data obtained from a recording of the on-board calibration lamp which was taken during image acquisition. This information was used to convert digital recordings into radiance ($Wm^{-2}sr^{-1}nm^{-1}$). The at-sensor radiance was converted to surface reflectance with corrections for the intervening atmosphere using proprietary Hycorr software (HyVista Corporation, 2004). The atmospheric model used in Hycorr was the standard mid-latitude summer profile with a continental aerosol model. A value of 0.34 atm-cm was used for ozone content. Visibility was set to 75 km and the water vapour was estimated from

the H_2O spectral absorption feature at 0.94 μm over vegetation. Geocorrection data files provide positional information for the radiance and reflectance pixels on a UTM zone 50 south projection and a WGS-84 datum.

Table 5.1: Summary of HyMap operational parameters during image acquisition

HyMap	Operational Parameters
Platform	light twin engine Cessna 404
Image acquisition date/time	23/04/2004; 04:50 UTC (12:50pm Local)
Altitude	1500 m
Heading	342°
Ground Speed	120 kts
FOV	61.3° (512 pixels)
Spatial Resolution	3.5 m
Swath	1.5 km
Scene centre lat/long	30°8'30" ; 114°57'15"
Solar zenith/azimuth	45° ; 350°

5.1.4 Model Inversion

The shallow water model and optimisation approach was applied to the HyMap data collected over Jurien Bay. The Hycorr generated surface reflectance, R, was converted to above-water remote sensing reflectance, R_{rs}, using,

$$R_{rs} = \frac{R}{\pi}, \tag{5.2}$$

where, R is irradiance reflectance and is defined as the ratio of upwelling irradiance to the downwelling irradiance just above the air-water interface. The 750 nm HyMap band was subtracted from the R_{rs} spectrum to minimise the effects of sunglint contamination (Lee et al., 1999), i.e.

$$\hat{R}_{rs}(\lambda) = R_{rs}(\lambda) - R_{rs}(750), \tag{5.3}$$

where, $\hat{R}_{rs}(\lambda)$ represents the above-water remote sensing reflectance spectrum to be fitted by the model. Figure 5.3 displays the geocorrected true colour image of

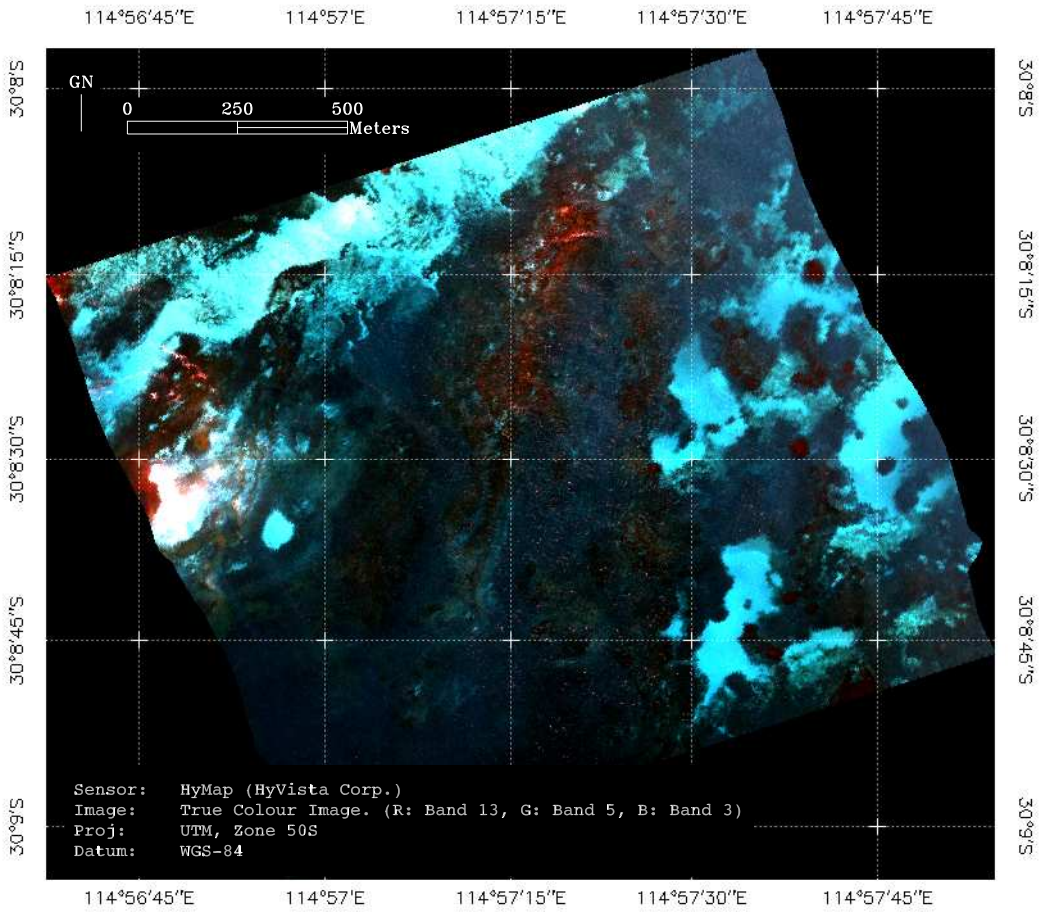

Figure 5.3: A composite HyMap true-color image (R=635.4 nm, G=517.4 nm, B=487.8 nm) of the Scientific Reference Zone within the Jurien Bay Marine Park and evaluation site recorded April 2004. The HyMap operational parameters during image acquisition are listed in Table 5.1.

the sunglint corrected R_{rs}. Model parameters for each pixel within the HyMap image scene were determined following the method outlined in Chapter 3.2 and were subsequently used to generate image-based bathymetry and key benthic cover classification products.

5.1.5 Jurien Bay Validation Data

A historical hydro-acoustic Jurien Bay data set of bathymetry was used to validate the model-retrieved bathymetry. The spatial resolution of the historical acoustic survey data were approximately 25 m along transects oriented in the E-W direction, with each transect spaced at approximately 100 m. The historical

bathymetry data are based on surveys carried out during 1985 and have an estimated vertical accuracy of ±0.2 m. Validation of the HyMap-derived bathymetry was carried out by determining co-located HyMap and acoustic data points. The HyMap scene includes over 65000 model-derived bathymetry pixels. The acoustic survey data provided approximately 1500 co-located data values.

Benthic cover data, to be used as ground truth for the HyMap derived classification maps, were collected during a SRFME field campaign in October, 2004 (Babcock et al., 2006). Approximately three hours of video footage was obtained using a cabled video submersible camera. The camera was suspended from a boat which maintained relatively constant positions at 25 station sites. For each recorded video frame, the GPS location was logged. The video data were visually classified based on the predominant benthic cover type. The relative proportion of each benthic cover type was estimated "by eye". The video data were further analysed to extract large regions (>10 m of video footage) of uniform cover to account for uncertainties in georeferencing the HyMap and video data.

5.1.6 HyMap Bathymetry and Benthic Cover Validation

Figure 5.4 shows the HyMap-derived bathymetry, represented by shades of blue, with the locations of the hydro-acoustic survey points overlaid as orange points. The remotely sensed depths were co-located with the hydro-acoustic sounding depths, and are presented as a scatter plot in Fig 5.5. The compared depths range from about 3 m to 11 m. For the 1500 data points compared, the normalised root-mean-square (RMS) difference is approximately 7%, or ±0.19 m.

The model-derived substrate reflectance albedos at 550 nm (Eqs. 4.5, 4.6 and 4.7) for sand (sd), seagrass (sg) and brown algae (ba) were used to generate a benthic cover classification map, displayed as a composite false-colour image, where Red = B_{ba}, Green = B_{sg} and Blue = B_{sd} (see Fig. 5.6). Areas of sand (blue) are evident along the northern edge of the image and toward the south-east corner of the image scene. Clusters of seagrass (green) areas predominantly fringe

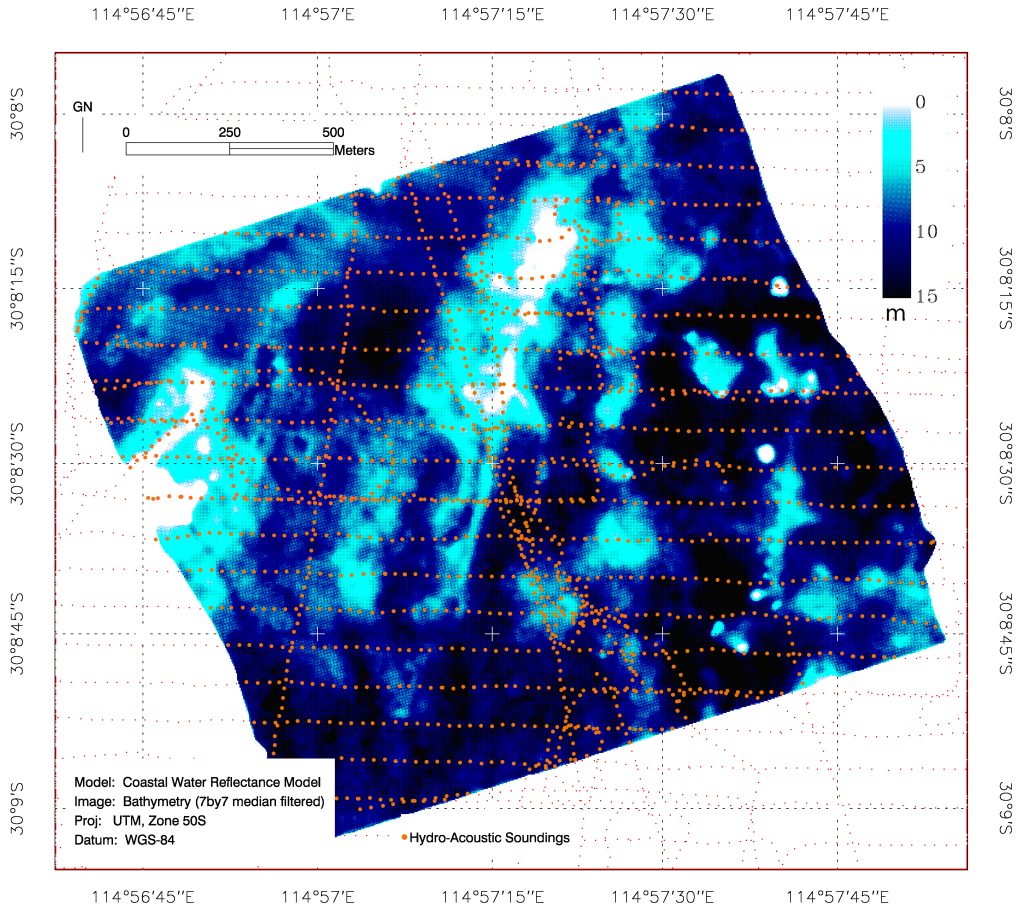

Figure 5.4: HyMap-derived bathymetry with hydro-acoustic survey points overlaid (orange points) for Jurien Bay Marine Park.

the sandy areas whilst the algae covered (red) areas are banded together across the majority of the middle of the scene. These three broad habitat categories correlate with the bathymetry image shown earlier in Fig. 5.4. The relative locations of the three classes are realistic in terms of distribution with depth and bottom topography. The bathymetry image, combined with observation of the true colour image, suggests the presence of reef running diagonally across the scene from the south west corner to the north east corner. One would not expect seagrass to be present on the reef, however the presence of algae is expected. Similarly, the presence of seagrass adjacent to and presumably covering some of the sandy areas also is to be expected. Dark image pixels correspond to lower retrieved values of the three key bottom weighting coefficients used to derive the mixtures of benthic cover. Dark green and dark red areas represent regions

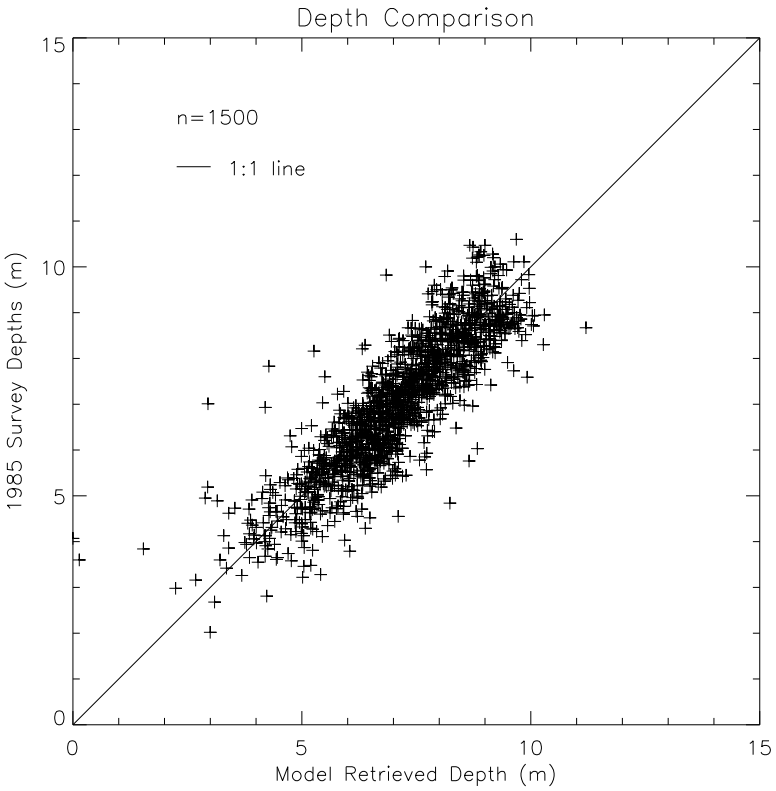

Figure 5.5: Scatter plot of acoustic survey bathymetry versus HyMap-derived bathymetry for Jurien Bay Marine Park.

of substrate where the albedo is low, and possibly represent different types of substrates within the general classes of sediment, seagrass and brown algae. In the following section, we differentiate between the light and dark shades of red and green and show how they correspond to different substrate classes as derived from towed video footage. The black areas inside the imaged scene (shown as white in Fig. 5.4) are small islands or exposed reef and are masked out. Mixtures of benthic cover with high reflectance values at 550 nm are also present, and are represented by yellow pixels (for example, near Fisherman's Island, top left corner in Fig. 5.6).

Table 5.2 summarises the HyMap classification and the video classification at the 25 validation sites. The HyMap data have been grouped into 5 broad classes (the 5 tabulated colours). The video-based classification corresponding to these locations are listed in the right hand column of Fig. 5.2. The summary

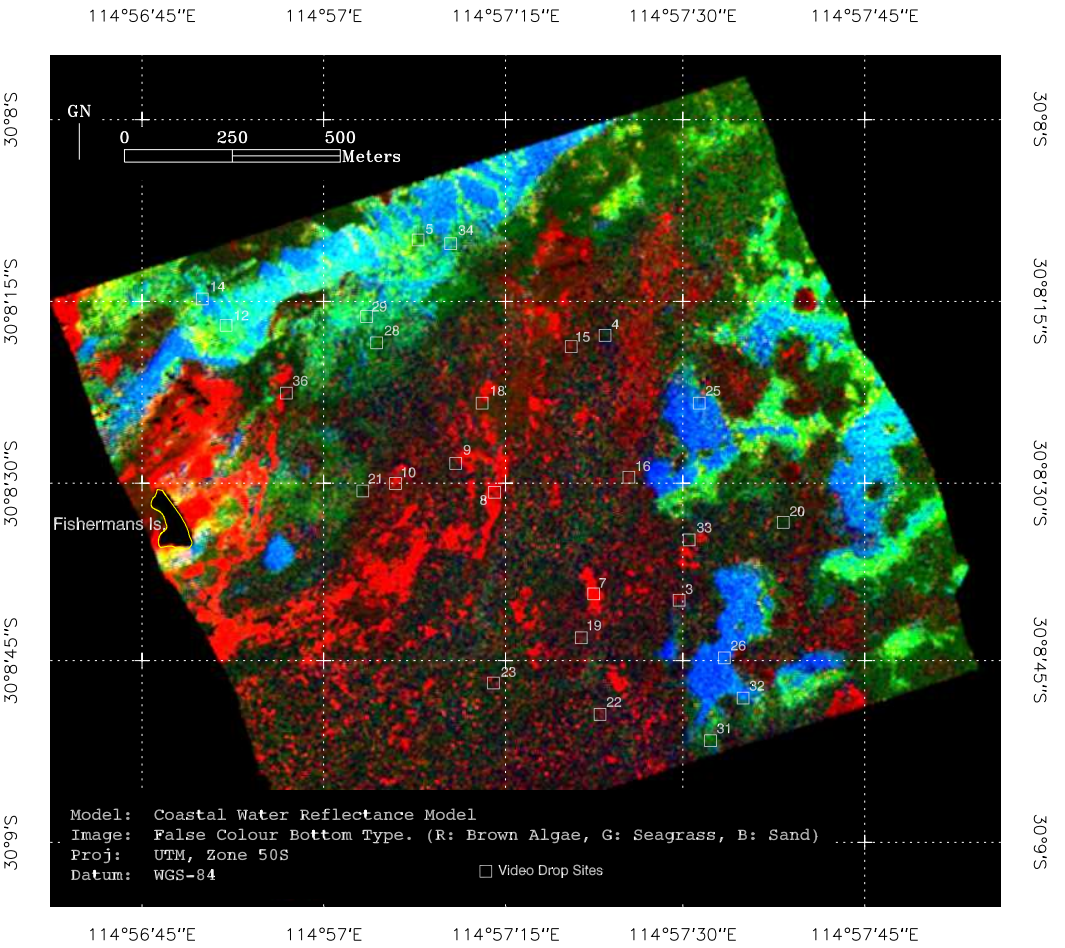

Figure 5.6: HyMap-derived 3 class substrate map for Jurien Bay Marine Park. Red = brown algae, green = seagrass and blue = sediment. White squares show the locations of towed video data collection.

illustrates that blue pixels correspond to sandy bottom environments, green pixels are associated with mainly seagrass with some stations also containing a small proportion of sand. Red pixels are associated with dense cover of the brown algae, *Ecklonia.sp* and *Sargassum.sp*. Dark green pixels are associated with mixtures of sparse brown algae and bare reef (rock). Dark red pixels are associated with mixtures of brown algae, sand and epiphytes. Although robust validation of the classification image with underwater video footage is problematic, mainly due to the difference in spatial coverage between image pixels (3.5 m) and video FOV (10 cm -1 m), the qualitative comparison indicated here, demonstrates close agreement between the HyMap derived benthic cover types and the video data.

Table 5.2: A tabulated comparison of image (classification) pixel colour with the benthic cover identified in video footage over selected ground-truthing sites at Jurien Bay Marine Park.

Station #	Pixel Colour	Bottom cover identified in video footage
14	Blue	Sand
32	Blue	Mostly sand/patchy *Halophila.sp*
26	Blue	Sand
25	Blue	Sand
12	Blue	Sand/patchy *Halophila.sp*
34	Blue	Sand/patchy *Halophila.sp*
29	Green	Sand/*Halophila.sp*
28	Green	Sand/*Halophila.sp*
5	Green	Dense seagrass/sand
31	Green	Sand/seagrass/lt. brown Epiphites
10	Red	*Sargassum.sp*
8	Red	*Ecklonia.sp*
3	Red	*Sargassum.sp*
7	Red	*Ecklonia.sp*
21	Dark green	*Sargassum.sp*/seagrass/ Epiphytes/sand
33	Dark green	Reef/*Sargassum.sp*
20	Dark green	Reef/*Sargassum.sp*
4	Dark green	Reef/*Sargassum.sp*
36	Dark red	*Ecklonia.sp*/seagrass/*Sargassum.sp*
9	Dark red	*Sargassum.sp*/sand/*Ecklonia.sp*/Epiphytes
19	Dark red	*Sargassum.sp*/sand*Ecklonia.sp*/Epiphytes
23	Dark red	*Sargassum.sp*/Epiphytes
22	Dark red	*Sargassum.sp*/sand/Epiphytes
16	Dark red	*Sargassum.sp*
15	Dark red	*Sargassum.sp*/sand

5.2 Ningaloo Marine Park Study

The Ningaloo Marine Park, situated in the northwest of Western Australia, is Australia's largest and most accessible fringing reef system. The shallow lagoons formed by the reef support a diverse array of habitats for a multitude of colourful corals and more than 500 species of fish, defining the region as a global biodiversity hotspot (Schönberg and Fromont, 2012). In 2006, a collaborative miltidisciniplary scientific research program "Ningaloo Collaboration Cluster" was set up to increase the knowledge of the reef system as a whole, which is important for the management and conservation of the Ningaloo Marine Park.

A part of the Ningaloo Collaboration Cluster focused on obtaining detailed information about the bathymetry of the Ningaloo reef and to identify benthic cover. This type of extensive information about the physical shape and biological resources are critical for the development of effective hydrodynamic and ecosystem models.

Detailed information about the ocean depth is vitally important for developing numerical models of current flow through the Ningaloo Reef system, providing an understanding of flow regimes, system flushing times, nutrient cycling, sediment transport and tidal forcing.

To better characterise the coral reef environment, accurate bathymetry with high-spatial resolution is required since coral reefs, by their very nature, are strongly influenced by the physical structure of the environment they inhabit (Stumpf and Holderied, 2004). Because of the relatively small horizontal spatial scales of corals that occupy reef outcrops, detailed knowledge of the bottom topography will improve characterisation of reef habitat for both corals and the species living within the reef system (Mumby et al., 1998). Currently, there is very little coverage of depth soundings within the extensive area of the Ningaloo Marine Park, whereby; the majority of soundings are spatially limited with a scale typically between tens to hundreds of meters.

Given the sheer extent of the reef system and the need for detailed bottom

topography, hyperspectral remote sensing was recognised as a viable option for the determination of high-spatial resolution bathymetry and benthic cover mapping within the Ningaloo Marine Park.

In late April 2006, an extensive hyperspectral aerial survey was conducted with the HyMap imaging system (HiVista Corp.), capturing detailed hyperspectral data across the entire Ningaloo Marine Park area. The imagery was processed to correct for atmospheric and air-water interface influences, in order to retrieve water quality, bathymetry and benthic cover using the physics-based model developed in Chapter 3. A field campaign was conducted during the same period, acquiring a variety of *in situ* measurements coincident with several overflights to support the retrieval of bathymetry and benthic cover from hyperspectral measurements as well as acquiring validation data to test the applicability of the model for such a complex and diverse ecosystem across the Ningaloo Marine Park.

5.2.1 Ningaloo Marine Park Region Description

The Ningaloo Reef, located 1,200 km north of Perth, Western Australia, is the largest fringing-barrier reef system in Australia and one of the longest fringing coral reefs in the world. Covering an area of 2,500 km^2, the Ningaloo Reef extends for 260 km along the west coast of the Cape Range Peninsula, ranging in width from 200 m to in excess of 6 km (Collins, 2011). Within the shallow, narrow lagoons, the water depth is typically 2-4 m, hosting a great diversity of corals and reef fish. Beyond the reef crest, the reef gently slopes off to a depth of 8-10 m with well-developed spur and groove structure. Outside the reef edge the bottom topography becomes progressively deeper up to the 100 m contour, which occurs approximately 5-6 km from the outer reef edge. Every few kilometres along shore, there are breaks along the reef where the water depth ranges from 6-8 m (Cassata and Collins, 2008).

5.2.2 Image Acquisition

The HyMap airborne hyperspectral imagery was collected between 22^{nd} of April 2006 and 1^{st} of May 2006. The survey comprised of 67 individual flight lines, each approximately 30 km in length, covering a total area of 3,400 km^2. Due to the large extent of the reef, the survey was partitioned into 11 individual blocks (Block A - K), with up to 2 blocks being captured per day. A map of the Ningaloo Marine Park region and the HyMap survey extent is shown in Fig. 5.7. The weather conditions during the survey period varied from almost perfect, with low winds and clear skys, to sub-optimal conditions with fresh winds and oceanic white caps visible. On days when the weather conditions were turning to sub-optimal, data collection was abandoned and the entire block was re-flown on a subsequent day. A summary of data acquisition times, area covered and conditions for each data block are given in Table 5.3.

The HyMap imagery was provided in terms of physical units of radiance ($\mu W cm^{-2} nm^{-1} sr^{-1}$). Each recorded raw flightline was corrected for dark current and electronic's offsets (collected during each flight) and converted to radiance using laboratory radiometric calibration information. The radiometric calibration of the HyMap sensor was performed prior to the survey on the 1^{st} of April 2006.

The HyMap ephemeris and attitude data were separately recorded using a high quality inertial monitoring unit, consisting of a Boeing CMIGITS II GPS/INS system and integrated differential GPS. The sensor pointing information was used to achieve accurate geocorrection of the flightline imagery.

The average survey altitude was between 1400 m and 1500 m above sea level, achieving a nominal ground spatial resolution of 3.5 m and swath of 1.8 km. Due to variability in aircraft ground speed and altitude during data acquisition, the actual pixel size at sea level may not be perfectly 3.5 m. However, all processed georeferrenced files were resampled to 3.5 m pixel size and spacing.

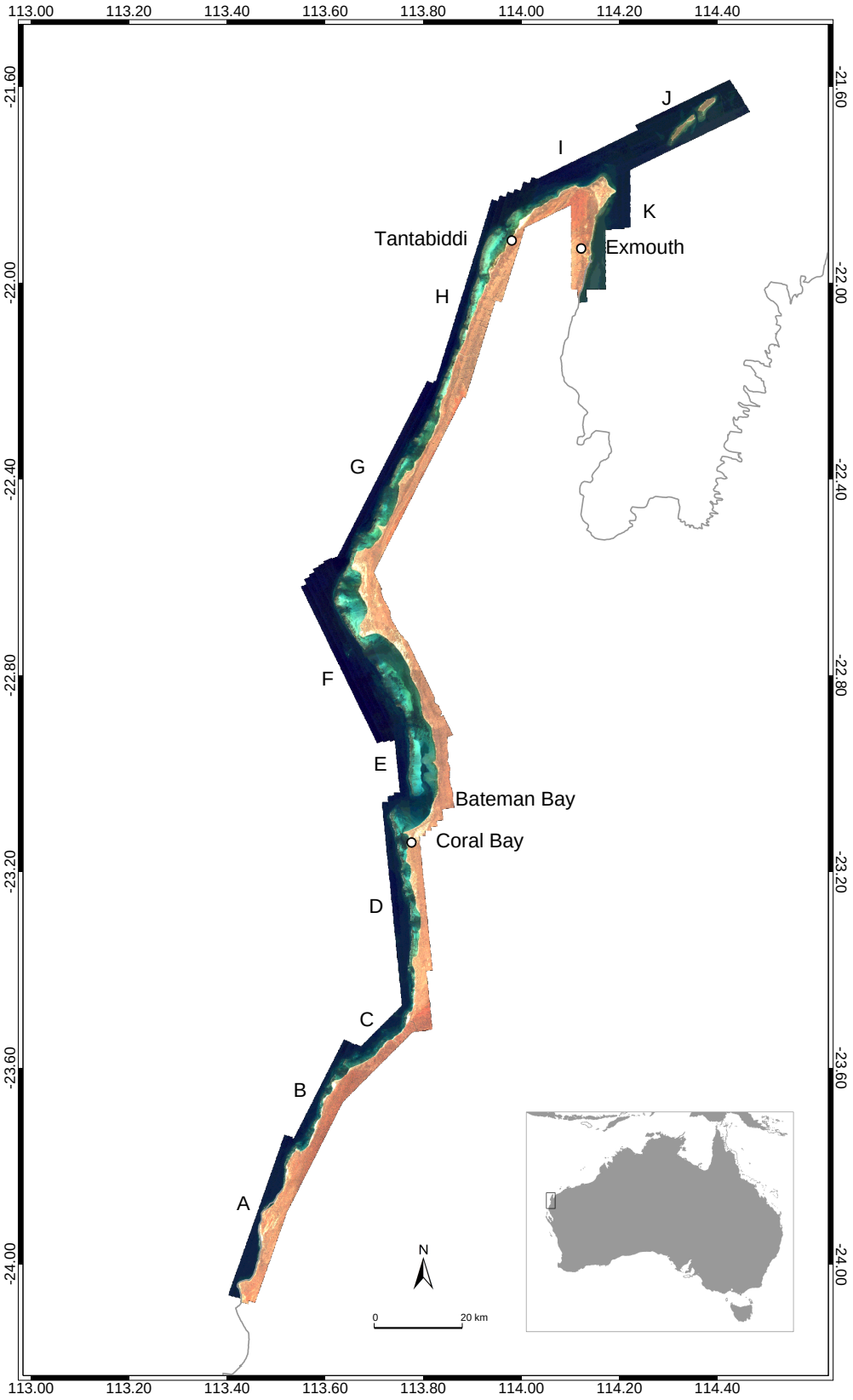

Figure 5.7: Map of Ningaloo Marine Park and the HyMap survey extent (Blocks A -K).

Table 5.3: Summary of HyMap data acquisition and conditions.

Block	Date (2006)	Times (start - end)	Area (km^2)	Pilot notes
A	Mon 1^{st} May	10:30 - 12:15	230	Good conditions, clear skies, light winds 10-15 knots.
B	Mon 1^{st} May	10:15 - 12:30	220	Good conditions, clear skies, light winds 10-15 knots.
C	Fri 28^{th} Apr	10:15 - 11:15	140	Almost perfect conditions. 2m swell. Sediment stirred in Reef channels.
D	Fri 28^{th} Apr	11:45 - 13:15	350	Almost perfect conditions. 2m swell. Sediment stirred in Reef channels.
E	Mon 1^{st} May	11:45 - 13:15	260	Good conditions, clear skies, light winds 10-15 knots.
F	Fri 28^{th} Apr	12:00 - 15:00	650	Almost perfect conditions. 2m swell. Sediment stirred in Reef channels.
G	Tue 25^{th} Apr	10:15 - 12:30	420	Strong winds 15-20 knots. White caps visible.
H	Mon 24^{th} Apr	10:45 - 12:20	410	Calm winds (10 knots), clear skies.
I	Sat 22^{nd} Apr	09:30 - 10:40	210	High winds 13/18 knots, 5% cirrus in the sky.
J	Sun 30^{th} Apr	09:30 - 10:40	240	Good conditions. Moderate swell.
K	Sat 22^{nd} Apr	11:30 - 13:15	270	High winds 13/18 knots, 5% cirrus in the sky.

5.2.3 Field Data

During the period 19-29 April 2006, a validation field campaign was conducted, acquiring a suite of physical and optical measurements coincident with several overflights of the hyperspectral aerial survey. A 6 m vessel was chartered to perform the field measurements, providing a suitable platform for instrument deployment. Boat ramps capable of launching the vessel were located at Coral Bay, Exmouth and Tantabiddi (see Fig. 5.7). These three areas were targeted for repeated sampling. Coral Bay was sampled on 20/4, 21/4, 25/4 and 28/4, Exmouth was sampled on 22/4 and Tantabiddi was sampled on 23/4 and 24/4.

The field measurements consisted of the underway above-water radiometric

observations, echo sounder depths, GPS locations and underwater video recordings, which were taken along transects within the shallow lagoons inside the Ningaloo Reef. Intermittent stops were made along the way, obtaining in-water profiles of optical backscatter with a HOBI Labs HydroScat-6. Discrete water samples were taken at station sites and filtered the same day for further laboratory analysis. The water samples were analysed for Chl-a and suspended sediment concentration, and phytoplankton and CDOM spectral absorption. The time and location of the discrete station measurements are provided in Table 5.4.

Table 5.4: Time and location of station measurements during the field experiment. *Area name abbreviations: CB: Coral Bay, EX: Exmouth, TB: Tantabiddi, BB: Batemans Bay.

Station Name (Area Name*)	Date/Time (Local)	Longitude (E)	Latitude (S)	Depth (m)
NMP001 (CB)	20/04/2006 09:45	113°44.900′	23°07.400′	3.2
NMP002 (CB)	21/04/2006 10:45	113°46.758′	23°21.613′	2.0
NMP003 (CB)	21/04/2006 13:14	113°47.236′	23°19.373′	3.1
NMP004 (CB)	21/04/2006 13:36	113°47.108′	23°17.953′	4.7
NMP005 (CB)	21/04/2006 14:07	113°46.890′	23°16.574′	2.2
NMP006 (CB)	21/04/2006 14:44	113°46.324′	23°14.015′	3.1
NMP007 (CB)	21/04/2006 15:00	113°45.009′	23°13.100′	3.8
NMP008 (EX)	22/04/2006 12:17	114°08.762′	21°56.050′	6.4
NMP009 (EX)	22/04/2006 13:28	114°09.581′	21°55.036′	11.6
NMP010 (EX)	22/04/2006 14:05	114°11.058′	21°53.470′	18.7
NMP011 (TB)	23/04/2006 10:00	113°58.486′	21°53.501′	5.0
NMP012 (TB)	23/04/2006 11:31	114°56.358′	21°57.270′	2.5
NMP013 (TB)	24/04/2006 10:10	113°55.724′	21°57.416′	1.6
NMP014 (TB)	24/04/2006 11:13	113°55.781′	21°59.821′	2.5
NMP015 (TB)	24/04/2006 12:10	113°54.546′	22°00.985′	1.7
NMP016 (BB)	25/04/2006 11:00	113°47.917′	22°57.669′	11.2
NMP017 (BB)	25/04/2006 12:48	113°44.211′	23°00.384′	2.8
NMP018 (CB)	28/04/2006 12:15	113°45.697′	23°11.141′	2.1
NMP019 (CB)	28/04/2006 12:38	113°45.743′	23°12.288′	9.3
NMP020 (CB)	28/04/2006 13:24	113°45.837′	23°13.781′	2.1

On days when no overflights were scheduled, bottom samples of a variety of substrate types were collected and their spectra acquired with a hand-held hyperspectral radiometer (Klonowski et al. 2003).

5.2.4 Underway Above-water Radiometry

Underway above-water radiometric observations were acquired with the Dynamic Above-water radiance (L) and irradiance (E) Collector (DALEC). The DALEC instrument is a hyperspectral radiometer designed for the automated and continuous collection of above-water reflectance during a vessel's transit. The DALEC incorporates three optical channels and an integrated GPS, which provides time and positional information associated with each spectral measurement. Figure 5.8 shows the DALEC instrument that was deployed for the fieldwork.

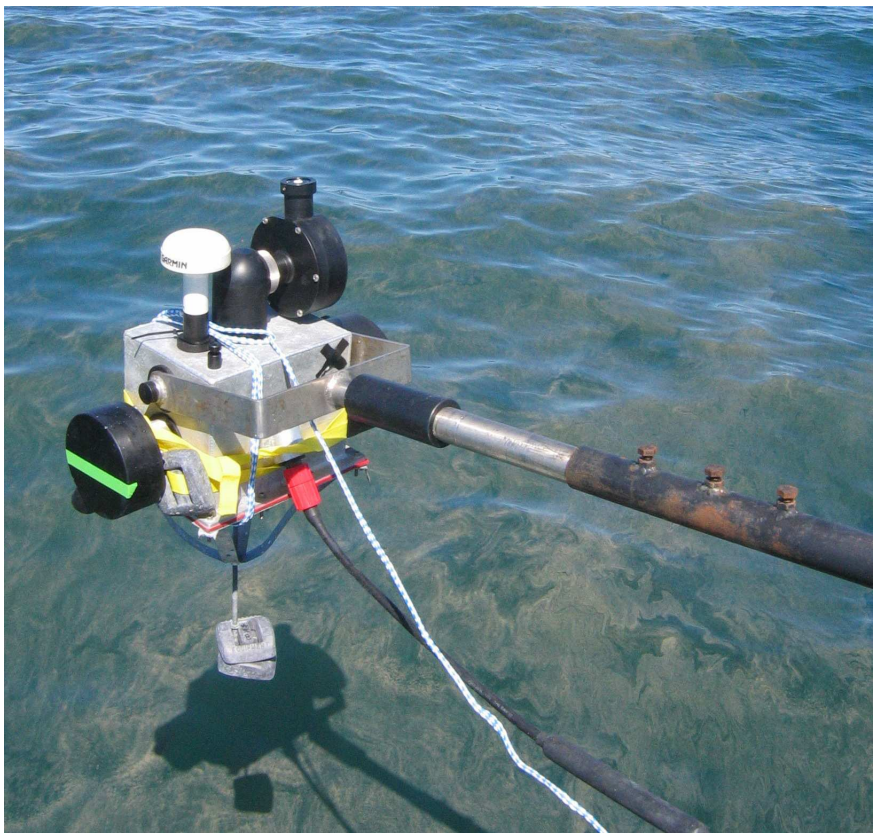

Figure 5.8: A photo of the DALEC instrument used during the fieldwork. Here, the DALEC is viewing a *Trichodesmium* bloom in Exmouth Gulf, seen as a brown slick on the water surface.

One of the optical channels incorporates a cosine diffuser and is orientated to point directly upward to permit measurements of the downwelling irradiance, E_d, incident on the ocean floor. The other 2 optical channels measure radiance within a narrow FOV of 10°. One of the radiance channels was orientated to

point downward at 40° degrees off nadir to measure the upwelling ocean reflected radiance, L_u. The remaining channel was orientated to point upward at an angle of 40° from zenith, measuring a small portion of the sky, L_{sky}. Each optical channel records a spectrum of light from 350 nm - 1150 nm into 256 spectral bins of 3.3 nm spacing. The three spectral quantities can be used to calculate the above-water remote sensing reflectance, as in Eq. 2.18.

The DALEC was mounted on the end a 2 m boom pole that incorporated a pivot mechanism, which was secured to the bow railings of the research vessel. The boom extension allowed for the DALEC to sample ocean water that was mostly undisturbed by the boat's wake, whilst also minimising boat shadow. The pivot system enabled the boom pole and DALEC to be rotated about its azimuth to provide an optimal sensor viewing geometry of 40° off-nadir and 135° from the solar plane (Mobley, 1999) over the course of varying transect headings.

The DALEC was deployed during daylight hours over the course of the field trip, capturing a total of 5 transects over 5 fine weather days. The sampling rate of the DALEC varied due to changes in spectrometer integration time settings that were automatically adjusted to achieve optimal signal under variable illumination conditions. Typically, however, the sampling rate ranged from 1 - 5 samples per second.

Each spectral measurement relating to $L_u(\lambda)$, $L_{sky}(\lambda)$ and $E_d(\lambda)$, was converted to radiometric quantities by correcting for dark current offsets and applying laboratory radiometric calibration coefficients. The DALEC was radiometrically calibrated prior to the field campaign on the 25^{th} of January 2006. The irradiance and radiance calibrations were performed using a 1000 W Quarts Tungsten Halogen FEL-type irradiance lamp standard with a known irradiance scale that is traceable to the National Institute of Standards and Technology (NIST). The calibration coefficients for irradiance and radiance were determined following the method outlined in the Ocean Optics Protocols (Mueller and Fargion, 2003).

The above-water remote sensing reflectance spectra for the 5 DALEC tran-

sects were calculated using Eq. 2.18. The Fresnel reflectance factor, ρ_R, used for correcting skyglint, was taken from a pre-determined LUT of ρ_R coefficients calculated for a variety of different solar-sensor geometries and wind speeds (used to generate sea surface roughness). The LUT was generated using Hydrolight following the approach described in Mobley (1999). The corrected DALEC reflectance data were subsequently used to vicariously calibrate the HyMap imagery.

5.2.5 Water Sample Analysis

Near-surface water samples were collected at 11 of the 20 measurement stations. These samples were subsequently filtered for phytoplankton absorption on 35 mm GF/F filters, pigment extraction on 47 mm GF/F filters and CDOM absorption on 0.2 micron filters. The filtered water samples were analysed by Lesley Clementson at CSIRO Marine and Atmospheric Research, Hobart. Phytoplankton associated pigments were extracted using High-Performance Liquid Chromatography (HPLC). The concentrations of the dominant pigments are displayed in Fig. 5.9. Generally, the total pigment concentrations were low, with the majority of concentrations between 0.5 mgm^{-3} and 1.0 mgm^{-3}. Greater concentrations, up to 2.3 mgm^{-3} were measured in the deeper open channel of Bateman Bay and in the Exmouth Gulf. A bloom of cyanophytes (Trichodesmium) was encountered in Exmouth Gulf. The magnitude of the total pigment concentration at NMP009 (Exmouth) was much greater than all other sites (over 10 mgm^{-3}).

The presence and abundance of certain pigments can be used to determine the species present in the water column. Figure 5.10 displays the relative abundance of pigments at each site. Generally, the relative pigment composition of the Phytoplankton sampled in the Ningaloo Marine Park were consistent. A significant difference in pigment structure was seen at stations NMP009 (a,b,c) due to the Trichodesmium bloom.

Absorption by pigments was measured following the SIMBIOS protocols (Mueller et al., 2003) using the method of Kishino et al. (1985). HPLC results indicate that

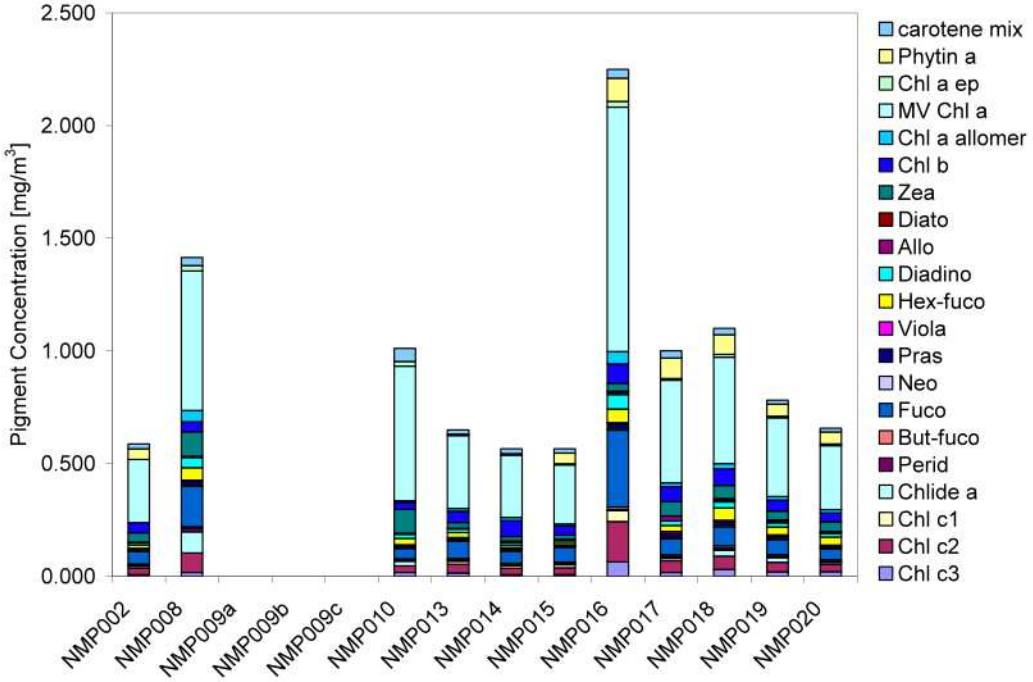

Figure 5.9: HPLC pigment results. Note that results from NMP009 have been omitted.

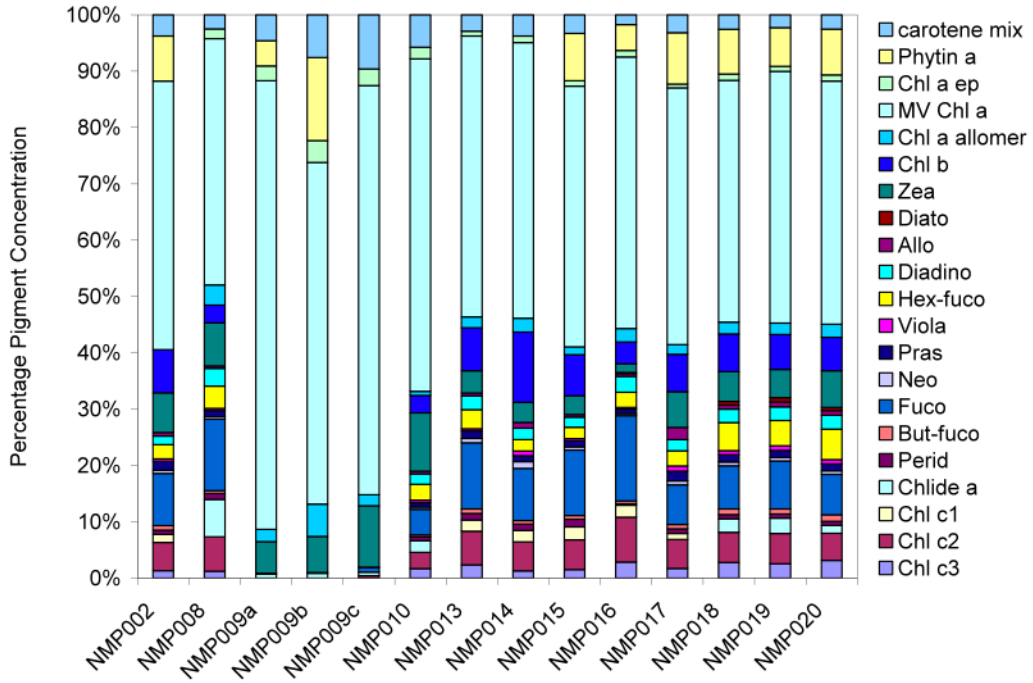

Figure 5.10: Relative abundance of pigments. Note the different distribution of pigments at sites NMP009 (a,b,c) compared with the rest.

a high concentration of cyanophytes were present at sites NMP009 and NMP010 (Exmouth Gulf). Cyanophytes contain pigments that are not extracted when measuring the spectral absorption of a sample. Therefore, the spectral absorption results at these sites were considered invalid.

A spatial representation of the magnitude of phytoplankton absorption at 440 nm is shown in Fig. 5.11. The magnitudes were typically low from 0.01 to 0.06 mgm^{-3}. The spectral form of the measured phytoplankton absorption were consistent with each other as seen in Fig. 5.12.

Figure 5.13 shows the spectral absorption due to CDOM for all stations. The calculated spectral slope , determined using Eq. 2.44, for most samples was 0.014, however, a few samples varied from this. The minimum spectral slope calculated was 0.012 and the maximum slope was 0.022. The spectral absorption due to non-algal particles is shown in Fig. 5.14. The absorption at 440 nm for most samples was relatively low and the spectral slopes were similar in nature with a value of 0.009.

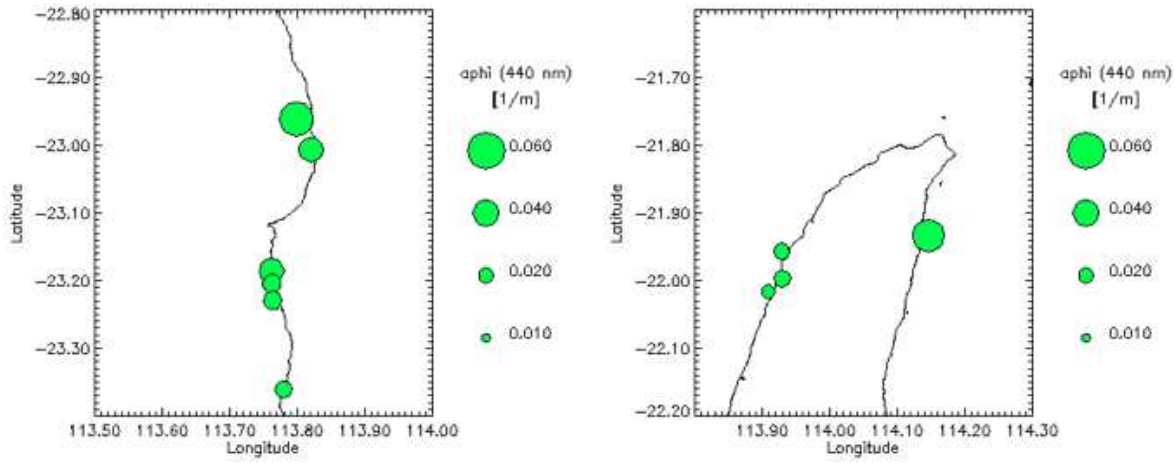

Figure 5.11: Absorption by phytoplankton at 440 nm for the Coral Bay area (left) and the Exmouth and Tantabiddi areas (right).

The low concentrations of Phytoplankton, CDOM and NAP measured in this study are consistent with findings in other clear water coral reef areas. For example, in the Great Barrier Reef (Australia), Blondeau-Patissier et al. (2009) reported phytoplankton absorption at 440 nm with range of 0.008-0.027 m^{-1} in

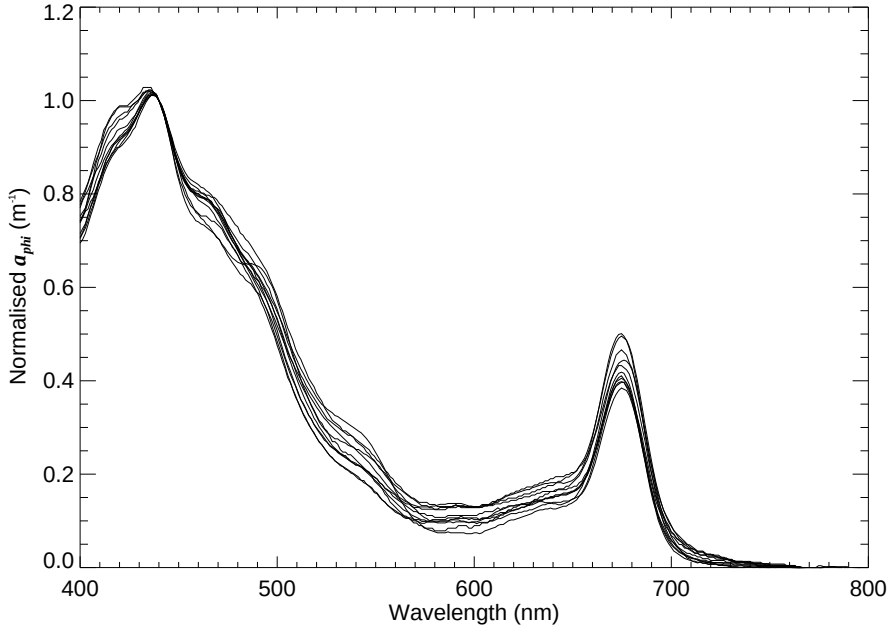

Figure 5.12: Normalised spectral absorption due to phytoplankton for stations sampled in the Ningaloo Marine Park.

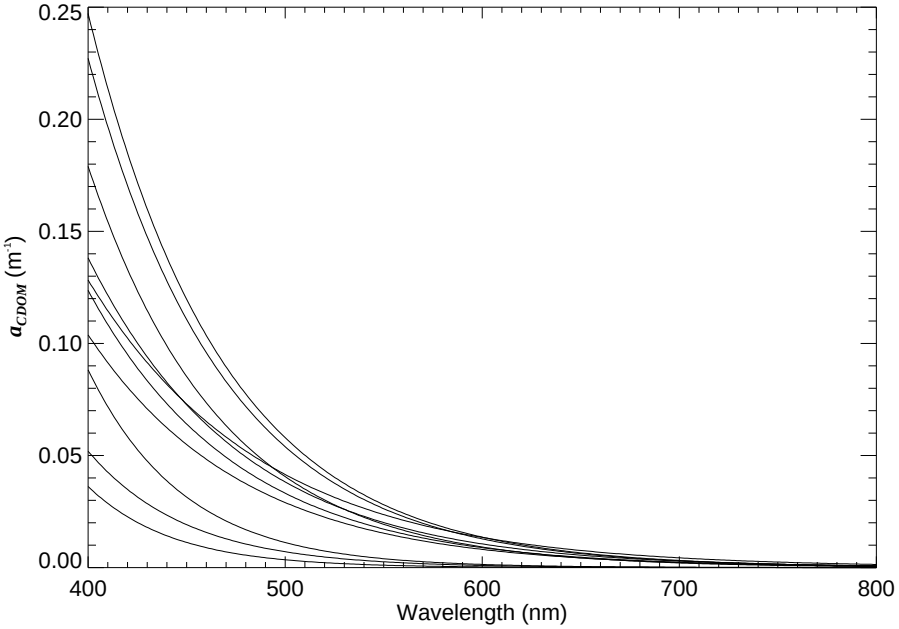

Figure 5.13: Spectral absorption due to CDOM for stations sampled in the Ningaloo Marine Park.

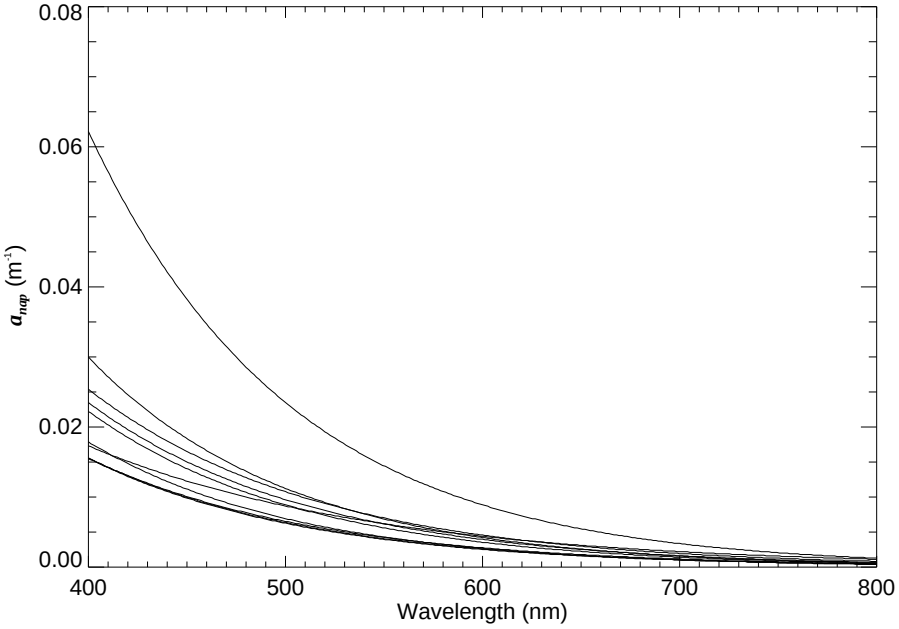

Figure 5.14: Spectral absorption due to non-algal particles for stations sampled in the Ningaloo Marine Park.

Reef Waters and CDOM absorption at 440 nm ranging from 0.014-0.083 m^{-1}.

5.2.6 Backscattering

In-water measurements of scattering at 140°, $\beta(140\lambda,^{\circ})$, at six wavelengths (442, 488, 550, 589, 676, and 850 nm) were obtained at 19 stations using a HOBI Labs HydroScat-6. At each site, the instrument profiled the water column to just above the sea bed. The instrument data was processed to engineering units (including dark corrections) using HOBI Labs HydroSoft version 2.70.

Estimates of particle backscattering, $b_{bp}(\lambda)$, were obtained from $\beta(\lambda, 140^{\circ})$ using the relation given in Maffione and Dana (1997),

$$b_{bp}((\lambda) = 2\pi\chi(\beta(\lambda, 140^{\circ}) - \beta_w(\lambda, 140^{\circ})), \tag{5.4}$$

where $\beta_w(\lambda, 140^{\circ})$ is the volume scattering function for water at a given temperature and salinity (Morel, 1974). χ is known to be dependent upon the volume scattering function of the observed water column. Here χ is given the value of

1.18 following Boss et al. (2004).

Figure 5.15 displays an example of profiles collected at Exmouth (NMP010), Tantabiddi (NMP011) and Coral Bay (NMP019). Examples of particulate backscattering measurements are shown in Fig. 5.15. Generally, the profiles of b_{bp} at shallow sites were approximately constant with depth. Only one site collected at Exmouth (NMP010) showed any significant vertical structure. Thus, it is appropriate to describe these properties by their depth-averaged value. Figure 5.5 displays the depth averaged b_{bp} at 550 nm for 19 stations. The averages for these stations at all HydroScat-6 wavelengths are listed in Table 5.5. The magnitude of b_{bp} at 550 nm (0.0032-0.0146 m^{-1}) encountered here would be considered low when compared to other coastal water areas (Aurin et al., 2010) (Blondeau-Patissier et al., 2009) (Snyder et al., 2008).

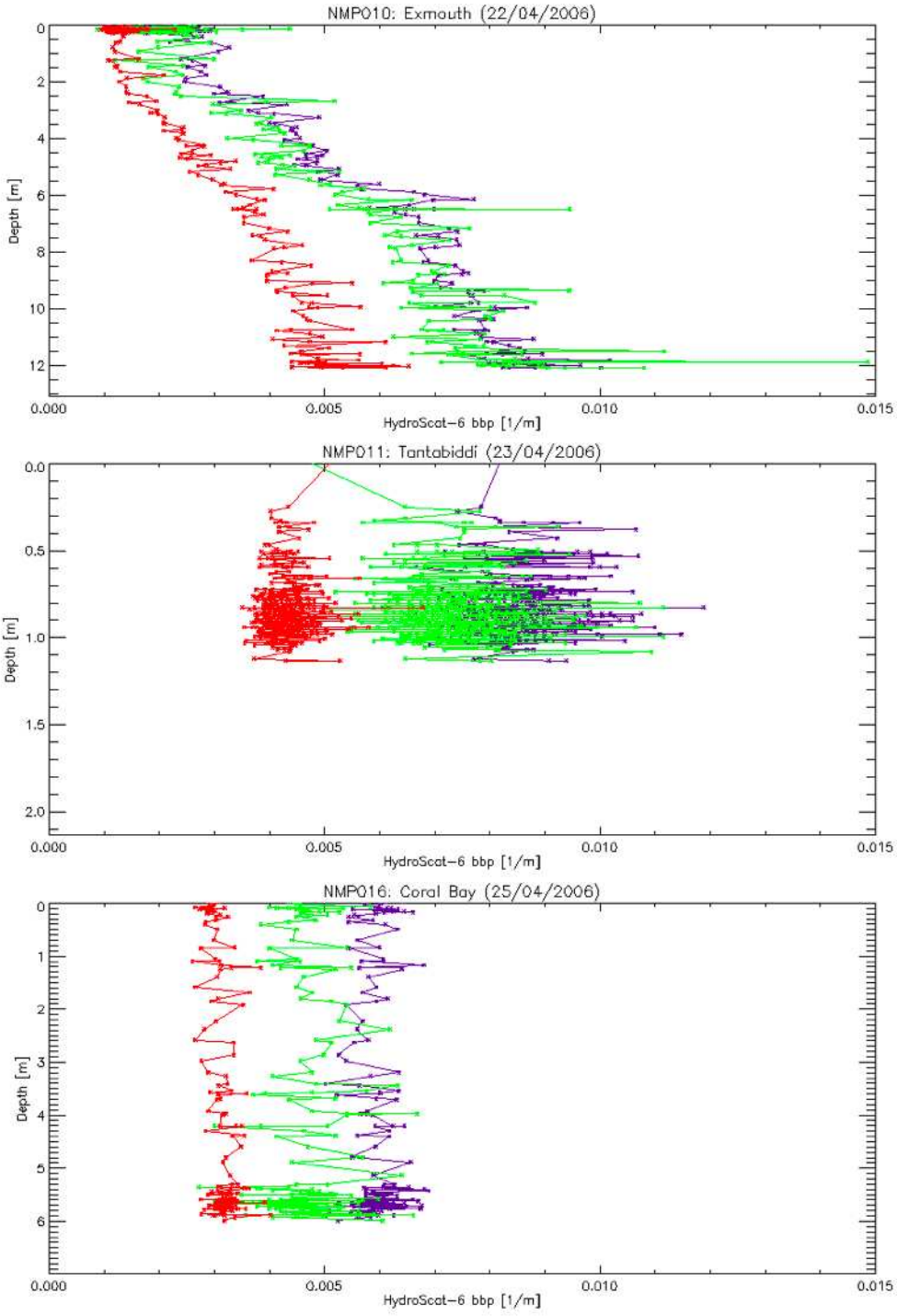

Figure 5.15: Profiles of particulate backscattering (b_{bp}) at 442, 550 and 850 nm (blue, green and red lines, respectively) at stations NMP010, 011 and 016.

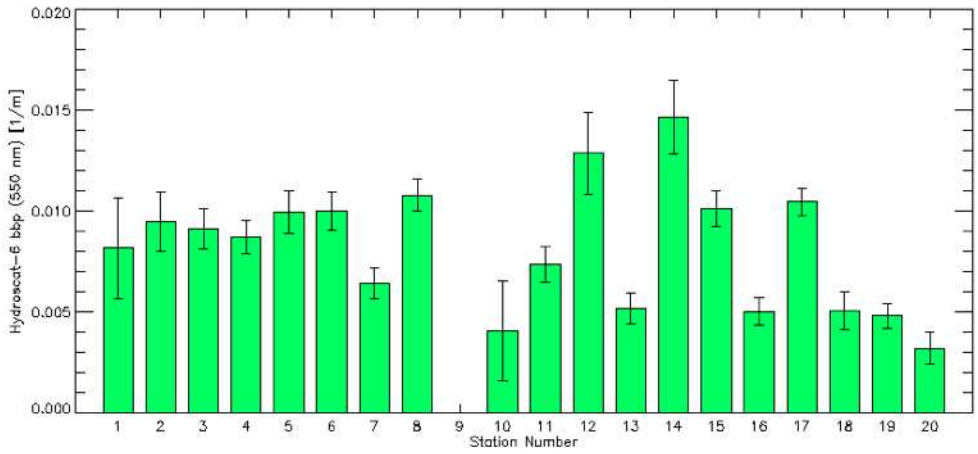

Figure 5.16: Particulate backscattering at 550 nm, $b_{bp}(550)$, at each of the NMP stations. Error bars indicate $\pm 1\sigma$.

Table 5.5: Average b_{bp} (m^{-1}) at each station where the HydroScat-6 was deployed.

(wavelength)	(442)	(488)	(550)	(589)	(676)	(850)
NMP001	0.0089	0.0092	0.0082	0.0082	0.0075	0.0054
NMP002	0.0100	0.0104	0.0095	0.0092	0.0084	0.0062
NMP003	0.0107	0.0104	0.0091	0.0084	0.0079	0.0054
NMP004	0.0100	0.0103	0.0087	0.0085	0.0077	0.0055
NMP005	0.0108	0.0108	0.0099	0.0094	0.0086	0.0062
NMP006	0.0116	0.0112	0.0100	0.0097	0.0090	0.0064
NMP007	0.0072	0.0072	0.0064	0.0061	0.0057	0.0041
NMP008	0.0113	0.0115	0.0108	0.0105	0.0095	0.0064
NMP009	-	-	-	-	-	-
NMP010	0.0045	0.0045	0.0041	0.0041	0.0038	0.0026
NMP011	0.0085	0.0084	0.0073	0.0070	0.0062	0.0043
NMP012	0.0153	0.0148	0.0129	0.0121	0.0111	0.0073
NMP013	0.0057	0.0058	0.0052	0.0051	0.0044	0.0028
NMP014	0.0164	0.0164	0.0146	0.0140	0.0123	0.0083
NMP015	0.0120	0.0121	0.0101	0.0099	0.0087	0.0059
NMP016	0.0058	0.0057	0.0050	0.0048	0.0045	0.0031
NMP017	0.0126	0.0121	0.0104	0.0097	0.0087	0.0057
NMP018	0.0057	0.0057	0.0051	0.0050	0.0046	0.0034
NMP019	0.0051	0.0052	0.0048	0.0047	0.0045	0.0033
NMP020	0.0038	0.0034	0.0032	0.0031	0.0029	0.0022

5.2.7 Underwater Video and Echo Sounder Data

An underwater video system (CSIRO MAR, Floreat) was deployed along segments of the cruise track. The video camera was tethered approximately 1 m above the sea floor at the vessel's stern. Information regarding time and location was obtained from a GPS positioned above video system. Echo sounder data was also recorded along with the positional information. The sounder transducer was positioned at the vessels stern, on the underside of the hull and located approximately 60 cm under the water surface. The echo sounder was calibrated against plumb line data for various depths up to 5 m. The echo sounder depths were corrected using the linear relationship,

$$Depth_C = 0.91 \times Depth_{Echo} - 0.64. \tag{5.5}$$

Figure 5.17(a) displays cruise tracks within the Coral Bay area. Figure 5.17(b) displays the broader area of interest, including Exmouth Gulf. Figure 5.18 displays the cruise tracks from the Exmouth and Tantabiddi areas. The video recordings and water depths were to be used in ground-truthing the bathymetry and benthic cover retrieved from the HyMap data sets.

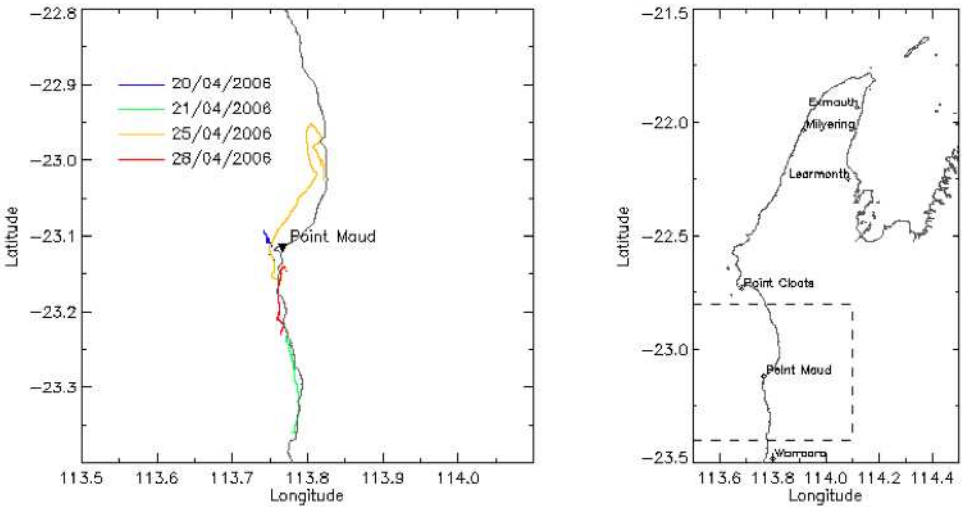

Figure 5.17: (a) Area of interest encompassing field activities in the Coral Bay area. Cruise tracks are overlaid with date of sampling denoted by colour. (b) Displays the broader area of interest.

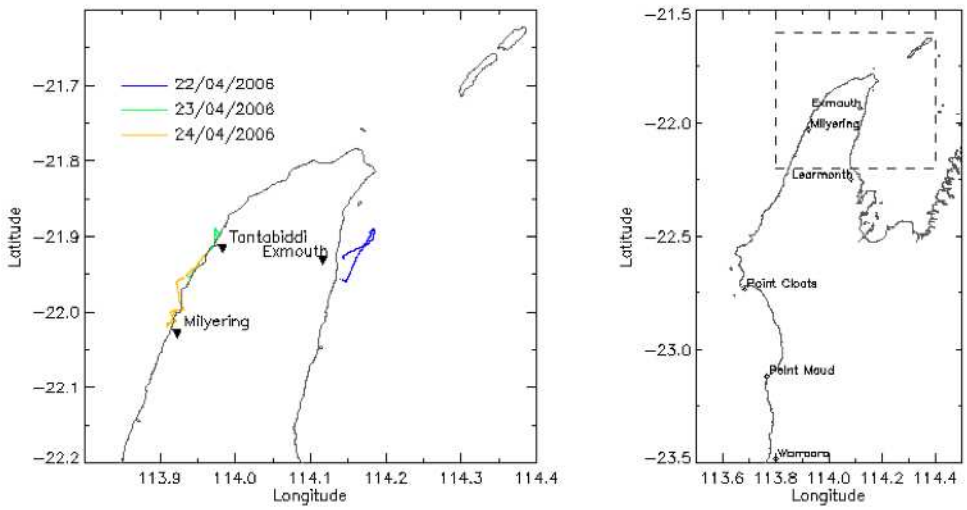

Figure 5.18: (a) Area of interest encompassing field activities in the Exmouth and Tantabiddi areas. Cruise tracks are overlaid with date of sampling denoted by colour. (b) The broader region of interest.

5.2.8 Substrate Reflectance

Substrates representative of each area were measured using Curtin's Zeiss. The Zeiss instrument is composed of two optical channels that measure above-water downwelling irradiance, E_d, total upwelling radiance, L_u. Measurements of E_d and L_u over a substrate were used to obtain the reflectance of the substrate, $\rho(\lambda)$.

In all, 17 substrate samples were collected during the field operations (see Table 5.6) and measurements were conducted out of the water following the method described in Section 5.1.2. Images of 16 of these substrates are presented in Fig. 5.20 (Note: Tantabiddi sand appeared similar to Coral Bay sand and therefore was not included in the collage). Figure 5.19 displays the reflectance spectra of all 17 bottom types.

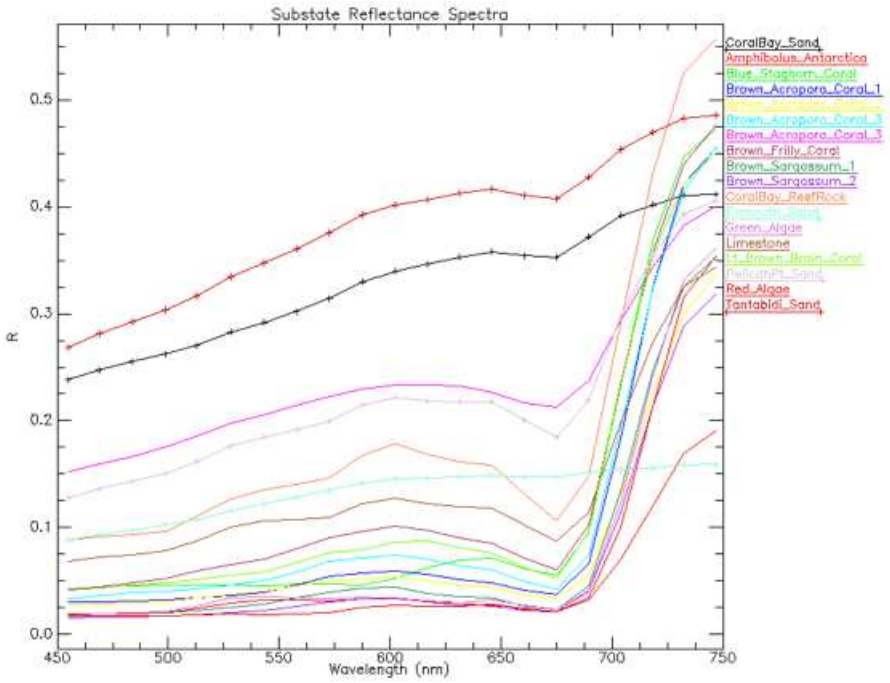

Figure 5.19: Reflectance spectra measured using the Zeiss instrument for each of the 17 bottom types collected during the field operations.

Table 5.6: Type and location of substrate measured with the Zeiss.

Sample Name	Date/Time (Local)	Longitude (E)	Latitude (S)
01 NMP001: Sand #001	20/04/2006 10:10	113° 44.926´	23° 7.464´
02 NMP001: Coral #001	20/04/2006 10:10	113° 44.926´	23° 7.464´
03 NMP001: Coral #002	20/04/2006 10:10	113° 44.926´	23° 7.464´
04 NMP001: Coral #003	20/04/2006 10:10	113° 44.926´	23° 7.464´
05 NMP002: Sand #002	21/04/2006 11:05	113° 46.758´	23° 21.613´
06 NMP002: Coral #004	21/04/2006 11:05	113° 46.758´	23° 21.613´
07 NMP002: Bleached Coral #005	21/04/2006 11:05	113° 46.758´	23° 21.613´
08 NMP002: Pavement	21/04/2006 11:05	113° 46.758´	23° 21.613´
09 NMP002: Sargassum #001	21/04/2006 11:05	113° 46.758´	23° 21.613´
10 NMP002: Sargassum #002	21/04/2006 11:05	113° 46.758´	23° 21.613´
11 NMP002: Red algae	21/04/2006 11:05	113° 46.758´	23° 21.613´
12 NMP002: Green algae	21/04/2006 11:05	113° 46.758´	23° 21.613´
13 NMP005: Sand #003	22/04/2006 12:22	114° 8.762´	21° 56.05´
14 NMP012: Sand #003	23/04/2006 11:50	114° 56.358´	21° 57.27´
15 NMP012: Coral #006	23/04/2006 11:50	114° 56.358´	21° 57.27´
16 NMP012: Coral #007	23/04/2006 11:50	114° 56.358´	21° 57.27´
17 NMP017: Amphibolis Antarctica	25/04/2006 12:48	113° 49.211’	23° 0.364´

Figure 5.20: Collage of 16 of the 17 substrates sampled during the experiment. Row 1 corresponds to samples 1-4, row 2: 5-8, row 3: 9-12, row 4: 13, 15-17 as listed in Table 5.6. Note that Tantabiddi sand is spectrally similar to Coral Bay sand and has been omitted from this figure.

5.3 Atmospheric Correction

Atmospheric correction of the HyMap data has been performed with TAFKAA (Montes et al., 2004) under an agreement with Naval Research Laboratory (NRL). TAFKAA utilises pre-determined tabulated atmospheric data calculated for a variety of solar-sensor geometries, altitudes and atmospheric conditions, with focus on coastal water environments. The atmospheric correction performed here aided the selection of the closest tabulated atmospheric data by using known meteorology. Prior to analysis of the HyMap data, a sensitivity analysis of the TAFKAA algorithm was performed to assess the response to variability in important environmental input parameters. The atmospheric correction for a sensor positioned at HyMap altitudes was found to be most sensitive to changes in the aerosol loading and total column water vapour. The correction was relatively insensitive to changes in the atmospheric temperature profile, the water vapour profile shape, ozone amount and the surface wind speed used in the model. TAFKAA has been executed to produce apparent reflectance (APREF) and remote-sensing reflectance (R_{rs}) for all water scenes in the dataset over the HyMap bands used in bathymetry and benthic cover retrieval (456 nm to 750 nm).

Remote sensing reflectance produced by TAFKAA did not compare well with *in situ* observations of reflectance collected during the field campaign. Comparison in the short wave blue bands was particularly poor. Surprisingly, while the apparent reflectance does not capture the column atmospheric physics it was shown to provide a better and more consistent atmospheric correction than either the TAFKAA R_{rs} or the HyVista-supplied atmospheric correction results. In this correction dataset, the *in situ* collected remote sensing reflectance was used as a benchmark estimate of the HyMap observed reflectance. Apparent reflectance was generated for each band (this has no correction for scattering or absorption) which was subsequently adjusted linearly to minimise the correlation between the HyMap apparent reflectance and the *in situ* remote sensing reflectance to yield the atmospherically corrected above-water remote sensing reflectance products.

Figure 5.21 shows the DALEC-measured R_{rs} at 547 nm along the transect conducted in the Tantibiddi area on the 24/04/2006. The HyMap apparent reflectance for the imagery collected on the same day (Block H) is also shown for comparison. The HyMap apparent reflectance for the wavelength channel of 547 nm follows the DALEC R_{rs} closely over the range of reflectances spanning from 0.02 to 0.1 sr^{-1}. However, there were subtle differences at different wavelengths. Figure 5.22 shows the comparison scatter diagrams between DALEC R_{rs} and HyMap apparent reflectance for 456, 547 and 635 nm wavelength channels. The linear regression line of best fit is also shown. The calculated linear regression slopes and y-intercepts for each HyMap wavelength that was used to convert the HyMap apparent reflectance product to the vicariously calibrated above-water remote sensing reflectance, measured using the DALEC, are shown in Figs. 5.23 and 5.24

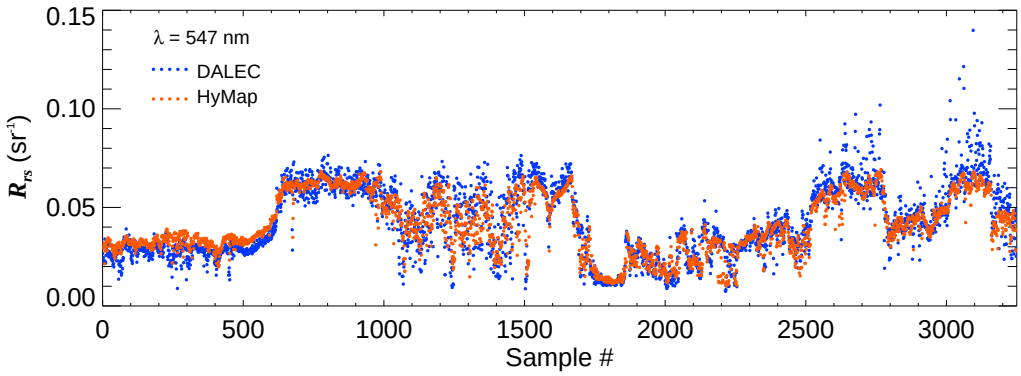

Figure 5.21: The remote sensing reflectance measured with the DALEC (blue data points) along the transect conducted on the 24^{th} April 2004 and the coincident HyMap apparent reflectance represented with orange data points.

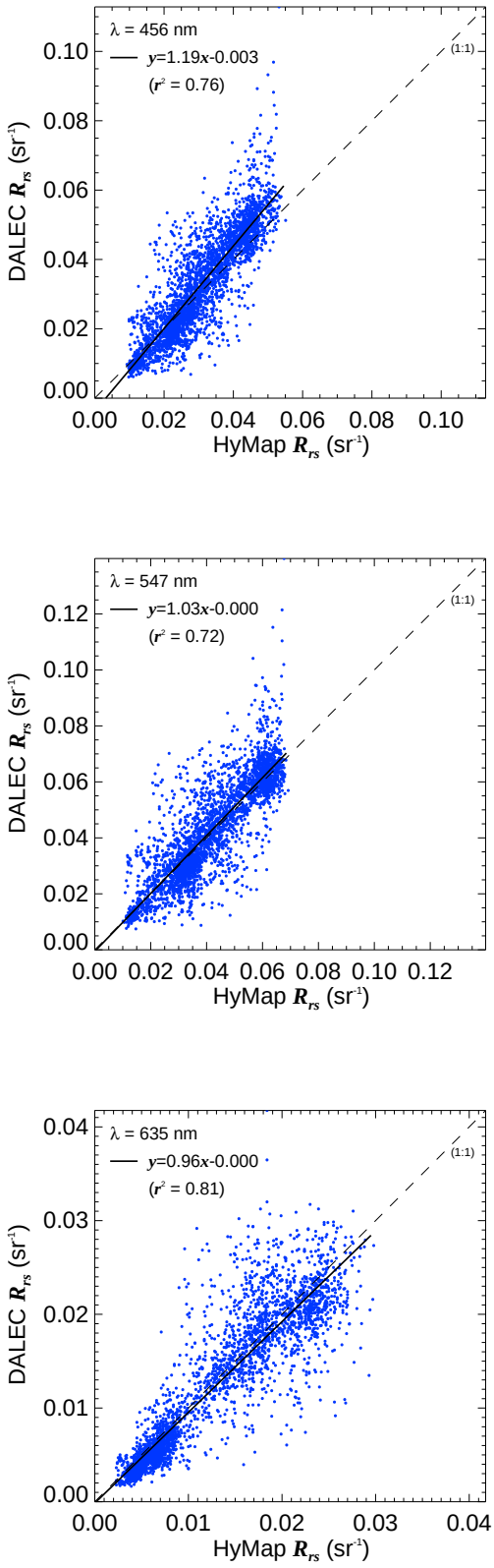

Figure 5.22: Comparison scatter diagrams between DALEC R_{rs} and HyMap apparent reflectance for blue (456 nm), green (547 nm) and red (635 nm) wavelength bands.

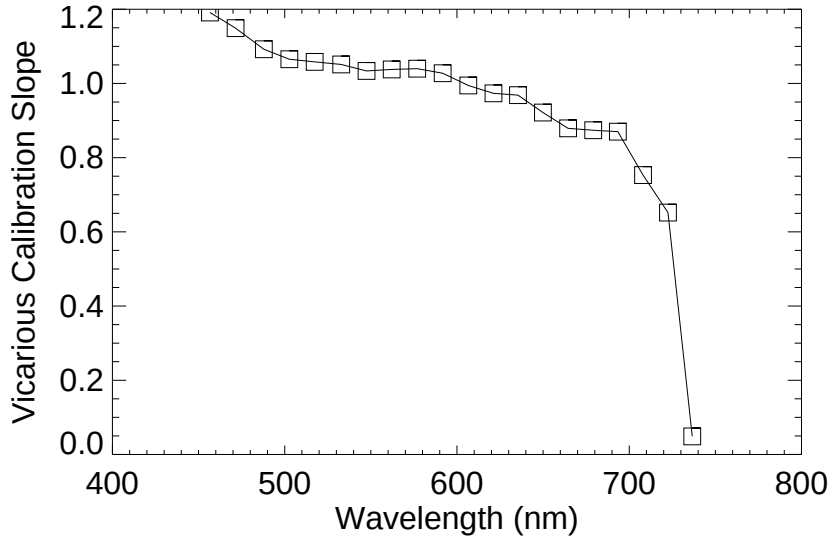

Figure 5.23: The linear regression slope coefficients as a function of wavelength used in the vicarious calibration of HyMap R_{rs}.

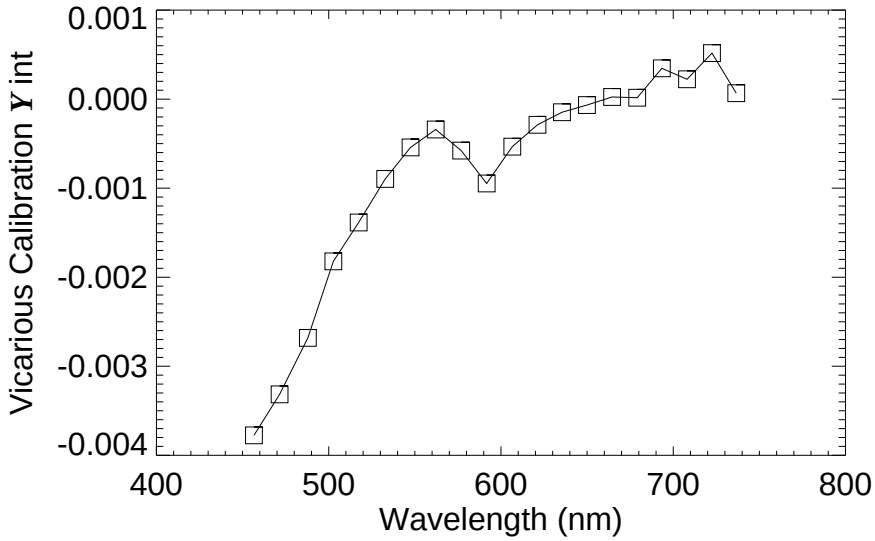

Figure 5.24: The linear regression y-intercept coefficients as a function of wavelength used in the vicarious calibration of HyMap R_{rs}.

5.4 HyMap Inversion

The shallow water model and numerical inversion scheme, developed in Chapter 3, was applied to the atmospherically corrected and vicariously calibrated HyMap data for the Ningaloo Marine Park survey. The model inputs relating to water column properties and substrate reflectance were based on region-specific spectral endmembers. The spectral absorption of phytoplankton was modelled using an average of *in situ* phytoplankton absorption spectra (normalised to 1 at 440 nm) that were sampled in the Ningaloo Marine Park. The spectral absorption of CDOM was modelled with Eq. 2.44 with a fixed spectral slope parameter, S, of 0.014, consistent with field observations. The spectral slope for particle backscattering, Y (see Eq. 5.4) was fixed at 0.85, taken from an average representative of *in situ* particle backscattering profiles.

The total bottom reflectance was parameterised by the linear combination of three reflectance spectral endmembers, representative of three key benthic cover classes; sediment, brown algae and coral. The spectral endmembers were taken from the substrate reflectance measurements collected in the Ningaloo Marine Park. The average representative reflectance within each class was used.

5.5 Results

A total of 67 HyMap image flight-lines were collected as part of the Ningaloo mapping survey, covering an area of approximately 3,500 km^2. A nominal ground resolution of 3.5 m was achieved for the imagery resulting in over 1 billion pixels to be processed. Due to the large volume of data, the hyperspectral imagery was processed at Western Australia's super computing facility, iVEC. Utilising iVEC's 192 central processing units the image data were tiled and processed simultaneously in just under 1 week of continuous computation. The retrieved-model parameters were stored as Band Interleaved by Line (BIL) format and included; $a_{phi}(440)$, $a_{CDOM}(440)$, $b_{bp}(550)$, the fractional components of sedi-

ment, brown algae and coral (f_{sd}, f_{ba}, f_{cor}) and corresponding scaling factors (S_{sg}, S_{ba}, S_{cor}), water depth and the ratio of the bottom reflectance to total reflectance (ω_{max}). The image-derived water depth and benthic cover weighting coefficients were used to generate mapped bathymetry and benthic habitat classification products. Bathymetry and benthic cover products for each flight line were geo-located using HyVista supplied GLT data, creating mapped outputs. A tide model developed for the Ningaloo Marine Park (Feng, 2011) was used to correct the image-derived water depths to a mean-sea-level datum. A scaled down version of the entire bathymetry mosaic is shown in Fig. 5.25. Figure 5.26 displays a focused section of the bathymetry map showing the high-resolution detail that has been captured.

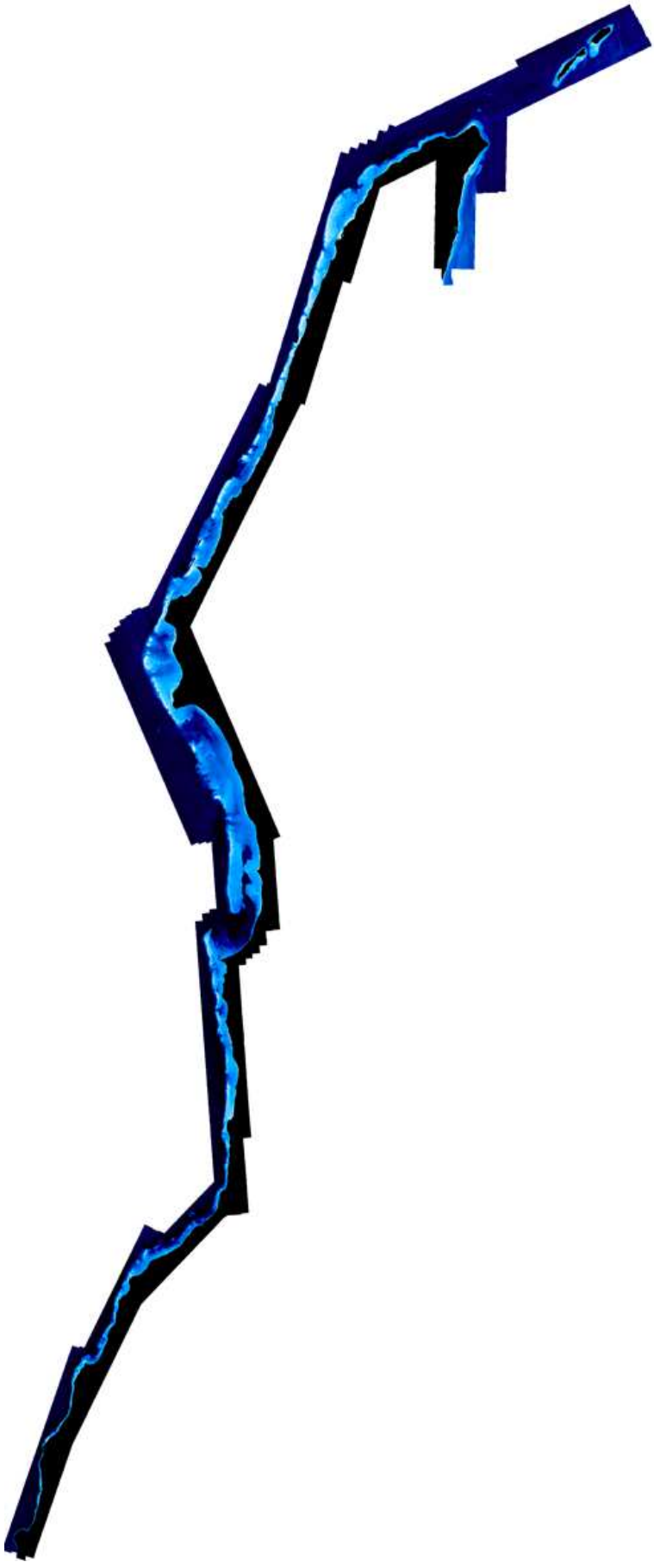

Figure 5.25: Hyperspectral image-derived bathymetry mosaic of the Ningaloo Marine Park. Depths range from 0 m (white/light blue) to 30 m (dark blue). Land mask is shown as black.

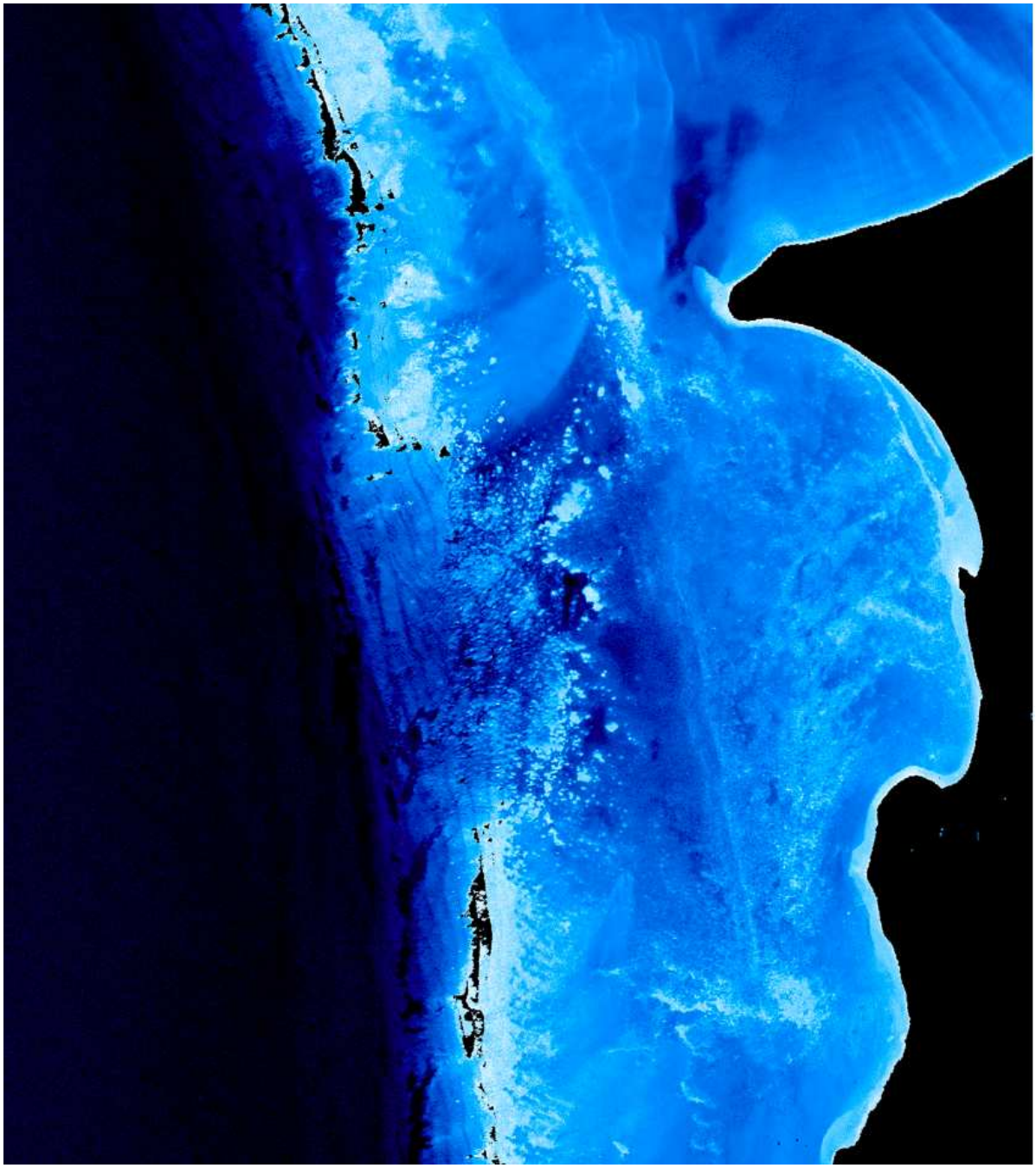

Figure 5.26: Full resolution hyperspectral image-derived bathymetry map of Coral Bay. Depths range from 0 m (white/light blue) to 30 m (dark blue). Land mask is shown as black.

5.5.1 IOP validation

The HyMap-retrieved water column properties were validated against available *in situ* measurements. Only station data with coincident HyMap overflights were used, and therefore correspond to station data collected on the 22^{nd}, 24^{th} and 28^{th} of April 2006. For each station, a 9 x 9 pixel area surrounding the site location was extracted, from which the mean and standard deviation of the model retrieved-parameters ($a_{phi}(440)$, $a_{CDOM}(440)$, $b_{bp}(550)$) were calculated.

Figures 5.27 (a) to (c) present the *in situ*-measured and HyMap-estimated $a_{phi}(440)$, $a_{CDOM}(440)$ and $b_{bp}(550)$ magnitudes for 8 coincident station sites. Considering the small number of station sites available for comparison and that the range of IOP magnitudes were very low, the HyMap-estimated values agree well with the *in situ* measurements for the 3 model parameters. On average, the closest agreement occurred for $a_{phi}(440)$ with a mean difference of 31.7% and a mean absolute difference of 0.009 m^{-1}. The next best agreement was for $a_{CDOM}(440)$ with a mean difference of 53.3% and a mean absolute difference of 0.025 m^{-1}. The HyMap-estimated $a_{phi}(440)$ and $a_{CDOM}(440)$ correlate well with the *in situ* measurements with correlation coefficients, r^2, of 0.72 and 0.63, respectively. The poorest accuracy in retrieval was for $b_{bp}(550)$. The mean difference was 133% and an absolute difference of 0.007 m^{-1} (r^2=0.03). The high percentage difference is due to one outlier at station NMP013 (Tantabiddi), where the retrieved $b_{bp}(550)$ was significantly overestimated by 0.025 m^{-1}. The reason for this large difference is unknown, however, the station site was very shallow at 1.6 m and given the very clear water column encountered, the model may retrieve erroneous magnitudes without affecting the overall remote sensing reflectance in such shallow, clear water situations. Another possibility could be due to sample time differences. For this station the HyMap overflight was conducted approximately 1 hour after the water sample was taken. Although, no large differences were evident in a_{phi} and a_{CDOM} comparisons, the possibility of sediment being resuspended after the station visit may provide an explanation for this difference,

especially given the very shallow depth. Omitting this station site, the mean difference for $b_{bp}(550)$ reduces to $\sim 50\%$, equivalent to a mean absolute difference of 0.004 m^{-1}.

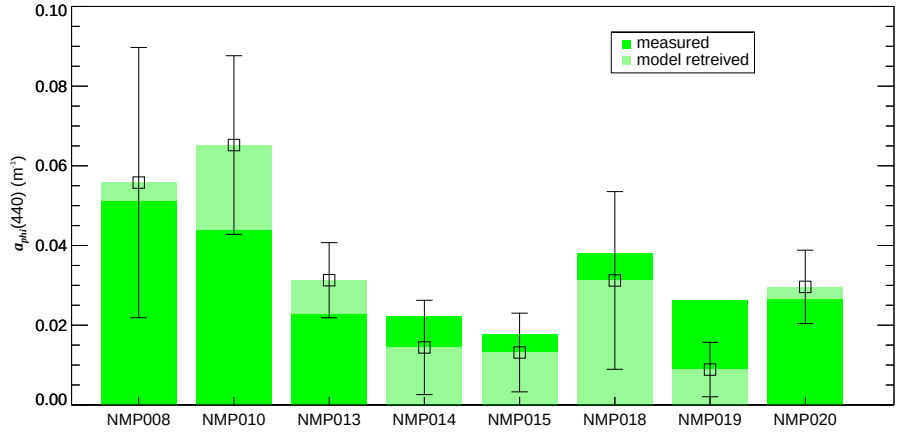

(a)

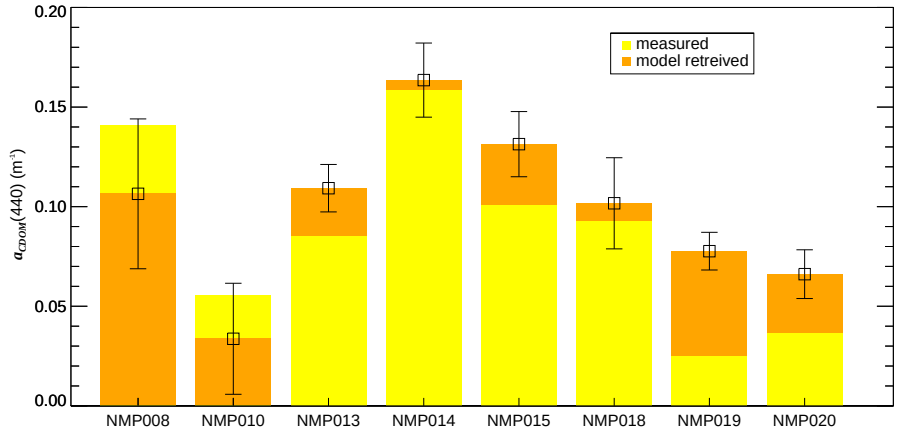

(b)

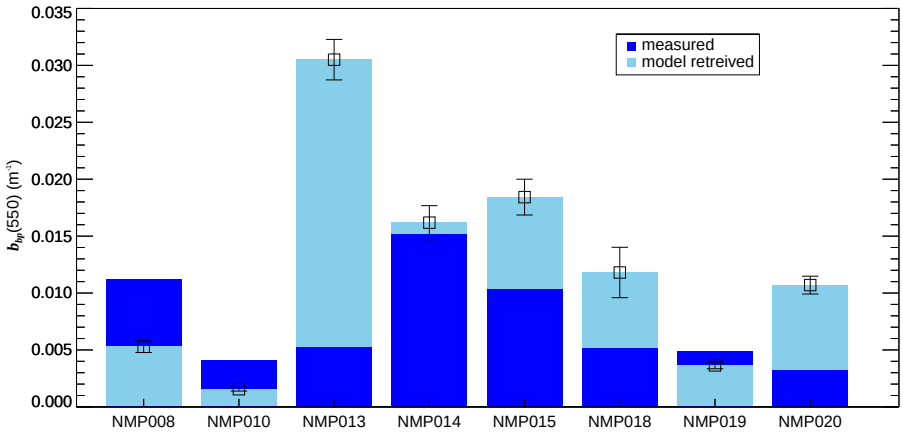

(c)

Figure 5.27: *In situ*-measured and HyMap-estimated $a_{phi}(440)$[top], $a_{CDOM}(440)$[middle] and $b_{bp}(550)$[bottom] for the 8 co-incident station sites sampled in the Ningaloo Marine Park. The error bars represent the standard deviation of the HyMap retrievals.

5.5.2 Bathymetry validation

The HyMap-derived water depths were co-located to the *in situ* echo sounder transects using the recorded vessel's GPS track information. Only the sounder transects collected during the HyMap overflights on the 22^{nd}, 24^{th} and 28^{th} of April 2006, were used. The extracted HyMap-derived water depths are shown along with the *in situ* echo sounder depths in Figs. 5.28 (a) to (c). The results show that the HyMap-derived water depths agree very closely with the echo sounder data for shallow depths up to 8 m. For the most part, the extracted HyMap-derived bathymetry resolves the detailed topography quite well. However, for very shallow areas of less that 5 m depth, there are some mismatches in derived depths for parts of the transect; for example, between sample numbers 800 and 1300 of the Tantabiddi transect, and again for sample numbers 2000 to 2200. Albeit, the mismatch offsets in depths are small, typically less than 0.5 m.

For depths greater than approximately 8 m, the HyMap-derived depths tend to be very noisy with retrieval errors in the order of ±5 m. At such depths, the spectral signal from the seafloor becomes more attenuated and reduces the signal-to-noise of the HyMap sensor. This in turn, gives rise to the increased noise in retrieved bathymetry. This is consistent with recent findings on the sensitivity analysis of bathymetry retrievals for a variety of hyperspectral sensors Garcia et al. (2014a) Botha et al. (2013). Impulse noise filtering may help in reducing the noise in retrieved depths as in Garcia et al. (2014b). The Trichodesmium bloom that was encountered during the Exmouth survey is also likely to cause depth retrieval errors.

Figure 5.29 shows the depth comparison scatter diagram for the combined transects. The overall mean difference in HyMap depth retrieval is 12.4% and an absolute error of ±0.7 m. The majority of large retrieval errors can be removed by applying the operational constraint that filters out depths where the ratio of the bottom signal to the total signal, ω_{max}, is less than 0.45. Figure 5.30 shows the comparison scatter diagram for the combined transect with the operational

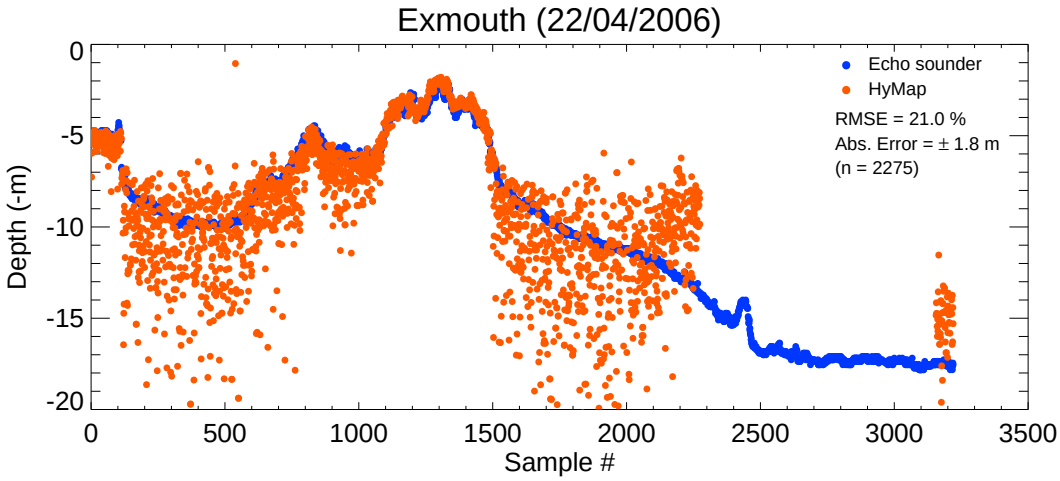

(a)

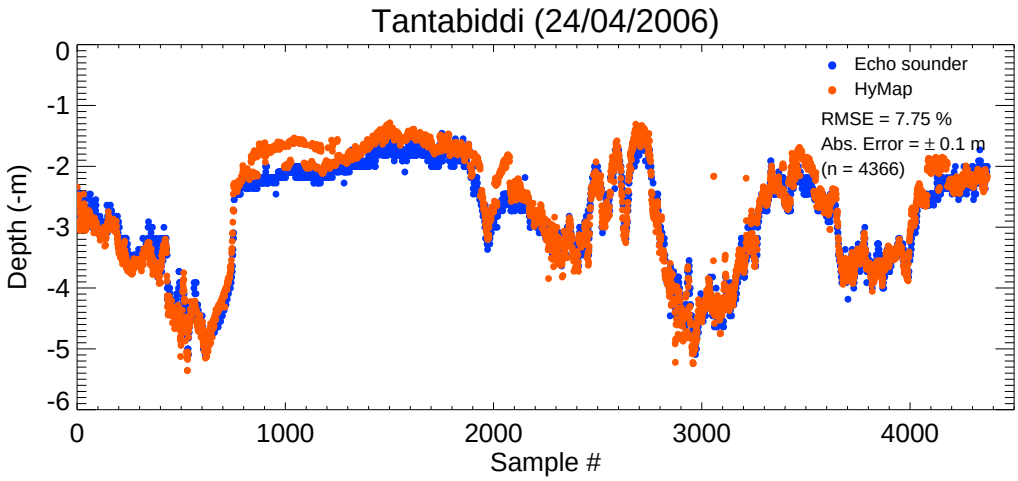

(b)

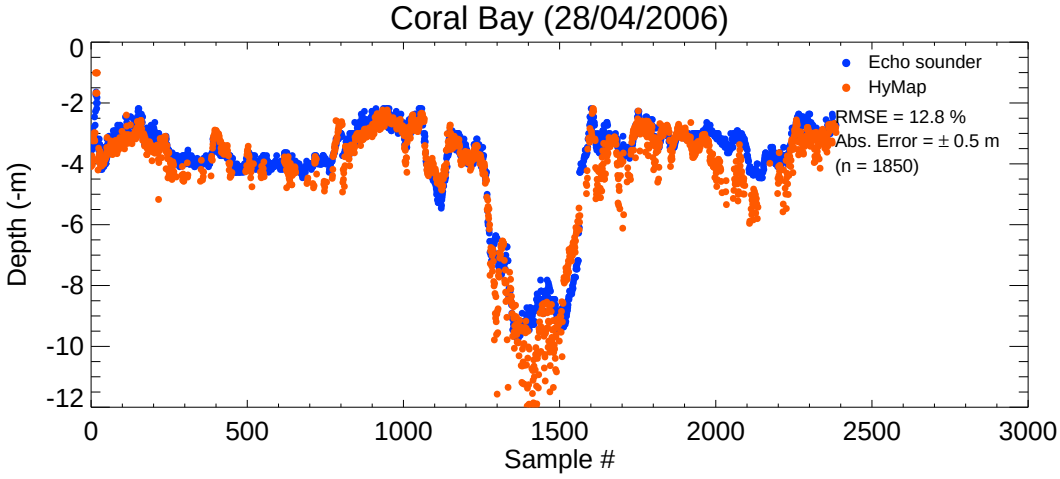

(c)

Figure 5.28: Echo sounder water depth transects and coincident HyMap bathymetry for 3 areas sampled within the Ningaloo Marine Park.

constraint applied. The overall mean difference in HyMap depth retrieval reduces to 8.1%, equivalent to a mean absolute error of ±0.2 m, valid up to depths reaching 10 m.

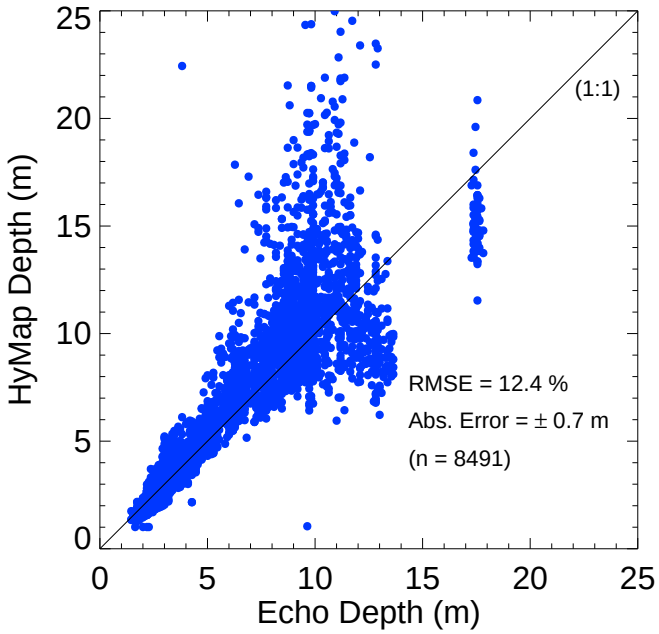

Figure 5.29: Comparison scatter diagram of echo sounder depths and HyMap-retrieved depths for all coincident data sampled within the Ningaloo Marine Park

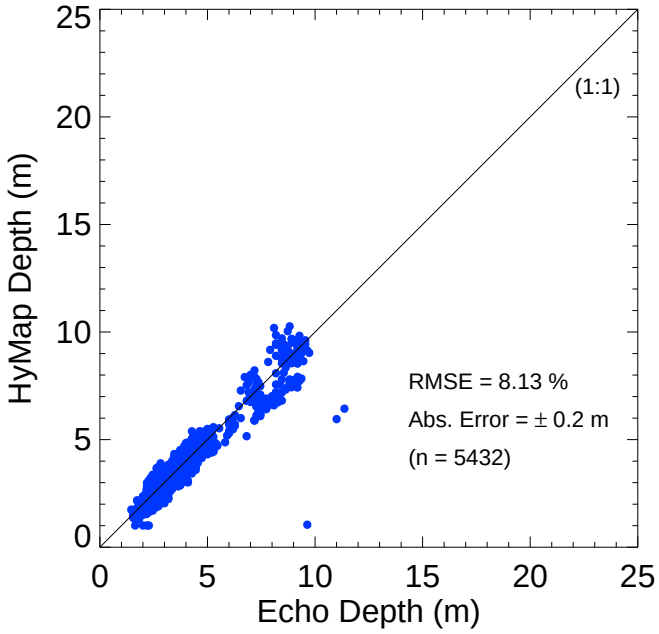

Figure 5.30: Comparison scatter diagram of echo sounder depths and HyMap-retrieved depths after removing unreliable depth retrievals using the condition ω_{max}<0.45.

5.5.3 Benthic Cover validation

The accuracy of HyMap-derived benthic cover retrievals were assessed against *in situ* underwater video footage. The underwater video footage was visually examined and classified based on the predominant benthic cover type. Unfortunately, due to vessel navigation constraints, the majority of the underwater video footage was collected over sand. However, the Coral Bay footage collected on the 20^{th} April 2006, provides a reasonable coverage of vegetation and coral benthic cover along the transect and therefore is used as the basis for the benthic cover validation presented here.

Figure 5.31 displays the vessels transect (from on-board GPS) that acquired underwater video over both a HyMap true colour image and a corresponding HyMap-derived benthic cover representation. The transect line is colour coded to highlight the predominant benthic cover type along the various cruise segments. Blue segments represent sand, green are brown algae, red are coral. On viewing the transect line in the HyMap true colour image (Fig. 5.31 left) the video segments that are identified as the sand bottom type occur over the bright highly reflective (light blue-green) areas within the lagoon, whereas brown algae and coral cover occur over the darker, lower reflectance areas. The HyMap-derived benthic cover information is presented as a false-colour composite image (Fig. 5.31 left), using the model retrieved fractional components of sand, brown algae and coral, represented as blue, green and red channels, respectively.

The benthic cover map effectively discriminates between key benthic cover types. The contiguous coverage of sand, brown algae and coral bottom types in large parts of the HyMap scene give confidence in the model's ability to provide a realistic estimate of benthic cover. The easily identifiable sand areas of the benthic cover map occur over the same highly reflective areas of the true colour image, where we would expect to find sand. Equally, over the reef (dark parts of the true colour image), high proportions of brown algae and coral are retrieved.

The HyMap benthic cover data along the transect were extracted and dis-

played in Fig 5.32. The relative proportions (normalised to unity) of sand, brown algae and coral are presented in the top, middle and bottom panels, respectively. The shaded portions in each panel indicate the segments of the transect where the corresponding benthic cover type was classified as dominant within that frame. Figure 5.32 demonstrates that there is a good match between the benthic cover classified from the underwater video footage and the relative proportions of corresponding fractional components retrieved by the model. Any anomalies that occurred were typically a result of low signal levels. These could identify partial cover, which is excluded from this examination of dominant cover only. Additionally, they may be attributed to the spatial difference between the narrow video frame and larger HyMap pixel area.

The accuracy of benthic cover retrievals was quantified through a comparison approach. For each benthic cover type, the number of pixels with a retrieved component greater than 20% was counted and compared with the number of underwater video pixels that were classified as dominant. To account for geolocation uncertainties, all HyMap pixels within a 10 m radius of the underwater video image location were counted in the match-up.

The table below summarises the results. Although only a small region of the Ningaloo reef was analysed in this study, the classification agreement under this comparison criterion are excellent. The retrieval match-up for sand is 99.8%, for brown algae it is 77.6% and coral 91.3%. This initial study is very promising for benthic cover retrieval match-up and demands further investigation to make it both statistically viable and also to expand the comparison approach to include fractional cover and greater depths.

Table 5.7: Summary of Validation Results

	video	HyMap	Classification Agreement
Sand	2501	2495	99.8%
Brown Algae	510	396	77.6%
Coral	126	115	91.3%

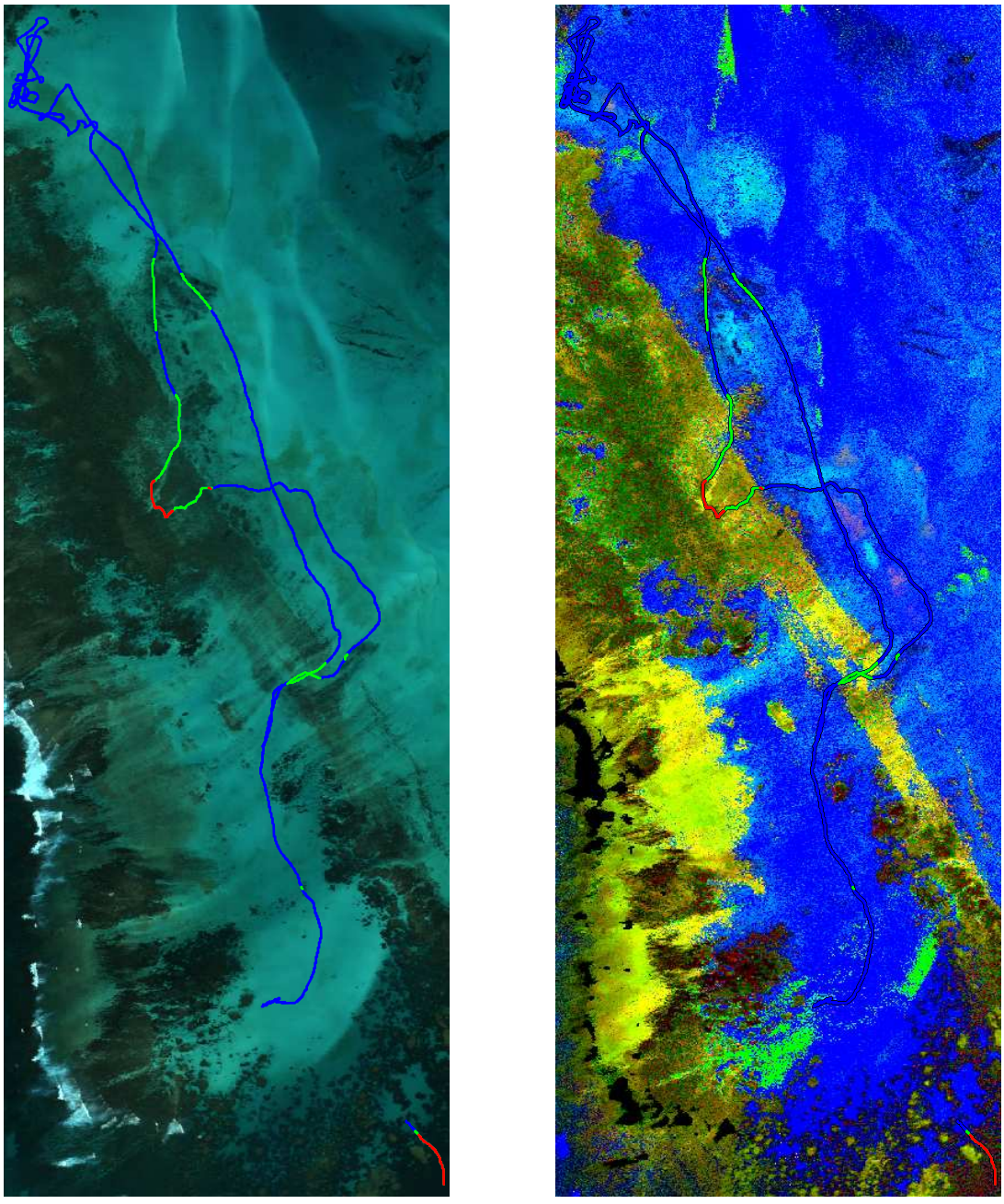

Figure 5.31: Underwater video transects plotted over Coral Bay HyMap image (left) and Benthic Cover Classification map (right). The vessel transect path is colour coded to highlight the predominant benthic cover type along the various segments. Blue segments represent sand, green denotes brown algae and red denotes coral cover.

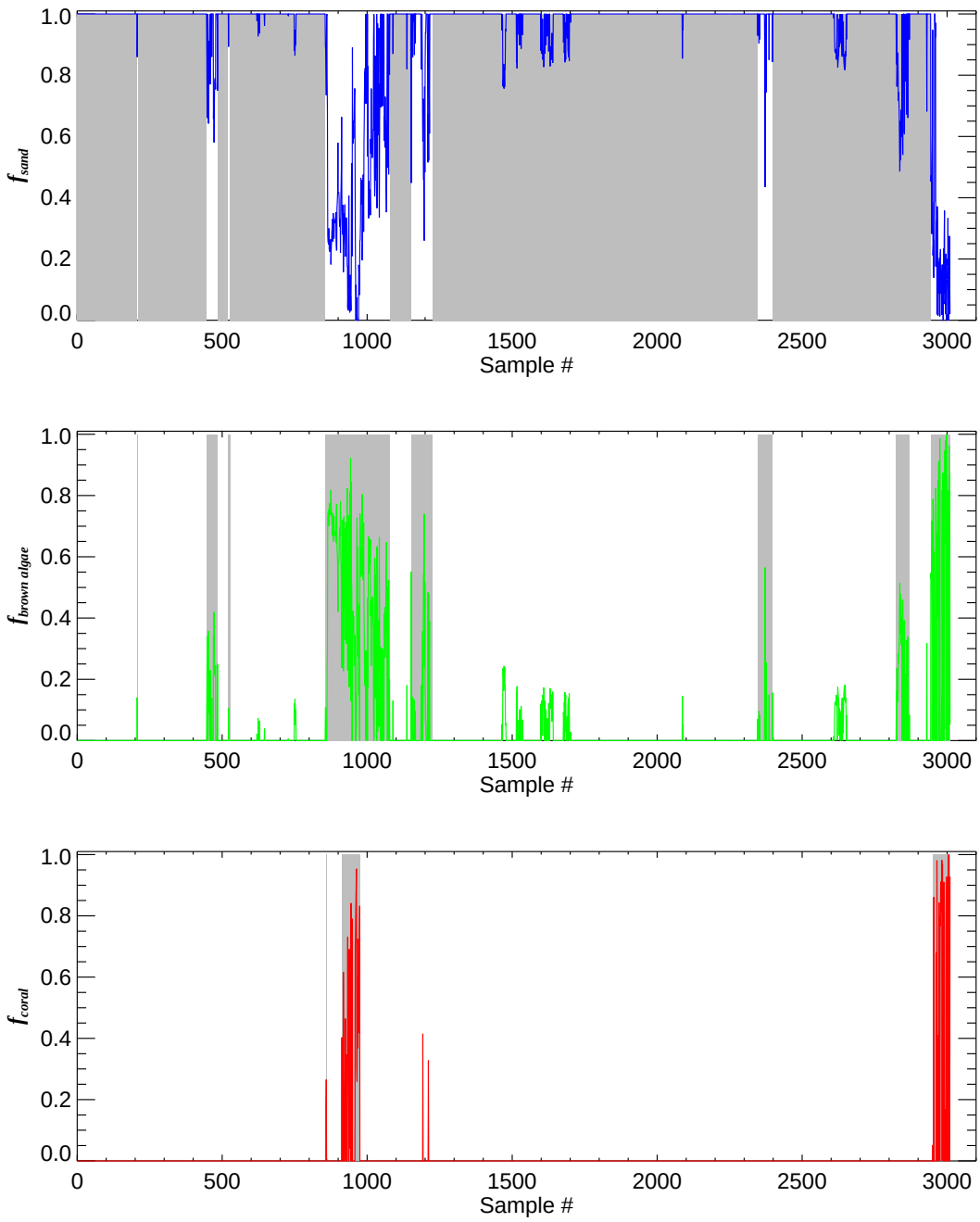

Figure 5.32: The model-retrieved fractional components of sand, brown algae and coral along the transect, top, middle and bottom panels, respectively. The shaded portions in each panel indicate the segments of the transect where the corresponding video benthic cover type was classified as dominant within that frame.

5.6 Summary

The two aerial surveys presented in this Chapter demonstrate the potential of the hyperspectral imagery and numerical inversion approach in delivering rapid and accurate appraisals of water quality, bathymetry and benthic cover over vast areas. The regions studied presented diverse and challenging environments for testing the shallow water retrieval model.

Jurien Bay was an initial, opportunistic study to obtain proof of concept over a temperate reef system dominated by sand, seagrass and brown algae. The numerical inversion approach was successfully applied to the atmospherically corrected hyperspectral imagery. The resulting bathymetry and benthic cover maps were realistic and compared well with validation data. The large fringing coral reef within the Ningaloo Marine Park provided a highly complex environment to test the accuracy of the model for the retrieval of detailed reef topography and benthic cover. The Ningaloo Marine Park image-derived products for water quality, bathymetry and benthic cover were validated against ground truth data.

Model-retrieved in-water optical properties compared well with *in situ* measurements, despite the very low concentrations encountered. The mean difference for Phytoplankton and CDOM absorption was $\sim 30\%$ or 0.01 m^{-1} and $\sim 50\%$ or 0.02 m^{-1}, respectively.

Incorporating a linear combination of three benthic cover reflectances in the model resulted in the retrieval of reliable bathymetry for the highly variable seabed environments assessed. The bathymetry products were validated against acoustic survey data covering a range from 1 m to 18 m depth. The depth retrievals for this study were reliable to depths of approximately 10 m. For greater depths the accuracy was low, mainly due to increased turbidity of the water which limits the bottom retrieval signal. However, unreliable depth retrieval was able to be removed by applying the operational constraint that filters out depths where the ratio of the bottom signal to the total signal, ω_{max}, is less than 0.45. The average RMS errors in depth retrieval were consistent for both coastal regions at

$\sim 8\%$, equivalent to an absolute average error of ± 0.2 m.

The inclusion of three benthic cover reflectances in the model also enabled the generation of primary benthic cover classification products from the imagery. Validation of these products were assessed by comparing inversion-derived benthic cover with a number of coincident underwater video observations. The retrieved benthic cover coefficients compared well for dominant types. The benthic cover retrieval over sand was the most reliable with 99.8% accuracy, followed by coral with an accuracy of 91.3% and finally brown algae with 77.6%. These promising results should be viewed in light of the limited ground truth data collected, given benthic cover validation was not the primary focus of this study. A more detailed benthic cover validation study is required to determine the potential of this approach for accurate classification of varied mixtures of benthic cover and for greater depths.

The shallow water model inversion demonstrated here makes use of general parameterisation of water column and benthic cover properties, which makes this physics based approach easily adaptable to other regions. The simultaneous extraction of biological and physical properties of an environment makes this approach highly practical for the monitoring and management of coastal waters worldwide.

Chapter 6

Conclusion and Recommendations

6.1 Review of Research Aims

The aims of this thesis were to;

1. Develop and implement a numerical retrieval scheme for extracting water quality, water depth and key benthic habitat types from Case 2 water hyperspectral data.

2. Test the developed shallow water numerical retrieval scheme against simulated data and investigate model performance in terms of model accuracy and highlight any limitations.

3. Apply the shallow water algorithm to airborne hyperspectral survey datasets and compare the retrieved products to available *in situ* data.

The outcomes of this dissertation with reference to each of the aims are discussed in Sections 6.2 to 6.4.

6.2 Semi-analytic Shallow Water Model

The development of an algorithm and inversion technique for optical remote sensing in shallow water was described in Chapter 3. The algorithm is based on an approximation of the radiative transfer equation to model the remote sensing reflectance in terms of the inherent optical properties of the water, bottom depth, sea floor reflectance, illumination conditions and sensor viewing geometry.

The approximation combines empirical model coefficients with analytical expressions of deep-water remote sensing reflectance, water column attenuation and the air-water interface to model the total above-water remote sensing reflectance. To account for the effects of sun position and sensor viewing geometry, a LUT of new empirical model coefficients were derived for specific solar-sensor geometry. The derivations were based on simulations of R_{rs}, with the well established and validated computer model Hydrolight. The simulations encompassed a wide range of environmental conditions, including water column IOPs representative of clear to turbid cases, a large range of water depths from 0.1 m to 20 m and realistic bottom reflectance endmembers typical of sand, seagrass and brown algae.

By incorporating the LUT of empirical coefficients, the remote sensing reflectance, as modelled for a variety of solar-sensor geometries, agree better with Hydrolight simulations than calculations with existing equations, which only use nadir-derived coefficients. Comparisons between modelled and Hydrolight R_{rs} as a function of sensor viewing angle showed stable performance up to 40°, with RMS errors between 1.5% - 2%.

A numerical retrieval scheme for simultaneously extracting water column IOPs, water depth and bottom type from remote sensing reflectance was introduced. By further parameterisation of the spectral absorption, backscattering and bottom reflectance terms, the shallow water remote sensing reflectance model can be described by a number of adjustable parameters, which account for phytoplankton and CDOM absorption, particle backscattering, water depth and bottom reflectance. To account for variable bottom cover, the bottom re-

flectance was parameterised by the linear combination of 3 spectrally distinct bottom types, representative of sand, seagrass and brown algae. The solution of the unknown model parameters are then obtained from measured $R_{rs}(\lambda)$ by incorporating non-linear curve fitting methods. In this dissertation, because of its flexibility, the Levenberg-Marquardt retrieval scheme was adopted. The process involves iterative adjustments to the model parameter values in order to minimise the difference between modelled and measured $R_{rs}(\lambda)$. Once a minimum is reached, the solution of the model parameters are considered solved.

6.3 Inversion Performance Tested Against Computer-Simulated Data.

Examples of model inversion performance based on computer simulated Hydrolight data were presented in Chapter 4. The results showed that the shallow water model and numerical retrieval scheme worked well for a wide range of environmental conditions that simulate those encountered for typical coastal waters. The Levenberg-Marquardt optimisation approach showed sensitivity to the initial values of the fit parameters. A robust methodology, based on a coarse look-up-table of modelled R_{rs}, was developed to find the initial values of water constituent concentration, bottom depth and the relative proportions of sand, seagrass and brown algae endmembers. On average, the CLUT-derived initial guess values were within 30% of the Hydrolight inputs. The inversion tests showed that this was sufficient for the numerical retrieval scheme to return a solution, whereby, exactly the same retrieval accuracies were obtained as compared to inversions that used known values for the initial conditions.

For inversions performed using "ideal" noise-free Hydrolight data, the retrieval accuracies of the water column parameters were excellent. RMS errors of 2.7%, 1.9% and 1.8% were obtained for the retrieved values of $a_{phi}(440)$, $a_{cdom}(440)$ and $b_{bp}(550)$, respectively. For water depth retrievals, excellent agreement up to

7 m were obtained. However, for increasing depth the relative errors increased with higher attenuation. The large errors in depth retrievals were prominent for situations where the relative contribution of the bottom signal to the total signal was low. The ratio of the bottom signal to the total signal can be derived from the model, and can provide a useful operational constraint to only provide data for cases where the bottom can be detected. The RMS error in depth retrieval for waters with sufficient bottom signal is 4.0%. The maximum detectable depth occurred at approximately 20 m which was for clear water with a bright sand bottom. For the lower albedo seagrass and brown algae bottom cover, the maximum retrievable depth was approximately 15 m. The retrieved relative proportions of benthic cover type were shown to adequately discriminate between sand, seagrass and brown algae.

The influence of sensor-specific noise, digitisation and spectral resolution greatly affected the retrieval accuracy of the model. The errors in retrieving water column parameters increased to between 12% and 20%. For noisy R_{rs} data, reliable water column depth and bottom albedo retrievals were achieved by applying a stringent filtering criterion based on the relative contribution of apparent bottom signal. For data where the bottom component was greater than 45% of the total signal, the RMS error in depth retrievals reduced to 6.2% and still allowed a maximum depth of 20 m to be detected. Similarly, the relative proportions of sand, seagrass and brown algae were also appropriately discriminated, with an average difference of 6.2% for sand, 12.3% for seagrass and 10.8% for brown algae for water depths between 1 m and 15 m.

The promising results presented here demonstrate the potential for mapping water quality parameters, water depth and benthic cover information from remotely sensing data, using a sound physically-based approach. The inversion tests used generic spectral forms for phytoplankton absorption, particle backscattering and benthic cover reflectance endmembers. The model is easily adaptable to incorporate regionally-specific spectral endmembers. Although the initial tests

performed here are shown to work well for the Hydrolight data that were simulated using generic spectral forms, the suitability of the use of general spectral endmembers over more complex Hydrolight simulations that use a wider array of spectral shapes as inputs needs further testing. Similarly, since the empirical model coefficients were tuned using Hydrolight data that were simulated with a specific particle phase function, understanding the applicability of the model for waters that exhibit different particle phase functions would benefit from more detailed modelling work. The real test however, is to demonstrate the performance of the shallow water model from real-life data.

6.4 Application to Airborne Hyperspectral Data

Chapter 5 presented the application of the shallow water model to airborne hyperspectral survey data. The image-derived products relating to water quality, bathymetry and benthic cover were successfully retrieved with the numerical inversion scheme and validated against a broad suite of ground truth data. Overall, the model retrieved products compared well with *in situ* observations in the challenging and highly complex coastal water environments examined. Phytoplankton and CDOM absorption coefficients were adequately retrieved for the very low concentrations encountered. The model was unable to resolve the particle backscattering coefficients however, due to the low particle concentration apparent in such pristine waters. The three benthic reflectance terms incorporated within the shallow water model appeared to benefit the retrieval of reliable bathymetry and benthic cover over the variable environments studied. The depth retrievals in this study were reliable to a depth of 10 m, with an overall RMS error of only 8%, or ± 0.2 m. Additionally, by including the three benthic reflectance terms, key benthic cover classification products were derived from the imagery. Areas of dominant benthic cover and their mixtures were easily identified within the classification products. The image-derived benthic classifications proved very accurate when compared with underwater video observations classified by their

predominant benthic cover type. However, due to the limited number of benthic cover types sampled, further validation work is required to better assess the model's accuracy for a more detailed classification of the seafloor.

The shallow water model has proven to be a powerful tool for the rapid and accurate appraisal of vast coastal waters, following its successful application across varied and complex environments. The strength of the shallow water model is that it is a physics-based approach where the parameterisation can be generic, or fine-tuned with region-specific endmembers for improved accuracy. It may possibly prove to be the most viable solution for the efficient, economic and accurate mapping of coastlines on a global scale utilising hyperspectral sensors on board earth-orbiting satellites.

6.5 Further work

The work presented here is considered a work in progress. The intention of the initial algorithm development was to improve the accuracy of existing nadir-based semi-analytical shallow water models to cover a wider range of solar-sensor geometries. Similarly, the plan included extending the models for use over waters with variable bottom cover, which led to the promise of mapping key benthic cover types from endmember spectral unmixing. However, several potentially important considerations were neglected from the model development and remain to be addressed with further work.

- Re-derive empirical model coefficients from radiative transfer simulations that incorporate a wide array of *in situ* measurements of spectral absorption and backscattering, including new measurements of volume scattering functions (Sullivan and Twardowski, 2009) to replace the well-used but somewhat dated Petzolds-type.

- Re-derive empirical model coefficients incorporating the BRDF of different bottom types and include structure (i.e coral "bommies", sloping sand holes

and direction of seagrass leaves).

- Include the effects of CDOM and Phytoplankton fluorescence as well as fluorescence from benthic cover. (e.g. fluorescing corals and biofilm).

- Include noise to simulated data based on sensor calibration statistics and incorporate realistic atmospheric contribution to the noise modelling.

- Investigate the influence of systematic errors such as absolute radiometric calibration, stray light, and image distortions.

- Investigate new curve fitting techniques such as wavelet transform minimisation which promises to be less sensitive to systematic errors in atmospheric correction or sensor-specific noise.

- Perform inversion tests over a wider range of benthic cover types at subspecies level, including corals.

- Investigate the separability of benthic cover retrievals from more complex benthic environments and understand the limitations due to optical clarity, depth and sensor-specific noise

- Investigate the limitations of benthic separability and retrieval accuracy for a range of imaging systems with particular interest in sensor and environmental noise.

- Apply the shallow water model to Hyperspectral imagery over complex ecosystems such as coral reefs and validate the derived products with coincident *in situ* measurements that include above-water remote sensing reflectance, inherent optical properties and concentrations of constituents, independent bathymetry (i.e lidar or multi beam sonar), diver-based measurements of benthic reflectance (i.e. BRDF) and independent assessment of benthic cover.

Chapter 7

Appendix

7.1 Two-Flow Approximation

The theoretical considerations in approximating the radiative transfer equation for shallow water environments follows the work presented in Maritorena et al. (1994). In shallow waters, the upwelling irradiance just below the water's surface, $E_u(0)$, can be thought of resulting from the summation of the flux backscattered from the water column itself and the flux reflected off the sea bottom and then transmitted through the column so that,

$$E_u(0) = E_u(0)_C + E_u(0)_B, \tag{7.1}$$

where the subscripts C and B represent the water column and the sea bottom respectively.

The first term represents the photon flux that is backscattered within the water column itself that never interacts with the bottom. The second term represents photons that have interacted with the sea bottom at least once.

An estimate of the first term is achieved by considering an infinitely thin layer of thickness dz at depth z of a plane parallel, spatially homogeneous water column.

The downwelling irradiance at depth z is written as $E_d(z)$. Using a hybrid

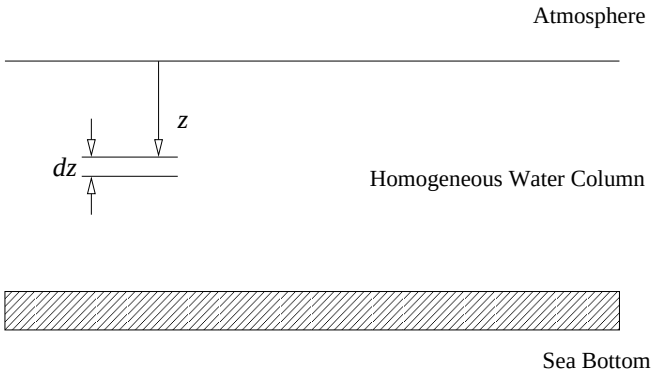

Figure 7.1: A representation of a plane parallel, spatially homogeneous water column bounded by the atmosphere and a sea bottom.

property of the water medium such as the reflectance function for the downwelling light stream, denoted as b_{bd}, the contribution of the upwelling irradiance created by this layer is,

$$dE_u(z) = b_{bd}E_d(z)dz. \tag{7.2}$$

Using the assumption that the water column is vertically homogeneous, Beer's law is adopted to express $E_d(z)$ in terms of $E_d(0)$ such that,

$$E_d(z) = E_d(0)e^{-k_d z}, \tag{7.3}$$

where, k_d represents the diffuse attenuation coefficient for downwelling irradiance within the water column. The differential element of upwelling irradiance at depth z undergoes attenuation during its propagation towards the water's surface. This attenuation may be expressed as $e^{-k_u z}$, where k_u is the diffuse attenuation coefficient for upwelling irradiance. The upwelling irradiance at null depth originating from the thin layer at depth z is denoted by, $dE_u(z \to 0)$, and is expressed as,

$$dE_u(z \to 0) = b_{bd}E_d(0)e^{-(k_u+k_d)z}dz. \tag{7.4}$$

Using the assumption that b_{bd}, k_d and k_u are invariant with respect to z, the

contribution of each layer between z and 0 can be summed so that,

$$\begin{aligned} E_u(0,z) &= b_{bd}E_d(0)\int_0^z e^{[-(k_u+k_d)z]}dz \\ &= (k_u+k_d)^{-1}b_{bd}E_d(0)1-e^{-[k_u+k_d]z}. \end{aligned} \tag{7.5}$$

To simulate a deep water column the above equation is applied to an infinitely deep water column where $z=\infty$, thus reducing Eq. 7.5 to,

$$E_u(0,\infty) = R_\infty E_d(0), \tag{7.6}$$

where R_∞ replaces $(k_d+k_u)b_{bd}$, representing the reflectance function for deep waters. For a finite water depth where the sea bottom restricts the water column to a depth H, the upwelling irradiance at null depth is expressed as,

$$E_u(0,H) = R_\infty E_d(0)\{1-e^{-[k_u+k_d]H}\}, \tag{7.7}$$

representing the first term in Eq. 7.1.

Introducing the sea bottom as an ideal Lambertian reflector with an albedo, A, the flux just above the bottom is,

$$E_u(H)_B = AE_d(0)e^{-k_dH}. \tag{7.8}$$

After undergoing further attenuation when propagating up to the water surface the contribution of the bottom just below the water surface is,

$$E_u(0)_B = AE_d(0)e^{-[k_u+k_d]H}. \tag{7.9}$$

With this, the total upwelling irradiance just below the water surface becomes,

$$E_u(0) = R_\infty E_d(0)\{1-e^{-[k_u+k_d]H}\} + AE_d(0)e^{-[k_u+k_d]H}. \tag{7.10}$$

After dividing Eq. 7.10 by the downwelling irradiance, $E_d(0)$, we arrive at the irradiance reflectance just below the water surface, $R(0)$ and is approximated as,

$$R(0) = R_\infty\{1 - e^{-[k_u+k_d]H}\} + Ae^{-[k_u+k_d]H}. \tag{7.11}$$

Eq. 7.11 becomes the starting point of the algorithm development work presented in this study.

7.2 Absorption Coefficients of Water

Table 7.1: Spectral absorption coefficients of pure water (Pope and Fry, 1997).

λ (nm)	a_w (m^{-1})	λ (nm)	a_w (m^{-1})	λ (nm)	a_w (m^{-1})
380.0	0.01137	497.5	0.01910	615.0	0.26780
382.5	0.01044	500.0	0.02040	617.5	0.27070
385.0	0.00941	502.5	0.02280	620.0	0.27550
387.5	0.00917	505.0	0.02560	622.5	0.28100
390.0	0.00851	507.5	0.02800	625.0	0.28340
392.5	0.00829	510.0	0.03250	627.5	0.29040
395.0	0.00813	512.5	0.03720	630.0	0.29160
397.5	0.00775	515.0	0.03960	632.5	0.29950
400.0	0.00663	517.5	0.03990	635.0	0.30120
402.5	0.00579	520.0	0.04090	637.5	0.30770
405.0	0.00530	522.5	0.04160	640.0	0.31080
407.5	0.00503	525.0	0.04170	642.5	0.32200
410.0	0.00473	527.5	0.04280	645.0	0.32500
412.5	0.00452	530.0	0.04340	647.5	0.33500
415.0	0.00444	532.5	0.04470	650.0	0.34000
417.5	0.00442	535.0	0.04520	652.5	0.35800
420.0	0.00454	537.5	0.04660	655.0	0.37100
422.5	0.00474	540.0	0.04740	657.5	0.39300
425.0	0.00478	542.5	0.04890	660.0	0.41000
427.5	0.00482	545.0	0.05110	662.5	0.42400
430.0	0.00495	547.5	0.05370	665.0	0.42900
432.5	0.00504	550.0	0.05650	667.5	0.43600
435.0	0.00530	552.5	0.05930	670.0	0.43900
437.5	0.00580	555.0	0.05960	672.5	0.44800
440.0	0.00635	557.5	0.06060	675.0	0.44800
442.5	0.00696	560.0	0.06190	677.5	0.46100
445.0	0.00751	562.5	0.06400	680.0	0.46500
447.5	0.00830	565.0	0.06420	682.5	0.47800
450.0	0.00922	567.5	0.06720	685.0	0.48600
452.5	0.00969	570.0	0.06950	687.5	0.50200
455.0	0.00962	572.5	0.07330	690.0	0.51600
457.5	0.00957	575.0	0.07720	692.5	0.53800
460.0	0.00979	577.5	0.08360	695.0	0.55900
462.5	0.01005	580.0	0.08960	697.5	0.59200
465.0	0.01011	582.5	0.09890	700.0	0.62400
467.5	0.01020	585.0	0.11000	702.5	0.66300
470.0	0.01060	587.5	0.12200	705.0	0.70400
472.5	0.01090	590.0	0.13510	707.5	0.75600
475.0	0.01140	592.5	0.15160	710.0	0.82700
477.5	0.01210	595.0	0.16720	712.5	0.91400
480.0	0.01270	597.5	0.19250	715.0	1.00700
482.5	0.01310	600.0	0.22240	717.5	1.11900
485.0	0.01360	602.5	0.24700	720.0	1.23100
487.5	0.01440	605.0	0.25770	722.5	1.35600
490.0	0.01500	607.5	0.26290	725.0	1.48900
492.5	0.01620	610.0	0.26440	727.5	1.67800
495.0	0.01730	612.5	0.26650		

7.3 Backscattering Coefficients of Water

Table 7.2: Spectral backscattering coefficients of pure water (Morel, 1974).

λ (nm)	b_{bw} (m^{-1})	λ (nm)	b_{b_w} (m^{-1})
400.0	0.00379	580.0	0.00076
405.0	0.00359	585.0	0.00073
410.0	0.00341	590.0	0.00071
415.0	0.00323	595.0	0.00068
420.0	0.00307	600.0	0.00066
425.0	0.00292	605.0	0.00063
430.0	0.00277	610.0	0.00061
435.0	0.00264	615.0	0.00059
440.0	0.00251	620.0	0.00057
445.0	0.00239	625.0	0.00055
450.0	0.00228	630.0	0.00053
455.0	0.00217	635.0	0.00051
460.0	0.00207	640.0	0.00050
465.0	0.00198	645.0	0.00048
470.0	0.00189	650.0	0.00047
475.0	0.00180	655.0	0.00045
480.0	0.00172	660.0	0.00044
485.0	0.00165	665.0	0.00042
490.0	0.00158	670.0	0.00041
495.0	0.00151	675.0	0.00040
500.0	0.00145	680.0	0.00038
505.0	0.00138	685.0	0.00037
510.0	0.00133	690.0	0.00036
515.0	0.00127	695.0	0.00035
520.0	0.00122	700.0	0.00034
525.0	0.00117	705.0	0.00033
530.0	0.00112	710.0	0.00032
535.0	0.00108	715.0	0.00031
540.0	0.00104	720.0	0.00030
545.0	0.00100	725.0	0.00029
550.0	0.00096	730.0	0.00028
555.0	0.00092	735.0	0.00027
560.0	0.00089	740.0	0.00027
565.0	0.00085	745.0	0.00026
570.0	0.00082	750.0	0.00025
575.0	0.00079		

7.4 Phytoplankton Absorption Coefficients

Table 7.3: Spectral absorption coefficients of phytoplankton (Morel, 1988).

λ (nm)	a^*_{phi} (m^{-1})	λ (nm)	a^*_{phi} (m^{-1})
400.0	0.687	580.0	0.291
405.0	0.781	585.0	0.274
410.0	0.828	590.0	0.282
415.0	0.883	595.0	0.249
420.0	0.913	600.0	0.236
425.0	0.939	605.0	0.279
430.0	0.973	610.0	0.252
435.0	1.001	615.0	0.268
440.0	1.000	620.0	0.276
445.0	0.971	625.0	0.299
450.0	0.944	630.0	0.317
455.0	0.928	635.0	0.333
460.0	0.917	640.0	0.334
465.0	0.902	645.0	0.326
470.0	0.870	650.0	0.356
475.0	0.839	655.0	0.389
480.0	0.798	660.0	0.441
485.0	0.773	665.0	0.534
490.0	0.750	670.0	0.595
495.0	0.717	675.0	0.544
500.0	0.668	680.0	0.502
505.0	0.645	685.0	0.420
510.0	0.618	690.0	0.329
515.0	0.582	695.0	0.262
520.0	0.528	700.0	0.215
525.0	0.504	705.0	0.160
530.0	0.474	710.0	0.110
535.0	0.444	715.0	0.075
540.0	0.416	720.0	0.040
545.0	0.384	725.0	0.030
550.0	0.357	730.0	0.020
555.0	0.321	735.0	0.015
560.0	0.294	740.0	0.010
565.0	0.273	745.0	0.000
570.0	0.276	750.0	0.000
575.0	0.268		

7.5 Bottom Reflectance Spectra

Table 7.4: Bottom Reflectances of sand (sd), seagrass (sg) and brown algae (ba)

λ (nm)	ρ_{sd}	ρ_{sg}	ρ_{ba}
400.0	0.377	0.056	0.022
405.0	0.384	0.057	0.023
410.0	0.391	0.057	0.023
415.0	0.399	0.057	0.023
420.0	0.407	0.057	0.023
425.0	0.415	0.058	0.023
430.0	0.424	0.058	0.023
435.0	0.432	0.058	0.023
440.0	0.442	0.059	0.023
445.0	0.450	0.060	0.024
450.0	0.459	0.061	0.024
455.0	0.469	0.062	0.025
460.0	0.478	0.063	0.026
465.0	0.485	0.063	0.026
470.0	0.492	0.064	0.027
475.0	0.500	0.065	0.028
480.0	0.507	0.066	0.029
485.0	0.514	0.067	0.030
490.0	0.521	0.068	0.030
495.0	0.527	0.070	0.031
500.0	0.534	0.071	0.032
505.0	0.542	0.074	0.033
510.0	0.550	0.077	0.035
515.0	0.556	0.081	0.037
520.0	0.562	0.086	0.039
525.0	0.568	0.091	0.041
530.0	0.573	0.094	0.044
535.0	0.579	0.098	0.046
540.0	0.583	0.101	0.049
545.0	0.588	0.103	0.053
550.0	0.593	0.106	0.058
555.0	0.596	0.108	0.064
560.0	0.600	0.110	0.071
565.0	0.606	0.110	0.077
570.0	0.610	0.110	0.082
575.0	0.614	0.109	0.085
580.0	0.620	0.109	0.086
585.0	0.628	0.107	0.086
590.0	0.635	0.106	0.088
595.0	0.638	0.103	0.091
600.0	0.640	0.100	0.094
605.0	0.643	0.097	0.093
610.0	0.645	0.095	0.087
615.0	0.647	0.093	0.081
620.0	0.647	0.090	0.076
625.0	0.649	0.090	0.074
630.0	0.651	0.089	0.072
635.0	0.653	0.089	0.072
640.0	0.654	0.088	0.074
645.0	0.654	0.087	0.077
650.0	0.655	0.085	0.075
655.0	0.656	0.084	0.065
660.0	0.652	0.083	0.051
665.0	0.645	0.082	0.039
670.0	0.642	0.089	0.033
675.0	0.640	0.103	0.032
680.0	0.644	0.122	0.036
685.0	0.654	0.151	0.049
690.0	0.669	0.181	0.075
695.0	0.685	0.209	0.116
700.0	0.696	0.293	0.167
705.0	0.705	0.390	0.213
710.0	0.711	0.449	0.247
715.0	0.715	0.506	0.271
720.0	0.719	0.552	0.287
725.0	0.722	0.586	0.298
730.0	0.727	0.608	0.305
735.0	0.727	0.621	0.312
740.0	0.729	0.630	0.317
745.0	0.733	0.635	0.320
750.0	0.734	0.638	0.323

7.6 Deep-water r_{rs} model coefficients LUT

Table 7.5: Deep water remote sensing reflectance model parameters

Solar Zenith θ_s	Sensor View (θ_v, ϕ_v)	g_w	G_0	G_1	G_2	G_3	g_{wp}
0°	nadir	0.108	0.156	0.472	7.245	1.441	0.115
	(10°,90°)	0.108	0.158	0.487	6.668	1.392	0.120
	(20°,90°)	0.108	0.163	0.520	5.721	1.293	0.128
	(30°,90°)	0.108	0.170	0.559	4.852	1.178	0.142
	(40°,135°)	0.106	0.181	0.581	4.627	1.023	0.198
15°	nadir	0.108	0.165	0.528	5.247	1.270	0.103
	(10°,90°)	0.109	0.167	0.541	4.957	1.233	0.104
	(20°,90°)	0.109	0.171	0.564	4.551	1.169	0.110
	(30°,90°)	0.109	0.176	0.589	4.216	1.095	0.119
	(40°,135°)	0.117	0.186	0.583	3.985	1.006	0.148
30°	nadir	0.108	0.167	0.554	4.746	1.183	0.105
	(10°,90°)	0.108	0.169	0.563	4.612	1.159	0.108
	(20°,90°)	0.109	0.172	0.577	4.424	1.117	0.114
	(30°,90°)	0.109	0.176	0.591	4.320	1.069	0.125
	(40°,135°)	0.120	0.184	0.564	4.221	1.024	0.157
45°	nadir	0.107	0.171	0.576	4.421	1.062	0.093
	(10°,90°)	0.107	0.172	0.576	4.474	1.057	0.096
	(20°,90°)	0.107	0.173	0.575	4.621	1.050	0.101
	(30°,90°)	0.108	0.176	0.570	4.906	1.040	0.110
	(40°,135°)	0.126	0.180	0.519	5.217	1.057	0.154
60°	nadir	0.107	0.172	0.569	4.403	1.025	0.082
	(10°,90°)	0.107	0.172	0.568	4.484	1.023	0.084
	(20°,90°)	0.107	0.174	0.564	4.670	1.020	0.089
	(30°,90°)	0.108	0.177	0.556	5.005	1.016	0.096
	(40°,135°)	0.128	0.183	0.513	5.150	1.022	0.162

7.7 Diffuse attenuation model coefficients LUT

Table 7.6: Distribution function coefficients for modelling diffuse attenuation

Solar Zenith θ_s	Sensor View (θ_v, ϕ_v)	D_0^C	D_1^C	D_0^B	D_1^B
0°	nadir	1.000	1.672	1.091	4.174
	(10°,90°)	1.000	1.780	1.103	4.148
	(20°,90°)	1.000	2.027	1.130	4.100
	(30°,90°)	1.000	2.641	1.180	4.018
	(40°,135°)	1.000	7.219	1.420	3.670
15°	nadir	1.000	1.385	1.067	5.763
	(10°,90°)	1.000	1.540	1.078	5.740
	(20°,90°)	1.000	1.913	1.104	5.698
	(30°,90°)	1.000	2.727	1.152	5.615
	(40°,135°)	1.043	6.488	1.388	5.105
30°	nadir	1.000	1.013	1.087	4.489
	(10°,90°)	1.000	1.178	1.098	4.481
	(20°,90°)	1.000	1.573	1.124	4.470
	(30°,90°)	1.000	2.421	1.173	4.446
	(40°,135°)	1.000	7.236	1.408	4.159
45°	nadir	1.000	2.482	1.097	5.565
	(10°,90°)	1.000	2.651	1.108	5.544
	(20°,90°)	1.000	3.054	1.134	5.506
	(30°,90°)	1.000	3.890	1.181	5.432
	(40°,135°)	1.000	8.350	1.407	5.095
60°	nadir	1.000	1.000	1.000	5.448
	(10°,90°)	1.000	1.019	0.998	5.735
	(20°,90°)	1.000	0.958	1.011	5.906
	(30°,90°)	1.000	1.462	1.053	5.894
	(40°,135°)	1.000	5.720	1.288	5.263

7.8 Air-water interface model coefficients LUT

Table 7.7: Air-water interface model coefficients

Solar Zenith θ_s	Sensor View (θ_v, ϕ_v)	ζ	*Gamma*
0°	nadir	0.516	1.458
	(10°,90°)	0.519	1.456
	(20°,90°)	0.516	1.455
	(30°,90°)	0.519	1.459
	(40°,135°)	0.512	1.472
15°	nadir	0.524	1.313
	(10°,90°)	0.526	1.308
	(20°,90°)	0.524	1.300
	(30°,90°)	0.525	1.340
	(40°,135°)	0.517	1.366
30°	nadir	0.518	1.419
	(10°,90°)	0.521	1.418
	(20°,90°)	0.518	1.414
	(30°,90°)	0.520	1.431
	(40°,135°)	0.513	1.442
45°	nadir	0.521	1.379
	(10°,90°)	0.524	1.365
	(20°,90°)	0.522	1.353
	(30°,90°)	0.520	1.439
	(40°,135°)	0.512	1.469
60°	nadir	0.505	1.351
	(10°,90°)	0.508	1.340
	(20°,90°)	0.506	1.325
	(30°,90°)	0.505	1.387
	(40°,135°)	0.497	1.406

Bibliography

D.A. Aurin, H.M. Dierssen, M.S. Twardowski, and C.S. Roesler. Optical complexity in long island sound and implications for coastal ocean color remote sensing. *Journal of Geophysical Research*, 115, 2010.

R. Babcock, G. Clapin, P. England, N. Murphy, J. Phillips, A. Sampey, M. Vanderklift, and M. Westera. The development and validation of algorithms for remotely sensing case ii waters. Technical report, CSIRO, 2006.

M. Babin, D. Stramski, G.M. Ferrari, H. Claustre, A. Bricaud, G. Obolensky, and N. Hoepffner. Variations in the light absorption coefficients of phytoplankton, non-algal particles, and dissolved organic matter in coastal waters around europe. *Journal of Geophysical Research*, 108(C7), 2003.

M.J. Behrenfeld, J.T. Randerson, C.R. McClain, G.C. Feldman, S.O. Los, C.J. Tucker, P.G Falkowski, C.B. Field, R. Frouin, W.E. Esais, D.D. Kolber, and N.H. Pollack. Biospheric primary production during an enso transition. *Science*, 291:2594–2597, 2001.

M.J. Behrenfeld, R.T. O'Malley, D.A. Siegel, C.R. McClain, J.L. Sarmiento, G.C. Feldman, A.J. Milligan, P.G. Falkowski, R.M. Letelier, and E.S. Boss. Climate-driven trends in contemporary ocean productivity. *Nature*, 444:752–755, 2006.

P.N. Bierwirth, T.J. Lee, and R.V. Burne. Shallow sea-floor reflectance and water depth derived by unmixing multispectral imagery. *Photogrammetric Engineering & Remote Sensing*, 59:331–338, 1993.

D. Blondeau-Patissier, V.E. Brando, K. Oubelkheir, A.G. Dekker, L.A. Clementson, and P. Daniel. Bio-optical variability of the absorption and scattering properties of the queensland inshore and reef waters, australia. *Journal of Geophysical Research: Oceans*, 114(C5), 2009.

Craig F. Bohren and Donald R. Huffman. *Absorption and Scattering by a Sphere*, pages 82–129. Wiley-VCH Verlag GmbH, 2007. ISBN 9783527618156. doi: 10.1002/9783527618156.ch4. URL `http://dx.doi.org/10.1002/9783527618156.ch4`.

E. Boss, W. S. Pegau, M. Lee, M. Twardowski, E. Shybanov, G. Korotaev, and F. Baratange. Particulate backscattering ratio at leo 15 and its use to study particle composition and distribution. *Journal of Geophysical Research*, 109 (C1), 2004.

E.J. Botha, V.E. Brando, J.M. Anstee, A.G. Dekker, and S. Sagar. Increased spectral resolution enhances coral detection under varying water conditions. *Remote Sensing of Environment*, 131:247–261, 2013.

V.E. Brando, J. Anstee, M. Wettle, A. Dekker, S. Phinn, and C. Roelfsema. A physics based retrieval and quality assessment of bathymetry from suboptimal hyperspectral data. *Remote Sensing of the Environment*, 113(4):755–770, 2009.

A. Bricaud and A. Morel. Light attenuation and scattering by phytoplanktonic cells: a theoretical modeling. *Applied Optics*, 25(4):571–580, 1986.

A. Bricaud, A. Morel, and L. Prieur. Absorption by dissolved organic matter of the sea (yellow substance) in the uv and visible domains. *Limnology and Oceanography*, 26(1):43–53, 1981.

H. Buiteveld, J. M. H. Hakvoort, and M. Donze. The optical properties of pure water. In J. S. Jaffe, editor, *SPIE Proceedings on Ocean Optics XII*, volume 2258, pages 174–183, 1994.

R.P. Bukata, J.H. Jerome, K.Y. Kondratyev, and D.V. Pozdnyakov. *Optical properties and remote sensing of inland and coastal waters.* CRC Press, Inc., Florida, 1995.

L. Cassata and L. Collins. Coral reef communities, habitats, and substrates in and near sanctuary zones of ningaloo marine park. *Journal of Coastal Research*, 24:1 –40, 2008.

M. Chami, E.B. Shybanov, T.Y Churilova, G.A. Khomenko, M.E.-G. Lee, O.V. Martynov, G.A. Berseneva, and G.K. Korotaev. Optical properties of the particles in the crimea coastal waters (black sea). *Journal of Geophysical Research*, 110, 2005.

Áurea M. Ciotti, Marlon R. Lewis, and John J. Cullen. Assessment of the relationships between dominant cell size in natural phytoplankton communities and the spectral shape of the absorption coefficient. *Limnology and Oceanography*, 47(2):404–417, 2002. URL `http://www.jstor.org/stable/3068986`.

L. Collins. Ningaloo marine park - reef morphology and growth history. Final report, WAMSI, Febuary 2011.

C. Cox and W. Munk. Measurement of the roughness of the sea surface from photographs of the sun's glitter. *Journal of the Optical Society of America*, 44 (11):838–850, 1954.

A.G. Dekker, S.R. Phinn, J. Anstee, P. Bisset, V.E. Brando, B. Casey, P. Fearns, J. Hedley, W. Klonowski, Z.P. Lee, M. Lynch, M. Lyons, C. Mobley, and C. Roelfsema. Intercomparison of shallow water bathymetry, hydro-optics, and benthos mapping techniques in australian and caribbean coastal environments. *Limnology and Oceanography: Methods*, 9:396–425, 2011.

L. M. N. Duysens. The flattening effect of the absorption spectra of suspensions as compared to that of solution. *Biochimica et Biophysica Acta*, 1956.

A. Einstein. Theorie der opaleszenz von homogenen flüssigkeiten und flüssigkeitsgemischen in der nähe des kritischen zustandes. *Annalen der Physik*, 33:1275–1298, 1910.

F. Eugenio, J. Marcello, and J. Martin. High-resolution maps of bathymetry and benthic habitats in shallow-water environments using multispectral remote sensing imagery. *IEEE Transactions on Geoscience and Remote Sensing*, 53 (7), 2015.

Exelis, 2015. URL `http://www.exelisvis.com/ProductsServices/IDL/Language.aspx`.

P.R.C.S. Fearns, W.M. Klonowski, R.C. Babcock, P. England, and J.Phillips. Shallow water substrate mapping using hyperspectral remote sensing. *Continental Shelf Reasearch*, 31(12):1249–1259, 2011.

M. Feng. Oceanic conditions at ningaloo reef—analysis of downscaling ocean climate into the ningaloo reef tract. Technical report, WAMSI, 2011.

R.A. Garcia, P.R.C.S. Fearns, and L.I. McKinna. Detecting trend and seasonal changes in bathymetry derived from hico imagery: A case study of shark bay, western australia. *Remote Sensing of Environment*, 147:186–205, 2014a.

R.A. Garcia, L.I. McKinna, J.D. Hedley, and P.R.C.S. Fearns. Improving the optimization solution for a semi-analytical shallow water inversion model in the presence of spectrally correlated noise. *Limnology and Oceanography: Methods*, 12(10):651–669, 2014b.

R.A. Garcia, J.D. Hedley, J.D. Tin, and P.R.C.S. Fearns. A method to analyze the potential of optical remote sensing for benthic habitat mapping. *Remote Sensing*, 7(10):13157–13189, 2015.

C. Giardino, M. Bartoli, G. Candiani, M. Bresciani, and L. Pellegrini. Recent changes in macrophyte colonisation patterns: an imaging spectrometry-based evaluation of southern lake garda (northern italy). *Journal of Applied Remote Sensing*, 1(011509), 2007.

C. Giardino, M. Bresciani, I. Cazzaniga, K. Schenk, P. Rieger, F. Braga, R. Matta, and V.E. Brando. Evaluation of multi-resolution satellite sensors for assessing water quality and bottom depth of lake garda. *Sensors*, 14(12):24116–24131, 2014.

J. A. Goodman, Z.P. Lee, and S.L Ustin. Influence of atmospheric and sea-surface corrections on retrieval of bottom depth and reflectance using a semi-analytical model: a case study in kaneohe bay, hawaii. *Applied Optics*, 47(28):F1–F11, 2008.

J.A. Goodman and S.L Ustin. Classification of benthic composition in a coral reef environment using spectral unmixing. *Journal of Applied Remote Sensing*, 1(011501), 2007.

H.R. Gordon and O.B. Brown. Influence of bottom depth and albedo on the diffuse reflectance of a flat homogenous (homogeneous) ocean. *Applied Optics*, 13(9):2153–2159, 1974.

H.R. Gordon and A.Y. Morel. *Remote Assessment of ocean colour for satellite visible imagery: A review.* Lecture notes on coastal and estuarine studies. Springer-Verlag, New York, 1983.

H.R. Gordon and M. Wang. Influence of oceanic whitecaps on atmospheric correction of ocean-color sensors. *Applied Optics*, 33(33):7754–7763, 1994.

H.R. Gordon, O.B. Brown, and M.M. Jacobs. Computed relationships between the inherent and apparent optical properties of a flat homogeneous ocean. *Applied Optics*, 14(2):417–427, 1975.

H.R. Gordon, D.K. Clark, J.W. Brown, O.B. Brown, R.H. Evans, and W.W. Broenkow. Phytoplankton pigment concentrations in the middle atlantic bight: comparison of ship determinations and czcs estimates. *Applied Optics*, 22(1): 20–36, 1983.

H.R. Gordon, O.B. Brown, R.H. Evans, J.W. Brown, R.C. Smith, K.S. Baker, and D.K. Clark. A semianalytic radiance model of ocean colour. *Journal of Geophysical Research*, 93(D9):10909–10924, 1988.

W. W. Gregg and K. L. Carder. A simple spectral solar irradiance model for cloudless marine atmospheres. *Limnology and Oceanography*, 35(8):1657 – 1675, 1990.

G.M. Hale and M.R. Querry. Optical constants of water in the 200-nm to 200-μm wavelength region. *Applied Optics*, 12(3):555–562, 1973.

A. W. Harrison and C. A. Coombes. An opaque cloud cover model of sky short wavelength radiance. *Solar Energy*, 41(4):387–392, 1988.

J. Hedley. A three-dimensional radiative transfer model for shallow water environments. *Opt. Express*, 16(26):21887–21902, 2008.

J. Hedley, C. Roelfsema, and S.R. Phinn. Efficient radiative transfer model inversion for remote sensing applications. *Remote Sensing of Environment*, 2009.

J. Hedley, C. Roelfsema, and S. Phinn. Propagating uncertainty through a shallow water mapping algorithm based on radiative transfer model inversion. *Proceedings of Ocean Optics XX*, 2010.

J.D. Hedley and P. J. Mumby. A remote sensing method for resolving depth and subpixel composition of aquatic benthos. *Limnology and Oceanography*, 48(1): 480–488, 2003.

N.K. Højerslev and E. Aas. Spectral light absorption by yellow substances in the kattegat-skagerrak area. *Oceanologia*, 43:39–60, 2001.

H. Holden. Characterisation of optical water quality in bunaken national marine park, indonesia. *Singapore Journal of Tropical Geography*, 23:23–36, 2002.

HyVista Corporation. Hymap data acquisition report, jurien bay, wa. Technical report, HyVista Corporation, North Ryde, 2004.

IOCCG. Remote sensing of ocean colour in coastal, and other optically-complex, waters. Technical Report 3, International Ocean-Colour Coordinating Group, 2000.

W. M. Irvine and J. B. Pollack. Infrared optical properties of water and ice spheres. *Icarus*, 8(324–360), 1968.

R. Iturriaga and D. Siegel. Microphotometric characterization of phytoplankton and detrital absorption properties in the sargasso sea. *Limnology and Oceanography*, 34(8):1706, 1989.

S. Jay and M. Guillaume. A novel maximum likelihood based method for mapping depth and water quality from hyperspectral remote-sensing data. *Remote Sensing of Environment*, 147:121–132, 2014.

N.G. Jerlov. *Marine Optics*. Elsevier Scientific Publishing Company, Amsterdam, 1976. pages 19-20.

G.W. Kattawar and G.N. Plass. Radiative transfer in the earth's atmosphere-ocean system: Ii. radiance in the atmosphere and ocean. *Journal of Physical Oceanography*, 2(2):148–156, 1972.

J. T. O. Kirk. A theoretical analysis of the contribution of algal cells to the attenuation of light within natural waters. 1. general treatements of suspention of living cells. *New Phytologist*, 75:1–20, 1975a.

J. T. O. Kirk. A theoretical analysis of the contribution of algal cells to the attenuation of light within natural waters. 2. spherical cells. *New Phytologist*, 75(21-36), 1975b.

J. T. O. Kirk. A theoretical analysis of the contribution of algal cells to the attenuation of light within natural waters. 3. cyllindrical and spheroidal cells. *New Phytologist*, 77(341-358), 1976.

J.T.O Kirk. *Light and Photsynthesis in aquatic ecosystems*. Cambridge University Press, Cambridge, 1983.

J.T.O. Kirk. Volume scattering function, average cosines, and the underwater light field. *Limnology and Oceanography*, 36(3):455–467, 1991.

M. Kishino, M. Takahashi, N. Okami, and S. Ichimura. Estimation of the spectral absorption coefficients of phytoplankton in the sea. *Bulletin of Marine Science*, 37(634-642), 1985.

W. M. Klonowski. The development and validation of algorithms for remotely sensing case ii waters. Technical report, CSIRO, 2006.

W.M. Klonowski, M.J. Lynch, P.R.C.S. Fearns, and L. Clementson. Hyperspectral remote sensing of western australian coastal waters. *SPIE*, 22(5155-25): 1–10, 2003.

W.M. Klonowski, P.R.C.S. Fearns, and M.J. Lynch. Retrieving key benthic cover types and bathymetry from hyperspectral imagery. *Journal of Applied Remote Sensing*, 1(011505), 2007.

V. O. Kopelevich. Optical properties of pure water in the 250-600nm range. *Opt. Spectrosc*, 41:391, 1976.

G. Kullenberg. Scattering of light by sargasso sea water. *Deep Sea Research*, 15: 423–432, 1968.

C. Le, C. Hu, D. English, Cannizzaro J, Z. Chen, C. Kovach, C.J. Anastasiou, J.Zhao, and K.L. Carder. Inherent and apparent optical properties of the complex estuarine waters of tampa bay: What controls light? *Estuarine, Coastal and Shelf Science*, 117:54–69, 2013.

E. LeDrew, H. Holden, D. Peddle, J. Morrow, R. Murphy, and W. Bour. Towards a proceadure for mapping coral stress from spot imagery with in situ optical

correction. *Proceedings of the 3rd Thematic Conference on Remote Sensing of the Marine Coastal Environment*, 1:211–219, 1995.

Z. P. Lee. *Visible-infrared remote-sensing model and applica- tions for ocean watersits dependence on Sun angles as influenced by the molecular Visible-infrared remote-sensing model and applications for ocean waters.* PhD thesis, Department of Marine Science, University of South Florida, St. Petersburg, Florida, 1994.

Z. P. Lee and K. L. Carder. Effect of spectral band numbers on the retrieval of water column and bottom properties from ocean color data. *Applied Optics*, 41(12):2191–2201, 2002.

Z. P. Lee, K. L. Carder, and K. Du. Effects of molecular and particle scatterings on the model parameter for remote-sensing reflectance. *Applied Optics*, 43(25): 4957–4964, 2004.

Z.P. Lee, K.L. Carder, C.D. Mobley, R.G. Steward, and J.S. Patch. Hyperspectral remote sensing for shallow waters. i. a semianalytic model. *Applied Optics*, 37 (27):6329–6338, 1998.

Z.P. Lee, K.L. Carder, C.D. Mobley, R.G. Steward, and J.S. Patch. Hyperspectral remote sensing for shallow waters: 2. deriving bottom depths and water proprties by optimization. *Applied Optics*, 38(18):3831–3843, 1999.

Z.P. Lee, K.L. Carder, R. F. Chen, and T.G. Peacock. Properties of the water column and bottom derived from airborne visible infrared imaging spectrometer (aviris) data. *Journal of Geophysical Research*, 106(6):11639–11651, 2001.

Z.P. Lee, K.P Du, and R. Arnone. A model for the diffuse attenuation coefficient of downwelling irradiance. *Journal of Geophysical Research*, 110, 2005.

Z.P. Lee, D. Keping, K. J. Voss, G. Zibordi, B. Lubac, R. Arnone, and A. Weidemann. An inherent-optical-property-centered approach to correct the angular effects in water-leaving radiance. *Applied Optics*, 50(19):3155–3167, 2011.

K. Levenberg. A method for the solution of certain non-linear problems in least squares. *The Quarterly of Applied Mathematics*, 2:164–168, 1944.

K. Liou. *An Introduction to Atmospheric Radiation*. Academic Press, New York, 1980.

H. Loisel and A. Morel. Non-isotropy of the upward radiance field in typical coastal (case 2) waters. *International Journal of Remote Sensing*, 22(2):227–295, 1998.

E.M. Louchard, R.P. Reid, F.C. Stephens, C.O. Davis, R.A. Leathers, and T.V. Downes. Optical remote sensing of benthic habitats and bathymetry in coastal environments at lee stocking island, bahamas: A comparative spectral classification approach. *Limnology and Oceanography*, 48:511–521, 2003.

David R. Lyzenga. Passive remote sensing techniques for mapping water depth and bottom features. *Appl. Opt.*, 17 (3):379–383, Feb 1978. doi: 10.1364/AO.17.000379. URL `http://ao.osa.org/abstract.cfm?URI=ao-17-3-379`.

R. A. Maffione and D. R. Dana. Instruments and methods for measuring the backward-scattering coefficient of ocean waters. *Applied Optics*, 36:6057–6067, 1997.

S. Maritorena, A. Morel, and B. Gentili. Diffuse reflectance of oceanic shallow waters: influence of water depth and bottom albedo. *Limnology and Oceanography*, 39(7):1689–1703, 1994.

C. Markwardt. Mpfit, 2012. URL `http://cow.physics.wisc.edu/ craigm/idl/idl.html`.

D. W. Marquardt. An algorithm for least-squares estimation of nonlinear parameters. *Journal of the Society for Industrial and Applied Mathematics*, 11(2): 431–441, 1963.

H. Maske, W.S. Pegau, R. Zaneveld, and R.C. Duarte. Photobleaching of colored dissolved organic matter (cdom) and the temporal and spatial variability of cdom in the gulf of california. In *The 4th Pacific Ocean Remote Sensing Conference*, pages 28–31, Qingdao, China, July 1998.

L.I. McKinna, P.R.C.S. Fearns, S.J. Weeks, J.P. Werdell, M. Reichstetter, B.A. Franz, D.M. Shea, and G.C. Feldman. A semianalytical ocean color inversion algorithm with explicit water column depth and substrate reflectance parameterization. *Journal of Geophysical Research: Oceans*, 120(3):1741–1770, 2015.

G. Mie. Beiträge zur optik trüber medium, speziell kolloidaler metallösungen. *Annalen der Physik*, 1908.

B.G. Mitchell and D.A. Kiefer. Determination of absorption and fluorescence excitation spectra for phytoplankton. In O. Holm-Hansen, L. Bolis, and R. Giles, editors, *Marine Phytoplankton and Productivity*, pages 157–169. Springer-Verlag, Berlin, 1984.

B.G. Mitchell and D.A. Kiefer. Chlorophyll *a* specific absorption and fluorescence excitation spectra for light-limited phytoplankton. *Deep Sea Research*, 35:639–663, 1988.

C. D. Mobley. *Light and Water Radiative Transfer in Natural Waters*. Academic Press Inc., 1994.

C. D. Mobley, B. Gentili, H.R. Gordon, Z. Jin, G.W. Kattawar, A. Morel, P. Reinersman, K. Stamnes, and R.H. Stavn. Comparison of numerical models for computing underwater light fields. *Applied Optics*, 32(36):7484–7504, 1993.

C. D. Mobley, H. Zhang, and K. J. Voss. Effects of optically shallow bottoms on upwelling radiances: Bidirectional reflectance distribution function effects. *Limnology and Oceanography*, 48(1, part 2):337–345, 2003.

C.D. Mobley. Polarized reflectance and transmittance properties of wind-blown sea surfaces. *Applied Optics*, 54(15):4828–4849, 2015.

C.D. Mobley, L.K. Sundman, C. O. Davis, J.H. Bowles, T.V. Downes, R.A. Leathers, M. J. Montes, W.P. Bissett, D. D. R. Kohler, R.P. Reid, E. M. Louchard, and A. Gleason. Interpretation of hyperspectral remote-sensing imagery by spectrum matching and look-up tables. *Applied Optics*, 44(17): 3576–3592, 2005.

Curtis D. Mobley. Estimation of the remote-sensing reflectance from above-surface measurements. *Appl. Opt.*, 38 (36):7442–7455, Dec 1999. doi: 10.1364/AO.38.007442. URL `http://ao.osa.org/abstract.cfm?URI=ao-38-36-7442`.

M. J. Montes, B. Gao, and C. O. Davis. Tafkaa atmospheric correction of hyperspectral data. In *Imaging Spectrometry IX*, volume 5159. SPIE, 2004.

A. Morel. Optical properties of pure water and sea water. In N.G. Jerlov and E. Steeman, Nielsen, editors, *Optical Aspects of oceanography*, chapter 1, pages 1–24. Academic Press Inc., 1974.

A. Morel. Optical modeling of the upper ocean in relation to its biogenous matter content (case 1 waters). *Journal of Geophysical Research*, 93(C9):10749–10768, 1988.

A. Morel and B. Gentili. Diffuse reflectance of oceanic waters: its dependence on sun angle as influenced by the molecular scattering contribution. *Applied Optics*, 30(30):4427–4438, 1991.

A. Morel and L. Prieur. Analysis of variations in ocean color. *Limnology and Oceanography*, 22(4):709–722, 1977.

André Morel and Annick Bricaud. Theoretical results concerning light absorption in a discrete medium, and application to specific absorption of phytoplankton. *Deep Sea Research Part A. Oceanographic Research Papers*, 28(11):1375 – 1393, 1981. ISSN 0198-0149. doi: DOI: 10.1016/0198-0149(81)90039-X.

W. J. Moses, J. H. Bowles, R. L. Lucke, and M. R. Corson. Impact of signal-to-noise ratio in a hyperspectral sensor on the accuracy of biophysical parameter estimation in case ii waters. *Opt. Express*, 20(4):4309–4330, 2012.

J.L. Mueller and G.S. Fargion. *Ocean Optics Protocols for Satellite Ocean Color Sensor Validation, Revision 3, Volume 2*. NASA, Febuary 2002.

J.L. Mueller and G.S. Fargion. Ocean optics protocols for satellite ocean color sensor validation, revision 4, volume ii:. Nasa/tm-2003-21621/rev-vol ii, NASA, 2003.

J.L. Mueller, G.S. Fargion, and C. R. McClain. Ocean optics protocols for satellite ocean color sensor validation, revision 5, volume v:. Nasa/tm-2003/rev-vol v, NASA, 2003.

P. J. Mumby, C. D. Clarke, E. P. Green, and A. J. Edwards. Benefits of water column correction and contextual editing for mapping coral reefs. *International Journal of Remote Sensing*, 19:203–210, 1998.

P.J. Mumby, J.R.M. Chisholm, C.D. Clark, J.D. Hedley, and J. Jaubert. A bird's-eye view of the health of coral reefs. *Nature*, 413(36), 2001.

F. E. Nicodemus, J. C. Richmond, J. J. Hsia, I. W. Ginsberg, and T. Limperis. Geometrical considerations and nomenclature for reflectance. Nbs monograph, National Bureau of Standards, 1977.

A. Pacheco, J. Horta, C. Loureiro, and Ó. Ferreira. Retrieval of nearshore bathymetry from landsat 8 images: A tool for coastal monitoring in shallow waters. *Remote Sensing of Environment*, 159:102–116, 2015.

T.J. Petzold. Volume scattering functions of selected ocean waters. In J.E. Tyler, editor, *Light in the sea - Benchmark Papers in Optics*, volume 3, pages 152–174. Dowden, Hutchison & Ross, Inc., Stroudsburg, Pennsylvania, 1977.

William D. Philpot. Bathymetric mapping with passive multispectral imagery. *Appl. Opt.*, 28(8):1569–1578, Apr 1989. doi: 10.1364/AO.28.001569. URL `http://ao.osa.org/abstract.cfm?URI=ao-28-8-1569`.

G.N. Plass and G.W. Kattawar. Monte carlo calculations of radiative transfer in the earth's atmosphere-ocean system: I. flux in the atmosphere and ocean. *Journal of Physical Oceanography*, 2(2):139–147, 1972.

R. M. Pope. *Optical absorption of pure water and sea water using the integrating cavity absorption meter.* PhD thesis, Texas A&M University, 1993.

R.M. Pope and E.S. Fry. Absorption spectrum (380-700 nm) of pure water. ii integrating cavity measurements. *Applied Optics*, 36(33):8710–8723, 1997.

R.W. Preisendorfer. Application of radiative transfer theory to light measurements in the sea - union geod. geophys. inst. Monograph No. 10, 1961.

R.W. Preisendorfer. Application of radiative transfer theory to light measurements in the sea. In John E. Tyler, editor, *Light in the Sea*, chapter 3. Dowden, Hutchinson & Ross, Inc. Stroudsburg, Pennsylvania, 1977.

L. Prieur and S. Sathyendranath. An optical classification of coastal and oceanic waters based on the specific spectral absorption curves of phytoplankton pigments, dissolved organic matter, and other particulate materials. *Limnology and Oceanography*, 26(4):671–689, 1981.

M. R. Querry, D. M. Wieliczka, and D. J. Segelstein. Water (H_2O). In *Handbook of Optical Constants of Solids II*, pages 1059–1077. Academic Press, 1991.

L.L. Richardson and E.F. LeDrew. Remote sensing and the science, monitoring, and management of aquatic coastal ecosystems. In L.L. Richardson and E.F. LeDrew, editors, *Remote Sensing of Coastal Aquatic Environments: Science and Management Applications*. Springer, 2006.

W. Rock, M. Bonn, and S. H. Parekh. Near shot-noise limited hyperspectral stimulated raman scattering spectroscopy using low energy lasers and a fast cmos array. *Opt. Express*, 21(13):15113–15120, 2013.

C.S. Roesler and M.J. Perry. Modeling in situ phytoplankton absorption from total absorption spectra in productive inland marine waters. *Limnology and Oceanography*, 34(8):1510–1523, 1989.

C.S. Roesler and M.J. Perry. In situ phytoplankton absorption, fluorescence emission, and particulate backscattering spectra determined from reflectance. *Journal of Geophysical Research*, 100(C7):13279–13294, 1995.

S. Sathyendranath, L. Prieur, and A. Morel. A three-component model of ocean colour and its application to remote sensing of phytoplankton pigments in coastal waters. *International Journal of Remote Sensing*, 10(8):1373–1394, 1989.

C. H. L. Schönberg and J. Fromont. Sponge gardens of ningaloo reef (carnarvon shelf, western australia) are biodiversity hotspots. *Hydrobiologica*, 687(1):143–161, 2012.

R.A. Serway, C.J. Moses, and C.A. Moyer. *Modern Physics*. Saunders College Publishing, 2nd edition edition, 1997.

K.S. Shifrin. Physical optics of ocean water. Master's thesis, Institue of Physics, College Park, 1988.

R.C. Smith and K.S. Baker. Optical properties of the clearest natural waters. *Applied Optics*, 20(2):177–184, 1981.

M. Smoluchowski. Molekular-kinetische theorie der opaleszenz von gasen im kritischen zustande, sowie einiger verwandter erscheinungen. *Annalen der Physik*, 25:205–226, 1908.

W.A. Snyder, R.A. Arnone, C. O. Davis, W. Goode, R.W. Gould, S. Ladner, G. Lamela, W.J. Rhea, R. Stavn, M. Sydor, and A. Weidemann. Optical scattering and backscattering by organic and inorganic particulates in u.s. coastal waters. *Applied Optics*, 47(5), 2008.

F. M. Sogandares. *The spectral absorption of pure water*. PhD thesis, Texas A&M University, August 1991.

D. J. Stegelstein. *The complex refractive index of water*. PhD thesis, University of Missouri-Kansas City, 1981.

R.P. Stumpf and K. Holderied. Determination of water depth with high-resolution satellite imagery over variable bottom types. *Limnology and Oceanography*, 48 (1):547–556, 2003.

R.P. Stumpf and K. Holderied. Determination of water depth with high-resolution satellite imagery over variable bottom types. *Limnology and Oceanography*, 48 (1, Part 2):547–556, 2004.

J. M. Sullivan and M. Twardowski. Angular shape if the oceanic particulate volume scattering function in the backward direction. *Applied Optics*, 48(35): 6812–6819, 2009.

J. M. Sullivan, M. Twardowski, R. Zaneveld, C. Moore, A. Barnard, P. Donaghay, and B. Rhoades. Hyperspectral temperature and salt dependencies of absorption by water and heavy water in the 400-750 nm spectral range. *Applied Optics*, 45(21):5294–5309, 2006.

S. A. Sullivan. Experimental study of the absorption in distilled water, artificial sea water, and heavy water in the visible region of the spectrum. *Journal of the Optical Society of America*, 53(962–968), 1963.

A. C. Tam and C. K. N. Patel. Optical absorption of light and heavy water by laser optoacoustic spectroscopy. *Appl. Opt.*, 18:3348–3358, 1979.

M.S. Twardowski, E. Boss, J.M. Sullivan, and P.L. Donaghay. Modelling the spectral shape of absorption by chromophoric dissolved organic matter. *Marine Chemistry*, 89:69–88, 2004.

J.E. Tyler. Scattering properties of distilled and natural waters. *Limnology and Oceanography*, 6(4):451–456, 1961.

M. Tzortziou, J.R. Herman, C.L. Gallegos, P.J. Neale, A. Subramaniam, L.W. Harding Jr, and Z. Ahmad. Bio-optics of the chesapeake bay from measurements and radiative transfer closure. *Estuarine, Coastal and Shelf Science*, 68(1-2):348–362, 2006.

K. J. Voss, A. Chapin, M. Monti, and H. Zhang. Instrument to measure the bidirectional reflectance distribution function of surfaces. *Applied Optics*, 39: 6197–6206, 2000.

C.S. Yentsch. Measurement of visible light absoprtion by particulate matter in the ocean. *Limnology and Oceanography*, 7:207–217, 1962.

R.J. Zaneveld, M.J. Twardowski, A. Barnard, and M.R. Lewis. Intoduction to radiative transfer. In R.L. Miller, C.E. Del Castillo, and B.A. McKee, editors, *Remote Sensing of Coastal Aquatic Environments: Technologies, Techniques and Applications*. Springer, 2005.

H. Zhang, K. J. Voss, R. P. Reid, and E. M. Louchard. Bidirectional reflectance measurements of sediments in the vicinity of lee stocking island, bahamas. *Limnology and Oceanography*, 48:380–389, 2003.

M.L. Zoffoli, R. Frouin, and M. Kampel. Water column correction for coral reef studies by remote sensing. *Sensors*, 14(9):16881–16931, 2014.

material. I would be pleased to hear from any copyright owner who has been omitted or incorrectly acknowledged.